UNIVERSIY OF LJUBLJANA
FACULTY OF MATHEMATICS AND PHYSICS
DEPARTMENT OF PHYSICS

Andrej Mihelič

FLUORESCENCE OF DOUBLY EXCITED STATES OF HELIUM IN HOMOGENEOUS ELECTRIC FIELD

Doctoral thesis

ADVISER: doc. dr. Matjaž Žitnik

Ljubljana, 2006

Andrej Mihelič

FLUORESCENCA DVOJNO VZBUJENIH STANJ HELIJEVEGA ATOMA V HOMOGENEM ELEKTRIČNEM POLJU

Doktorska disertacija

MENTOR: doc. dr. Matjaž Žitnik

Ljubljana, 2006

Abstract

The Stark effect on doubly excited states of helium atom is investigated below the $N = 2$ threshold and for high electric field strengths. The ground state photoionisation and inelastic photon scattering cross sections are calculated ab initio. The method of complex scaling is used to completely take into account the bound-continuum and continuum-continuum interactions. A CI approach is used to represent the nonrelativistic Stark Hamilton operator in a Sturmian basis set with several pairs of nonlinear scaling parameters. The treatment includes the calculation of free atom eigenstates and eigenenergies of singly and doubly excited states below $N = 2$ with principal quantum numbers $n \leq 15$, of both parities, and with the total orbital angular momenta $L \leq 10$. These zero field states are used to expand the eigenstates of the helium atom in the non zero external electric field. The effect of radiation damping is taken into account by calculating fluorescence rates of singly and doubly excited states in the electric field. A series of measured photoionisation cross sections is compared to calculations for electric field strengths up to 84.4 kV/cm. The present theory describes well the prominent spectral features even at high field strengths for the incident polarisation perpendicular to the external field ($\boldsymbol{F} \parallel \boldsymbol{P}$), whereas only theoretical predictions could be given for the perpendicular setup ($\boldsymbol{F} \perp \boldsymbol{P}$). It is shown that the propensity rule holds also in this geometry: the majority of the ion signal originates from the states with a similar correlation pattern as the states from the principal $a\ ^1P^o$ series, the most likely excited from the ground state. Theoretical fluorescence yields are in good agreement with VUV and primary fluorescence yields measured as functions of the incoming photon energy. While the method can be extended to give reliable results also for higher series members, the present calculations are limited to interpret measured spectral features for n up to $10 - 11$. The series of prominent peaks that appear in the spectra recorded with the polarisation perpendicular to the field are shown to evolve from $^1P^e$ zero field states. Furthermore, the decrease in intensity of the $(n-1)c/nb\ ^1P^o$ doublet is attributed to coupling of optically allowed $^1P^o$ states to strongly autoionising $^1S^e$ (for $\boldsymbol{F} \parallel \boldsymbol{P}$) and $^1D^e$ resonances (for $\boldsymbol{F} \parallel \boldsymbol{P}$ and $\boldsymbol{F} \perp \boldsymbol{P}$), whereas the broad peaks following the $na\ ^1P^o$ resonances near the $N = 2$ threshold are shown to originate from field induced dark states with high angular momenta. In addition, the validity of the same propensity rule from photoionisation is confirmed explicitly for the case of fluorescence decay in both experimental geometries, $\boldsymbol{F} \parallel \boldsymbol{P}$ and $\boldsymbol{F} \perp \boldsymbol{P}$.

Povzetek

Obravnavamo Starkov efekt na dvojno vzbujena stanja helijevega atoma pod ionizacijskim pragom $N = 2$ za visoke električne poljske jakosti. Iz prvih principov izračunamo fotoionizacijski presek za atom v osnovnem stanju in presek za neelastično sipanje fotonov. Uporabljena je metoda kompleksne rotacije, s katero so v račun vključene interakcije tipa vezano stanje-kontinuum in kontinuum-kontinuum. Rešitve nerelativističnega Hamiltonovega operatorja za atom v električnem polju iščemo z mešanjem konfiguracij. Operator zapišemo v bazi Sturmovih funkcij z različnimi pari nelinearnih parametrov za oba elektrona. Obravnava obsega izračun lastnih stanj in pripadajočih lastnih energij enojno in dvojno vzbujenih stanj prostega atoma obeh parnosti z glavnimi kvantnimi števili $n \leq 15$ in celotnimi tirnimi vrtilnimi količinami $L \leq 10$. Po teh stanjih razvijemo lastna stanja atoma v zunanjem električnem polju. Učinke radiativnega razpadnega kanala upoštevamo z izračunom verjetnosti za fluorescenčni razpad enojno in dvojno vzbujenih stanj v električnem polju. Izmerjene fotoionizacijske preseke primerjamo z izračunanimi za električne poljske jakosti do 84.4 kV/cm. Model dobro opiše strukture, ki so prisotne v izmerjenih spektrih, tudi pri visokih poljskih jakostih tedaj, ko je polarizacija vpadne svetlobe usmerjena vzdolž zunanjega električnega polja ($\boldsymbol{F} \parallel \boldsymbol{P}$). Za primer $\boldsymbol{F} \perp \boldsymbol{P}$ podamo teoretične napovedi. Pokažemo, da velja prednostno pravilo fotoionizacije tudi v tej geometriji: večina izrazitih vrhov izhaja iz stanj s podobnim korelacijskim značajem, kot ga imajo stanja glavne serije $a\ ^1P^o$, ki jih najverjetneje vzbudimo iz osnovnega stanja. Tudi izračunani fluorescenčni pridelki se dobro ujemajo z izmerjenimi pridelki VUV in primarne fluorescence. Metoda, ki smo jo uporabili, je načeloma lahko zanesljiva tudi pri višjih Rydbergovih stanjih, vendar lahko v okviru trenutne računske sheme obravnavamo stanja s kvantnimi števili n do približno 10 ali 11. Pokažemo, da izvira serija močnih vrhov v spektrih s pravokotno usmerjeno polarizacijo ($\boldsymbol{F} \perp \boldsymbol{P}$) iz stanj, ki imajo v polju nič simetrijo $^1P^e$. Zmanjšanje dubleta $(n-1)c/nb\ ^1P^o$ smo pripisali sklopitvi z resonancami simetrije $^1S^e$ (za $\boldsymbol{F} \parallel \boldsymbol{P}$) in $^1D^e$ (za $\boldsymbol{F} \parallel \boldsymbol{P}$ in $\boldsymbol{F} \perp \boldsymbol{P}$), za katere je zelo verjeten avtoionizacijski razpad. Pokazali smo, da so široki vrhovi, ki sledijo resonancam tipa $a\ ^1P^o$ v bližini praga $N = 2$, posledica stanj z visokimi vrtilnimi količinami, ki jih lahko vzbudimo v prisotnosti električnega polja. V nadaljevanju smo potrdili, da velja že omenjeno prednostno pravilo tudi za fluorescenčni razpad pri obeh orientacijah polarizacije vpadne svetlobe, $\boldsymbol{F} \parallel \boldsymbol{P}$ in $\boldsymbol{F} \perp \boldsymbol{P}$.

Contents

Chapter 1

Introduction

1.1 Overview

The helium atom represents the simplest nontrivial quantum mechanical system that is easy to manipulate experimentally. As such it has been a subject of many practical and theoretical studies since the early days of quantum physics [1]. The availability of tunable synchrotron radiation sources was essential for the first direct observation of helium doubly excited states in photoabsorption spectra by Madden and Codling in 1963 [2]. It immediately became clear that electrons in these states are strongly correlated [3]: a single configuration description of doubly excited states with two electrons moving independently in the average centrally symmetric potential is no longer adequate, not even in the zero order approximation. For the satisfactory explanation of the measured spectra, the electron-electron correlation should be considered explicitly. This stimulated the search for the corresponding good quantum numbers which still continues today [4].

All doubly excited states lie above the first ionisation threshold of helium at 24.587 eV ($N = 1$) and below the double ionisation threshold at 79.003 eV ($N \to \infty$). The energy diagram is schematically presented in Fig. 1.1. Most of the lowest lying states decay very fast by autoionisation. The weakest of the three dipole allowed $^1P^o$ series of states converging to the second ionisation threshold at 65.399 eV ($N = 2$), the so called c series, was detected in a photoionisation spectrum only 15 years ago [5]. The resonance profiles are very narrow and challenge the ultimate performance of synchrotron beamlines [6].

Autoionisation to the He$^+$ continuum was considered from the beginning to be the strongest decay channel of doubly excited states, and the ion yield measurements were taken as a fair measure of the absorption spectrum. Although fluorescence decay of these states was the first signature of their existence [7], it was believed to be of negligible importance until the recent experimental search for metastable atoms and photons clearly showed the presence of fluorescence in the resonant decay scheme below $N = 2$ [8]. This invoked a fresh interest in studying doubly excited states over the last decade, especially for spectroscopic purposes, because the fluorescence lines are not broadened due to the interaction with continuum [9]. Basically, the following reaction is studied:

$$
\begin{aligned}
\mathrm{He}(1s^2) + \gamma(\omega_0) \to \Psi_i &\to \mathrm{He}^+ + \mathrm{e}^- \,, && \text{autoionisation} \\
&\to \mathrm{He}(1snl) + \gamma(\omega \approx 40 \text{ eV}) \,, && \text{primary fluorescence} \\
&\hookrightarrow \mathrm{He}(1snl') + \gamma(\omega' \approx 2 \text{ eV}) \,, && \text{secondary fluorescence} \\
&\quad \cdots \\
&\qquad \hookrightarrow \mathrm{He}(1s^2) + \gamma(\omega''^{\cdots} \approx 20 \text{ eV}) \,,
\end{aligned}
$$

$$\text{(1.1)}$$
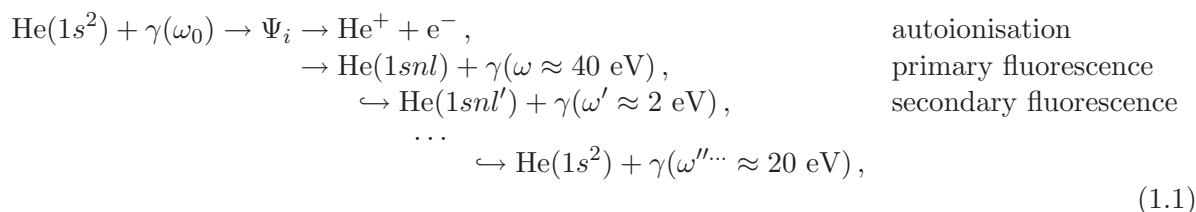
where Ψ_i denotes the resonant state below $N = 2$. It is easy to understand that the primary fluorescence transition of an inner electron should be more probable than autoionisation, at least for higher lying members of doubly excited state series (high n), when the average inter electron separation becomes large. The limiting value of n depends on the character of the Rydberg series and may not be extremely high. In fact, for the weak $^1P^o$ series mentioned above, the fluorescence decay is already more probable than autoionisation for the first member of the series [10]. The difference between the photoabsorption and photoionisation spectra for the lowest members of this series was demonstrated explicitly by Prince et al. [11]. Similar situation occurs for autoionising resonances $[2s]np$ $^1P^o$ in neon. The experimental study reported a signal of fluorescence decay and showed that it dominates the autoionisation for $n > 27$ [12].
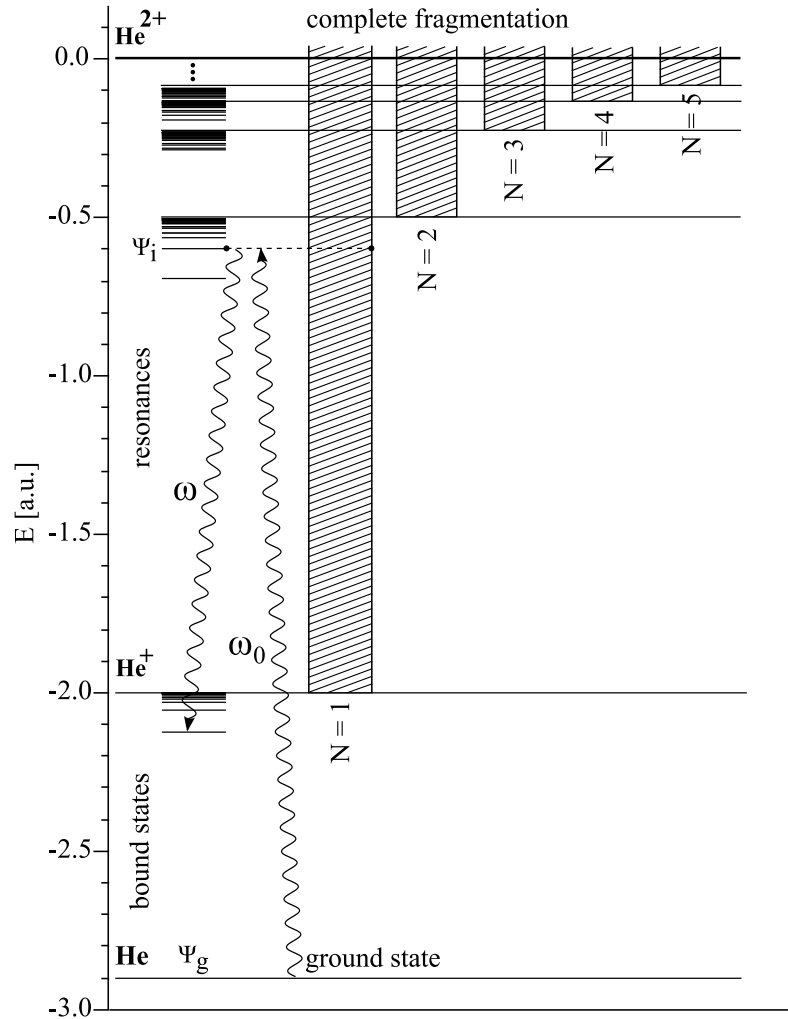
Figure 1.1: Schematic energy diagram of helium. In this work we study the photoexcitation of resonances below $N = 2$ threshold in the static electric field and their decay by the autoionisation (dotted line) and fluorescence.

Another consequence of ever larger separation of the Rydberg electron from the core is that fine (hyperfine) structure interaction of the inner electron with the nucleus becomes stronger than Coulomb interaction with the outer electron. When n approaches the threshold, the LS coupling scheme turns into the jK coupling [13]. This change is reflected in the shape of the helium

fluorescence spectrum and calls for relativistic description of the process in the region of high Rydberg states. Indeed, an excellent agreement of the calculated jK fluorescence probabilities with the measurements was demonstrated close to the $N = 2$ threshold [14]. In argon absorption spectrum, the low lying LS-forbidden states were already observed in 1969 [15], and also very recently, in the photoelectron spectra as a pair of mirroring resonances in $Ar^+[3p]_{1/2,3/2}$ cross sections [16]. One of the first absorption spectra in neon taken with synchrotron light was interpreted completely within the LS coupling scheme, except for the presence of two Rydberg series converging to the $Ne^+[2p^2]3s\ ^2P$ threshold [17]. It was most surprising that in helium, three of four series of triplet states with total angular momentum $J = 1$ were observed in the recent high resolution photoexcitation study below $N = 2$ threshold, this time in the fluorescence decay channel [9, 18]. A relatively simple experimental technique which favours observation of triplet states by the efficient detection of metastable atoms made it possible to observe triplet-singlet mixing already in the perturbative regime as shown later on in detail [19, 20]. The predicted angular distributions of emitted VUV photons were soon confirmed experimentally [21]. Spectra of primary and secondary emitted photons were patiently collected to verify the occurrence of predicted transitions and their relative yields [22–24].

A few years ago, the research started also in the time domain. Calculations show that the fluorescence of all doubly excited states bellow $N = 2$ display lifetimes of the order of 100 ps. This is similar to 99.717 ± 0.0075 ps, the lifetime of $2p$ state of the He^+ ion which is excited only above the $N = 2$ threshold and fluoresces into He^+ $1s$ [25]. With some effort, such lifetimes can nowadays be directly measured by recording the exponentially decaying flux of emitted photons upon pulsed excitation. The first member of the weakest $^1P^o$ series, the $3c$ state, for which the fluorescence is a dominant decay channel, was predicted to have a lifetime of 206 ps [19] and 194 ps [20]. The effect is explained to occur for doubly excited state due to the Stark mixing of an inner electron in the rotating electric field of an outer electron which generates a series specific admixture of $2p$ and $2s$ orbitals occupied by the inner electron which most probably makes a fluorescence transition [26]. The predictions were not far from the direct measurement, which reported the value of 190 ± 30 ps [27]. Later measurements for higher members of the same series show that the lifetime increases with n, as also suggested by calculations [28, 29]. On the other hand, the autoionisation of $^3D^o$ series below $N = 2$ is parity-forbidden. The lifetime of the first member of the series ($n = 3$) was measured by a beamfoil technique [30] and was determined to be 110 ± 20 ps, again in agreement with the theoretical description [20].

The field effects on the helium oscillator strength distribution in the energy region close to the first ionisation threshold was studied previously in detail [31]. Modelling of the field effect has mainly concentrated on transitions from the ground state of hydrogen [32, 33], since the hydrogen atom is the only atomic system for which the full separability of coordinates is possible in a non zero electric field. The Stark effect in helium was first studied many years ago by recording fluorescence from low singly excited states [34]. Later it provided a definitive test [35] of the quantum mechanical treatment given by Schrödinger [36]. The helium absorption spectrum around $N = 1$ shows similarity of the field dependent oscillator strength distribution with that of the hydrogen atom approaching the ionisation limit [31]. The oscillator strength distribution in the zero electric field above the ionisation limit only weakly depends on the energy, and below the limit the only contributions arise from the single $1s^2 \rightarrow 1snp$ series, similar to the hydrogen case. It was shown that the same tools (relatively small hydrogen-like basis and diagonalisation) can be used to explain the measured absorption spectrum.

It is much more complicated to understand the behaviour of helium doubly excited states. Many of predicted states are not accessible by simple photoabsorption, and it is of great fundamental interest to experimentally verify their existence, theoretical energies and other properties.

The energies of singlet and triplet S, P, D, and F doubly excited states of He below the $N = 2$ threshold have been calculated by Lipsky et al. [37], Liu et al. [19] and Chen (Ref. [38] and the references therein). There are ten singlet S, P, and D series below $N = 2$: two $^1S^e$, three $^1P^o$, one $^1P^e$, one $^1D^o$, and finally three $^1D^e$ series. This can be easily verified by composing the relevant two electron configurations. Beside the three optically allowed $^1P^o$ series, to date also some members of the $^3P^o$ and $^3D^o$ series have been studied [9, 18]. The first term of the $^1D_2^e$ series has been detected in angle resolved photoelectron spectra [39], and some of the low lying terms with $n \leq 5$ of $^1S^e$, $^{1,3}P^o$, and $^1D_2^e$ series have been studied by electron scattering [40, 41]. However, none of the six even series can be observed in simple photoabsorption due to the selection rule requiring a parity change.

Forbidden states of even parity can be made Stark allowed in an electric field, but detailed examination of the Stark effects on these doubly excited states is just beginning. Chung et al. [42] estimated that field strengths of about 50 kV/cm are necessary to observe the effects on doubly excited resonances below $N = 2$ and for $n = 6$, and this estimate appears reasonable: fields up to 500 kV/cm were employed to induce Stark effect in the related three body system, the hydrogen negative ion [43]. The photoionisation cross section was measured with the field parallel to the polarisation of the incoming light for the field strengths up to 84.4 kV/cm supporting this estimate [44]. Harries et al. concentrated on the energy region of $6a - 8a$ $^1P^o$ states below $N = 2$, which was found previously to be convenient for the implementation of the complex rotation saddle point method [42]. The calculated Stark map was essentially confirmed by the measurements, showing a wealth of new structures in the photoionisation spectrum. The propensity rule was proposed to predict the subsets of doubly excited states that are preferentially populated in such experiments [45]. It was also shown theoretically that the spin-orbit effect negligibly interferes with the Stark effect in the energy region of low lying resonances [46]: while the former provides a coupling of singlet and triplet states with the same parity, the later effect couples odd and even states with the same spin multiplicity.

1.2 Motivation and outlook

To explore the advantage of the fluorescence spectroscopy in the case of the Stark effect, it is important to quantify the fluorescence yield from dark (even) states or, in other words, to determine the fraction of the allowed $^1P^o$ symmetry in the states submitted to static electric fields. Beside the above mentioned photoionisation data which are still not reproduced in full, several measurements of the fluorescence and metastable atom yield were done recently by the research groups of Penent et al., Rubensson et al., Prince et al., and Harries et al. using the beamtimes at synchrotron Elettra (Trieste), Bessy2 (Berlin), Photon Factory (Tsukuba) and ALS (Berkeley). They investigate the effect of field strengths of a few kV/cm on the primary and secondary fluorescence below $N = 2$, in the energy, as well as in the time domain. The model input is absolutely essential for the interpretation of the acquired data, due to the wealth of new structures and decay paths which open in the nonzero field. It is a goal of this work to provide, at least partially, that missing model.

Firstly, there are indications from the VUV yield measurements [47] that previously unobserved higher members of $^1D^e$ and $^1P^e$ series can be detected at relatively weak electric field strengths compared to those used by Harries et al. [44]. To interpret this data we have used a perturbation approach to generate the first theoretical estimates of the total primary VUV fluorescence yield emitted by even parity resonances, after the photoexcitation of helium with linearly polarised light. This path, together with results, is described in Chapter 3 of this work, after some initial general observation about helium quantum states and the corresponding

experimental techniques are presented in Chapter 2.

Becoming aware of the limitations of the first order perturbation, we set to perform the non perturbative calculations based on the exact consideration of bound-continuum coupling in the frame of the method of complex scaling and retaining to the lowest order the coupling of the atom with the photon field. Realisation of this method, whose general principles and numerical implementation are described in Chapters 4 and 5, together with presentation of the results in Chapter 6, is our main achievement and occupies the rest of this work. By using a screened Sturmian basis and including total orbital angular momenta up to $L = 10$, we were able to reproduce measured photoionisation spectra in detail and predict the outcome of the similar measurements in the perpendicular geometry, taking into account the existence of the fluorescence channel. Considering carefully the inelastic photon scattering from the resonances calculated in the complex space, we could also calculate the total emitted photon yield depending on the incoming photon energy in the energy region of doubly excited states. This is compared to the above mentioned VUV photon yield measurements in the parallel and perpendicular geometry. The knowledge of theoretical photoionisation spectrum is very important here, since the data is partially contaminated by the spurious fluorescence signal unavoidably generated by electrons and ions hitting the electric field capacitor. Extracting theoretical values, we can also compare our calculations with a recent measurement of $^1P^e$ lifetimes in the electric field, which indicate a more prompt photon emission when the electric field strength is increased [48]. This effect can be attributed to the gradual opening of the otherwise forbidden autoionisation channel with the presence of the field which destroys the LS symmetry of the states. Due to the large but still finite size of the basis set, the accuracy of our calculations starts to diminish for the states with $n > 13$. As such, they complement a very recent study which also models doubly excited states in weak electric fields, but employs R matrix multichannel quantum defect theory to focus on the states with $n > 12$ [49].

Finally, Appendices A-E are added to list most of the details of calculations and to contain extended tables of the theoretically deduced properties of doubly excited states like energy positions, decay probabilities and asymmetry parameters which are also among essential results but rather boring to enter the main part of the work.

Hartree atomic units ($\hbar, m_e, e = 1$, $4\pi\epsilon_0 = 1$, $c = 1/\alpha$, cf. Appendix A) are used throughout this work, unless explicitly stated.

Chapter 2

Helium doubly excited states

2.1 A standard CI approach

The helium atom in an externally applied time independent homogeneous electric field is described by the Hamilton operator

$$H = H_0 + \Delta H \,, \qquad H_0 = \frac{\boldsymbol{p}_1^2}{2} + \frac{\boldsymbol{p}_2^2}{2} - \frac{Z}{r_1} - \frac{Z}{r_2} + \frac{1}{|\boldsymbol{r}_1 - \boldsymbol{r}_2|} \,,$$
$$\Delta H = -\boldsymbol{F} \cdot (\boldsymbol{r}_1 + \boldsymbol{r}_2) \,. \tag{2.1}$$

Above H_0 and ΔH denote the free atom Hamiltonian and the interaction of the atom with the electric field. The nucleus is taken as infinitely heavy and point-like, with charge $Z = 2$, $\boldsymbol{r}_1$, $\boldsymbol{r}_2$ and $\boldsymbol{p}_1$, $\boldsymbol{p}_2$ are the coordinates and the momenta of the two electrons, respectively, and $\boldsymbol{F}$ is the electric field vector.

We will be concerned with finding eigenstates of H for different values of F at energies approaching the ionisation thresholds. Keeping away from the very threshold, we can omit the (hyper)fine interaction from the calculation scheme and relay on the finite (but large) basis set. Although the inclusion of these effects was essential to understand the spectrum of the metastable atom, the contribution of photons emitted from triplets to the fluorescence yield in the zero field was found negligible if n was not excessively large. The interaction with the static electric field does not change that since it cannot generate singlet-triplet mixing. About 70 meV below $N = 2$ (this roughly corresponds to $n = 13$), the situation gradually changes as altogether seven LS series with $J = 1$ become interleaved, converging to the three slightly distinct thresholds of the helium ion: $2p_{1/2}$, $2p_{3/2}$, and $2s_{1/2}$. In that region, the measured ion and photon yield spectra severely depart from the LS prediction, as already mentioned.

Note that non relativistic free Hamiltonian H_0 does not favour any particular direction in space and therefore commutes with the square of the total orbital angular momentum operator $\boldsymbol{L}^2 = (\boldsymbol{l}_1 + \boldsymbol{l}_2)^2$ and the corresponding projection operator L_z. The total angular momentum L and its projection M are good quantum numbers, as well as obviously are the total spin S and its projection M_S. The states with different M and/or M_S are degenerate. From the inversion symmetry displayed by H_0 it follows that parity π is a good quantum number, too.

Opposite to the hydrogen case, the exact eigenfunctions of Eq. (2.1) cannot be found. One can construct very crude hydrogen like solutions assuming that both electrons move independently in the spherically symmetric Coulomb potential of the helium nucleus. Still better, the electron-electron interaction can be approximately accounted for by absorbing its central part into some effective spherically symmetric single electron potential, either by introduction of the

Coulomb screening (e.g., using the rules of J.C. Slater [50] or of M. Kregar [51]) or determined by the radial screening and radial orbitals by the self-consistent Hartree-Fock (HF) procedure based on minimisation of the configuration state energy [52]. In any of this cases, the solution is expressed by two single electron orthonormal wavefunctions

$$\langle \boldsymbol{q}_1 | n_1 l_1 m_1 m_{s_1} \rangle \qquad \text{and} \qquad \langle \boldsymbol{q}_2 | n_2 l_2 m_2 m_{s_2} \rangle . \tag{2.2}$$

As in the hydrogen case, they are described by the principal (radial) quantum numbers n_1 and n_2, the orbital and magnetic quantum numbers l_1, m_1 and l_2, m_2, and the spin magnetic quantum numbers m_{s_1} and m_{s_2}. The shorthand notation $\boldsymbol{q}_i = (\boldsymbol{r}_i, \sigma_i)$, $i = 1, 2$, has been introduced, where $\boldsymbol{r}_i$ denotes electron position coordinates and σ_i the components of the spins along the quantisation axis. A simple product of two electron function is usually replaced by linear superposition to generate the eigenfunction of $LMSM_S$ with parity π [13, 53],

$$\langle \boldsymbol{q}_1, \boldsymbol{q}_2 | n_1 l_1 n_2 l_2 LMSM_S \pi \rangle =$$
$$\sum_{\substack{m_1, m_{s_1} \\ m_2, m_{s_2}}} (l_1 m_1 l_2 m_2 | LM)(1/2\, m_{s_1} 1/2\, m_{s_2} | SM_S) \langle \boldsymbol{q}_1 | n_1 l_1 m_1 m_{s_1} \rangle \langle \boldsymbol{q}_2 | n_2 l_2 m_2 m_{s_2} \rangle . \tag{2.3}$$

Clebsch-Gordan coefficients are denoted by $(l_1 m_1 l_2 m_2 | LM)$ and $(1/2\, m_{s_1} 1/2\, m_{s_2} | MM_S)$. Further on, the wavefunction is antisymmetrised with respect to the $\boldsymbol{q}_1 \leftrightarrow \boldsymbol{q}_2$ interchange,

$$\begin{aligned} \psi_{LMSM_S\pi}^{n_1 l_1 n_2 l_2}(\boldsymbol{q}_1, \boldsymbol{q}_2) &\equiv \langle \boldsymbol{q}_1, \boldsymbol{q}_2 | \psi_{LMSM_S}^{n_1 l_1 n_2 l_2} \rangle \\ &= \mathcal{N} \big[\langle \boldsymbol{q}_1, \boldsymbol{q}_2 | n_1 l_1 n_2 l_2 LMSM_S \rangle - \langle \boldsymbol{q}_2, \boldsymbol{q}_1 | n_1 l_1 n_2 l_2 LMSM_S \rangle \big] . \end{aligned} \tag{2.4}$$

The normalisation constant $\mathcal{N}$ is determined by the condition

$$\| \psi_{LMSM_S\pi}^{n_1 l_1 n_2 l_2} \|^2 = 1 . \tag{2.5}$$

Using the symmetry property of the Clebsch-Gordan coefficients

$$(j_2 m_2 j_1 m_1 | jm) = (-1)^{j_1 + j_2 - j} (j_1 m_1 j_2 m_2 | jm) , \tag{2.6}$$

Eq. (2.4) becomes

$$\psi_{LMSM_S\pi}^{n_1 l_1 n_2 l_2} = \mathcal{N} \big[\langle \boldsymbol{q}_1, \boldsymbol{q}_2 | n_1 l_1 n_2 l_2 LMSM_S \rangle + (-1)^{L+S+l_1+l_2} \langle \boldsymbol{q}_1, \boldsymbol{q}_2 | n_2 l_2 n_1 l_1 LMSM_S \rangle \big] . \tag{2.7}$$

For equivalent electrons ($n_1 = n_2 \equiv n$, $l_1 = l_2 \equiv l$), the coupled wavefunctions are equal, and Eq. (2.7) simplifies further to

$$\psi_{LMSM_S\pi}^{nlnl} = \mathcal{N} \big[1 + (-1)^{L+S} \big] \langle \boldsymbol{q}_1, \boldsymbol{q}_2 | nlnl LMSM_S \rangle . \tag{2.8}$$

Eq. (2.8) represents a physically meaningful state only when $L + S$ is even. Eqs. (2.5), (2.7), and (2.8) give the normalisation constant equal to

$$\mathcal{N} = \begin{cases} 1/2 & \text{; equivalent electrons} \\ 1/\sqrt{2} & \text{; otherwise} \end{cases} \tag{2.9}$$

Parity π of the state is odd (o) if $l_1 + l_2$ is odd, and even (e) otherwise.

The functions (2.8) and (2.7) both represent single configuration approximation to the solution of H_0. If such approximation can yield satisfactory results for singly excited states of helium, this is in general not so for strongly correlated doubly excited states. The predictions

of the oscillator strength for the ground state excitations, the autoionisation probabilities, and also the fluorescence decay rates can be wrong for order of magnitudes [54]. To refine the results for singly excited states or to obtain usable approximation for doubly excited states in the zero field, one should allow the ith solution of the eigenvalue problem to be expressed as linear combination of the configuration states with the same $LMSM_S\pi$ numbers, the so-called configuration interaction (CI),

$$|\psi_i\rangle = \sum_{\substack{n_1,n_2 \\ l_1,l_2}} c_i^{n_1 n_2 l_1 l_2} |\psi_{LMSM_S\pi}^{n_1 l_1 n_2 l_2}\rangle. \tag{2.10}$$

The importance of such mixings in doubly excited He was first considered by Cooper, Fano and Prats [3] with their "$\pm$" classification of the $(2snp \pm 2pns)\,^1P^o$ Rydberg series. If a large number of appropriately selected configurations is included into the CI basis set, a substantial number of eigenenergies and eigenfunctions can be accurately obtained solely by diagonalisation of the matrix representation of H_0. Even more precise for small scale calculations is the approach where, for each state separately, the configuration weights and the shapes of radial orbitals are optimised by the self consistent MCHF procedure [52], but it may be sometimes hard to obtain the convergence.

2.2 Correlation quantum numbers

Very successful attempts to economically describe doubly excited states have been done in the past by using the so-called Hylleraas coordinates r_1, r_2 and r_{12} [55]. The state correlation pattern cannot depend on the three Euler angles which determine the orientation of the electron-nucleus-electron system. These can be filtered out of H_0. The solution of the rest is sought variationally as a linear combination of the Hylleraas coordinate (power) products describing the shape of the triangle. The triple integrals involved in the procedure are more difficult to deal with than the two dimensional radial integrals from the CI method, after the problem has been reduced by using the standard angular algebra. Anyway, the correlation pattern which is incorporated into CI solutions can be accessed easily by projecting out the Euler angles [56].

In general, as mentioned above, we hope in vain that a set of single electron quantum numbers n_1, n_2, l_1, l_2 would complete the collection of good quantum numbers for doubly excited states. There have been many efforts in the past to find the quantum numbers which would account as much as possible for the effect of electron-electron interaction. Due to the practical reasons, namely to present the state notation often employed by other references, we are going to mention briefly some attempts to find these quantum numbers for doubly excited states in the zero electric field. The validity of these, still approximate solutions, are generally checked against those obtained by using the large-scale conventional configuration interaction (CI) method, described above.

The approach, yielding two new quantum numbers K and T was presented by Herrick and Sinanoğlu [57]. The numbers resulted from the method involving diagonalisation of an operator $B^2 = (\boldsymbol{b}_1 - \boldsymbol{b}_2)^2$, where $\boldsymbol{b}_1$ and $\boldsymbol{b}_2$ are proportional to the Runge-Lenz vector for electrons 1 and 2, respectively [58]. The strong point of the DESB approach is that it predicts quite well (but not exactly) the intrashell mixings of two electron degenerate hydrogenic configurations (e.g., $2s^2 : 2p^2\,^1S^e$) subjected to electron-electron interaction. For given L and N, the ranges of K and T are determined as follows:

$$
\begin{aligned}
T &= 0, 1, \ldots, \min\{L, N-1\}, \\
\pm K &= N - T - 1, N - T - 3, \ldots, 1 \text{ (or 0)}.
\end{aligned}
\tag{2.11}
$$

For the states with $\pi = (-1)^{L+1}$, $T = 0$ is not allowed.

These two integer numbers are convenient indices for labelling angular correlations. In fact, K and T had also been used to label asymptotic dipole states for scattering systems like $\mathrm{e}^- - \mathrm{H}$, $\mathrm{e}^- - \mathrm{He}^+$, $\mathrm{e}^- - \mathrm{Li}^{2+}$, etc. [59], i.e., they label Stark states which have long range dipole interaction. In terms of the asymptotic properties of the two electrons, K is proportional to the average value of $r_1 \cos \theta_{12}$, where θ_{12} is the angle at which the two electrons are seen from the nucleus. T describes the magnitude of the overlap $\boldsymbol{l}_1 \cdot \hat{\boldsymbol{r}}_2$, or roughly speaking, the relative orientation between the orbitals of the two electrons. If the two electron orbits are on the same plane, then $T = 0$ [60].

Finally, the third new approximate quantum number which describes radial correlation arises from the well established quasi separability of H_0 in hyperspherical coordinates: the wave functions are expressed as $F_\mu^n(R)\Phi_\mu(R; \alpha, \hat{\boldsymbol{r}}_1, \hat{\boldsymbol{r}}_2)$ where hyperradius $R = \sqrt{r_1^2 + r_2^2}$ and hyperangle $\alpha = \arctan(r_2/r_1)$ describe the size and radial asymmetry of the atom, respectively. Lin [60] was able to relate the channel index μ to the apparent quantum number A which can assume only three values: 0 and ± 1. Channel functions Φ_μ either exhibit exactly or approximately an antinode ($A = +1$) or a node ($A = -1$) at $\alpha = \pi/4$. Channels that do not have either properties are assigned to have $A = 0$, and are similar to singly excited states of two electron atoms.

The classification scheme valid for all states of two electron atoms in the zero electric field assigns to a given doubly excited state a set of (exact and approximate) quantum numbers $nNLS\pi(K, T)^A$. According to the scheme, there are three dipole allowed $^1P^o$ series converging to the $N = 2$ threshold: $(0, 1)^+$, $(1, 0)^-$, and $(-1, 0)^0$. The last one is the previously mentioned weakly autoionising c series.

It is still a matter of investigation, also of this work, to what extent the approximate quantum numbers are conserved in the non zero electric field. To model the photoionisation and fluorescence yield spectra in the field, we have selected to use the *all in one* CI approach since we have to handle many states at many different field values. We choose to denote doubly excited states by very practical and simple notation scheme, which was introduced by Lipsky et al. [37]: the energetically lowest lying state with given $LS\pi$ symmetry above the $N - 1$ ionisation threshold is denoted as the first member of Rydberg a series, the second lowest lying state which does not fit into the Rydberg sequence of the a series is denoted as the first member of Rydberg b series, etc. The members of the same series are enumerated by means the quantum number n, starting from the lowest available value (this can be checked by considering different configurations of given $LS\pi$ symmetry where the (inner) electron is restricted to $n_1 = N$). It can be shown that below $N = 2$, only a small number of different Rydberg series with a given $LS\pi$ symmetry exist: (a, b) $^1S^e$, (a) $^1P^e$, (a, b, c) $^1P^o$, (a) $^1D^o$, (a, b, c) $^1D^e$, etc. Except for the $^1S^e$ symmetry, there are always 3 different singlet series when $L + \pi$ is even and 1 series otherwise. The rule is different and numbers are larger for series converging to higher ionisation thresholds. This notation maps 1:1 onto the $(K, T)^A$ classification scheme of Lin [60].

2.3 The Stark effect

As mentioned above, the approximate quantum numbers of field free helium doubly excited states bear some resemblance to the Stark quantum numbers which are used to describe the states of the hydrogen atom exposed to the homogeneous electric field. To make the understanding easier, we review below the basic characteristic of the latter system.

It is well known that, besides in spherical coordinates r, θ, and φ, the Schrödinger equation for the hydrogen atom is also separable in parabolic coordinates $r(1 - \cos \theta)$, $r(1 + \cos \theta)$, and φ [58]. The solutions can be written in the analytical form and are characterised by a set of

parabolic quantum numbers N_1, N_2, and m, where N_1 and N_2 take nonnegative integer values, and m has the usual meaning. This set exactly substitutes the usual spherical quantum numbers nlm by using the correspondence

$$n = N_1 + N_2 + |m| + 1 \,. \tag{2.12}$$

The energy spectrum of the hydrogen atom consists of bound states ($E \leq 0$) and continuum ($E > 0$). When the field is turned on ($F > 0$), there are no longer bound states – the energy spectrum is absolutely continuous. Fig. 2.3 shows the cross section of an attractive Coulomb well potential modified by the field presence. Note the lowering of the ionisation threshold for $-2\sqrt{F}$ and the finite thickness of the potential barrier on one side, due to which the tunnelling probability becomes different from zero. Physically, the atom would always ionise in the field direction if enough time were available. The bound hydrogenic wavefunctions become resonances in the field, and are labelled by the parabolic quantum number N_2 (it is conserved in the field since the potential on the other side of the well becomes even more confining), the magnetic quantum number m and the (continuous) energy E, which replaces N_1. The separation of the Schrödinger equation in parabolic coordinates is still effective in the non zero field. Although equations cannot be solved in the closed analytic form, they can be integrated numerically to any degree of accuracy [61]. Their properties close to the threshold can be efficiently studied by the non perturbative complex rotation method [62], which will be presented later in Chapter 4.
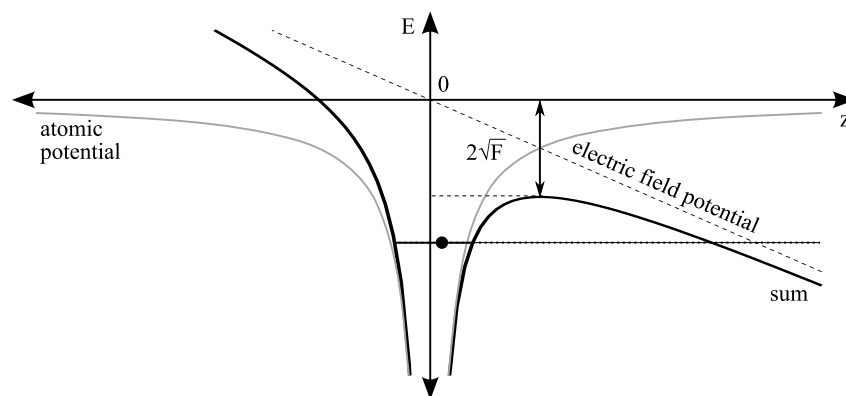
Figure 2.1: The Coulomb potential of the nucleus is modified by the external static electric field, allowing an electron to tunnel through the barrier.

However, for the *former* bound states deep in the potential well, the coupling to continuum is vanishingly small. Below the classical saddle point, the main effect of the field is to mix the neighbouring states with different parabolic quantum numbers but the same m, projection of the angular momentum l on the field direction. Apart from the spin degrees of freedom, m is the only remaining good quantum number in the non zero field, since l_z commutes with the electron coordinate along the field direction. Partially removing degeneracy, the mixing occurs first within the same manifold n, but as the field strength is increased, the states with the same m value from many manifolds become involved. The hydrogen atom in its first excited state behaves as though it had a permanent electric dipole moment of magnitude 3 that can be oriented in three different ways: one state parallel to the external field ($N_1 = 0$, $N_2 = 1$, $m = 0$), one state antiparallel to the field ($N_1 = 1$, $N_2 = 0$, $m = 0$), and two states with zero component along the field: $(0,0,1)$ and $(0,0,-1)$ [58].

E = -62.77 eV, (1,0)$^{-}$

$\Gamma = 185$ ns^{-1}

$\gamma = 5.2$ ns^{-1}

E = -63.68 eV, (0,1)$^{+}$

$\Gamma = 10000$ ns^{-1}

$\gamma = 7.2$ ns^{-1}

E = -64.12 eV, (-1,0)^{0}

$\Gamma = 0.18$ ns^{-1}

$\gamma = 4.9$ ns^{-1}
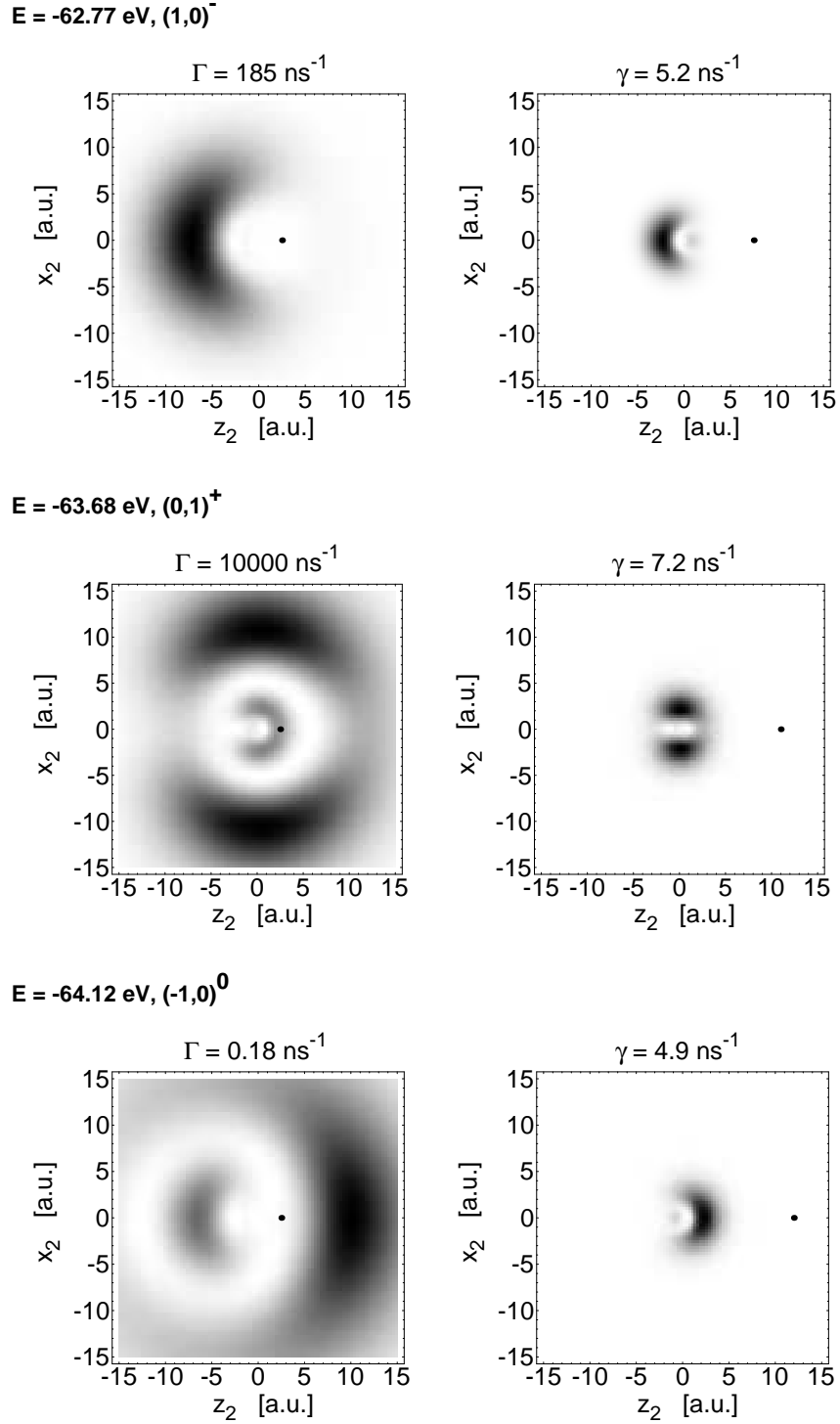
Figure 2.2: Conditional probability densities for the second electron in $n = 3$, $N = 2$, $^{1}P_{1}^{o}$ doubly excited states in He with no electric field. The nucleus is in the centre of the plot. The position of the first electron is marked by the black circle. Each state is denoted by $(K,T)^{A}$ numbers, the energy E, the autoionisation decay rate Γ, and the fluorescence decay rate γ.

The parabolic quantum numbers characterise correctly the dynamics of the helium doubly excited state if the outer electron is far away from the nucleus so that it merely creates a (constant) electric field for the inner one. The above mentioned classification scheme for helium is equivalent to the Stark scheme for the hydrogen atom, namely [4]

$$K = N_2 - N_1, \quad T = |m|. \tag{2.13}$$

Using that rule, one can immediately construct three (K, T) pairs of numbers, which match exactly those written above for the case of $^1P^o$ series converging to $N = 2$ threshold. In fact, since the rule involves neither L or π, it is valid for all singlet series converging to $N = 2$. The exception is $^1S^e$ symmetry, where only two series of this kind exist, and the series with $\pi = (-1)^{L+1}$ (for the latter, only one series exist). The maps of the conditional reduced probability density calculated from the correlated states $^1P^o$ with $n = 3$ clearly reveal the Stark character which follows from the state notation (Fig. 2.3) [56].

The information on the third approximate quantum number A is lost in the parabolic/DESB classification. It was shown to appear naturally in the two centre adiabatic approach [63], as the eigenvalue of the body-fixed electron exchange operator, which can assume only values ± 1. As mentioned above, Lin used the same values to mark the presence of antinodal/nodal line in the hyperspherical adiabatic wavefunctions, but used also $A = 0$ for no apparent symmetry with respect to line $r_1 = r_2$.

2.4 Propensity rules

Beside selection rules, which are strict and rely on good quantum numbers, propensity rules also exist that are based on approximate quantum numbers. These control, to some extent, the strength of the radiative and non radiative transitions to and from doubly excited states. The degree of accuracy of the propensity rules is checked by experiments and, eventually, by the precise large scale calculations. Below we describe only the zero field propensity rules, although recently the rules for the non zero electric field started to appear [45]. They will be discussed later in Chapter 6.

In general, the $(K, T)^+$ states autoionise with higher probability than the other states with the same n and N, regardless of their LS symmetry. The electrons in states with $A = +1$ are on average closer to each other than in the states which do not display the antinode at $r_1 = r_2$ (Fig. 2.3). The autoionisation widths of the corresponding $A = -1$ (0) states are usually two orders of magnitude smaller. The + states with $n = 3$ and $N = 2$ have largest widths. They are of the order of 100 meV, and can be easily directly measured [9]. Along the series, the autoionisation width decreases as n^{-3}. The oscillator strength for the ground state photoexcitation of dipole allowed $^1P^o$ states behaves exactly the same way [10, 18].

The propensity rule for the radiative dipole transitions applied to the ground state photoabsorption gives a preference to $\Delta T = 1$ transition. Since $T = 0$ for the ground state, there is only one $^1P^o$ series with $T = 1$ converging to ionisation threshold N that fulfils this condition. The predominant excitation of one, the so called *principal series* below the $N = 2 - 4$ thresholds was, first confirmed by experiments of Woodruff and Samson [64].

This approximate selection rule can be qualitatively understood in classical terms, as presented by Lin [60]. In the ground $^1S^e$ state, correlation between the two orbits of the two electrons are coplanar ($T = 0$) but of opposite senses, so that both electrons can approach the nucleus simultaneously ($A = +1$). Upon receiving the angular momentum and energy from the photon, it is easier for one of the electrons to change its orbit to a different orientation, such that

two orbits are no longer coplanar ($T = 1$), while at the same time the sense of rotation ($A = +1$) is maintained. To end up with $A = -1$ states, one of the electrons, after photoabsorption, has to change its sense of rotation and this is much harder than just changing the orientation of the orbit. However, the de Broglie wavelength for each electron is quite long and this explanation should not be taken too literally. For transitions between doubly excited states Rost et al. have given more elaborated propensity rules based on the analysis of the adiabatic molecular model of helium [4].

2.5   Experimental

In 1960's, at the beginning of the synchrotron radiation era, Madden and Codling performed classical photoabsorption experiments in the VUV region on several noble gases [2, 15, 17]. After passing through the gas cell, the attenuated photon signal was recorded on a photographic plate and read out by densitometer. Later on, these measurements were replaced by the ion current measurements if the incoming photon energy was above the first ionisation threshold. He^+ ions produced by the light were collected by a two parallel plate arrangement with the bias potential of few tens of volts [5].

Historically, the Stark effect was investigated by observing fluorescence from discharge sources [34], which were improved to reach the field strengths of over 1000 kV/cm [65]. For experiments in which the excitation step needs to be controlled, discharge sources are unsuitable, and the field is usually applied using two parallel plates. There is a large literature on studies of laser photoexcitation in an electric field, for example [66–68]. Such experiments reach field strengths of up to around 150 kV/cm, and achieve very high energy resolution, but they are limited to the region around the first ionisation thresholds due to the status of the present laser technology. In the important case of hydrogen, a two step laser excitation has been used to reach the ionisation threshold [69]. Extremely high effective field strengths of up to 2500 kV/cm can be obtained by making use of the fact that a relatively small static magnetic field in the laboratory frame can be experienced as a very large static electric field in the rest frame of relativistic particles [70]. These experiments aim to study situations which are out the focus of our work. We are interested in modelling the photoion and fluorescence signals in energy regions where the states and fields effects can still be reasonably well resolved by the presently available energy resolution of VUV beamlines which is of the order of 1 meV.
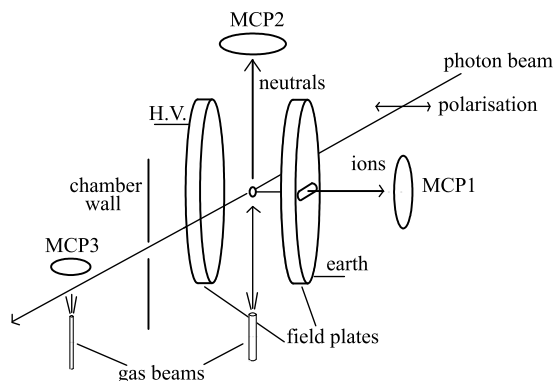
Figure 2.3: The experimental setup of Harries et al. [44] for measuring the yield of photoions in high electric fields.

Although one may argue that the above mentioned zero field photoionisation experiments were in fact done in a very weak electric field, this subject was thoroughly studied only recently. Harries et al. built an apparatus by which they were able to collect ion signal from the gas at very high fields, up to 120 kV/cm [71]. The experiment was performed at synchrotron undulator beamlines BL-16B of the Photon Factory (Tsukuba) and BL 10.0.1 of the Advanced Light Source (Berkeley, CA).

Two electrodes made from high grade stainless steel with a low carbon content are separated by 1 cm (variable). They straddle the interaction region. High voltage is applied to one of the plates, and the other plate is grounded (Fig. 2.3). The electrodes were carefully polished with a diamond paste to a smooth finish, and have edges rounded to 2 mm radius. In order to detect the photoions, the earthed electrode has a slit, behind which a microchannel plate (MCP) detector assembly is placed (labelled MCP1 in Fig. 2.3). A further detector assembly, labelled MCP2, is placed above the electrodes, and is sensitive to neutral particles, namely VUV photons with energies above around 10 eV and long lived excited neutral atoms (metastables with internal energy of above around 10 eV). Another detector, labelled MCP3, is placed in a separate vacuum chamber and is set up in such a way that zero field spectra (detecting either photoions or neutral particles) can be recorded simultaneously with the in-field spectra in the main chamber. Each in-field spectrum can be immediately calibrated in photon energy relative to the zero field spectrum. The geometry of the apparatus is fixed, so with standard synchrotron source beamlines that deliver light with a linear polarisation in the horizontal plane they were limited to studying the effects of an electric field parallel to the polarisation vector of the incoming radiation.

One of the main issues involved was calibration of the electric field strength. The effective plate separation, which differs from the actual one due to the effect of the slit and of the edges, was determined by measuring the shift in $N = 1$ ionisation potential of He as a function of voltage V applied to the high voltage electrode. This was done by recording the ion yield by MCP1. Classically, in units of kV/cm and meV the shift in IP is given by $\Delta_{\mathrm{IP}} = 24\sqrt{V/d_{\mathrm{eff}}}$. The fit to the results showed that the effective plate separation is $d_{\mathrm{eff}} = 0.845$ cm. The calibration procedure for MCP2 detector consisted of measuring the fluorescence yield from photoexcited Rydberg states below $N = 1$. The modelled spectrum fitted well the spectrum recorded in the region of $n = 6 - 8$ manifold of states if $d_{\mathrm{eff}} = 0.9$ cm.
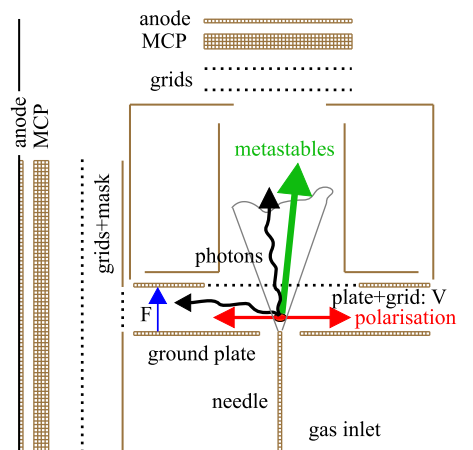
Figure 2.4: The experimental setup of Penent et al. [9, 21, 26] for detecting the yield of VUV photon and metastable atoms in low electric fields.

Setup for measuring VUV photon yield in weak fields (up to about 10 kV/cm) is actually quite simple, as shown in Fig. 2.4. The advanced version of the apparatus, which was installed at the Gasphase beamline at synchrotron Elettra (Trieste), can be rotated around direction of the incoming photon beam and allows the measurements in both geometries, with electric field vector parallel or perpendicular to the polarisation of the incoming light [72]. The lower electrode is grounded and has a hole for the needle tip through which the gas leaks into the target region. The upper electrode with non zero potential has a grid opening to allow particles to exit toward the upper MCP. This is equipped by additional two grids, which are able to prevent electrons and ions from hitting the MCP front surface if properly biased. The side MCP also has two grids and a mask to restrict its field of view to the interaction region. A similar setup is used by two other research groups which recently investigated the fluorescence yield in the field. Rubensson et al. [10] installed an additional thin aluminium filter in front of the MCP to discriminate between the primary ($\approx$ 40 eV) and secondary fluorescence (photon energy is bellow 24 eV). Coreno et al. [24] used a scintillator crystal (YAG) to convert VUV photons into the visible photons with 10% efficiency. Visible photons are counted by the standard photomultiplier. Dispersion grating spectrometers were also used to study in detail the energy distribution of the primary [22, 23] and secondary fluorescence [73]. The data, especially in the former case, are acquired tremendously slow due to very low collection efficiency.
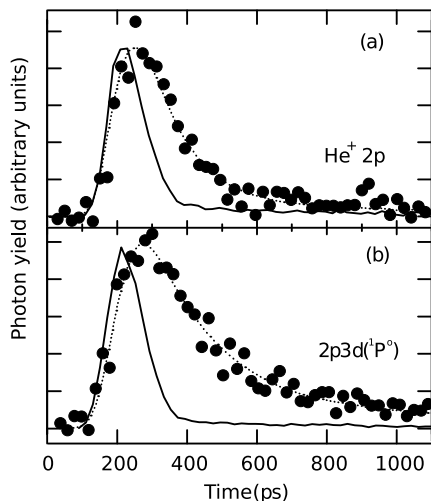
Figure 2.5: The time histograms recorded just above the $N = 2$ threshold (a) and below the threshold on the resonance 3c $^1P^o$ [27]. The full line represents the instrumental time broadening.

A setup similar to the one shown in Fig. 2.4 was used to study fluorescence in the time domain (Fig. 2.5). In this case the time difference is measured by time-to-amplitude converter (TAC) between START given by a detected VUV photon and a delayed STOP which marks the arrival time of the incoming light pulse. The time jitter introduced by combination of MCP, preamplifier, constant fraction discriminator, and TAC is of the order of 80 ps, allowing the measurements of lifetimes which are longer than few tens of ps. The instrumental function is measured by recording time histograms of the incoming photons which are elastically scattered of the needle tip (movable) toward the detector [27], or by taking the fluorescence signal from a very short lived resonance with the lifetime below 1 ps [29].

Chapter 3

Perturbative treatment

At the beginning, we investigate the simplest possible approach to quantify the fluorescence yield from doubly excited states in the electric field – the first order perturbation. As it was shown long ago by Lipsky et al. [37], in the zero field and below the $N = 2, 3$ ionisation thresholds, the low lying doubly excited states ($n < 8$) can be adequately described by a CI basis set of moderate size (approximately 50 configurations for each $LS\pi$ symmetry). One can then calculate the oscillator strengths for the ground state photoexcitation, and also the autoionisation and fluorescence decay probability of doubly excited states [20]. This is sufficient to estimate the primary and the secondary fluorescence yields for comparison with the experimental data [18], but not enough to predict the yield of photoions, since the coupling of bound states to continuum is entirely neglected.

Very recent VUV photon yield measurements from helium doubly excited states in a weak electric field of the order of few kV/cm indicated the presence of the signal from previously unobserved higher members of $^1D^e$ and $^1P^e$ series with n ranging from $6 - 10$ [47]. Since this observation concerns the fluorescence channel, it may be possible to explain it within the standard CI approach. To this purpose, we have extended the CI basis set to obtain reliable description of the zero order (zero field) doubly excited states up to $n = 10$. These states were then employed to compute the states perturbed by the field and, further on, to estimate primary fluorescence yields from these states. It comes out that the first order perturbation scheme may be applied to the problem up to $n = 10$ for a particular experimental geometry if the electric field strength F is not larger than approximately 5 kV/cm [74].

3.1 First order perturbation

Due to the non zero electric field, the dipole allowed $^1P^o$ zero order states are mixed into the $^1S^e$, $^1P^e$, and $^1D^e$ zero order states. The first order even singlet state with the projection M of the angular momentum L is given by

$$|\psi_i\,^1L^e, M\rangle_1 \approx |\psi_i\,^1L^e, M\rangle + \sum_j a_{ij}(M)|\psi_j\,^1P^o, M\rangle + \dots, \qquad (3.1)$$

where the sum over j runs over all $^1P^o$ resonances and index i counts the resonances within the same $^1L^e$ series according to the increasing energy. Only $L = 0, 1, 2$ and $M = \pm 1, 0$ contribute with the non zero expansion coefficients a_{ij}; selecting z axis along the electric field direction,

the coefficients are expressed as

$$a_{ij}(M) = -F(-1)^{1-M} \begin{pmatrix} 1 & 1 & L \\ -M & 0 & M \end{pmatrix} \frac{\langle \psi_j \,^1P^o \| \mathcal{D} \| \psi_i \,^1L^e \rangle}{E_i - E_j},$$ (3.2)

where the reduced dipole operator in the length form is expressed by $\mathcal{D} = r_1 C^1(\hat{\boldsymbol{r}}_1) + r_2 C^1(\hat{\boldsymbol{r}}_2)$. C^1 is the reduced spherical tensor of rank one [75]. Note that $a_{ij}(0) = 0$ for $^1P^e$ states and $a_{ij}(\pm 1) = 0$ for $^1S^e$ states. The two electron reduced matrix elements and state energies E_i were calculated by the ATSP codes [52]. The same package was employed to obtain CI expansions of the zero order $^1S^e$, $^1P^e$, $^1D^e$, and $^1P^o$ states. Non relativistic Hamiltonian for helium was diagonalised in the basis of hydrogen-like ($Z = 2$) two electron LS coupled configurations, including electron orbitals with $n \leq 15$ and $l \leq 4$,

$$|\psi_i \,^1L^\pi\rangle = \sum_{\substack{n_1,n_2 \\ l_1,l_2}} c_i^{n_1 n_2 l_1 l_2} |n_1 l_1 n_2 l_2 \,^1L^\pi\rangle .$$ (3.3)

This was sufficient to obtain reliable representation of states up to $n = 10$ for each of the four LS symmetries investigated, which extends the range of calculations of [20, 37] without further loss of precision. Note that the first order Stark energy correction of all these states is zero, and the energy shift of the resonances in the weak electric field can be safely neglected for the present purpose. As mentioned, in the absence of good quantum numbers we prefer to denote different series by letters in order of appearance as in [37, 44], but keep the LS notation which is still not excessively violated in the weak fields. There are 3 series (a, b, c) with $^1P^o$ and $^1D^e$ symmetry, 2 series (a, b) with $^1S^e$ symmetry, and a single $^1P^e$ a series converging to the $N = 2$ threshold. The translation to $(K, T)^A$ approximate correlation quantum numbers for each series is straightforward [60].

The photoabsorption cross section of even states depends on the orientation of the polarisation vector $\boldsymbol{P}$ of the incoming light with respect to the electric field direction. For perpendicular and parallel orientation, the length form yields

$$\sigma_i^{\perp,\|} = \frac{4}{3}\pi^2 \alpha E_i \left| \sum_j a_{ij}(1,0) \langle \psi_j \,^1P^o \| \mathcal{D} \| \psi_g \,^1S^e \rangle \right|^2,$$ (3.4)

where $|\psi_g \,^1S^e\rangle$ is the helium ground state wavefunction, represented by 21-term MCHF expansion [52], and E_i is the energy of doubly excited state above the ground state. Obviously, there is no photoexcitation of $^1S^e$ states in perpendicular orientation and there is no photoexcitation of $^1P^e$ states in parallel orientation because the corresponding coefficients in Eq. (3.4) vanish identically. The even states are therefore aligned by the photoexcitation process in the presence of weak electric field, whereas the alignment of $^1P^o$ states is still negligible. Under the same circumstances, $\sigma_i^\perp = \frac{3}{4}\sigma_i^\|$ for $^1D^e$ states.

We note that at 5 kV/cm first order perturbation scheme cannot fully describe the $^1S^e$ - $^1P^o$ coupling. Specifically, choosing $a_{ij}^2 < 0.1$ as a validity criterion, this is not fulfilled for pairs of states $(n + 1)b$ - nb, $(n + 3)a$ - $(n + 3)b$ and $(n + 1)b$ - $(n + 1)c$ for $n > 4$. The electric field should remain below 2 kV/cm to obtain valid mixing coefficients up to $n = 10$. For this reason, but also because the calculated energy separation between $^1S^e$ na, $^1S^e$ $(n - 1)b$, $^1P^o$ nb and $^1P^o$ $(n - 1)c$ states is similar to the error in calculated energy positions which introduces further uncertainty of the coefficient values, it has no sense to report the results for $^1S^e$ and $^1P^o$ series in the non zero field with parallel orientation $\boldsymbol{F} \parallel \boldsymbol{P}$. On the other hand, there are no problems in this respect with $^1D^e$ - $^1P^o$ and $^1P^e$ - $^1P^o$ coupling for $n \leq 10$, unless $F > 5$ kV/cm.

The zero field data for $n = 8$ [20] allow to estimate the absolute square of the spin-orbit coupling coefficient of the $^1P^o$ states by using the n^6 extrapolation [18]. The strongest spin-orbit coupling appears between $10a$ $^1P^o$ and $10a$ $^3D^o$ state, and reaches approximately 6% of the absolute square of the largest Stark mixing coefficients [Eq. (3.2)] at 5 kV/cm. Then, by magnitude, the spin orbit coupling is roughly comparable to the Stark coupling at about 1 kV/cm and produces only small effects in the primary fluorescence spectrum for low lying doubly excited states. Both perturbations are practically decoupled for $n \leq 10$ and the field strengths under consideration.

To generate primary fluorescence yields we need to estimate autoionisation decay rates Γ of doubly excited states into the only accessible $\text{He}^+(1s)$ continuum. For the first order states,

$$\frac{\Gamma_i(^1L^e)}{2\pi} = |A_i(^1L^e)|^2 + \begin{cases} \left|\sum_j a_{ij}(1)A_j(^1P^o)\right|^2, & \boldsymbol{F} \perp \boldsymbol{P} \\ \left|\sum_j a_{ij}(0)A_j(^1P^o)\right|^2, & \boldsymbol{F} \parallel \boldsymbol{P} \end{cases} \tag{3.5}$$

$$\frac{\Gamma_i(^1P^o)}{2\pi} = |A_i(^1P^o)|^2 + \begin{cases} \frac{2}{3}\left|\sum_j a_{ji}(1)A_j(^1D^e)\right|^2, & \boldsymbol{F} \perp \boldsymbol{P} \\ \frac{1}{3}\sum_{L=S,D}\left|\sum_j a_{ji}(0)A_j(^1L^e)\right|^2, & \boldsymbol{F} \parallel \boldsymbol{P} \end{cases} \tag{3.6}$$

The matrix elements A_j of electron-electron Coulomb repulsion between the zero order states (3.3) are obtained by the standard technique [53]. Explicitly, they are given by

$$A_i(^1S^e) = \sum_{n_1,n_2,l} c_i^{n_1 n_2 ll} \begin{Bmatrix} 1 \\ 2^{-1/2} \end{Bmatrix} \frac{(-1)^l}{\sqrt{[l]}} \left[R^l(1s\,\epsilon_i s, n_1 l\, n_2 l) + R^l(\epsilon_i s 1s, n_1 l\, n_2 l) \right],$$

$$A_i(^1P^o) = \sum_{n_1,n_2,l} c_i^{n_1 n_2 l(l+1)} (-1)^l \sqrt{l+1} \left[\frac{R^l(1s\,\epsilon_i p, n_1 l\, n_2(l+1))}{[l]} \right.$$

$$\left. + \frac{R^{l+1}(\epsilon_i p\, 1s, n_1 l\, n_2(l+1))}{[l+1]} \right], \tag{3.7}$$

$$A_i(^1D^e) = \sum_{n_1,n_2,l,l'} c_i^{n_1 n_2 ll'} \begin{Bmatrix} 1 \\ 2^{-1/2} \end{Bmatrix} \begin{pmatrix} 2 & l & l' \\ 0 & 0 & 0 \end{pmatrix} \left[\sqrt{\frac{[l']}{[l]}} R^l(1s\,\epsilon_i d, n_1 l\, n_2 l') \right.$$

$$\left. + \sqrt{\frac{[l]}{[l']}} R^{l'}(\epsilon_i d\, 1s, n_1 l\, n_2 l') \right].$$

In Eq. (3.7), a shorthand notation $[l] = 2l + 1$ has been introduced. The upper and lower normalisation constant in curly braces are used for non equivalent and equivalent electrons, respectively. The continuum waves $\epsilon_i l$ of the ejected electron were calculated in He^+ $1s$ potential by the GRASP code [76, 77]. For each resonance, ϵ_i equals $E_i - E(\text{He}^+ 1s)$, as required by energy conservation. Slater two dimensional radial integrals are denoted by R^l [53].

Finally, for each resonance we have calculated fluorescence decay rates into the dipole allowed *singly* excited atomic states $|\psi_s\,^1L'^\pi\rangle$ and with principal quantum number $n \leq 12$ and total angular momentum $L' \leq 3$. These states are again described by MCHF expansion. The primary fluorescence rate from the i-th resonance state in the zero electric field is given by $\gamma_i = \sum_s \gamma_{is}$, where

$$\gamma_{is} = \frac{4[\alpha(E_i - E_s)]^3}{3(2L+1)} |\langle \psi_s\,^1L'^{\pi+1} \|\mathcal{D}\| \psi_i\,^1L^\pi \rangle|^2. \tag{3.8}$$

In Eq. (3.8), E_s denotes the energy of the singly excited state $|\psi_s\,^1L'^{\pi+1}\rangle$.

State	E_i	f	Γ_0	$\Delta\Gamma$	γ_s	γ_d	γ	FY
$F[\text{kV/cm}]$	0	0	0	$5 \perp$	0	0	0	$5 \perp$
$^1P^o$	[eV]		$[\text{ns}^{-1}]$	$[\text{ns}^{-1}]$	$[\text{ns}^{-1}]$	$[\text{ns}^{-1}]$	$[\text{ns}^{-1}]$	
$(0,1)^+$ 2a	60.271	6.64−3	5.68+4	8.84−5	6.75+0	2.96-1	7.05+0	8.23−7
3a	63.689	1.05−3	1.21+4	9.33−4	5.75+0	1.51+0	7.26+0	6.30−7
4a	64.480	4.24−4	5.17+3	3.63−4	5.71+0	1.77+0	7.48+0	6.13−7
5a	64.824	2.13−4	2.65+3	4.79−4	5.73+0	1.87+0	7.60+0	6.09−7
6a	65.005	1.22−4	1.53+3	1.13−2	5.75+0	1.92+0	7.67+0	6.08−7
7a	65.113	7.61−5	9.65+2	6.29−2	5.77+0	1.94+0	7.71+0	6.03−7
8a	65.182	5.07−5	6.45+2	2.24−1	5.78+0	1.96+0	7.74+0	6.01−7
9a	65.229	3.55−5	4.52+2	6.37−1	5.79+0	1.97+0	7.76+0	5.98−7
10a	65.262	2.59−5	3.30+2	1.69+0	5.79+0	1.97+0	7.77+0	5.92−7
$(1,0)^-$ 3b	62.774	2.45−5	2.01+2	2.02−4	4.70+0	6.05-1	5.30+0	6.29−7
4b	64.144	2.13−5	1.25+2	3.64−3	3.56+0	4.25+0	7.81+0	1.25−6
5b	64.664	1.07−5	6.35+1	2.87−2	3.62+0	4.43+0	8.05+0	1.20−6
6b	64.917	5.94−6	3.52+1	1.37−1	3.65+0	4.55+0	8.20+0	1.12−6
7b	65.059	3.60−6	2.13+1	4.82−1	3.66+0	4.63+0	8.29+0	9.92−7
8b	65.147	2.34−6	1.38+1	1.39+0	3.66+0	4.69+0	8.35+0	8.30−7
9b	65.205	1.60−6	9.48+0	3.46+0	3.66+0	4.73+0	8.39+0	6.29−7
10b	65.245	1.14−6	6.76+0	7.55+0	3.63+0	4.74+0	8.37+0	4.21−7
$(-1,0)^0$ 3c	64.128	2.53−6	1.81−1	7.81−4	8.96−1	4.10+0	4.99+0	2.44−6
4c	64.655	2.05−6	4.72−1	5.41−3	6.34−1	3.69+0	4.33+0	1.84−6
5c	64.912	1.33−6	3.56−1	2.47−2	5.16−1	3.49+0	4.00+0	1.21−6
6c	65.056	8.65−7	2.37−1	8.62−2	4.55−1	3.35+0	3.81+0	7.97−7
7c	65.145	5.83−7	1.59−1	2.49−1	4.18−1	3.26+0	3.68+0	5.50−7
8c	65.203	4.07−7	1.00−1	6.23−1	3.94−1	3.19+0	3.58+0	3.38−7
9c	65.244	2.94−7	7.83−2	1.36+0	3.75−1	3.14+0	3.51+0	2.08−7

Table 3.1: The eigenenergies E_i, oscillator strengths f (length form), autoionisation Γ_0 and fluorescence rates $\gamma = \gamma_s + \gamma_d$ (velocity form) for $^1P^o$ states in zero electric field. Given are also corrections $\Delta\Gamma$ to autoionisation decay rate in DC electric field of 5 kV/cm ($\boldsymbol{F} \perp \boldsymbol{P}$) and the fluorescence yield FY.

State	E_i	f	Γ_0	$\Delta\Gamma$	γ_p	γ_f	γ	FY
F[kV/cm]	0	5 $\parallel$	0	5 $\parallel$	0	0	0	5 $\parallel$
$^1D^e$	[eV]		[ns^{-1}]	[ns^{-1}]	[ns^{-1}]	[ns^{-1}]	[ns^{-1}]	
$(1,0)^+$ 2a	60.022	7.4$-$12	1.22$+$5	4.42$-$4	4.04-1	4.94$-$5	4.04$-$1	2.4$-$17
3a	63.558	1.8$-$10	2.82$+$4	4.66$-$3	6.44$+$0	8.61$-$2	6.52$+$0	4.2$-$14
4a	64.421	0.63$-$9	1.18$+$4	1.68$-$3	6.07$+$0	2.24$-$1	6.30$+$0	3.4$-$13
5a	64.793	2.09$-$9	6.00$+$3	2.39$-$3	5.87$+$0	3.07$-$1	6.18$+$0	2.1$-$12
6a	64.987	6.10$-$9	3.43$+$3	5.70$-$2	5.76$+$0	3.58$-$1	6.12$+$0	1.1$-$11
7a	65.101	1.59$-$8	2.14$+$3	3.15$-$1	5.68$+$0	3.90$-$1	6.07$+$0	4.5$-$11
8a	65.174	3.73$-$8	1.42$+$3	1.12$+$0	5.63$+$0	4.11$-$1	6.04$+$0	1.6$-$10
9a	65.224	8.00$-$8	9.91$+$2	3.18$+$0	5.58$+$0	4.26$-$1	6.01$+$0	4.8$-$10
10a	65.259	1.31$-$7	7.19$+$2	8.50$+$0	5.53$+$0	4.35$-$1	5.96$+$0	1.06$-$9
$(0,1)^0$ 3b	63.874	5.0$-$10	1.09$+$3	1.01$-$3	3.13$+$0	7.13$-$1	3.84$+$0	1.7$-$12
4b	64.549	5.90$-$9	6.06$+$2	1.82$-$2	3.72$+$0	7.00$-$1	4.42$+$0	4.3$-$11
5b	64.857	3.33$-$8	3.46$+$2	1.43$-$1	3.97$+$0	6.90$-$1	4.66$+$0	4.4$-$10
6b	65.024	1.30$-$7	2.11$+$2	6.85$-$1	4.11$+$0	6.87$-$1	4.80$+$0	2.88$-$9
7b	65.125	4.01$-$7	1.37$+$2	2.41$+$0	4.19$+$0	6.87$-$1	4.88$+$0	1.35$-$8
8b	65.190	1.05$-$6	9.39$+$1	6.95$+$0	4.25$+$0	6.87$-$1	4.94$+$0	4.90$-$8
9b	65.234	2.40$-$6	6.68$+$1	1.73$+$1	4.29$+$0	6.88$-$1	4.97$+$0	1.34$-$7
10b	65.266	4.74$-$6	4.94$+$1	3.77$+$1	4.31$+$0	6.83$-$1	4.99$+$0	2.57$-$7
$(-1,0)^0$ 4c	64.606	4.8$-$10	4.66$-$1	3.90$-$3	5.10-2	8.89$+$0	8.94$+$0	4.6$-$10
5c	64.886	3.51$-$9	4.80$-$1	2.70$-$2	3.41-2	8.86$+$0	8.90$+$0	3.32$-$9
6c	65.040	1.50$-$8	3.81$-$1	1.23$-$1	2.46-2	8.85$+$0	8.88$+$0	1.42$-$8
7c	65.135	4.83$-$8	2.87$-$1	4.31$-$1	1.88-2	8.84$+$0	8.86$+$0	4.66$-$8
8c	65.197	1.29$-$7	2.15$-$1	1.25$+$0	1.49-2	8.84$+$0	8.85$+$0	1.11$-$7
9c	65.239	3.03$-$7	1.62$-$1	3.11$+$0	1.22-2	8.83$+$0	8.84$+$0	2.21$-$7

Table 3.2: The eigenenergies E_i, autoionisation Γ_0 and fluorescence decay rates $\gamma = \gamma_p + \gamma_f$ (velocity form) for $^1D^e$ series in zero electric field. Given are also oscillator strengths f (length form) and corrections $\Delta\Gamma$ to the autoionisation rate for DC electric field of 5 kV/cm ($\boldsymbol{F} \parallel \boldsymbol{P}$) and the fluorescence yield FY.

State	E_i	f	$\Delta\Gamma$	γ	FY
F[kV/cm]	0	$5 \perp$	$5 \perp$	0	$5 \perp$
$^1P^e$	[eV]		[ns^{-1}]	[ns^{-1}]	
$(0,1)^-$ 3a	63.230	5.39−11	6.04−4	1.05+1	5.39−11
4a	64.318	8.19−10	1.03−2	1.00+1	8.11−10
5a	64.747	5.38−9	7.08−2	9.84+0	5.34−9
6a	64.963	2.31−8	3.10−1	9.77+0	2.24−8
7a	65.087	7.66−8	1.03+0	9.74+0	6.93−8
8a	65.165	2.12−7	2.88+0	9.70+0	1.63−7
9a	65.217	5.15−7	7.02+0	9.65+0	2.98−7
10a	65.254	1.15−6	1.54+1	9.58+0	4.41−7

State	E_i		Γ_0	γ	
F[kV/cm]	0		0	0	
$^1S^e$	[eV]		[ns^{-1}]	[ns^{-1}]	
$(1,0)^+$ 2a	57.909		2.18+5	6.09-2	
3a	63.001		7.04+4	3.63+0	
4a	64.203		2.50+4	4.80+0	
5a	64.688		1.08+4	5.75+0	
6a	64.929		5.47+3	6.40+0	
7a	65.066		3.12+3	6.83+0	
8a	65.151		1.94+3	7.12+0	
9a	65.208		1.28+3	7.30+0	
10a	65.247		8.94+2	7.41+0	
$(-1,0)^+$ 2b	62.256		2.37+4	8.22-1	
3b	64.122		8.38+3	4.53+0	
4b	64.660		4.99+3	3.81+0	
5b	64.917		3.13+3	3.24+0	
6b	65.059		2.06+3	2.85+0	
7b	65.147		1.41+3	2.57+0	
8b	65.205		1.01+3	2.37+0	
9b	65.245		7.38+2	2.22+0	
10b	65.274		5.50+2	2.34+0	

Table 3.3: Oscillator strengths f (length form) and corrections $\Delta\Gamma$ to the autoionisation rate for $^1P^e$ series in electric field of 5 kV/cm ($\boldsymbol{F} \perp \boldsymbol{P}$). Given are also eigenenergies E_i, autoionisation Γ_0 and fluorescence decay rates γ (velocity form) in zero field for $^1P^e$ and $^1S^e$ series. FY is the fluorescence yield.

3.2 Results

In Tables 3.1-3.3 above, we report the resonance oscillator strengths $f_i = \sigma_i/(2\pi^2\alpha)$. The $^1P^o$ oscillator strengths remain basically unchanged from their zero field values at $F = 5$ kV/cm, while for even resonances they increase in proportion to F^2. The autoionisation decay rates Γ_0
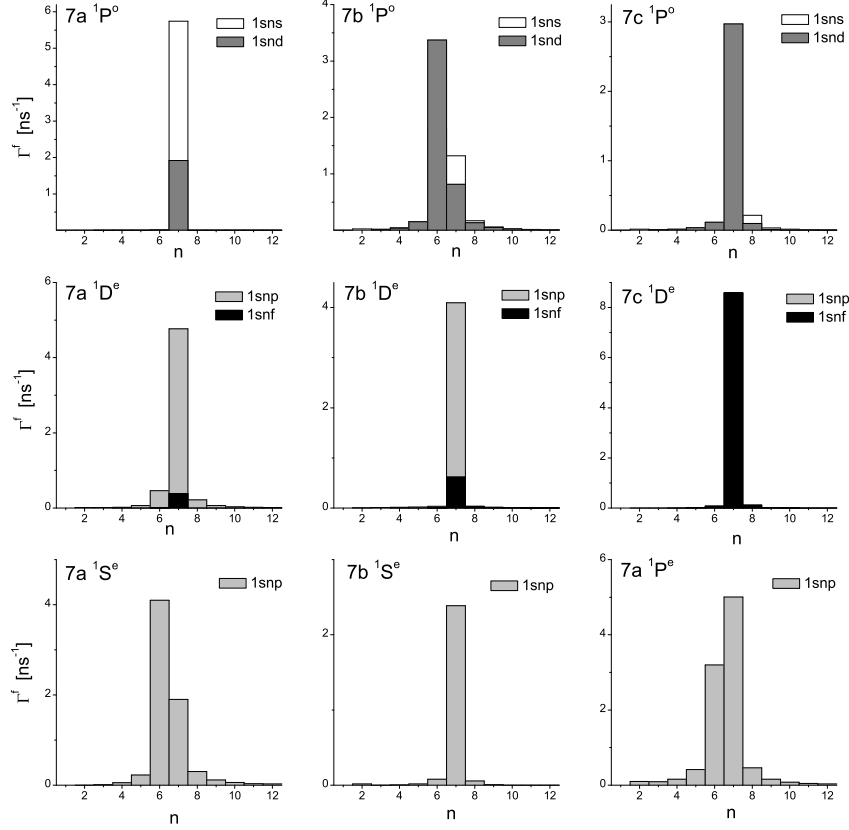
Figure 3.1: Partial fluorescence decay rates of the nine resonant states below $N = 2$ into the singly excited states $1snl$ in helium.

in the zero electric field are represented by the first term on the right of Eqs. (3.6) and (3.5). They are given in Tables 3.1-3.3 together with corrections $\Delta\Gamma$ to the autoionisation rate at 5 kV/cm used to obtain the total autoionisation rate $\Gamma = \Gamma_0 + \Delta\Gamma$ in the non zero field. For pure LS states below the $N = 2$ threshold, the autoionisation is forbidden for resonances with $(-1)^{L+1}$ parity. Therefore, the autoionisation of $^1P^e$ states in weak electric fields is driven solely by the small admixture of the strongly ionising $^1P^o$ states represented by the first order term $\Delta\Gamma$ in Eq. (3.6); we have neglected the admixture of weakly autoionising $^1D^o$ states (according to [60], quantum number $A = 0$ for these states). For $^1D^e$ a states, the zero field autoionisation rate is large so that it is not changed substantially by the first order admixture of $^1P^o$ states. The same is true for $^1P^o$ a states: their autoionisation rates are essentially not modified by the weak electric field, so that $\Gamma \approx \Gamma_0$. On the contrary, $^1P^o$ b and especially $^1P^o$ c states display very small zero order autoionisation rate which can be largely modified by the presence of the field, i.e., small admixtures of strongly autoionising even parity states represented by the summation term in Eq. (3.5) dominantly contribute to the autoionisation decay rate of high series members, so that $\Gamma \approx \Delta\Gamma(F)$. We have calculated the correction only for $\boldsymbol{F} \perp \boldsymbol{P}$ due to the quantitatively

uncertain but qualitatively similar effect of strongly autoionising $^1S^e$ states at 5 kV/cm in the parallel orientation (Table 3.1). Similar holds for $^1D^e$ b and c series: their autoionisation rates are considerably changed by the admixture of $^1P^o$ states. Note that corrections $\Delta\Gamma$ for $\boldsymbol{F} \perp \boldsymbol{P}$ are obtained when the corresponding values from Table 3.2 are multiplied by 3/4. Note also that $\Delta\Gamma$ scales with F^2. The effect of these corrections is to produce the observed nonlinear dependence of the VUV fluorescence yield on the electric field strength [47].
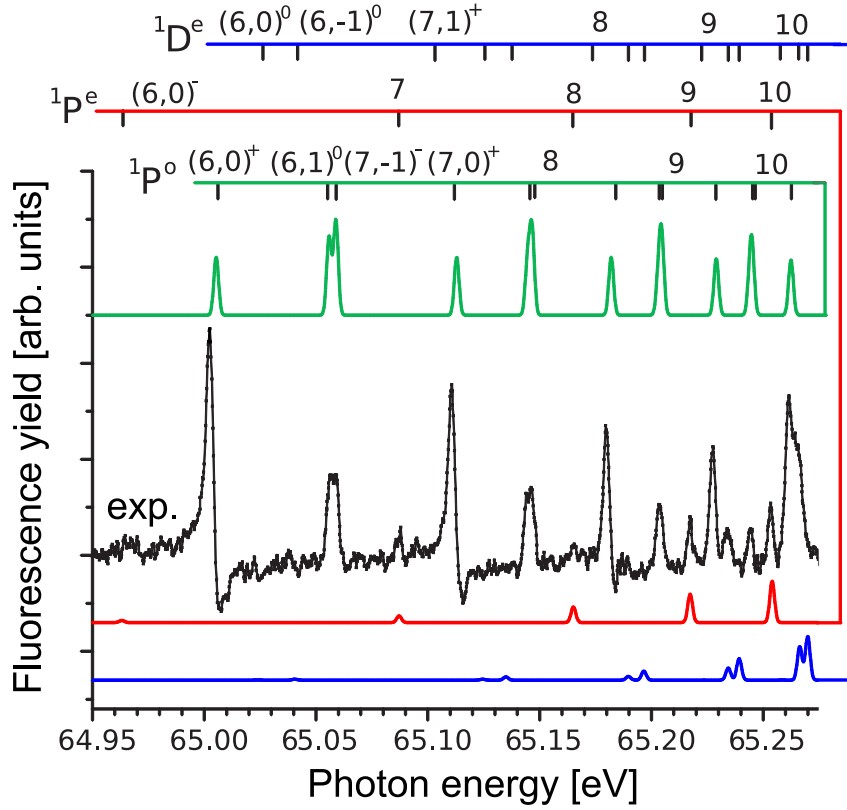
Figure 3.2: Comparison of the experimental VUV photon yield and calculated primary fluorescence yields from the $^1P^o$ state (green line) and $^1P^e$, $^1D^e$ states (red and blue line) perturbed by the electric field of 5 kV/cm ($\boldsymbol{F} \perp \boldsymbol{P}$).

Since the zero field fluorescence rates γ_i (Tables 3.1-3.3) are of the same order of magnitude for all the studied symmetries, their values in the non-zero field are almost unaffected by the small first order perturbation admixtures, either in the initial or the final state. While for $^1S^e$ and $^1P^e$ states there exists a single primary fluorescence decay mode, $^1S^e \rightarrow {}^1P^o + \gamma$ and $^1P^e \rightarrow {}^1P^o + \gamma$, respectively, there are two modes in the case of $^1P^o$ and $^1D^e$ resonances:

$$
\begin{aligned}
\gamma_s : \quad &^1P^o \rightarrow {}^1S^e + \gamma &&\text{and} &&\gamma_d : \quad {}^1P^o \rightarrow {}^1D^e + \gamma \,, \\
\gamma_p : \quad &^1D^e \rightarrow {}^1P^o + \gamma &&\text{and} &&\gamma_f : \quad {}^1D^e \rightarrow {}^1F^o + \gamma \,.
\end{aligned}
\tag{3.9}
$$

These partial rates are also reported in Tables 3.1-3.2. The length and velocity form results disagree at most for 10% for $n = 2$ resonances and agree much better at higher n. For $n = 7$ states of nine resonant series considered here, we present partial fluorescence rates into the allowed singly excited atomic states in Fig. 3.2. We can see that except for the $^1P^o$ b and $^1S^e$ a type of resonances, all the transitions are mainly vertical, i.e., the inner electron makes transition

from L to K shell in the presence of spectator electron in the outer atomic shell. Also, $^1D^e$ c series mainly decays to $1snf$ states while a,b states of the same symmetry most likely fluoresce into $1snp$ states.

The data presented in Tables 3.1-3.3 estimate the total primary fluorescence yield

$$\text{FY} = f \frac{\gamma}{\gamma + \Gamma} \tag{3.10}$$

from resonances in the weak electric field. This is helpful to explain recent experimental observations [47]. The comparison with calculated FY is presented in Fig. 3.2 for the field strength of 5 kV/cm. FY reproduces well the newly observed photon yield of $^1P^e$ resonances. The calculated contribution of two out of three $^1D^e$ series seems to be important at the high energy side of the principal series a, but their intensities are not large enough so that there may be some other states contributing to the yield in that energy region.

According to our first order calculations, it is expected that $^1P^e$ states are the strongest dark source of photons. For example, at $n = 10$ the total primary fluorescence yield from $^1P^e$ $10a$ state at 5 kV/cm already amounts to 74% of the yield from the dipole allowed $^1P^o$ $10a$ state; the fluorescence signals from both states should display comparable intensity in PIFS spectra when the electric field is perpendicular to the polarisation of the incoming light. On the other hand, under the same circumstances the fluorescence signal from the dipole allowed $^1P^o$ $10b$ and $^1P^o$ $10c$ state is expected to decrease to 66% and 72% of the zero field signal, respectively.

We could only partially confirm the experimental observations. The first order calculations cannot tell anything reliable about the data collected for $\boldsymbol{F} \parallel \boldsymbol{P}$, although it appears that the reduced fluorescence yield of the $^1P^o$ $(n-1)c$ - nb doublet is due to the mixing with strongly autoionising $^1S^e$ series. To resolve these question and answer to some others, we should be able to work out the non perturbative model, which will achieve higher accuracy and allow the considerations of fluorescence yield *and* ion yield spectra at much higher electric fields and for both experimental geometries.

Chapter 4

Non perturbative treatment

4.1 Two electron Coulomb Sturmian functions

For a reliable description of singly and doubly excited states of the helium atom in the homogeneous electric field, accurate wavefunctions of the atomic eigenstates are needed. Suitable basis is to be chosen that allows a good representation of the wavefunctions both at small radial distances from the nucleus r, where the Coulomb potential is dominant, but also at large distances, where the effect of the electric field is more pronounced. Accurate wavefunctions close to the nucleus are also required because it is expected that the overlap between doubly and singly excited state wavefunctions is considerable in this region.

Basis functions commonly used in problems that involve Coulomb potential are the Coulomb Sturmian functions [78]. The single electron Coulomb Sturmian functions are the solutions of the Sturm-Liouville problem

$$\left[-\frac{1}{2} \frac{\mathrm{d}^2}{\mathrm{d}r^2} + \frac{1}{2} \frac{l(l+1)}{r^2} - \frac{nk}{r} + \frac{k^2}{2} \right] S_{nl}^k(r) = 0 \,, \tag{4.1}$$

$$S_{nl}^k(0) = 0 \qquad \text{and} \qquad S_{nl}^k(r) \xrightarrow{r \to \infty} 0 \,, \tag{4.2}$$

and subject to a rather unusual normalisation condition involving a $1/r$ weight:

$$\int_0^\infty \mathrm{d}r S_{nl}^k(r) \frac{1}{r} S_{n'l}^k(r) = \delta_{nn'} \,. \tag{4.3}$$

It should be noted that the normalisation plays no role when two electron wavefunctions are constructed from the single electron wavefunctions since the resultant two electron wavefunctions are nonorthogonal. Eq. (4.3) is therefore written merely for completeness. It should be noted that the total single electron wavefunction (omitting the spin part) is written as

$$\psi_{nlm}^k(\boldsymbol{r}) = \frac{S_{nl}^k(r)}{r} Y_{lm}(\theta, \phi) \,. \tag{4.4}$$

The functions satisfying Eqs. (4.2) and (4.3) are [78, 79]

$$S_{nl}^k(r) = \sqrt{\frac{(n-l-1)!}{(n+l)!}} \, e^{-kr} (2kr)^{l+1} L_{n-l-1}^{2l+1}(2kr) \,, \tag{4.5}$$

where $L_n^\alpha(x)$ denotes an associated Laguerre polynomial [80]. For $k = Z/n$, the Sturmian function $S_{nl}^k(r)$ represents, up to a normalisation constant, a solution of a hydrogen-like atom

of nuclear charge Z. As can be shown for a fixed parameter k, the Coulomb Sturmian functions form a complete set [78].

The simplest generalisation of the latter results to the case of two electrons is by writing two electron basis functions as a linear combination of products of single electron wavefunctions,

$$\frac{S_{nl}^{k}(r_1)}{r_1}\,Y_{lm}(\hat{\boldsymbol{r}}_1)\,\chi_{m_s}(\sigma_1)\,\cdot\,\frac{S_{\nu\lambda}^{\kappa}(r_2)}{r_2}\,Y_{\lambda\mu}(\hat{\boldsymbol{r}}_2)\,\chi_{\mu_s}(\sigma_2)\,, \tag{4.6}$$

where $Y_{lm}(\theta,\phi) = Y_{lm}(\hat{\boldsymbol{r}}) = \langle \hat{\boldsymbol{r}}|lm\rangle$ are the usual spherical harmonics [13, 53] and $\chi_{m_s}(\sigma) = \langle\sigma|m_s\rangle = \delta_{m_s,\sigma}$ spin wavefunctions [13]. If the normalisation constant is disregarded, the anti-symmetrised LS coupled two electron basis function for a given electron configuration $nl\nu\lambda$ and fixed nonlinear parameters k and κ is equal to [cf. Eq. (2.7)]

$$\psi_{LMSM_S}^{knl\kappa\nu\lambda}(\boldsymbol{q}_1,\boldsymbol{q}_2) = \frac{S_{nl}^{k}(r_1)}{r_1}\frac{S_{\nu\lambda}^{\kappa}(r_2)}{r_2}\,\Upsilon_{LMSM_S}^{l\lambda}(\hat{\boldsymbol{r}}_1,\sigma_1,\hat{\boldsymbol{r}}_2,\sigma_2)$$
$$+\,(-1)^{L+S+l+\lambda}\,\frac{S_{\nu\lambda}^{\kappa}(r_1)}{r_1}\frac{S_{nl}^{k}(r_2)}{r_2}\,\Upsilon_{LMSM_S}^{\lambda l}(\hat{\boldsymbol{r}}_1,\sigma_1,\hat{\boldsymbol{r}}_2,\sigma_2)\,, \tag{4.7}$$

where $\Upsilon_{LMSM_S}^{l\lambda}(\hat{\boldsymbol{r}}_1,\sigma_1,\hat{\boldsymbol{r}}_2,\sigma_2)$ is the coupled spin orbital part:

$$\Upsilon_{LMSM_S}^{l\lambda}(\hat{\boldsymbol{r}}_1,\sigma_1,\hat{\boldsymbol{r}}_2,\sigma_2) = \sum_{\substack{m,\mu \\ m_s,\mu_s}} (lm\lambda\mu|LM)(1/2\,m_s 1/2\,\mu_s|SM_S)\,\cdot$$
$$\cdot\,Y_{lm}(\hat{\boldsymbol{r}}_1)Y_{\lambda\mu}(\hat{\boldsymbol{r}}_2)\chi_{m_s}(\sigma_1)\chi_{\mu_s}(\sigma_2)\,. \tag{4.8}$$

The functions from Eq. (4.7) are not normalised to unity. As mentioned earlier, the functions with different $nl\nu\lambda$ and/or different scaling parameters (k,κ) are in general not orthogonal.

Often, the nonlinear scaling parameters are chosen equal $(k = \kappa)$ since the integrals involved in the calculation of the matrix elements of the Hamiltonian can then be simplified by the use of the recursion and orthogonality formulas for the Laguerre polynomials [80]. In that case, the matrix elements of the Hamilton operator are subject to strict selection rules (i.e., many of the elements are zero) and the matrices involved in the eigenvalue problem are sparse band diagonal (e.g., cf. Ref. [81]).

In the case of equal scaling parameters, however, a large basis set is needed to accurately describe high lying states of a Rydberg series converging to a specified ionisation threshold. This stems from the fact that such *high asymmetrically excited atomic states* [82] are characterised by two different radial scales attributed to the motion of the two electrons: on the average, the electrons move far away from each other. A suitable basis should therefore account for this radial asymmetry by spanning the two radial regions simultaneously. If the basis functions from Eq. (4.7) are used, this is achieved by assigning two distinct values to k and κ. This choice means, however, that the computation of the matrix elements becomes more demanding since the orthogonality relations of the Laguerre polynomials cannot be used and the integration has to be carried out numerically.

In choosing the suitable nonlinear scaling parameters, we follow the method of Lagmago Kamta et al. [82]. Only a short overview is given here, whereas the reader should refer to Ref. [82] and Chapter 5 for details. The solutions of the Schrödinger equation are written as a CI expansion over the Sturmian basis functions as

$$\Psi(\boldsymbol{q}_1,\boldsymbol{q}_2) = \sum_{s}\sum_{l,\lambda}\sum_{n,\nu} x_{LMSM_S}^{k_s nl\kappa_s\nu\lambda}\,\psi_{LMSM_S}^{k_s nl\kappa_s\nu\lambda}(\boldsymbol{q}_1,\boldsymbol{q}_2)\,, \tag{4.9}$$

with $n = l+1, \ldots, l+\Delta n_{ls}$ and $\nu = \lambda+1, \ldots, \lambda+\Delta\nu_{\lambda s}$. Note that besides the usual CI expansion involving different pairs of orbital momenta (l, λ), several sets of scaling parameters (k_s, κ_s) are used in Eq. (4.9). Since the parameters k_s, κ_s, n, and ν all influence the radial spread of the wavefunction, k_s, κ_s, Δn_{ls}, and $\Delta\nu_{\lambda s}$ are adjusted in such a manner to increase the number of Sturmian functions simultaneously describing the radial regions of both electrons. The values of k_s and κ_s are chosen as follows. The Sturmian function $S_{nl}^k(r)$ describes an electron with the energy

$$E = -\frac{k^2}{2} = -\frac{Z^2}{2n^2} \tag{4.10}$$

moving in the Coulomb potential of nuclear charge Z. In the case of two electrons characterised by quantum numbers n and ν, the nuclear charge that affects the motion of the electron is screened by the charge of the additional electron, thus Z should be replaced by the effective charge $Z - \sigma$, where $0 < \sigma \leq 1$. The parameters k and κ are set to

$$k = \frac{Z - \sigma_k}{n} \quad \text{and} \quad \kappa = \frac{Z - \sigma_\kappa}{\nu}. \tag{4.11}$$

The number of Sturmian functions Δn_{ls} and $\Delta\nu_{\lambda s}$ in Eq. (4.9) depends on the values of k_s and κ_s. It should be noted that using distinct values for k_s and κ_s can reduce the basis size substantially for asymmetrically excited states since the number of Sturmian functions in the expansion Δn_{ls} and $\Delta\nu_{\lambda s}$ need not be equal and since the electron movement becomes less correlated and thus fewer angular configurations are needed for a reliable description.

The usual variational approach involves optimisation of the nonlinear parameters of the basis functions prior to diagonalisation. In this way, accurate energies and wavefunctions for a chosen atomic state or a group of close lying states can be obtained. Rather than seeking optimal parameters for each of the states, the convergence is achieved by including several pairs of scaling parameters (k_s, κ_s) in Eq. (4.9) that cover the range of suitable values. On the expense of the larger basis size, the eigenstates and eigenenergies are obtained simultaneously, *in a single diagonalisation*. This is particularly important since for an adequate description of the helium atom in the external electric field, the higher angular momenta L could also become relevant, and a large number of states would thus have to be optimised.

In Chapter 5 we describe in detail the basis parameters used in the calculation of the singly and doubly excited states of the helium atom below the second ($N = 2$) ionisation threshold, for angular momenta $L \leq 10$ and principal quantum numbers $n \leq 15$.

4.2 Hamilton operator in Sturmian basis

The most transparent way of studying the effects of the external electric field strength on the eigenstates of the system is by expanding the eigenstates of the total Hamiltonian H in the basis of the free atom eigenstates. If the solution $|\Psi_i\rangle$ of the field free eigenvalue problem with eigenenergy E_i,

$$H_0|\Psi_i\rangle = E_i|\Psi_i\rangle, \tag{4.12}$$

is expanded in the basis of Coulomb Sturmian functions $\langle \boldsymbol{q}_1, \boldsymbol{q}_2|\psi_\gamma\rangle$,

$$|\Psi_i\rangle = \sum_\gamma x_{i,\gamma}|\psi_\gamma\rangle, \tag{4.13}$$

one obtains a generalised eigenvalue problem

$$\mathsf{H}_0\,\mathsf{x}_i = E_i\,\mathsf{B}\,\mathsf{x}_i, \tag{4.14}$$

with

$$H_{0,\beta\gamma} = \langle \psi_\beta | H_0 | \psi_\gamma \rangle \quad \text{and} \quad B_{\beta\gamma} = \langle \psi_\beta | \psi_\gamma \rangle \,. \tag{4.15}$$

The Greek indices were used as a shorthand notation for the set of quantum numbers

$$(knl, \kappa\nu\lambda, LMSM_S) \,. \tag{4.16}$$

Since the basis is real, the matrix $\mathbf{H}_0$ from Eq. (4.14) is real symmetric and the overlap matrix $\mathbf{B}$ is real symmetric positive definite. The ortho-normalisation condition

$$\langle \Psi_i | \Psi_j \rangle = \delta_{ij} \tag{4.17}$$

leads to the normalisation equation for the column vectors $\mathbf{x}_i$:

$$\mathbf{x}_i^\dagger \mathbf{B} \mathbf{x}_j = \delta_{ij} \,. \tag{4.18}$$

Once the field free solutions are obtained, the eigenvalues $\mathcal{E}_p$ and the eigenstates $|\Phi_p\rangle$ of the total Hamilton operator H,

$$H|\Phi_p\rangle = \mathcal{E}_p|\Phi_p\rangle \,, \tag{4.19}$$

are sought by the expansion

$$|\Phi_p\rangle = \sum_j y_{p,j} |\Psi_j\rangle \,. \tag{4.20}$$

Eqs. (4.19), (4.20), and the normalisation requirement for the eigenstates of the full Hamiltonian

$$\langle \Phi_p | \Phi_q \rangle = \mathbf{y}_p^\dagger \mathbf{y}_q = \delta_{pq} \tag{4.21}$$

then lead to the equation

$$(\boldsymbol{\mathcal{A}} + \boldsymbol{\mathcal{B}}) \, \mathbf{y}_p = \mathcal{E}_p \, \mathbf{y}_p \,. \tag{4.22}$$

The matrices $\boldsymbol{\mathcal{A}}$ and $\boldsymbol{\mathcal{B}}$ in Eq. (4.22) are given by

$$\mathcal{A}_{ij} = E_i \, \delta_{ij} \qquad \text{and} \qquad \mathcal{B}_{ij} = \langle \Psi_i | \Delta H | \Psi_j \rangle \,. \tag{4.23}$$

The key advantage of using the expansion (4.20) is that only the eigenstates $|\Psi_i\rangle$ for which the coupling through ΔH is strongest in the specified energy region can be included in the sum. This can drastically reduce the size of the matrices involved and thus allows higher angular momenta to be included in the calculation. The drawback of the expansion over the unperturbed states is, however, that an additional diagonalisation (or, more precisely, an additional diagonalisation for every symmetry LS and parity π) is required. As already mentioned, more details on the numerical treatment of the problem will be given in Chapter 5.

In the following, only the outline of the ab inito treatment is given, whereas the detailed derivations of matrix elements of the Hamilton operator in Sturmian basis are gathered in Appendix B, and the numerical implementation of the problem is described in Chapter 5.

4.3 The method of complex scaling

In the energy region of doubly excited states, the eigenstates of the Hamiltonian are represented by a superposition of bound and continuum components, while the basis of square integrable functions generally used is appropriate only for the former. Since the coupling between the bound and continuum channels in this region, which results in autoionisation, may be strong,

it should be treated properly. To bring continuum channel asymptotics into the reach of the exponentially decreasing basis, it is common to use the method of complex scaling, also known as the complex dilatation (dilation) or the complex rotation method. This method has become standard for treating resonances of atomic, molecular, and nuclear systems. It is beyond the scope of this work to describe it in detail, especially because of its nontrivial mathematical background. The reader is therefore encouraged to start with the review articles by Ho [83], Junker [84], Reinhardt [85], and Moiseyev [86], which also include a extensive list of references. Furthermore, for its application in the frame of atomic physics, the articles by Buchleitner et al. [87] and Rost et al. [4] are of relevance, together with the study of the expectation values of resonance states by Bürgers and Rost [88].

Using the method of complex scaling, it is possible to treat the effect of the atomic continuum exactly, together with the discrete-continuum and continuum-continuum interactions. This treatment also includes the exact representation of atomic resonances. The method is based on the analytic continuation of Green's operator into the complex plane [87]. For a time independent Hamilton operator H (e.g., $H = H_0$ or $H_0 + \Delta H$), Green's operator is defined as

$$G(E) = (E - H)^{-1} \,, \tag{4.24}$$

where $E \in \mathbb{C}$. Each bound state of the Hamiltonian H corresponds to a pole of $G(E)$, while the continuous part of the spectrum corresponds to a cut along the real axis. Physically relevant is the value of Green's operator on the real axis. It depends on whether the axis is approached from the lower or the upper side, and therefore two continuations of $G(E)$ into the complex plane are defined,

$$G^{\pm}(E) = (E \pm i\epsilon - H)^{-1} \,, \tag{4.25}$$

where the limit $\epsilon \to 0^+$ is taken. Resonances (Gamow or Siegert states) satisfy the purely outgoing wave boundary condition [88]. They are characterised by the complex poles of the analytic continuation $G^+(E)$ of Green's operator to the lower half of the complex energy plane. With complex scaling, the complex energies of the resonances can be directly calculated by seeking the eigenvalues of *the complex scaled Hamiltonian*, which we denote by $H(\Theta)$. The operator $H(\Theta)$ is obtained by making the positions and momenta of H complex by making substitutions

$$\boldsymbol{r}_k \to \boldsymbol{r}_k \, e^{i\Theta} \qquad \text{and} \qquad \boldsymbol{p}_k \to \boldsymbol{p}_k \, e^{-i\Theta} \,, \quad k = 1, 2 \,, \tag{4.26}$$

for a real parameter Θ (often called "rotation angle"). Formally, the same effect is obtained by the transformation

$$H(\Theta) = R(\Theta) H R(-\Theta) \,, \tag{4.27}$$

where $R(\Theta)$ is the complex dilatation operator

$$R(\Theta) = \exp\left(-\Theta \sum_k \frac{\boldsymbol{p}_k \cdot \boldsymbol{r}_k + \boldsymbol{r}_k \cdot \boldsymbol{p}_k}{2}\right) \,. \tag{4.28}$$

The scaled Hamiltonian $H(\Theta)$ is obviously no longer a Hermitian operator. The spectrum of $H(\Theta)$,

$$H(\Theta)|\Psi_\Theta\rangle = E_\Theta|\Psi_\Theta\rangle \,, \tag{4.29}$$

is generally complex and has the following properties [83–87] compared to the spectrum of H (Fig. 4.1):

  1. The continua are rotated by the angle -2Θ away from the real axis around the branching points (thresholds).
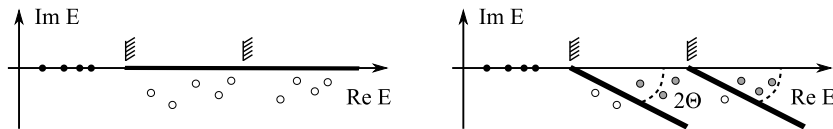
Figure 4.1: Left: the spectrum of the unrotated Hamiltonian. Black circles denote bound states. Continuum cuts starting from the ionisation thresholds lie on the real axis and the resonances remain hidden (empty circles). Right: the spectrum of the complex scaled Hamiltonian $H(\Theta)$. Continua are rotated around the ionisation thresholds, and the resonances are uncovered (gray circles) if the angle Θ is large enough.

2. The bound spectrum is invariant under the complex rotation (i.e., the eigenvalues pertaining to bound states are real and Θ-independent). The wavefunctions of complex scaled bound states remain square integrable.

3. If the rotation angle Θ is large enough, the resonances are uncovered (Fig. 4.1, left). The eigenvalues of resonance states are independent of Θ. The real part of the eigenvalue describes the energy position of the resonance, and the imaginary part is equal to the negative autoionisation half-width of the resonance ($E_\Theta = E - i\Gamma/2$). The complex scaled resonance state wavefunctions are square integrable.

For a suitably chosen Θ, diagonalisation of the rotated Hamiltonian therefore gives not only the resonance positions, but also the resonance widths. For $\Theta > 0$, the discrete part of the spectrum of $H(\Theta)$ is associated with the wavefunctions which behave asymptotically as outgoing waves if the imaginary part of the eigenvalue is nonzero [87, 88]. Furthermore, a resonance state is associated with a *single* square integrable function of $H(\Theta)$. On the contrary, for $\Theta < 0$, the discrete complex eigenvalues are attributed to the wavefunctions with the incoming wave asymptotics.

Green's operator $G(E)$ can be related to the complex scaled Green's operator as

$$G(E) = R(-\Theta)G_\Theta(E)R(\Theta) = R(-\Theta)\frac{1}{E - H(\Theta)}R(\Theta) \,. \qquad (4.30)$$

With this approach, the divergent behaviour of unrotated Green's operator on the real axis has been circumvented. Eq. (4.30) represents the analytic continuation of Green's operator. For $\Theta > 0$, complex scaled Green's operator is the analytic continuation of $G^+(E)$, while for $\Theta < 0$, it is the analytic continuation of $G^-(E)$.

If the complex scaled Hamiltonian is represented in a truncated basis of square integrable functions ($\mathcal{L}^2$), the continuum cuts are represented by a discrete set of points approximately lying on a line rotated off the axis by the angle -2Θ (Fig. 4.2).

As has already been done before, eigenstates and eigenenergies of the total complex scaled Hamilton operator $H(\Theta) = H_0(\Theta) + \Delta H(\Theta)$ are obtained by first seeking solutions of the field free eigenproblem

$$H_0(\Theta)|\Psi_{i\Theta}\rangle = E_{i\Theta}|\Psi_{i\Theta}\rangle \,, \qquad (4.31)$$

where $|\Psi_{i\Theta}\rangle$ is expanded in the basis of Sturmian basis functions [cf. Eq. (4.13)]:

$$|\Psi_{i\Theta}\rangle = \sum_\beta x_{i,\beta}|\psi_\beta\rangle \,. \qquad (4.32)$$
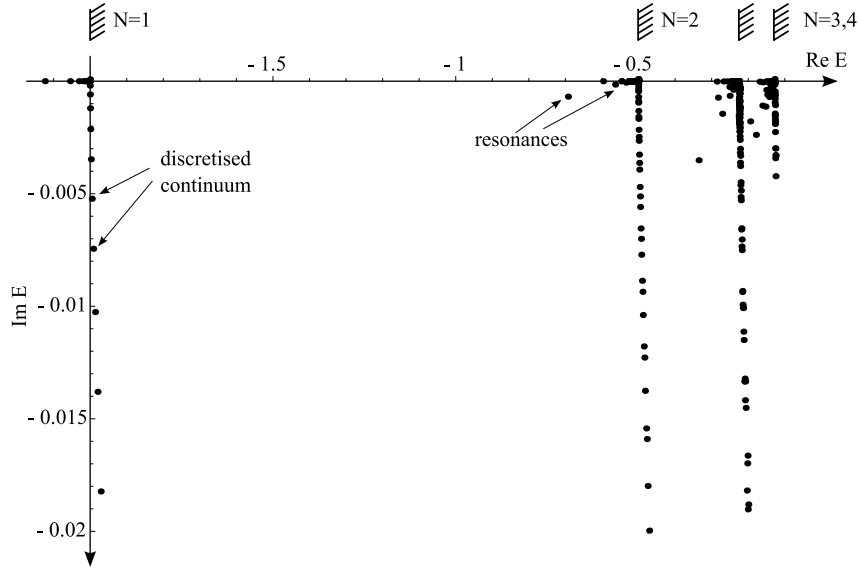
Figure 4.2: Complex energy spectrum of $^1P^o$ states of the helium atom for the rotated Hamiltonian $H(\Theta)$ represented in Sturmian square integrable ($\mathcal{L}^2$) basis. The continua are discretised and lie approximately on lines rotated around ionisation thresholds $N = 1, \ldots, 4$. The matrix size used in diagonalisation is 7665×7665 and the rotation angle set to $\Theta = 0.2$.

This results in a matrix equation

$$\mathbf{H}_0(\Theta)\, \mathbf{x}_i = E_{i\Theta}\, \mathbf{B}\, \mathbf{x}_i \,, \tag{4.33}$$

where $\mathbf{H}_0(\Theta)$ is complex symmetric (*not* Hermitian), while $\mathbf{B}$ remains real symmetric positive definite. It should be noted that explicit dependence of the coefficients $x_{i,\beta}$ on the parameter Θ has been dropped for brevity.

Although any Hermitian or real symmetric matrix can be diagonalised and the resulting eigenvectors can be made orthonormal, there is no guarantee that an *arbitrary* complex symmetric matrix $\mathbf{A}$ can be diagonalised. If it can be, however, its eigenvector matrix $\mathbf{X}$ can be chosen such that [89]

$$\mathbf{X}^\mathsf{T} \mathbf{A}\, \mathbf{X} = \mathbf{D} \qquad \text{and} \qquad \mathbf{X}^\mathsf{T} \mathbf{X} = \mathbf{I} \,, \tag{4.34}$$

where $\mathbf{D}$ is diagonal. For a generalised eigenproblem with a matrix pencil $(\mathbf{H}(\Theta), \mathbf{B})$, this property is changed accordingly to the generalised column product containing overlap matrix $\mathbf{B}$:

$$\mathbf{x}_i^\mathsf{T} \mathbf{B}\, \mathbf{x}_j = \delta_{ij} \,. \tag{4.35}$$

Note that because of the properties of complex symmetric matrices, the transposition is used in place of Hermitian conjugation [cf. Eq. (4.18)]. If furthermore the notation

$$|\overline{\Psi_{i\Theta}}\rangle = \sum_\beta x_{i,\beta}^* |\psi_\beta\rangle \qquad \text{and} \qquad \langle\overline{\Psi_{i\Theta}}| = \sum_\beta x_{i,\beta} \langle\psi_\beta| \tag{4.36}$$

is introduced, the following relations hold for the eigenvectors $|\Psi_{i\Theta}\rangle$:

$$\langle\overline{\Psi_{i\Theta}}|\Psi_{j\Theta}\rangle = \langle\Psi_{j\Theta}|\overline{\Psi_{i\Theta}}\rangle = \delta_{ij} \,, \tag{4.37}$$

$$\sum_i |\Psi_{i\Theta}\rangle\langle\overline{\Psi_{i\Theta}}| = \sum_i |\overline{\Psi_{i\Theta}}\rangle\langle\Psi_{i\Theta}| = 1 \,. \tag{4.38}$$

Since for a real basis set changing Θ to $-\Theta$ is equivalent to changing $H(\Theta)$ into its complex conjugate, the states $|\overline{\Psi_{i\Theta}}\rangle$ and the conjugated energies $E_{i\Theta}^*$ are eigenvectors and eigenvalues of $H(-\Theta)$ [87],

$$H(-\Theta)|\overline{\Psi_{i\Theta}}\rangle = E_{i\Theta}^*|\overline{\Psi_{i\Theta}}\rangle, \tag{4.39}$$

i.e., $|\Psi_{i,-\Theta}\rangle = |\overline{\Psi_{i\Theta}}\rangle$ and $E_{i,-\Theta} = E_{i\Theta}^*$.

Eq. (4.38) is the completeness relation for the complex scaled eigenstates. It holds in general for the eigenstates of the complex scaled Hamiltonian for a generalised inner product of complex scaling [88]

$$\langle \overline{A_\Theta}|B_\Theta\rangle, \tag{4.40}$$

where the product is formed in the usual way, except that the radial part of A_Θ is deconjugated prior to integration, i.e., the square rather than the square modulus of the radial part is calculated. This is in accord with the nature of the complex dilatation which, indeed, affects only the radial parts of the wavefunctions and leaves the angular parts intact.

To find eigenvalues $\mathcal{E}_{p\Theta}$ and eigenvectors $|\Phi_{p\Theta}\rangle$ of the total complex scaled Hamiltonian $H(\Theta)$,

$$H(\Theta)|\Phi_{p\Theta}\rangle = \mathcal{E}_{p\Theta}|\Phi_{p\Theta}\rangle, \tag{4.41}$$

an expansion analogous to Eq. (4.20) is used:

$$|\Phi_{p\Theta}\rangle = \sum_j y_{j,p}|\Psi_{j\Theta}\rangle. \tag{4.42}$$

As a consequence of the above orthogonality relations, the perturbed eigenproblem from Eq. (4.22) is changed as follows: the real matrices $\mathcal{A}$ and $\mathcal{B}$ are replaced by the complex matrices $\mathcal{A}(\Theta)$ and $\mathcal{B}(\Theta)$, and the energy $\mathcal{E}_p$ with the corresponding eigenvalue of $H(\Theta)$,

$$[\mathcal{A}(\Theta) + \mathcal{B}(\Theta)]\,\mathbf{y}_p = \mathcal{E}_{p\Theta}\,\mathbf{y}_p, \tag{4.43}$$

where

$$\mathcal{A}_{ij}(\Theta) = E_{i\Theta}\,\delta_{ij} \qquad \text{and} \qquad \mathcal{B}_{ij}(\Theta) = \langle\overline{\Psi_{i\Theta}}|\Delta H(\Theta)|\Psi_{j\Theta}\rangle. \tag{4.44}$$

It should be noted that the introduction of $R(\Theta)$ is of a rather formal value in many cases: the complex scaling for the helium atom in the homogeneous electric field results in the total Hamiltonian which can be immediately written as

$$H(\Theta) = T\,e^{-2i\Theta} + U\,e^{-i\Theta} + V\,e^{-i\Theta} + \Delta H\,e^{i\Theta}, \tag{4.45}$$

where $H = H_0 + \Delta H \equiv T + U + V + \Delta H$ is the unscaled Hamiltonian operator and T, U, V, and ΔH are the kinetic, nuclear potential, electron-electron, and external field contributions, respectively. Thus, the complex scaled Hamilton operator is easily obtained from the constituent terms by multiplication by suitable phase factors.

4.4 Interaction of an atom with a radiation field

So far we have considered an atom in a static external field. Since we are interested in the fluorescence decay, we introduce the framework by which we describe an interaction of an atom with a radiation field. The usual approach of a quantised electromagnetic field is used and the reader is referred to Refs. [90–92] for further details.

The behaviour of an atom interacting with the radiation field can be formally described by the Hamilton operator

$$H_{\text{tot}} = H_0 + H_{\text{rad}} + H_{\text{int}} . \tag{4.46}$$

H_0 denotes the atomic Hamiltonian,[1] H_{rad} the free radiation field,

$$H_{\text{rad}} = \sum_{\boldsymbol{k},\beta} \omega_{\boldsymbol{k}} a^{\dagger}_{\boldsymbol{k},\beta} a_{\boldsymbol{k},\beta} \equiv \sum_{\boldsymbol{k},\beta} \omega_{\boldsymbol{k}} n_{\boldsymbol{k},\beta} , \tag{4.47}$$

and H_{int} the interaction between the atom and the radiation field ($\boldsymbol{p} = \boldsymbol{p}_1 + \boldsymbol{p}_2$),

$$H_{\text{int}} = \boldsymbol{A} \cdot \boldsymbol{p} + \frac{\boldsymbol{A}^2}{2} . \tag{4.48}$$

The Coulomb gauge ($\nabla \cdot \boldsymbol{A} = 0$) is assumed in Eq. (4.48). The operators $a_{\boldsymbol{k},\beta}$ and $a^{\dagger}_{\boldsymbol{k},\beta}$ are the occupation number (Fock) space annihilation and creation operators for photons with propagation wave vector $\boldsymbol{k}$, frequency $\omega_{\boldsymbol{k}} = c|\boldsymbol{k}| = \alpha^{-1}|\boldsymbol{k}|$, and polarisation $\hat{\boldsymbol{e}}_\beta$. $\boldsymbol{A}(\boldsymbol{r})$ is the vector potential of the radiation field,

$$\boldsymbol{A}(\boldsymbol{r}) = \sum_{\boldsymbol{k},\beta} \sqrt{\frac{4\pi}{2V\omega_{\boldsymbol{k}}}} \left[a_{\boldsymbol{k},\beta} \, \hat{\boldsymbol{e}}_\beta e^{i\boldsymbol{k}\cdot\boldsymbol{r}} + a^{\dagger}_{\boldsymbol{k},\beta} \, \hat{\boldsymbol{e}}^*_\beta e^{-i\boldsymbol{k}\cdot\boldsymbol{r}} \right] . \tag{4.49}$$

The sum in Eq. (4.49) runs over two linearly independent polarisations (denoted by the index β) and over all possible values of $\boldsymbol{k}$ in the normalisation volume V. In the limit $V \to \infty$, the sum over $\boldsymbol{k}$ is to be replaced by the integral

$$\sum_{\boldsymbol{k}} \to \frac{V}{(2\pi)^3} \int \mathrm{d}^3k . \tag{4.50}$$

In the frame where the free radiation field is included in the total Hamilton operator, the interaction between the atom and the radiation field is time independent [93]. The eigenstates of H_{tot} can be written as a superposition of states in the form

$$|\Psi\rangle_{\text{tot}} = |\Psi\rangle \otimes |n_{\boldsymbol{k}_1,\beta_1}, n_{\boldsymbol{k}_2,\beta_2}, \ldots\rangle , \tag{4.51}$$

where the total state vector $|\Psi\rangle_{\text{tot}}$ has been written as a direct product of the atomic part $|\Psi\rangle$ and the radiation field part $|n_{\boldsymbol{k}_1,\beta_1}, n_{\boldsymbol{k}_2,\beta_2}, \ldots\rangle$. The number of photons of particular mode $(\boldsymbol{k}, \hat{\boldsymbol{e}}_\beta)$ has been denoted by $n_{\boldsymbol{k},\beta}$.

Exact solutions of H_{tot} will not be sought. The incident photon flux is assumed to be low enough to allow the photon interaction to be treated perturbatively. Only the lowest orders of the power series expansion in $\boldsymbol{A}$ will be kept. For the calculation of the photoionisation cross section, where a single photon is absorbed, or for spontaneous emission of a photon by an excited atom, only the first order term $\boldsymbol{A} \cdot \boldsymbol{p}$ is kept (Fig. 4.3a and 4.3b). The wavelength of the emitted and absorbed photons in our region of interest (a few tens of eV) are assumed much greater then the dimension of the atom,

$$\lambda = \frac{2\pi}{|\boldsymbol{k}|} \gg R_{\text{atom}}. \tag{4.52}$$

---

[1]The interaction between the atom and the external static electric field is included in Eq. (4.46) by replacing H_0 with $H = H_0 + \Delta H$.

(a) (b) (c) (d) (e)
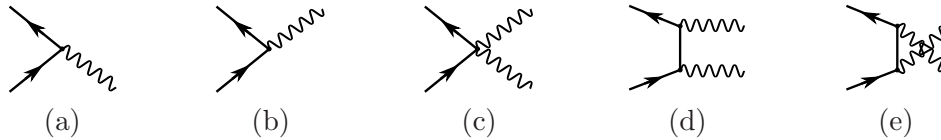
Figure 4.3: First order processes: diagrams describing (a) photon absorption and (b) photon emission by an atom. Second order processes: (c) elastic scattering, (d,e) inelastic scattering. Time is assumed to run from bottom to top.

The transition operator describing absorption and emission of a photon may therefore be written in the dipole-length approximation [90–92]

$$T = i \sum_{\boldsymbol{k},\beta} \sqrt{\frac{4\pi\,\omega_{\boldsymbol{k}}}{2V}} \left[a_{\boldsymbol{k},\beta}\, D(\hat{\boldsymbol{e}}_\beta) - a_{\boldsymbol{k},\beta}^\dagger\, D^\dagger(\hat{\boldsymbol{e}}_\beta) \right] \,, \tag{4.53}$$

where $D(\hat{\boldsymbol{e}}_\beta) = \hat{\boldsymbol{e}}_\beta \cdot (\boldsymbol{r}_1 + \boldsymbol{r}_2)$.

Photon scattering is treated in a similar manner: the second order terms $\boldsymbol{A}^2$ and $(\boldsymbol{A} \cdot \boldsymbol{p})^2$ represented by diagrams in Figs. 4.3c, 4.3d, and 4.3e describe elastic and inelastic scattering of a photon. Higher order processes (e.g., absorption of a photon followed by an emission cascade) can be treated in the same way: products of those permutations of the terms $\boldsymbol{A} \cdot \boldsymbol{p}$ and $\boldsymbol{A}^2$ should be considered that give non vanishing matrix elements for the chosen number of photons in the initial, intermediate, and the final states.

4.5 Photoionisation cross section

In the first part of this section, we derive the photoionisation cross section of an atom in the ground state using the formalisms of complex scaling. We follow the path first introduced by Rescigno and McKoy [94], and the formal procedure and interpretation of Buchleitner et al. [87] and Rost et al. [4]. To illuminate the physical interpretation of the method, we summarise the well known results of Fano [95, 96] describing the photoionisation profile of an autoionising state based on the so called configuration interaction between bound and unbound states. Those results are used to extract the parameters of the photoionisation cross section in the region of a resonance state written in the frame of the complex dilatation method. We further extend the results by taking into account radiation damping [97]. The second part of the section generalises the results to the case of an atom in a homogeneous electric field.

4.5.1 Fano profile

Consider an atomic system described by a bound state $|\varphi\rangle$ and a non resonant continuum state $|\psi_E\rangle$ with the energy E. The states $|\varphi\rangle$ and $|\psi_E\rangle$ are zero approximation states normalised to $\langle\varphi|\varphi\rangle = 1$ and $\langle\psi_{E'}|\psi_E\rangle = \delta(E - E')$ for which the configuration interaction between bound and continuum states has not been taken into account. Let the matrix elements of the total atomic Hamilton operator H_0 describing $|\varphi\rangle$ and $|\psi_E\rangle$ be equal to

$$\begin{aligned}
\langle\varphi|H_0|\varphi\rangle &= E_\varphi \,, \\
\langle\psi_{E'}|H_0|\psi_E\rangle &= E\,\delta(E - E') \,, \\
\langle\psi_E|H_0|\varphi\rangle &\equiv \langle\psi_E|V|\varphi\rangle = V_E \,.
\end{aligned} \tag{4.54}$$

Formally, $|\varphi\rangle$ and $|\psi_E\rangle$ are the eigenstates of $\mathcal{P}H_0\mathcal{P}$ and $\mathcal{Q}H_0\mathcal{Q}$ if $\mathcal{P}$ and $\mathcal{Q}$ denote the projection operators to bound and (non resonant) continuum states, while the non diagonal, i.e., configuration interaction, term is described by

$$V = \mathcal{P}H_0\mathcal{Q} + \mathcal{Q}H_0\mathcal{P}. \tag{4.55}$$

An energy normalised solution $|\phi_E\rangle$ of the total Hamiltonian is sought,

$$H_0|\phi_E\rangle = E|\phi_E\rangle, \tag{4.56}$$

$$\langle\phi_{E'}|\phi_E\rangle = \delta(E - E'), \tag{4.57}$$

where $|\phi_E\rangle$ is written as a superposition of the bound and continuum states,

$$
\begin{aligned}
|\phi_E\rangle &= |\varphi\rangle\langle\varphi|\phi_E\rangle + \int \mathrm{d}E'|\psi_{E'}\rangle\langle\psi_{E'}|\phi_E\rangle \\
&= a(E)|\varphi\rangle + \int \mathrm{d}E' b_{E'}(E)|\psi_{E'}\rangle.
\end{aligned}
\tag{4.58}
$$

By inserting Eq. (4.58) into Eqs. (4.56) and (4.57), the energy dependent coefficients in Eq. (4.58) are shown to be [95, 98]

$$a(E) = \frac{V_E^*}{E - E_\varphi - F(E) + i\Gamma(E)/2} \tag{4.59}$$

and

$$b_{E'}(E) = \left[\mathfrak{P}\frac{1}{E - E'} + z(E)\delta(E - E')\right] V_{E'}\, a(E), \tag{4.60}$$

where

$$z(E) = \frac{E - E_\varphi - F(E)}{|V_E|^2}. \tag{4.61}$$

The quantities introduced in Eqs. (4.59)-(4.61) are the autoionisation width

$$\Gamma(E) = 2\pi|V_E|^2 \tag{4.62}$$

and the energy shift present due to the finite bound-continuum coupling

$$F(E) = \mathfrak{P}\int \mathrm{d}E' \frac{|V_{E'}|^2}{E - E'}. \tag{4.63}$$

$\mathfrak{P}$ denotes the Cauchy principal value of the integral. The photoionisation cross section is proportional to $|\langle\phi_E|T|i\rangle|^2$ and exhibits an asymmetrical shape with respect to the resonance energy (the Beutler-Fano profile),

$$|\langle\phi_E|T|i\rangle|^2 = |\langle\psi_E|T|i\rangle|^2 \left|\frac{\epsilon + q}{\epsilon + i}\right|^2 = |\langle\psi_E|T|i\rangle|^2 \frac{(\epsilon + q)^2}{\epsilon^2 + 1}, \tag{4.64}$$

where T is the transition operator and $|i\rangle$ the initial atomic state. In. Eq. (4.64), ϵ indicates the energy with respect to the central position of the resonance in units of $\Gamma/2$, and q the so called asymmetry parameter of the resonance,

$$\epsilon = \frac{2(E - E_\varphi - F)}{\Gamma}, \qquad q = \frac{\langle\Phi|T|i\rangle}{\pi V_E^*\langle\psi_E|T|i\rangle}. \tag{4.65}$$
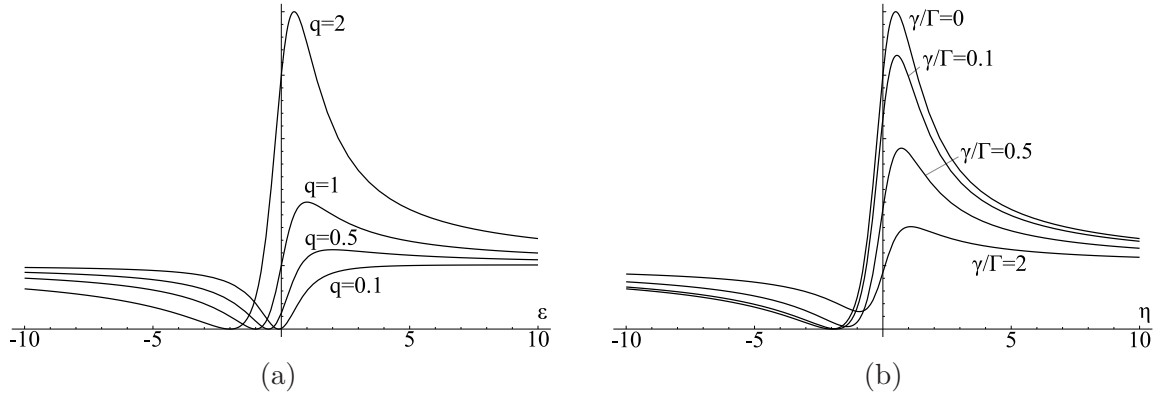
Figure 4.4: (a) Fano profile [Eq. (4.64)] for different values of parameter q. The profiles for negative values of q are obtained by replacing ϵ with $-\epsilon$. (b) Fano profile with damping [Eq. 4.68] for $q = 2$ and various ratios γ/Γ.

In Eq. (4.65), $|\Phi\rangle$ denotes the state $|\varphi\rangle$ modified by an admixture of the continuum state $|\psi_E\rangle$:

$$|\Phi\rangle = |\varphi\rangle + \mathfrak{P}\int \mathrm{d}E' \frac{V_{E'}|\psi_{E'}\rangle}{E - E'} \, . \tag{4.66}$$

The parameter q describes the shape of the resonance profile: q tends to zero if the coupling between the bound and the continuum parts of the wavefunction is very strong (i.e., the resonance state autoionises strongly), whereas large $|q|$ values indicate the vanishing continuum coupling. Fig. 4.5.1a shows examples of Fano asymmetrical photoionisation profiles for different values of parameter q. Note that the minimum value of the cross section is zero for any q.

If the resonance line width Γ, the shift F, and the parameter q may be regarded as constant in the region where the contribution of the resonance to the cross section is non negligible, the integrated photoionisation cross section of a resonance may be written as

$$\int \mathrm{d}E\left[|\langle\phi_E|T|i\rangle|^2 - |\langle\psi_E|T|i\rangle|^2\right] = |\langle\Phi|T|i\rangle|^2 - \frac{\pi\Gamma}{2}|\langle\psi_E|T|i\rangle|^2$$
$$= \frac{\pi\Gamma}{2}|\langle\psi_E|T|i\rangle|^2(q^2 - 1) \tag{4.67}$$
$$\equiv |\langle\varphi|T|i\rangle|^2 \, .$$

The last line in Eq. (4.67) follows from the fact that the transformation connecting the states $|\varphi\rangle$, $|\psi_E\rangle$, and $|\phi_E\rangle$ that diagonalises the total Hamiltonian is unitary [95]. As a matter of fact, any discrepancy between the second and the third line of Eq. (4.67) may be attributed to the energy dependence of Γ, F, or q.

It is often said that the asymmetrical line shape results from the interference between the two possible pathways resulting in the ejected electron: the direct photoionisation of the ground state (Fig. 4.5a) and the transition to the resonance state which decays to the continuum by an electron emission (Fig. 4.5b). This interpretation can be misleading and is suitable only if the bound-continuum coupling is described perturbatively. The final state can then be approximated by the unperturbed continuum state $|\psi_E\rangle$. In the case of Fano diagonalisation, however, one can no longer talk about interference. As can be seen from Eq. (4.54), the states $|\psi_E\rangle$ and $|\varphi\rangle$ are not eigenstates of the atomic Hamiltonian H_0, and therefore they do not represent the possible final atomic states. There is only a single atomic final state composed of localised and non
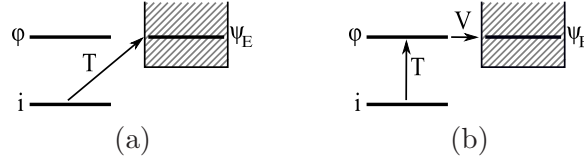
Figure 4.5: Perturbative treatment of photoionisation: (a) direct transition to the continuum state $|\psi_E\rangle$, and (b) indirect transition to $|\psi_E\rangle$ through the resonance state $|\varphi\rangle$.

localised components. The superposition principle – corresponding to the interference between the direct and the indirect photoionisation of the perturbative treatment – in this case applies for the bound and continuum component of this single final state.

4.5.2 Fano profile with radiation damping

Beside atomic ionisation, other decay mechanisms may also be important. Of particular importance in our case is the radiative decay. By emitting a photon, an atom in an autoionising state decays to a bound atomic state. It is clear that the inclusion of radiative decay possibility lower the ionisation branching ratio. The amplitudes of the resonance peaks in the ion yield spectra are lowered and their energy widths are increased. The effect of the radiative decay channel in the model description may be achieved by means of a radiation damping potential described by Robicheaux et al. [97]. This potential is nonlocal and non Hermitian, and describes single photon radiative transitions to lower lying atomic states in a non perturbative manner. Only the results are given here, and the reader is referred to Ref. [97] for details. If the radiative energy width of the bound part of the total wavefunction is denoted by γ, the photoionisation cross section of the resonance state embedded in the continuum is described by

$$|\langle\psi_E|T|i\rangle|^2 \frac{(\eta + q_R)^2 + \mu_R^2}{\eta^2 + 1} . \tag{4.68}$$

In Eq. (4.68), the notation

$$\eta = \frac{2(E - E_\varphi - F(E))}{\Gamma + \gamma}, \quad \mu_R = \frac{\gamma}{\Gamma + \gamma} \quad \text{and} \quad q_R = q \frac{\Gamma}{\Gamma + \gamma} \tag{4.69}$$

has been used. In the treatment given by Robicheaux, the radiation induced energy shift is neglected, and it is assumed that only the decay of the bound part of the wavefunction is non negligible. Note that due to radiation damping, the peak amplitude is lowered and that the cross section no longer falls to zero (Fig. 4.5.1b). Eq. (4.68) reduces to the ordinary Fano profile if $\gamma = 0$.

It should be mentioned that if the width γ is known, this result is obtained by replacing E_r with $E_r - i\gamma/2$ in the coefficients $a(E)$ and $b_{E'}(E)$, i.e., by replacing the matrix element $\langle\psi_E|T|i\rangle[(\epsilon + q)/(\epsilon + i)]$ from Eq. (4.64) with

$$\langle\psi_E|T|i\rangle \left[\frac{\epsilon + i\gamma/\Gamma + q}{\epsilon + i\gamma/\Gamma + i} \right] \tag{4.70}$$

and taking into account that $\eta = \epsilon/(1 + \gamma/\Gamma)$. The same result is obtained by the non perturbative treatment of a three level atom given by Agarwal et al. [99, 100] if: (i) the radiative decay of the upper autoionising state to the initial state is neglected, and (ii) the coupling of

the continuum part of the autoionising state to the lower lying bound state – which is needed to describe the radiative decay of the autoionising state – is disregarded (in Refs. [99] and [100] this is referred to as virtual recombination).

It is instructive to check the result of Eq. (4.68) in the limit $|\langle\psi_E|T|i\rangle| \to 0$: the cross section in this case is proportional to a Lorentzian with the energy width $\Gamma + \gamma$, as expected:

$$|\langle\Phi|T|i\rangle|^2 \frac{\Gamma}{(E - E_\varphi - F)^2 + (\Gamma + \gamma)^2/4} \, . \tag{4.71}$$

The effect of replacing the resonance energy E_φ with the complex energy $E_\varphi - i\gamma$ is not merely the broadening of the spectral features (which could be achieved by a convolution with a Lorentzian with the total width γ): the radiative decay reduces the line strength in the photoionisation spectrum rather than just redistributing it.

4.5.3 Field free photoionisation

Let $|\varphi_g\rangle$ denote the bound atomic ground state with energy E_g, and ω_0 and $\hat{e}_0$ the energy and the polarisation vector of linearly polarised incident photons, respectively. According to Fermi's golden rule, the photoionisation cross section is equal to [87]

$$\sigma(\omega_0) = 4\pi^2\alpha\omega_0 \sum_j |\langle\phi_{jE}|D(\hat{e}_0)|\varphi_g\rangle|^2 \, , \tag{4.72}$$

where $|\phi_{jE}\rangle$ is an energy normalised continuum eigenstate with energy $E = E_g + \omega_0$ accessible from the ground state, and j denotes a set of additional quantum numbers of the state. Photoionisation is described by a diagram of the type shown in Fig. 4.3a, where the final atomic state is a continuum state. It should be noted that the photoionisation cross section (4.72) differs from the photoabsorption cross section by the contributions of true bound states $|\varphi_i\rangle$

$$4\pi^2\alpha\omega_0 \sum_i |\langle\varphi_i|D(\hat{e}_0)|\varphi_g\rangle|^2 \, \delta(E_g + \omega_0 - E_i) \, . \tag{4.73}$$

To the latter, the *measured* photoabsorption cross section, which is typically obtained from the ratio of the incoming and the transmitted photon flux, also includes contributions from higher-order processes, i.e., processes that involve more than one photon propagation line. These higher order processes all diminish the transmission and thus additionally contribute to the total measured absorption cross section. It has indeed been shown [11] that the radiative decay of the resonance state, which corresponds to the inelastic photon scattering (diagrams d and e in Fig. 4.3), results in pronounced differences between the measured photoionisation and photoabsorption signal.

Eq. (4.72) can be written as

$$\sigma(\omega_0) = 4\pi^2\alpha\omega_0 \sum_j \langle\varphi_g|D(\hat{e}_0)|\phi_{jE}\rangle\langle\phi_{jE}|D(\hat{e}_0)|\varphi_g\rangle \, , \tag{4.74}$$

where we have used the fact that $D(\hat{e}_0)$ is a Hermitian operator. The projection operator $\sum_j |\phi_{jE}\rangle\langle\phi_{jE}|$ is expressed by complex scaled Green's operators as [87]

$$\sum_j |\phi_{jE}\rangle\langle\phi_{jE}| = \frac{1}{2\pi i}\left[R(-\Theta)\frac{1}{H(\Theta) - E}R(\Theta) - R(\Theta)\frac{1}{H(-\Theta) - E}R(-\Theta)\right] \, . \tag{4.75}$$

Eq. (4.75) is rather formal. As will be explained, it is obtained from

$$\delta(E - H) = \frac{1}{2\pi i}\left[G^-(E) - G^+(E)\right]$$

$$= \lim_{\epsilon \to 0^+} \frac{1}{2\pi i}\left[R(-\Theta)\frac{1}{H(\Theta) - E - i\epsilon}R(\Theta) - R(\Theta)\frac{1}{H(-\Theta) - E + i\epsilon}R(-\Theta)\right],$$

(4.76)

which follows from the well known equality ($\mathfrak{P}$ is the Cauchy principal value of the integral)

$$\lim_{\epsilon \to 0^+} \frac{1}{x \pm i\epsilon} = \mathfrak{P}\frac{1}{x} \mp i\pi\delta(x).$$

(4.77)

If $|\varphi_i\rangle$ and $|\phi_{jE}\rangle$ form a complete set of states, Eq. (4.76) is equal to

$$\delta(E - H) = \sum_i |\varphi_i\rangle\,\delta(E - E_i)\,\langle\varphi_i| + \sum_j |\phi_{jE}\rangle\langle\phi_{jE}|.$$

(4.78)

We insert the completeness relation [Eq. (4.38)] in Eq. (4.76), i.e, we use the spectral representation of Green's operators to arrive at

$$\sum_i |\varphi_i\rangle\,\delta(E - E_i)\,\langle\varphi_i| + \sum_j |\phi_{jE}\rangle\langle\phi_{jE}| =$$

$$\lim_{\epsilon \to 0^+} \frac{1}{2\pi i}\sum_n \left[\frac{R(-\Theta)|\Psi_{n\Theta}\rangle\langle\overline{\Psi_{n\Theta}}|R(\Theta)}{E_{n\Theta} - E - i\epsilon} + \frac{R(\Theta)|\overline{\Psi_{n\Theta}}\rangle\langle\Psi_{n\Theta}|R(-\Theta)}{E_{n\Theta}^* - E + i\epsilon}\right].$$

(4.79)

The contributions of the bound states $|\varphi_i\rangle$ in Eq. (4.79) can be identified as those contributions of the complex scaled states $|\Psi_{n\Theta}\rangle$ which represent bound atomic states. Both contributions cancel out if the basis in which the complex scaled eigenstates are represented is complete. This follows from the reality of the energies $E_{n\Theta}$ pertaining to the bound states and the fact that the bound states can be represented in a square integrable basis even for $\Theta = 0$. The parameter ϵ may be set to zero in the resulting expression because of the finite imaginary part of the remaining resonance and continuum states. Nevertheless, if the completeness relation is used in Eq. (4.75), the expression diverges whenever E is equal to the energy of a bound state. For energies above the ionisation threshold, however, the contributions of $G^-(E)$ and $G^+(E)$ exactly cancel for bound states, and the complete set of states may therefore be inserted in Eq. (4.75). Needless to say, in practice, the contributions of bound states are not calculated.

With the ideas of the last paragraph in mind, Eq. (4.72) can be transformed into

$$\sigma(\omega_0) = \frac{4\pi^2\alpha\omega_0}{2\pi i}\sum_n\left[\frac{\langle\varphi_g|D(\hat{e}_0)R(-\Theta)|\Psi_{n\Theta}\rangle\langle\overline{\Psi_{n\Theta}}|R(\Theta)D(\hat{e}_0)|\varphi_g\rangle}{E_{n\Theta} - E_g - \omega_0}\right.$$

$$\left. - \frac{\langle\varphi_g|D(\hat{e}_0)R(\Theta)|\overline{\Psi_{n\Theta}}\rangle\langle\Psi_{n\Theta}|R(-\Theta)D(\hat{e}_0)|\varphi_g\rangle}{E_{n\Theta}^* - E_g - \omega_0}\right].$$

(4.80)

The second term in Eq. (4.80) is just the complex conjugate of the first term. It thus follows that

$$\sigma(\omega_0) = 4\pi\alpha\omega_0\,\mathrm{Im}\sum_n\frac{\langle\varphi_g|D(\hat{e}_0)R(-\Theta)|\Psi_{n\Theta}\rangle\langle\overline{\Psi_{n\Theta}}|R(\Theta)D(\hat{e}_0)|\varphi_g\rangle}{E_{n\Theta} - E_g - \omega_0}.$$

(4.81)

The product of matrix elements in Eq. (4.81) can be further simplified as follows. Since the state $|\varphi_g\rangle$ is represented by a real wavefunction in Sturmian basis, the first and the second matrix

element are equal:

$$\langle \varphi_g | D(\hat{e}_0) R(-\Theta) | \Psi_{n\Theta} \rangle = \langle \Psi_{n\Theta} | R(-\Theta) D(\hat{e}_0) | \varphi_g \rangle^*$$
$$= \langle \overline{\Psi_{n\Theta}} | R(\Theta) D(\hat{e}_0) | \varphi_g \rangle \, . \tag{4.82}$$

Instead of calculating $|\varphi_g\rangle$ separately, the complex scaled ground state

$$|\Psi_{g\Theta}\rangle = R(\Theta)|\varphi_g\rangle \tag{4.83}$$

is obtained in the diagonalisation of $H(\Theta)$. Since the state $|\varphi_g\rangle$ can be represented in a square integrable basis, Eq. (4.83) can be reverted to give the final result

$$\sigma(\omega_0) = 4\pi\alpha\omega_0 \operatorname{Im} \sum_n \frac{\langle \overline{\Psi_{n\Theta}} | R(\Theta) D(\hat{e}_0) R(-\Theta) | \Psi_{g\Theta} \rangle^2}{E_{n\Theta} - E_g - \omega_0} \, . \tag{4.84}$$

Note that it is now trivial to calculate the matrix element in Eq. (4.84): the complex scaled operator $D(\hat{e}_0)$ is simply

$$R(\Theta) D(\hat{e}_0) R(-\Theta) = D(\hat{e}_0) \, e^{i\Theta} \equiv D_\Theta(\hat{e}_0) \, . \tag{4.85}$$

It is now clear that for the calculation of the photoionisation cross section, only the eigenstates and eigenvalues of $H(\Theta)$ are required (i.e., $R(\Theta)$ and $|\varphi_g\rangle$ are not needed). It should be noted that the calculation of an unscaled state from the corresponding complex scaled state (i.e., "back rotation") would not be possible for continuum or resonance states as they cannot be represented in the framework of an $\mathcal{L}^2$ basis set.

As can be seen from Eq. (4.84), for a given ω_0, only states with energies close to $E_g + \omega_0$ contribute substantially to the total cross section (Fig. 4.6). Obviously, to describe a continuum state, continuum *and* resonance eigenstates $|\Psi_{n\Theta}\rangle$ are included in the summation. This
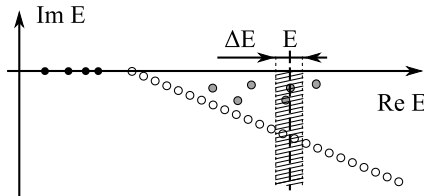
Figure 4.6: The role of the projection operator $\sum_j |\phi_{jE}\rangle\langle\phi_{jE}|$: eigenstates of $H_0(\Theta)$ with $\operatorname{Re} E_{n\Theta}$ close to $E = E_g + \omega_0$ contribute most notably to the cross section.

means that a continuum atomic state *always* consists of localised and non localised components. However, the influence of localised components of the wavefunction is negligible for energies far away from the regions of resonances. Furthermore, if an eigenstate $|\Psi_{n\Theta}\rangle$ is characterised by a large imaginary part of the corresponding eigenenergy (as is the case for the continuum points which do not lie in the vicinity of the pertinent ionisation threshold), its contribution to the cross section represents a smooth background. It should be made clear that for an accurate calculation of the contributions from continuum cuts, the discrete grid of points describing the cuts should be very dense. This, in turn, requires a large basis size. In the case of a Sturmian basis, this means that high order polynomials should be used to describe oscillatory behaviour of the wavefunction.

If the state $|\Psi_{n\Theta}\rangle$ in the sum Eq. (4.84) represents a resonance, its contribution is given by

$$\sigma_n(\omega_0) = 4\pi\alpha\omega_0 \operatorname{Im} \frac{\langle\overline{\Psi_{n\Theta}}|D_\Theta(\hat{e}_0)|\Psi_{g\Theta}\rangle^2}{E_n - E_g - \omega_0 - i\Gamma_n/2}, \tag{4.86}$$

where the complex resonance energy has been written as $E_{n\Theta} = E_n - i\Gamma_n/2$. Eq. (4.86) can be cast into a form that exactly corresponds to Fano's parameterisation of the partial photoionisation cross section. In this way, it is possible to gain insight into the physical meaning of the complex matrix elements. Let B_n and C_n denote the real and imaginary parts of $\langle\overline{\Psi_{n\Theta}}|D_\Theta(\hat{e}_0)|\Psi_{g\Theta}\rangle$, respectively,

$$B_n + iC_n = \langle\overline{\Psi_{n\Theta}}|D_\Theta(\hat{e}_0)|\Psi_{g\Theta}\rangle \tag{4.87}$$

and

$$\epsilon_n = \frac{E_g + \omega_0 - E_n}{\Gamma_n/2}, \tag{4.88}$$

$$q_n = -\frac{B_n}{C_n}, \tag{4.89}$$

$$\mu_n^2 = \frac{8\pi\alpha\omega_0 C_n^2}{\Gamma_n}. \tag{4.90}$$

The contribution of the resonance $|\Psi_{n\Theta}\rangle$ is then equal to

$$\sigma_n = \mu_n^2 \left[\frac{(\epsilon_n + q_n)^2}{\epsilon_n^2 + 1} - 1\right], \tag{4.91}$$

whereas the total photoionisation cross section can be written as a sum of a non resonant and resonant terms:

$$\sigma(\omega_0) = \sigma_0(\omega_0) + \sum_n \sigma_n(\omega_0). \tag{4.92}$$

In Eq. (4.92), $\sigma_0(\omega_0)$ is a smooth background that originates from the (discretised) continuum cuts. Since a single complex scaled state describes a resonance, it follows that ϵ_n corresponds to the dimensionless energy ϵ, and the asymmetry parameter q_n to the q parameter, as defined in Eq. (4.65). Furthermore, it can be seen from Eq. (4.90) that the square of the imaginary part C_n^2 is proportional to the square modulus of the dipole matrix element $|\langle\psi_E|T|i\rangle|^2$ between the initial bound state and the structureless continuum. It can therefore be deduced that the square of the real part of the matrix element B_n^2 represents the dipole coupling between the initial and the quasi bound part (the modified bound part) of the total wavefunction, i.e., it is proportional to $|\langle\Phi|T|i\rangle|^2$ (cf. also Ref. [4]). This latter property can also be seen from the integrated cross section, i.e., from the area under the resonance:

$$\begin{aligned}
\int_{-\infty}^{\infty} dE\,\sigma_n(E) &= \frac{\Gamma_n}{2} \int_{-\infty}^{\infty} d\epsilon_n\,\sigma_n(\epsilon_n) \\
&= 4\pi^2\alpha\omega_0 \left[B_n^2 - C_n^2\right] \\
&= 4\pi^2\alpha\omega_0 \operatorname{Re}\langle\overline{\Psi_{n\Theta}}|D_\Theta(\hat{e}_0)|\Psi_{g\Theta}\rangle^2.
\end{aligned} \tag{4.93}$$

Eq. (4.93) is obviously the analog of Eq. (4.67). According to the latter, the integrated cross section is equal to the square modulus of the dipole matrix element between the unperturbed bound state (denoted by $|\varphi\rangle$) and the initial state. The real part of the square of the complex scaled matrix element is therefore equal to the transition matrix element where the configuration

interaction between the bound and continuum part is neglected. An expression similar to Eq. (4.93) will be used in the following to approximate the radiative decay rate of a resonance state.

It should be noted that each term that belongs to a resonance in Eq. (4.84) becomes negative for some range of values of ω_0. The *total* sum, however, is guaranteed to be positive, since it represents the cross section. To be physically meaningful, the contributions of all the states must yield a positive result. The negative values of $\sigma_n(\omega_0)$ are to be understood as a decrease of the cross section below the value of the bare, non resonant continuum. This, following Fano, is the result of the destructive interference between localised and continuum components of the wavefunction.

At the end it should be mentioned that the photoionisation cross section for the case of linearly polarised incident light does not depend on $\hat{\boldsymbol{e}}_0$ since the quantisation axis of the atom may be chosen arbitrarily in the absence of an external field. Therefore, if $\hat{\boldsymbol{e}}_0 = \hat{\boldsymbol{z}}$ is set and the Wigner-Eckart theorem [13, 53] is applied, Eq. (4.84) simplifies to

$$\sigma(\omega_0) = 4\pi\alpha\omega_0 \operatorname{Im} \sum_n \begin{pmatrix} L_n & 1 & L_g \\ -M_n & 0 & M_g \end{pmatrix}^2 \frac{\langle \overline{\Psi_{n\Theta}} \| \mathcal{D}_\Theta \| \Psi_{g\Theta} \rangle^2}{E_{n\Theta} - E_g - \omega_0} . \tag{4.94}$$

The meaning of the reduced matrix element $\langle \overline{\Psi_{n\Theta}} \| \mathcal{D}_\Theta \| \Psi_{g\Theta} \rangle$ is explained in Appendix B. In the absence of external fields, the quantisation axis of an atom can be arbitrarily chosen, too. This means that the total cross section may be obtained by an average over the possible values of M_g. For the ground state of the helium atom, $L_g = 0$, and therefore $M_g = 0$. Due to the chosen polarisation and the properties of the 3-j symbols, only final states with $M_n = 0$ give non vanishing contributions. As a consequence, the only accessible final states are those with $L_n = 1$ and odd parity π_n. The final result is thus

$$\sigma(\omega_0) = \frac{4\pi\alpha\omega_0}{3} \operatorname{Im} \sum_n' \frac{\langle \overline{\Psi_{n\Theta}} \| \mathcal{D}_\Theta \| \Psi_{g\Theta} \rangle^2}{E_{n\Theta} - E_g - \omega_0} , \tag{4.95}$$

where the prime is used to denote summation over the whole set of final state quantum numbers, with the exception of magnetic quantum numbers M_n.

4.5.4 Spontaneous emission

The ability of an autoionising state to emit an electron due to the finite coupling between localised and continuum components is completely described by Eq. (4.84). However, the treatment of the preceding subsection does not take into account other decay mechanisms that are also present. Specifically, it does not take into account the decay due to interaction of the atom with the radiation field. The radiative decay channel represents the only possible decay path for a bound atomic state, but may also become dominant for resonance states when the autoionisation width is very small.

The aim of this section is to calculate the widths resulting from the radiative decay of a state. In the following, the photon density of the incident light is assumed small so that the spontaneous photon emission dominates over the stimulated emission. We first proceed with the spontaneous emission rate from a bound state, and later generalise the results to the case of a resonance state.

Let $|\varphi_n\rangle$ be a state vector describing a bound excited atomic state of the helium atom below the $N = 2$ ionisation threshold. The atom initially in this state can emit a photon with the propagation vector $\boldsymbol{k}$, energy $\omega = |\boldsymbol{k}|/\alpha$, and polarisation $\hat{\boldsymbol{e}}_\beta$. This is described by the probability

rate γ_n per unit photon energy per unit solid angle of the emitted photon as [90]

$$\frac{\partial^2 \gamma_n}{\partial \omega \partial \hat{k}} = \frac{\alpha^3 \omega^3}{2\pi} \sum_\beta \left(\sum_i |\langle \varphi_i | D(\hat{e}_\beta) | \varphi_n \rangle|^2 \delta(E_n - E_i - \omega) + \sum_j |\langle \phi_{jE} | D(\hat{e}_\beta) | \varphi_n \rangle|^2 \right) . \qquad (4.96)$$

We have used $|\varphi_i\rangle$ to denote bound final eigenstates with energies E_i and $|\phi_{jE}\rangle$ for continuum eigenstates with the energy $E = E_n - \omega$. The first term in Eq. (4.96) describes the usual fluorescence decay to bound atomic states [90], while the second term describes a radiative transition to a continuum or an autoionising state, i.e., a process eventually resulting in a photon, an ion, and a free electron. Note that the initial state $|\varphi_n\rangle$ need not lie below the $N = 1$ threshold: the states above the first ionisation threshold with parity equal to $\pi_n = (-1)^{L+1}$ are also true bound states. An example of such a process is a decay of a $^1P^e$ doubly excited state. It is also clear that in this case continuum eigenstates are indeed accessible: the $^1P^e$ state can decay to $^1P^o$ states which lie above the $N = 1$ threshold.

The contribution of the continuum term can be treated in the same manner as the photoionisation cross section [cf. Eq. (4.75)]. The resulting expression is then integrated over the energies and angles of the emitted photon and summed over the two independent polarisations to give the total radiative rate. In the following, this contribution will be neglected. Testing calculations where doubly excited states are treated as bound show that the sum of ω^3-weighted squared matrix elements between an initial doubly excited state and final singly excited states is at least an order of magnitude larger that the corresponding sum connecting doubly excited states. This is expected since partial contributions to the total radiative transition rate (owing to the ω^3 dependence) may contribute substantially only if occupation numbers of both electrons change. Since the dipole transition operator is a sum of single particle operators, the matrix element in this case is small because of the small overlap of the single electron wavefunctions. Thus, a doubly excited state most probably decays to a singly excited state where one of the electrons does not participate actively in the transition (*spectator electron*). The same argument holds for a continuum final state if fluorescence and autoionisation are both considered as first order perturbations. It turns out that the main contribution to the total radiative decay rate stems from the $2p \rightarrow 1s$ transition of the inner electron [19]. This is why all fluorescence decay rates of doubly excited states below the $N = 2$ threshold are approximately of same order of magnitude (cf. Appendix E). Their rates are to be compared to the decay rate of the He$^+$ ion $\gamma_{\mathrm{He}^+} \approx 2.42 \times 10^{-7}$ a.u. ($\tau_{\mathrm{He}^+} \approx 100$ ps). The discrepancies from the ionic rate reflect the effect of configuration interaction and the failure of the single configuration description for doubly excited states [19]. It thus follows that we may approximate the fluorescence rate by[2]

$$\gamma_n \approx \frac{\alpha^3}{2\pi} \sum_\beta \sum_i \int d^2\hat{k} \, (E_n - E_i)^3 \langle \varphi_i | D(\hat{e}_\beta) | \varphi_n \rangle^2 . \qquad (4.97)$$

The preceding discussion applies to the case where $|\varphi_n\rangle$ is a bound state. If, however, the initial state is a *resonance* represented by the complex scaled state vector $|\Psi_{n\Theta}\rangle$, we substitute the expression under the integral by

$$(E_n - E_i)^3 \, \mathrm{Re} \, \langle \Psi_{i\Theta} | D_\Theta(\hat{e}_\beta) | \Psi_{n\Theta} \rangle^2 , \qquad (4.98)$$

where $E_n = \mathrm{Re} \, E_{n\Theta}$ and where $|\Psi_{i\Theta}\rangle$ denotes a complex scaled bound state. This means that the real part of the square of the complex matrix element may be used to calculate radiative

---

[2]Note that dipole matrix elements of bound states represented in a basis of real Sturmian basis functions is a real quantity.

transition rates. As has been shown [Eq. (4.93)], the real part of the squared dipole matrix element between a resonance and a bound state represents a quantity proportional to the integrated cross section, and the latter is proportional to the square modulus of the dipole matrix element between the unmodified bound part of the resonance wavefunction and the bound state. Eq. (4.98) therefore gives approximately the same result as would be obtained in the framework where doubly excited resonance states were treated as true bound states. It should be mentioned that the continuum contribution (the contribution of $|\phi_{jE}\rangle$) to the radiative transition rate was considered for the case of photodissociation through the radiative channel of exotic molecular ions [101, 102]: the treatment given is similar to the derivation of the photoionisation cross section, with the initial state being a resonance. However, no justification or comment was given about the validity of the latter approach.

The angular integration in Eq. (4.97) can easily be performed. It is described in Appendix C in detail. The final result applicable to both, a bound and a resonance initial state is shown to be

$$\gamma_n = \frac{4\alpha^3}{3(2L_n + 1)} \sum_i{}' (E_n - E_i)^3 \operatorname{Re} \langle \overline{\Psi_{i\Theta}} \| \mathcal{D}_\Theta \| \Psi_{n\Theta} \rangle^2 \,. \tag{4.99}$$

In Eq. (C.12), L_n is the total angular momentum of the initial state. The prime again means that the magnetic quantum numbers of the final state M_i are to be omitted from the sum. If L_i, π_i, and π_n denote the total angular momentum of the final state $|\Psi_{i\Theta}\rangle$, the parity of the final state, and the parity of the initial state, respectively, the index i in Eq. (4.99) runs over those final states for which

$$|L_i - L_n| \le 1 \le L_i + L_n \qquad \text{and} \qquad \pi_i = -\pi_n \,. \tag{4.100}$$

With the calculated radiative rates γ_n, the photoionisation cross section from Eq. (4.84) can be corrected in accordance with Eq. (4.68). Since the radiative damping affects only the bound part of the total wavefunction, the terms pertaining to discretised continuum cuts in Eq. (4.84) remain unchanged, whereas resonance contributions $\sigma_n(\omega_0)$ are replaced by

$$\sigma_n^{\text{corr}}(\omega_0) = 4\pi\alpha\omega_0 \operatorname{Im} \frac{(B_n + iC_n)^2 + \mathcal{R}_n}{E_n - E_g - \omega_0 - i(\Gamma_n + \gamma_n)/2} \,, \quad \mathcal{R}_n = -\frac{\gamma_n(B_n^2 + C_n^2)}{\Gamma_n + \gamma_n} \,. \tag{4.101}$$

Note again that this is quite different from replacing Γ_n with the total width $\Gamma_n + \gamma_n$ since the amplitude of the resulting peak is additionally lowered.

4.5.5 Photoionisation in electric field

In the field free case, three types of eigenstates emerge in the diagonalisation of the scaled Hamilton matrix $\mathbf{H}_0(\Theta)$: bound states, states representing discretised continuum cuts, and resonance states. When the electric field is applied, however, no true bound states exist anymore. They are all turned into resonances (cf. for example Alvarez et al. [62]). It can be thought that the electron tunnels through the finite barrier that results from the atomic potential after the field has been applied. Nevertheless, the states that were strongly bound in the field free case are only weakly affected by the external field if its electric field strength is small compared to the field strength of the nucleus. Such states may therefore be treated as bound.

In this subsection we study the (electric field) ground state photoionisation of the helium atom in the homogeneous electric field, whereby the initial state is treated as a true bound state. This approximation can be well justified: the helium atom ground state is energetically well separated from all higher lying states, even when the electric field is applied, thus the field

induced mixing with the higher states is negligible. Furthermore, both electrons on average move very close to the nucleus, where the potential of the external field is several orders of magnitude smaller then the effective nuclear potential.

The treatment similar to the field free case applies to the case of the external field. Here, however, the results depend on the relative orientation of the polarisation $\hat{e}_0$ and the electric field vector $\boldsymbol{F}$. Additional complications also arise since the energies are no longer independent of magnetic quantum numbers.

We start from Eq. (4.84), where the eigenvectors and eigenvalues of $H_0(\Theta)$ are replaced by the eigenvectors and eigenvalues of the total Hamiltonian $H(\Theta)$,

$$\sigma(\omega_0) = 4\pi\alpha\omega_0 \operatorname{Im} \sum_n \frac{\langle \overline{\Phi_{n\Theta}}|D_\Theta(\hat{e}_0)|\Phi_{g\Theta}\rangle^2}{\mathcal{E}_{n\Theta} - \mathcal{E}_g - \omega_0} \,. \qquad (4.102)$$

In Eq. (4.102), $|\Phi_{g\Theta}\rangle$ denotes the helium ground state in the electric field and $|\Phi_{n\Theta}\rangle$ the excited state with energy $\mathcal{E}_{n\Theta}$. As before, the matrix element is calculated from the complex scaled state $|\Phi_{g\Theta}\rangle$ that is obtained by diagonalising $\mathbf{H}(\Theta)$. As has been explained, $|\Phi_{g\Theta}\rangle$ is treated as a bound state. This implies that only the real part of the corresponding energy $\mathcal{E}_{g\Theta}$ is considered, i.e., $\mathcal{E}_g = \operatorname{Re} \mathcal{E}_{g\Theta}$. The calculation of transition matrix elements is explained in Appendix B in detail. It is to be noted that since the form of Eq. (4.102) is the same as in the field free case, exactly the same parameterisation [Eqs. (4.87)-(4.90)] can be used for the resonance photoionisation cross section.

4.5.6 Spontaneous emission in electric field

Radiative decay in an externally applied homogeneous electric field is treated in the same manner as in the field free case. The same assumption is made regarding the incident photon flux. Only the final states below the first ionisation threshold will be considered as final states. Furthermore, it is assumed that *the final singly excited states may be treated as true bound states*. This approximation is suitable when the external electric field strengths are several orders of magnitude below the strengths the electrons are subject to due to the nucleus. The assumption is well justified for field strengths $F \leq 20$ kV/cm for singly excited states with principal quantum numbers $n \leq 10$: autoionisation widths resulting from diagonalisation of the total Hamilton matrix which includes states with total angular momenta $L \leq 10$ and both parities (cf. Chapter 5) are of order 10^{-10} a.u. Singly excited states with $n \leq 5$ are characterised by energy widths of order 10^{-12} a.u., which is approximately the accuracy of the current calculations. The latter approximation is a crude one for high lying singly excited states and for high field strengths: for $F \leq 50$ kV/cm, energy widths for states with $n \leq 10$ are of order 10^{-9} a.u., but rise to 10^{-6} a.u. -10^{-5} a.u. when the field reaches 100 kV/cm. Furthermore, for $n = 15$, the diagonalisation of $\mathbf{H}(\Theta)$ results in energy widths of order 10^{-7} a.u. for $F \leq 10$ kV/cm, 10^{-6} a.u. for the field around 50 kV/cm, and approximately 10^{-5} a.u. for the field strengths close to 100 kV/cm.

If the accessible final states $|\Phi_{i\Theta}\rangle$ are considered bound, the total fluorescence rate γ_n may be approximated by [cf. Eq. (4.97)]

$$\frac{\partial \gamma_n}{\partial \hat{k}} \approx \frac{\alpha^3}{2\pi} \sum_\beta \sum_i (\mathcal{E}_n - \mathcal{E}_i)^3 \operatorname{Re} \langle \overline{\Phi_{i\Theta}}|D_\Theta(\hat{e}_\beta)|\Phi_{n\Theta}\rangle^2 \,, \qquad (4.103)$$

where $\mathcal{E}_n = \operatorname{Re} \mathcal{E}_{n\Theta}$ and $\mathcal{E}_i = \operatorname{Re} \mathcal{E}_{i\Theta}$. The index i runs over all accessible states below the first ionisation threshold. Since for the case of an initial doubly excited state below the $N = 2$ threshold the sum formally also includes high singly excited Rydberg states, for which our

assumption does not hold anymore, this approximation seems to fail. In this case, however, transitions to singly excited states characterised by principal quantum numbers n' much higher than the principal quantum number n of the outer electron contribute negligibly. We have already mentioned (cf. pg. 57) that the radiative decay is most probable when one of the electrons acts as a spectator: a transition to a high lying singly excited state would imply that occupation numbers of both electrons are changed, resulting in a small transition matrix element.

As has been done for the field free case, γ_n is used to account for radiation damping in the photoionisation cross section equation: in Eq. (4.101), the eigenstates, the energies, and the widths are replaced by the corresponding quantities describing the atom in an external field.

4.6   Inelastic photon scattering cross section

In the following, the cross section for the inelastic scattering of photons is derived. The results for the field free case are presented and later generalised to the case of electric field. The treatment with the Kramers-Heisenberg formula is used, and the reader is referred to Refs. [90–92] for details.

4.6.1   Field free scattering

Inelastic scattering cross section per unit emitted photon energy per unit solid angle of the emitted photon describing photon scattering from an atom in the ground state may be approximated by [103]

$$\frac{\partial^2 \sigma}{\partial \omega \partial \hat{k}} \approx \alpha^4 \omega^3 \omega_0 \sum_{\beta} \sum_{m} |\langle \varphi_m | D(\hat{e}_\beta) G_0(E_g + \omega_0) D(\hat{e}_0) | \varphi_g \rangle|^2 \, \delta(E_g + \omega_0 - E_m - \omega) \,. \quad (4.104)$$

The kets $|\varphi_g\rangle$ and $|\varphi_m\rangle$ represent the initial ground state and bound final states with energies E_g and E_m, respectively. The energy and polarisation of the incident photons are denoted by ω_0 and $\hat{e}_0$, while ω, $\boldsymbol{k}$, and $\hat{e}_\beta$ are used for the energy, propagation vector, and polarisation of the emitted photons, respectively. $G_0(E) = (E - H_0)^{-1}$ is the free atom propagator. From the second order processes depicted in Fig. 4.3, only the resonant term (Fig. 4.3d) is considered in Eq. (4.104). Since in our case the initial state is the ground state of the helium atom, the energy of the emitted photon cannot be greater than the energy of the incident photon due to energy conservation. Therefore, the inelastic scattering process represented by the diagram in Fig. 4.3e does not contribute to the scattering cross section. Furthermore, in our treatment of the scattered photons, the contribution of the elastic scattering term is small and will be neglected. This is because the amplitude describing the resonant term (Fig. 4.3d) is of the order of $c/\omega_0 \simeq 3 \times 10^{-9}$ m for incident photons with energies ω_0 in the region of doubly excited states below the $N = 2$ threshold, while the amplitude of the elastic scattering term (Fig. 4.3c) is of the order of the classical electron radius $r_0 \approx 2.8 \times 10^{-15}$ m [90].

The contribution of the final doubly excited states to the total cross section will be assumed small for the same reasons as in the case of spontaneous emission from a doubly excited state (cf. pgs. 57 and 59 for discussion). This type of inelastic scattering involves coherent transitions between doubly excited states and will be neglected. The sum over m in Eq. (4.104) therefore includes only singly excited states.

Integrating Eq. (4.104) over the energy of the emitted photon and rewriting the propagator

$G_0(E_g + \omega_0)$ by means of complex scaled Green's operator, one obtains

$$\frac{\partial \sigma}{\partial \hat{k}} \approx \alpha^4 \omega_0 \sum_\beta \sum_m (E_g + \omega_0 - E_m)^3 |\mathcal{M}_{mg}|^2 \,, \tag{4.105}$$

where

$$\mathcal{M}_{mg} = \sum_n \frac{\langle \overline{\Psi_{m\Theta}} | D_\Theta(\hat{e}_\beta) | \Psi_{n\Theta} \rangle \langle \overline{\Psi_{n\Theta}} | D_\Theta(\hat{e}_0) | \Psi_{g\Theta} \rangle}{E_g + \omega_0 - E_{n\Theta}} \,. \tag{4.106}$$

For the accessible final states in Eq. (4.105), $E_m \leq E_g + \omega$ holds. The completeness relation of the complex scaled eigenstates has been used and the initial and final states expressed with their complex scaled counterparts. Since the eigenvalues are independent of magnetic quantum numbers, angular integration can be performed by means of the parameterisation of $\hat{k}$ and $\hat{e}_\beta$ described in Appendix B. The result for the ground state of the helium atom is

$$\sigma \approx \frac{8\pi \alpha^4 \omega_0}{27} {\sum_m}' (E_g + \omega_0 - E_m)^3 \left| {\sum_n}' \frac{\langle \overline{\Psi_{m\Theta}} \| \mathcal{D}_\Theta \| \Psi_{n\Theta} \rangle \langle \overline{\Psi_{n\Theta}} \| \mathcal{D}_\Theta \| \Psi_{g\Theta} \rangle}{E_g + \omega_0 - E_{n\Theta}} \right|^2 . \tag{4.107}$$

As before, the summation sign with the prime denotes that magnetic quantum numbers are omitted from the sum. The index n in Eq. (4.107) runs over $^1P^o$ states, whereas the index m runs over $^1S^e$ and $^1D^e$ states.

In Eqs. (4.105) and (4.107), the summation over the intermediate states includes bound states, as well as resonances and continuum states. For an isolated narrow resonance intermediate state, the square modulus of the matrix element $|\mathcal{M}_{mg}|^2$ has a pronounced peak centred at the resonance energy $E_n = \text{Re}\, E_{n\Theta}$, while for a bound state, the cross section is divergent if ω_0 is exactly equal to the energy difference $E_{n\Theta} - E_g = E_n - E_g$. The latter behaviour can be corrected if radiation damping is accounted for in Eq. (4.105) by substituting

$$E_n - i\Gamma_n/2 \qquad \text{with} \qquad E_n - i\Gamma_n/2 - i\gamma_n/2 \,. \tag{4.108}$$

in the matrix element $\mathcal{M}_{mg}$ (cf. pg. 51). Note that this treatment is consistent with the radiation damping introduced earlier.

A comment should be made at the end about the shapes of the peaks in the inelastic scattering spectra originating from bound and resonance intermediate states. In general, those peaks are *not* symmetrically shaped. Their asymmetry is a consequence of the interference with the continuum and close lying resonances and bound states (total energy widths of the latter may be finite due to radiative decay). This is in contrast with the treatment where the inelastic scattering is regarded incoherently, as a two step process, resulting in a cross section composed of symmetric peaks. The latter approximation is valid only when the states are isolated, so that their overlap with the neighbouring resonance or bound states is negligible, and when the contribution of the continuum is small and can also be neglected. If this is the case, the square modulus of $\mathcal{M}_{mg}$ may be approximated by

$$|\mathcal{M}_{mg}|^2 \approx \sum_n \left| \frac{\langle \overline{\Psi_{m\Theta}} | D_\Theta(\hat{e}_\beta) | \Psi_{n\Theta} \rangle \langle \overline{\Psi_{n\Theta}} | D_\Theta(\hat{e}_0) | \Psi_{g\Theta} \rangle}{E_g + \omega_0 - E_{n\Theta}} \right|^2 . \tag{4.109}$$

4.6.2 Inelastic scattering in electric field

Results from Eqs. (4.105) and (4.106) are straightforward to generalise to the case when electric field is applied: as before, the field free eigenenergies and eigenvectors are replaced by the

corresponding eigenpairs of $H(\Theta)$. The result is

$$\frac{\partial \sigma}{\partial \hat{k}} \approx \alpha^4 \omega_0 \sum_\beta \sum_m (\mathcal{E}_g + \omega_0 - \mathcal{E}_m)^3 |\mathcal{M}_{mg}|^2 \tag{4.110}$$

with

$$\mathcal{M}_{mg} = \sum_n \frac{\langle \overline{\Phi_{m\Theta}} | D_\Theta(\hat{e}_\beta) | \Phi_{n\Theta} \rangle \langle \overline{\Phi_{n\Theta}} | D_\Theta(\hat{e}_0) | \Phi_{g\Theta} \rangle}{\mathcal{E}_g + \omega_0 - \mathcal{E}_{n\Theta}} \, . \tag{4.111}$$

Only contributions of final singly excited states are considered in Eq. (4.110), and the states $|\Phi_{g\Theta}\rangle$ and $|\Phi_{m\Theta}\rangle$ are again treated as if they were bound. The energies $\mathcal{E}_g$ and $\mathcal{E}_m$ denote the real parts of $\mathcal{E}_{g\Theta}$ and $\mathcal{E}_{m\Theta}$, respectively. The matrix elements in Eq. (4.111) are calculated using Eqs. (B.51) and (B.52). After summing over the intermediate states, $|\mathcal{M}_{mg}|^2$ has the form

$$|\mathcal{M}_{mg}|^2 = \left| \sum_{q'} \epsilon^\beta_{q'} a_{q'} \right|^2 . \tag{4.112}$$

If Eq. (4.112) is parameterised as described in Appendix C and integrated over the directions of the scattered photon, the result simplifies to:

$$\int d^2\hat{k} \, |\mathcal{M}_{mg}|^2 = \frac{2\pi}{3} \left(4|a_0|^2 + |a_1|^2 + |a_{-1}|^2 \right) \quad \text{for } \beta = 1 \, ,$$
$$\int d^2\hat{k} \, |\mathcal{M}_{mg}|^2 = 2\pi \left(|a_1|^2 + |a_{-1}|^2 \right) \qquad\qquad \text{for } \beta = 2 \, . \tag{4.113}$$

As before, if the energy of the intermediate state is written as $\mathcal{E}_{n\Theta} = \mathcal{E}_n - i\Gamma_n/2$, radiation damping is taken into account by replacing $\mathcal{E}_n$ with $\mathcal{E}_n - i\gamma_n$.

Chapter 5

Numerical implementation

5.1 Solutions of the field free eigenproblem

As already mentioned in Chapter 4, eigenstates of the field free Hamiltonian H_0 are used for the representation of the total Hamilton operator H. In this section we describe how the eigenstates and eigenenergies of the free helium atom are calculated. It has been told that non orthogonal Sturmian basis leads to a generalised eigenvalue problem[1]

$$\mathbf{H}_0\,\mathbf{x}_i = E_{i\Theta}\,\mathbf{B}\,\mathbf{x}_i \,, \tag{5.1}$$

where $\mathbf{H}_0 \in \mathbb{C}^{N\times N}$ is the matrix representation of $H_0(\Theta)$ and $\mathbf{B} \in \mathbb{R}^{N\times N}$ the overlap matrix of the basis functions. Since the basis is real, $\mathbf{H}_0$ is complex symmetric, whereas $\mathbf{B}$ is real symmetric positive definite. The eigenvectors $\mathbf{x}_i$ are chosen to satisfy the normalisation relation

$$\mathbf{x}_i^\mathsf{T}\,\mathbf{B}\,\mathbf{x}_j = \delta_{ij} \,. \tag{5.2}$$

The basis consisting of several pairs of nonlinear parameters $(k_1, \kappa_1), (k_2, \kappa_2), \ldots$ is almost inevitably over-complete for basis sizes N above a few hundred wavefunctions, yielding matrices $\mathbf{H}_0$ and $\mathbf{B}$ that are numerically singular. A simple reduction of Eq. (5.1) to an ordinary eigenvalue equation using the inverse of $\mathbf{B}$ (e.g., by Cholesky decomposition) is thus not possible. Furthermore, standard diagonalisation techniques based on the QZ algorithm, which is commonly used to solve generalised eigenproblems, are numerically unstable for singular pencils $(\mathbf{H}_0, \mathbf{B})$ and produce large numerical errors [89]. A pseudo inverse of the overlap matrix is possible, however, if singular value decomposition (SVD) is used to determine linearly independent vectors [104]. In the following, a method that transforms Eq. (5.1) into an ordinary eigenvalue problem with a complex symmetric matrix is described.

As the overlap matrix is symmetric, using diagonalisation instead of SVD decomposition can be computationally less demanding.[2] The matrix $\mathbf{B}$ is therefore diagonalised,

$$\mathbf{\Sigma} = \mathbf{U}^\mathsf{T}\mathbf{B}\mathbf{U} \,, \qquad \mathbf{U} = (\mathbf{u}_1, \ldots, \mathbf{u}_N) \,, \qquad \mathbf{\Sigma} = \mathrm{diag}(\sigma_1, \ldots, \sigma_N) \,, \tag{5.3}$$

$$\mathbf{B}\,\mathbf{u}_i = \sigma_i\,\mathbf{u}_i, \qquad i = 1, \ldots, N \,, \tag{5.4}$$

---

[1] Explicit dependence of the matrices and column vectors on parameter Θ will be dropped for brevity throughout this chapter.

[2] Singular value decomposition $\mathbf{B} = \mathbf{U}\mathbf{\Sigma}\mathbf{V}^\mathsf{T}$ of a real symmetric positive definite matrix $\mathbf{B}$ is equivalent to diagonalisation since for this special case $\mathbf{U} = \mathbf{V}$. The smallest eigenvalues, however, that are close to numerical errors of the matrix elements are less accurate than in the case of SVD. For a symmetric positive definite matrix $\mathbf{B}$ it may even happen that the lowest computed eigenvalues become negative and should be discarded.

where the eigenvalues σ_i are taken to be ordered in descending order,

$$\sigma_1 \geq \sigma_2 \geq \ldots \geq \sigma_N \,. \tag{5.5}$$

To span the same vector subspace as is spanned by the over-complete Sturmian basis, only those vectors that are linearly independent are retained. In our case, only the eigenvectors $\mathbf{u}_j$ pertaining to non-zero eigenvalues σ_j are linearly independent. These vectors are chosen to represent the vector subspace of interest. In practice, numerical diagonalisation of $\mathbf{B}$ gives eigenvalues that are not strictly zero but are very small instead. Thus, out of N eigenpairs, P eigenpairs are chosen that have eigenvalues above some threshold parameter ϵ, $\sigma_j \geq \epsilon$, $j = 1, \ldots, P$. If we define

$$\mathbf{U}' = (\mathbf{u}_1, \ldots, \mathbf{u}_P) \in \mathbb{R}^{N \times P} \,, \tag{5.6}$$

every vector $\mathbf{x}_i$ can be projected into the space spanned by the vectors $\mathbf{u}_1, \ldots, \mathbf{u}_P$ by

$$\mathcal{P} = \sum_{j=1}^{p} \mathbf{u}_j \mathbf{u}_j^{\mathsf{T}} = \mathbf{U}' \mathbf{U}'^{\mathsf{T}} \,. \tag{5.7}$$

Thus, instead of solving Eq. (5.1), we wish to solve the modified projected generalised eigenvalue problem,

$$\mathcal{P} \mathbf{H}_0 \mathcal{P} \mathbf{x}_i = E_{i\Theta} \, \mathcal{P} \mathbf{B} \mathcal{P} \mathbf{x}_i \,. \tag{5.8}$$

In Eq. (5.8), the matrix $\mathbf{B}$ can be approximated by means of the P chosen eigenvectors $\mathbf{u}_j$ and eigenvalues σ_j,

$$\mathbf{B} = \mathbf{U} \mathbf{\Sigma} \mathbf{U}^{\mathsf{T}} \approx \mathbf{U}' \mathbf{\Sigma}' \mathbf{U}'^{\mathsf{T}} \,, \tag{5.9}$$

where

$$\mathbf{\Sigma}' = \mathrm{diag}(\sigma_1, \ldots, \sigma_P) \in \mathbb{R}^{P \times P} \,. \tag{5.10}$$

If furthermore the matrices

$$\mathbf{\Sigma}'^{\pm 1/2} = \mathrm{diag}(\sigma_1^{\pm 1/2}, \ldots, \sigma_P^{\pm 1/2}) \,, \qquad \mathbf{S}' = \mathbf{U}' \mathbf{\Sigma}'^{-1/2} \qquad \text{and} \qquad \mathbf{S}'^{-1} = \mathbf{\Sigma}'^{1/2} \mathbf{U}'^{\mathsf{T}} \tag{5.11}$$

are defined and the equalities

$$\mathbf{\Sigma}'^{1/2} \mathbf{\Sigma}'^{-1/2} = \mathbf{\Sigma}'^{-1/2} \mathbf{\Sigma}'^{1/2} = \mathbf{I} \qquad \text{and} \qquad \mathbf{U}'^{\mathsf{T}} \mathbf{U}' = \mathbf{I} \tag{5.12}$$

are used, Eq. (5.8) is transformed to

$$\mathbf{S}'^{\mathsf{T}} \mathbf{H}_0 \mathbf{S}' \, (\mathbf{S}'^{-1} \mathbf{x}_i) = E_{i\Theta} \, (\mathbf{S}'^{-1} \mathbf{x}_i) \,. \tag{5.13}$$

Eq. (5.13) is an ordinary eigenvalue problem for the column vector $\mathbf{x}'_i = \mathbf{S}'^{-1} \mathbf{x}_i$, where

$$\mathbf{x}'^{\mathsf{T}}_i \mathbf{x}'_j = \delta_{ij} \,. \tag{5.14}$$

Since the matrix $\mathbf{H}_0$ is symmetric, the transformation $\mathbf{S}'^{\mathsf{T}} \mathbf{H}_0 \mathbf{S}'$ also yields a symmetric matrix. If needed, the eigenvectors of the transformed matrix can easily be transformed back to the original basis frame by inverting Eq. (5.13). Henceforth, the representation of states in the linearly independent basis will be referred to as the *reduced basis set* expansion, and the original Sturmian basis set expansion as the *non reduced basis set* expansion.

5.2 Eigenstates and eigenvalues of the total Hamiltonian

The generalised eigenvalue problem describing the helium atom in a homogeneous electric field can be written by means of the matrices $\mathcal{A}$ and $\mathcal{B}$ [Eqs. (4.43) and (4.44)]:

$$\mathcal{A}_{ij} = E_{i\Theta}\,\delta_{ij} \qquad \text{and} \qquad \mathcal{B}_{ij} = \langle\overline{\Psi_{i\Theta}}|\Delta H(\Theta)|\Psi_{j\Theta}\rangle\,. \tag{5.15}$$

The nontrivial matrix element $\mathcal{B}_{ij}$ can be expressed as

$$
\begin{aligned}
\mathcal{B}_{ij} &= \langle\overline{\Psi_{i\Theta}}|\Delta H(\Theta)|\Psi_{j\Theta}\rangle \\
&= \sum_{\beta,\delta}\sum_{\gamma,\omega} x'_{i,\beta} S'_{\gamma\beta}\langle\overline{\psi_\gamma}|\Delta H(\Theta)|\psi_\omega\rangle S'_{\omega\delta} x'_{j,\delta} \\
&= \mathbf{x}'^{\mathsf{T}}_i \left(\mathbf{S}'^{\mathsf{T}}\,\Delta\mathbf{H}\,\mathbf{S}'\right)\mathbf{x}'_j \\
&= \mathbf{x}^{\mathsf{T}}_i\,\Delta\mathbf{H}\,\mathbf{x}_j\,,
\end{aligned}
\tag{5.16}
$$

where $\Delta\mathbf{H}$ has been used to denote the representation of $\Delta H(\Theta)$ in the Sturmian basis. In Eq. (5.16), the angular part of the integrals can be evaluated by means of the Wigner-Eckart theorem [cf. Eq. (B.39)], giving

$$
\begin{aligned}
\langle\overline{\Psi_{i\Theta}}|\Delta H(\Theta)|\Psi_{j\Theta}\rangle &= -F\,\langle\overline{\Psi_{i\Theta}}|\mathcal{D}_0(\Theta)|\Psi_{j\Theta}\rangle \\
&= -F(-1)^{L_i-M_i}\begin{pmatrix} L_i & 1 & L_j \\ -M_i & 0 & M_j \end{pmatrix}\langle\overline{\Psi_{i\Theta}}\|\mathcal{D}(\Theta)\|\Psi_{j\Theta}\rangle\,.
\end{aligned}
\tag{5.17}
$$

Since for an isolated atom the total angular and spin momenta are conserved, the free-atom Hamiltonian $H_0(\Theta)$ is formally represented by a block diagonal matrix (Fig. 5.1, left),
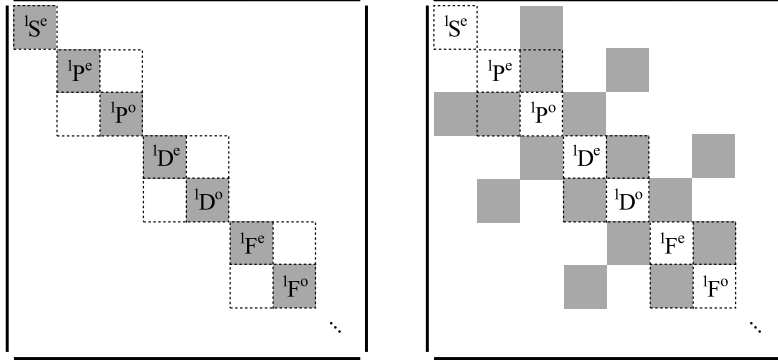
Figure 5.1: Matrix representations of $\mathbf{H}_0$ (left) and $\Delta\mathbf{H}$ (right) for the case $\boldsymbol{F} \parallel \hat{\boldsymbol{z}}$.

$$\mathbf{H}_0 = \mathbf{H}_0(^1S^e) \oplus \mathbf{H}_0(^1P^e) \oplus \mathbf{H}_0(^1P^o) \oplus \ldots \equiv \bigoplus_{(L,\pi)}\mathbf{H}_0(^1L^\pi)\,. \tag{5.18}$$

Therefore, the generalised eigenvalue problem resulting from the non reduced basis expansion is formally transformed into an ordinary eigenvalue problem if the transformation matrix is written as a direct sum

$$\mathbf{S}' = \bigoplus_{(L,\pi)}\mathbf{S}'(^1L^\pi)\,. \tag{5.19}$$

Let the submatrices of $\mathbf{H}_0(^1L^\pi)$ and $\mathbf{S}'(^1L^\pi)$ have the following dimensions, in accord with the notation used in the previous section:

$$\begin{aligned}
\mathbf{H}_0(^1L^\pi) &\in \mathbb{C}^{N(^1L^\pi) \times N(^1L^\pi)}, \\
\mathbf{S}'(^1L^\pi) &\in \mathbb{R}^{N(^1L^\pi) \times P(^1L^\pi)}.
\end{aligned} \tag{5.20}$$

With the latter forms of $\mathbf{H}_0$ and $\mathbf{S}'$, the Hamilton operator is written in reduced representation as

$$\mathbf{H}_0' = \mathbf{S}'^\mathsf{T}\mathbf{H}\mathbf{S}' = \bigoplus_{(L,\pi)} \mathbf{H}_0'(^1L^\pi), \tag{5.21}$$

and the electric field interaction $\Delta H(\Theta)$ as

$$\Delta\mathbf{H}' = \mathbf{S}'^\mathsf{T}\Delta\mathbf{H}\mathbf{S}'. \tag{5.22}$$

The matrix $\Delta\mathbf{H}$ is composed of (generally *rectangular*) blocks above and below diagonal (Fig. 5.1, right). Both, $\mathbf{H}_0'$ and $\Delta\mathbf{H}'$ retain the same block structure as $\mathbf{H}_0$ and $\Delta\mathbf{H}$ except that the blocks are smaller for the reduced basis representations. The total Hamilton matrix $\mathbf{H}_0 + \Delta\mathbf{H}$ can therefore be represented in the reduced basis as

$$\mathbf{S}'^\mathsf{T}(\mathbf{H}_0 + \Delta\mathbf{H})\mathbf{S}' = \mathbf{H}_0' + \Delta\mathbf{H}'. \tag{5.23}$$

Instead of keeping $P(^1L^\pi)$ eigenvectors of the block $^1L^\pi$ in the expansion, only $Q(^1L^\pi)$ eigenvectors are chosen that lie in the region of interest. With this approach, the final matrix size used in diagonalisation and the number of matrix elements that are to be calculated are drastically reduced. The inclusion of only a part of the calculated eigenvectors reduces the size of the diagonal blocks to $Q(^1L^\pi) \times Q(^1L^\pi)$, while the size of the non diagonal blocks is reduced to $Q(^1L^\pi) \times Q(^1L'^{\pi'})$. Thus, the total number of eigenvectors is equal to

$$Q = \sum_{(L,\pi)} Q(^1L^\pi) \tag{5.24}$$

Eq. (4.43) remains valid, except that $\mathbf{y}_k$ now represents the truncated column vector:

$$\mathbf{y}_k = \begin{pmatrix} y_{k,1} \\ \vdots \\ y_{k,Q} \end{pmatrix}. \tag{5.25}$$

The meaning of $\mathcal{B}_{ij}$ is the following: if $\mathbf{x}_i'$ represents an eigenstate of symmetry $^1L_1^{\pi_1}$ and $\mathbf{x}_j'$ an eigenstate of the symmetry $^1L_2^{\pi_2}$, the matrix element $\mathcal{B}_{ij}$ is equal to

$$\begin{aligned}
\mathcal{B}_{ij} &= \mathbf{x}_i'^\mathsf{T} \cdot \mathbf{S}'^\mathsf{T}(^1L_1^{\pi_1}) \cdot \Delta\mathbf{H}(^1L_1^{\pi_1}; {}^1L_2^{\pi_2}) \cdot \mathbf{S}'(^1L_2^{\pi_2}) \cdot \mathbf{x}_j' \\
&= \mathbf{x}_i^\mathsf{T} \cdot \Delta\mathbf{H}(^1L_1^{\pi_1}; {}^1L_2^{\pi_2}) \cdot \mathbf{x}_j.
\end{aligned} \tag{5.26}$$

In practice, the eigenproblem for each of the symmetries $^1L^\pi$ is calculated and diagonalised separately to save space. Details about numerical implementation are the subject of the next section.

5.3 Construction of the basis set

Probably the most nontrivial part of the calculations is choosing the parameters of the Sturmian basis functions that are used to represent the field free eigenstates. Since the complete set of parameters used in the present calculations would result in a series of lengthy tables, the principles upon which the choice of parameters is based are illustrated on an example rather than reporting the parameter values for all the symmetries.

Although the construction of the basis set is not based on mathematical rigour, the choice of the basis parameters is by no means counterintuitive. It has already been mentioned in Chapter 4 that by tuning the parameters k and κ and the indices n and ν, the radial spread of the wavefunction is affected: by increasing n and ν and/or by decreasing k and κ, the oscillations of the single electron Sturmian functions S_{nl}^{k} and $S_{\nu\lambda}^{\kappa}$ are moved further away from the nucleus, and the opposite. Sturmian functions with high n and ν or low k and κ can be used for a description of states where one or both electrons on average move far away from the nucleus.

It should be clear that in order to adequately describe continuum, which is characterised by oscillations of the radial part in the asymptotic region of the wavefunction, the basis should include two electron Sturmian functions with high n and ν. Since the same basis is used to describe wavefunctions close to the nucleus, this implies a large number of basis functions. The need for a large basis size may be at least partly compensated by adding Sturmian sets where one or both scaling parameters k_s and κ_s are small. Furthermore, by choosing $k_s \neq \kappa_s$, asymmetrical two electron states (e.g., high lying members of Rydberg series) can be efficiently described. With appropriate scaling parameters, excellent results are obtained even for low total angular momenta, for which the electron movement can be highly correlated: with a single pair of scaling parameters (k, κ), the energy of the lowest singly excited $^1F^o$ state is calculated accurately to seven decimal places with the basis of only 168 two electron basis functions [82].

As has already been described in Chapter 4, eigenstates of H_0 are expanded in a basis of Sturmian functions as [cf. Eq. (4.9)]

$$\Psi_{LMSM_S\pi} = \sum_s \sum_{l,\lambda} \sum_{n,\nu} x_{LMSM_S}^{k_s n l \kappa_s \nu \lambda} \, \psi_{LMSM_S}^{k_s n l \kappa_s \nu \lambda}, \tag{5.27}$$

where the summation indices n and ν take the values [82]

$$\begin{aligned} n &= l+1, \ldots, l+\Delta n_{ls}, \\ \nu &= \lambda+1, \ldots, \lambda+\Delta\nu_{\lambda s}. \end{aligned} \tag{5.28}$$

Similarly as was done for $^1S^e$ doubly excited states [82, 105], various sets of Sturmian functions are used. As an example, basis parameters used in the calculation of singly and doubly excited $^1D^e$ states are shown in Tables 5.1 and 5.2. For doubly excited states below $N = 2$, one of the values of the scaling parameters is chosen in a way to approximately describe electron motion in the $n = 2$ shell. Since the nuclear charge is effectively screened by the presence of another electron, the parameter k is set to the value

$$k = \frac{Z - \sigma_k}{n} = 1.5. \tag{5.29}$$

To be able to obtain several doubly excited states by means of a single diagonalisation, various κ_s values are used to describe different average distances between the two electrons. As mentioned, singly *and* doubly excited states are obtained in a single diagonalisation. Therefore, to accurately calculate the wavefunction near the origin, as required by low lying singly excited states, a set

s	k	κ	Δn	$\Delta \nu$
1	2.0	2.0	15	15
2	1.0	0.6	9	10
3	1.5	1.0	9	10
4	1.5	0.3	9	20
5	0.1	0.7	17	8
6	1.5	0.04	9	25

Table 5.1: Nonlinear scaling parameters k and κ used in the calculation of $^1D^e$ basis states.

l	λ	sets
0	2	1 2 3 4 5 6
1	1	1 2 3 4 5 6
1	3	1 2 3 4 5 6
2	2	1 2 3 4 5 6
2	4	1 2 3 4 5 6
3	3	1 2 3 4 5 6
3	5	2 3 4 5
4	4	2 3 4 5
4	6	2 3 4 5
6	6	2 3 4 5

Table 5.2: Sets of Sturmian functions used used in the calculation of $^1D^e$ basis states. The indices in the last column refer to the designations in Table 5.1.

of basis functions with $k = \kappa = 2.0$ is also included. Finally, to account for the case of high average radial distances of the electrons, $k = 0.1$ and $\kappa = 0.7$ is used.

So far, nothing has been told about the single electron angular momenta l and λ. According to the independent electron model, for a chosen L, three Rydberg series exist for doubly excited states with parity $\pi = (-1)^L$ below $N = 2$. They are described by configurations $2s\,nL$, $2p\,n(L-1)$, and $2p\,n(L+1)$. For states with parity equal to $\pi = (-1)^{L+1}$, a single Rydberg series described by configurations $2p\,nL$ exists. We take the values s, p and $L, L\pm 1$ for the values of l and λ, but extend the basis by adding Sturmian functions with $(l+1)\,(\lambda-1)$, $(l+2)\,(\lambda-2)$, etc., and functions with $(l+1)\,(\lambda+1)$, $(l+2)\,(\lambda+2)$, etc., as shown in Table 5.2.

It turns out that the accuracy of the resonances characterised by small energy widths can be enhanced, if Sturmian functions with $l \neq \lambda$ and $k_s \neq \kappa_s$ are complemented with the functions where the role of k_s and κ_s (or, which is the same, the role of l and λ) is interchanged. This effectively increases the number of basis functions with which the continuum cuts are described. The parameters from Tables 5.1 and 5.2, enhanced with Sturmian functions with k_s and κ_s interchanged, are used to obtain the energies of singly and doubly excited states from Appendix E. The basis for other angular momenta L and parities π, as well as for triplet $(S = 1)$ states, can be constructed in a similar manner.

At the end it should be told that although basis parameters are optimised for states below $N = 2$, the calculations show that with basis sets like the one presented in Tables 5.1 and 5.2, doubly excited states converging to higher thresholds, specifically, $N = 3$ and $N = 4$, are also obtained in the same diagonalisation. In Table 5.3, results for some of the $^1F^o$ doubly excited

states are compared to the values found in the literature.

	present		refs.	
	$-E$	$\Gamma/2$	$-E$	$\Gamma/2$
$N = 3$	0.304219765	1.628215(-3)	0.30424196	1.62598(-3)
	0.277962218	4.5104(-5)	0.2779623	4.51(-5)
	0.261015081	3.45662(-4)	0.2610194	3.46(-4)
	0.257868730	2.37647(-4)	0.257874	2.37(-4)
	0.253415163	2.6101(-5)	0.2534148	2.62(-5)
	0.251427649	6.425(-6)	0.251432	6.35(-6)
$N = 4$	0.187917520	2.175544(-3)	0.187912	2.175(-3)
	0.179125885	1.599944(-3)	0.179127	1.598(-3)
	0.166283775	3.9188(-5)	0.1662838	3.92(-5)
	0.162109297	9.81624(-4)	0.1621167	9.7950(-4)
	0.158828646	1.7946(-5)	0.1588291	1.79(-5)
	0.157561238	1.156539(-3)	0.157558	1.154(-3)
	0.156071112	5.4969(-5)	0.156072	5.510(-5)
	0.152330141	7.51738(-4)	0.15233	7.50(-4)

Table 5.3: Doubly excited $^1F^o$ states converging to the $N = 3$ and $N = 4$ thresholds. Present calculations are compared to the results of Bhatia and Ho [106] (right). Results are reported to nine decimal places, but the accuracy of the calculations is not checked.

5.4 Implementation

5.4.1 Radial integrals

Due to various nonlinear scaling parameters (k_s, κ_s) of the Sturmian basis set, orthogonality relations of Laguerre polynomials cannot be used in the evaluation of the integrals. Instead, integration is performed numerically. Since the integrands have the form of a polynomial weighted by an exponential function and the integral is evaluated on an interval $[0, \infty)$, Gauss-Laguerre type quadrature formulas are used [80]. Using an N point quadrature formula guarantees, up to the machine precision, *exact* results for polynomials of the order not greater than $2N - 1$. In our case, the basis for each total orbital momentum L and parity π consist of Sturmian functions with polynomial orders $n, \nu \lesssim 40$. Polynomials of highest orders appear in the calculation of matrix elements of the two particle operator $|\boldsymbol{r}_1 - \boldsymbol{r}_2|^{-1}$. The form of the integrand – a product of a couple of two electron Sturmian functions – in this case suggests that $N \approx 80$ should be used. It turns out that using double precision IEEE floating point arithmetics, numerical errors due to near cancellation are still bearable in this case.

The Gauss-Laguerre integration formula of the order N is

$$\int_0^\infty e^{-x} f(x) \, \mathrm{d}x \approx \sum_{k=1}^N w_k f(x_k) \, . \tag{5.30}$$

In Eq. (5.30), $f(x)$ is an arbitrary integrable function defined on the interval $[0, \infty)$, and x_k denotes the kth zero of the (non associated) Laguerre polynomial $L_N(x) \equiv L_N^0(x)$. The weights

w_k are obtained from [107]

$$w_k^{-1} = \sum_{j=0}^{N-1} L_j^2(x_k).\qquad(5.31)$$

Since the integrals involving the single particle operators of the total Hamiltonian have the form (cf. Appendix B)

$$\int_0^\infty dr\, e^{-Kr} P(r),\qquad(5.32)$$

where $P(r)$ is a polynomial and K is a real positive number, Eq. (5.30) can be applied directly in this case. Slater integrals [Eq. (B.18)], however, which are used in the calculation of inter electron potential matrix elements, involve a double integral,

$$\int_0^\infty dr_1\, e^{-K_1 r_1} \int_0^\infty dr_2\, e^{-K_2 r_2} P_1(r_1) P_3(r_1) \frac{r_<^q}{r_>^{q+1}} P_2(r_2) P_4(r_2)$$
$$= \int_0^\infty dr_1\, e^{-K_1 r_1} P_1(r_1) P_3(r_1) \frac{1}{r_1^{q+1}} \int_0^{r_1} dr_2\, e^{-K_2 r_2} P_2(r_2) P_4(r_2)\, r_2^q\qquad(5.33)$$
$$+ \int_0^\infty dr_1\, e^{-K_1 r_1} P_1(r_1) P_3(r_1)\, r_1^q \int_{r_1}^\infty dr_2\, e^{-K_2 r_2} P_2(r_2) P_4(r_2) \frac{1}{r_2^{q+1}},$$

where $r_< = \min\{r_1, r_2\}$ and $r_> = \max\{r_1, r_2\}$, K_1 and K_2 are real positive constants, and P_1, P_2, P_3, and P_4 are polynomials. To be able to use the quadrature formula (5.30) to evaluate the integrals in Eq. (5.33), the order of integration in the first term on the right hand side is changed and the substitution $r_1 = r_2(\xi + 1)$ is made:

$$\int_0^\infty dr_1\, e^{-K_1 r_1} P_1(r_1) P_3(r_1) \frac{1}{r_1^{q+1}} \int_0^{r_1} dr_2\, e^{-K_2 r_2} P_2(r_2) P_4(r_2)\, r_2^q$$
$$= \int_0^\infty dr_2\, e^{-K_2 r_2} P_2(r_2) P_4(r_2)\, r_2^q \int_{r_2}^\infty dr_1\, e^{-K_1 r_1} P_1(r_1) P_3(r_1) \frac{1}{r_1^{q+1}}\qquad(5.34)$$
$$= \int_0^\infty dr_2\, e^{-K_2 r_2} P_2(r_2) P_4(r_2) \int_0^\infty d\xi\, e^{-K_1 r_2(\xi+1)} P_1(r_2(\xi+1)) P_3(r_2(\xi+1)) \frac{1}{\xi^{q+1}}.$$

Eq. (5.30) can now be used twice to evaluate the double integral in Eq. (5.34). The second term in Eq. (5.33) is obtained from Eq. (5.34) if the interchanges $r_1 \leftrightarrow r_2$, $K_1 \leftrightarrow K_2$, $P_1 \leftrightarrow P_2$, and $P_3 \leftrightarrow P_4$ are made.

In the present calculations, the Gauss-Laguerre zeros and weights are tabulated using Mathematica [108], and the tables are incorporated into the program codes. To save computation time for integrals which involve low order polynomials, quadrature tables of several sizes N are used. Integration routines automatically choose the suitable table by examining the polynomial order of the integrand: the shortest quadrature table that still gives an exact result is used. The accuracy of the numerical integration has been well tested. For Sturmian functions of highest orders, numerical results agree with the exact results to at least twelve decimal places.

5.4.2 Calculation and diagonalisation of the Hamilton matrix

To express the total Hamiltonian H with the field free solutions, the matrices $\mathbf{H}_0(^1L^\pi)$ are first calculated. We choose not to seek the optimal value of the Θ parameter, but set it to the value $\Theta = 0.2$. In the present calculations, field free eigenstates with $L \leq L_{\max} \equiv 10$ of even and odd parities are used to represent the eigenstates of the total Hamiltonian. For each $^1L^\pi$, a

typical basis consists of approximately $N(^1L^\pi) \simeq 10000$ Sturmian functions. Eliminating linearly dependent vectors with the threshold parameter ϵ set to

$$\epsilon = \rho \max_{1 \leq i \leq N} \{\sigma_i\} \equiv \rho \, \sigma_1 \,, \quad \rho \equiv 10^{-12} \,, \tag{5.35}$$

(s. pg. 64) results in a reduced basis of size $P(^1L^\pi) \simeq 8000$. The reduced basis Hamilton matrix $\mathbf{H}_0'$ is diagonalised, and from the calculated eigenvectors, only those column vectors $\mathbf{x}_i'$ are chosen, for which $\mathrm{Re}\, E_{i\Theta} \leq E_{\max} \equiv -0.2265$ a.u. The threshold energy $E_{\max}$ is set high enough to include some of the resonances converging to the $N = 3$ threshold ($E_{N=3} = -2/9$ a.u. ≈ -0.2222 a.u.), as well as the $N = 2$ continuum. After restricting the calculation to the selected eigenvectors, the resulting total Hamilton matrix $\mathbf{H}$ which contains *all* of the included symmetries $^1L^\pi$ has dimensions 2557×2557 (i.e., $Q = 2557$).

Since matrix sizes of the individual matrices involved in the computation are relatively small, an exact diagonalisation is used. We use the well established LAPACK (Linear Algebra Package) routines [109]: the real symmetric positive definite overlap matrices $\mathbf{B}(^1L^\pi)$ are diagonalised using the specialised packed storage routine DSPEV, while for the complex symmetric matrices $\mathbf{H}_0'(^1L^\pi)$ and the total Hamilton matrix $\mathbf{H}$, the ordinary eigenproblem routine for general complex matrices ZGEEV is used. The accuracy of the calculated eigenvectors and eigenvalues is *not* improved by inverse iteration.

The computer codes for the calculation of matrix elements of the matrices $\mathbf{H}_0(^1L^\pi)$ and $\mathbf{H}$, photoionisation and inelastic scattering cross section, and various utility programs are written in C++. It should be noted that the programs are portable and platform independent. Since the matrices are not sparse and a large number of matrix elements therefore need to be calculated, the codes for the matrix element calculation are parallelised, i.e., they are written in a manner that allows the problem to be solved on parallel computers, e.g. clusters or SMP (Symmetric Multiprocessing) machines. Since MPI (Message Passing Interface) libraries are widely used, standardised, and have been ported to many architectures and operating systems, we choose them for the implementation of our codes.

A very simple distribution among the parallel processes is used: if n_{proc} processes exist, rows of a $N \times N$ matrix are divided into chunks of n_{proc} rows. The first process calculates the first row, the second process the second row, etc., until all the rows in the current chunk have been calculated. The procedure is repeated on each of the $\lceil N/n_{\mathrm{proc}} \rceil$ chunks. Beside calculating the matrix elements, the first process stores the matrix and takes care of the inter process communication with the other $n_{\mathrm{proc}} - 1$ processes.

All the calculations were performed on a PC workstation with a 2400 MHz 64-bit dual core microprocessor and 4 GB RAM. A typical computation time for the calculation of matrix elements of a single matrix $\mathbf{H}_0(^1L^\pi)$ is approximately 16 hours for $n_{\mathrm{proc}} = 2$, whereas the time needed for its diagonalisation is typically around 32 hours. Note that the timing reported here for the diagonalisation of the matrices applies for the non parallel eigensolver routines (i.e., for $n_{\mathrm{proc}} = 1$).

Chapter 6

Results

This chapter is dedicated to the presentation of results which were calculated with methods described in Chapter 4 and to (re)interpretation of some published and yet unpublished measured data.

We have accurately calculated singly and doubly excited singlet states up to $n = 15$ and up to the total angular momentum $L \leq 10$ in the zero electric field. The energies, autoionisation and fluorescence widths of the states are tabulated in Appendix E and compared with the literature output. Most of the existing values for doubly excited states refer to $^1S^e$ (up to $n = 15$) and to $^1P^o$ series (up to $n = 10$) while for the few other series ($^1P^e$, $^1D^e$, $^1D^o$, $^1F^o$ and $^1G^e$) only the numbers for the lowest lying members have been published before. We could not find any previously published data on doubly excited states with $^1F^e$ and $^1H^{e,o} - {}^1N^{e,o}$ symmetry. As mentioned before, these states were further employed to represent doubly excited states in the non zero electric field.

6.1   Stark maps

To characterise the features in the photoionisation and inelastic scattering spectra that emerge when the external field is applied, we examine the effect of the field on the eigenstates of the total Hamiltonian. This is commonly done by means of the *Stark map*, a diagram which is used to present the evolution of the energy levels with the applied electric field strength. In the Stark maps shown in Figs. 6.1 and 6.2, the dependence of the energy levels on the field strength is shown for the parallel ($\boldsymbol{F} \parallel \boldsymbol{P}$) and perpendicular ($\boldsymbol{F} \perp \boldsymbol{P}$) orientations of the polarisation of the incident photons with respect to the electric field vector. The energy region in Figs. 6.1 and 6.2 comprises $n = 7$, $n = 8$, and $n = 9$ resonances. The energy scale in the figures is shifted by 0.00229715 eV to account for the fact that the calculated ground state is too loosely bound (i.e., its energy is too high). Henceforth, the spectra displaying Stark maps will be shifted by the given value. The Stark maps are obtained by seeking the coefficient with maximum modulus in the expansion over the field free states [Eq. (4.42)] for each of the eigenvectors of the total Hamiltonian. The symmetries $^1L^\pi$ of the leading components can thus be represented by symbols of different shapes and colours. Note that for $\boldsymbol{F} \parallel \boldsymbol{P}$, the Stark diagram includes only the states which evolve with electric field from the zero field states $^1L^\pi$ with parity $\pi = (-1)^L$. This is because for $M = 0$, for this particular orientation of the electric field and polarisation vectors, mixing between the states with parities equal to $(-1)^L$ and for those with parities $(-1)^{L+1}$ is exactly zero, i.e., the states of both types form two non interacting sub blocks of the total Hamilton matrix. As a consequence, the states with parities equal to $(-1)^{L+1}$ remain
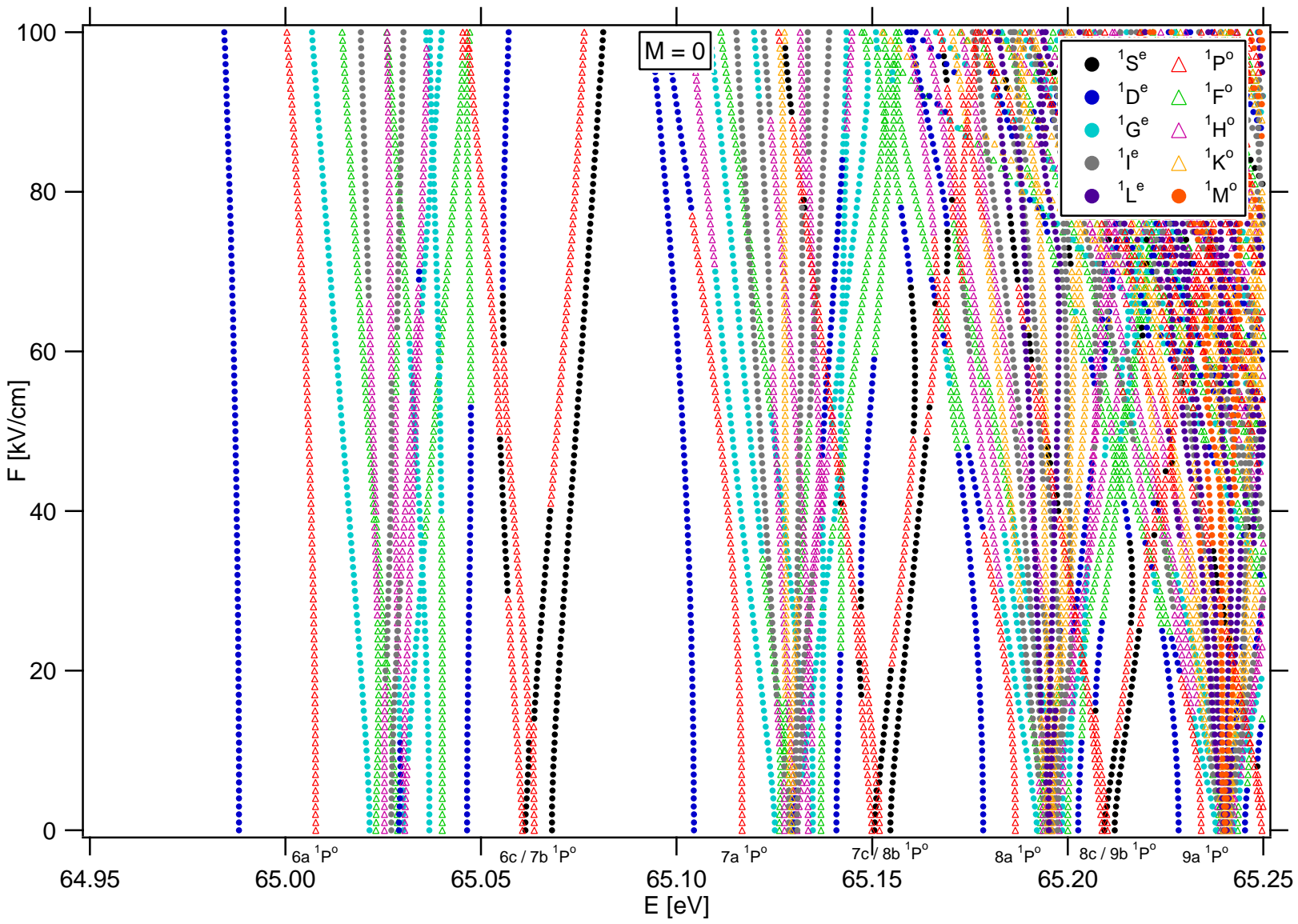
Figure 6.1: Stark map for the parallel experimental setup ($\boldsymbol{F} \parallel \boldsymbol{P}$). The legend shows the symmetry $^1L^e_\pi$ of the leading expansion coefficient.

Figure 6.2: Stark map for the perpendicular experimental setup ($\boldsymbol{F} \perp \boldsymbol{P}$). The legend shows the symmetry $^1L_\pi$ of the leading expansion coefficient.

unaccessible from the ground state for the parallel setup.

Many states with various symmetries $^1L^\pi$ lie close in energy to the a, b, and c $^1P^o$ states, which are directly accessible from the ground state with photoexcitation. It is therefore expected that even for moderate n, contributions originating from a large number of states (including high angular momenta) will be observed in the photoionisation spectra. But it turns out, that the field induced coupling is considerable only for some of the states, for which the energies lie close to the energies of the $^1P^o$ a states.

6.2 Photoionisation

The accurate calculation of photoionisation spectra is not merely a distraction from the path leading to the calculation of the inelastic scattering cross section. As a start, photoionisation cross section serves as a test of the validity of the current calculations in the electric field. More importantly, it turns out that due to the experimental setup used to measure the fluorescence yield, the measured spectra are superpositions of the photon and photoion signals. The calculation of the accurate photoionisation cross sections is therefore essential for an accurate interpretation of the measured inelastic scattering cross section.

6.2.1 Comparison with experiment

In the following, we compare the calculated photoionisation cross section spectra with the experimental data by Harries et al. [44]. It should be mentioned that, at the time of writing, these are the only available measurements of the photoionisation cross section below the $N = 2$ threshold of the helium atom in high static electric fields. The data is recorded for the parallel experimental geometry only, whereas no experiments for $\boldsymbol{F} \perp \boldsymbol{P}$ exist. Furthermore, only qualitative comparison of the present calculations with the results found in the literature is possible: no calculations of the photoionisation cross section for high field strengths for $\boldsymbol{F} \parallel \boldsymbol{P}$ have been published, and no calculations whatsoever are available for $\boldsymbol{F} \perp \boldsymbol{P}$.

An example of a calculated photoionisation spectrum is shown in Fig. 6.3. Even though the electric field strength is as low as 3 kV/cm, the calculated spectrum exhibits a rich level structure already in the region of $n = 8$ and $n = 9$ resonances. The spectral details are almost completely smeared out by the typically available experimental resolution.

It should be noted that due to the finite basis size used in the calculation of the cross section, the calculated spectra may depart from the actual photoionisation cross section by an arbitrary smooth energy dependent background. This is a consequence of an inadequately represented $N = 1$ continuum cut. Since the energy region where the cross section is calculated is relatively narrow, the contribution of the missing continuum eigenstates is fairly constant. Owing to the latter shift, the calculated cross section can become negative for very narrow resonances. Although the calculated spectra may be vertically shifted, relative intensities of the photoionisation peaks in the region of resonances below $N = 2$ are still calculated correctly. Since the absolute cross section is not required for the interpretation of the experimental data, the calculated spectra suffice for the identification of contributions of the individual eigenstates describing the helium atom in an external electric field.

In a typical experiment, the wealth of field induced spectral features is smeared by an instrumental function with FWHM of the order of 1 meV. The effect of finite experimental resolution in Fig. 6.3 is modelled by a convolution with a Gaussian with 1.4 meV FWHM (cf. Appendix D), since this is the experimental broadening reported by Harries et al. As will be seen shortly, for a discernible effect of the electric field in the photoionisation spectra, field strengths of an order of magnitude larger are required in the $n = 6$ and $n = 7$ energy region.

In Fig. 6.4, measured and calculated photoionisation spectra for several values of the electric field strength F are shown for the case $\boldsymbol{F} \parallel \boldsymbol{P}$. In the experiment performed by Harries and coworkers, the experimental ion yield signal is *"normalized to the current of electrons in the storage ring and the dwell time"* [44]. To be comparable to the measured ionisation signal, the calculated spectra are scaled to match the size of the individual features above the $6a\ ^1P^o$ resonance. Where possible, the size of the $6a\ ^1P^o$ peak amplitude is matched. The multiplication factors used in Fig. 6.4 are taken constant for all the calculated spectra, except for the 50.5

Figure 6.3: Calculated photoionisation cross section.

The figure shows a plot of photoionisation [a.u.] versus E [eV]. The legend reads "3 kV/cm, F ⊥ P", "calculated" (black), "conv. 1.4 meV" (red). Peaks are labeled $6a\ {}^1P^o$, $7a\ {}^1P^o$, $8a\ {}^1P^o$, $9a\ {}^1P^o$, $10a\ {}^1P^o$, $11a\ {}^1P^o$.
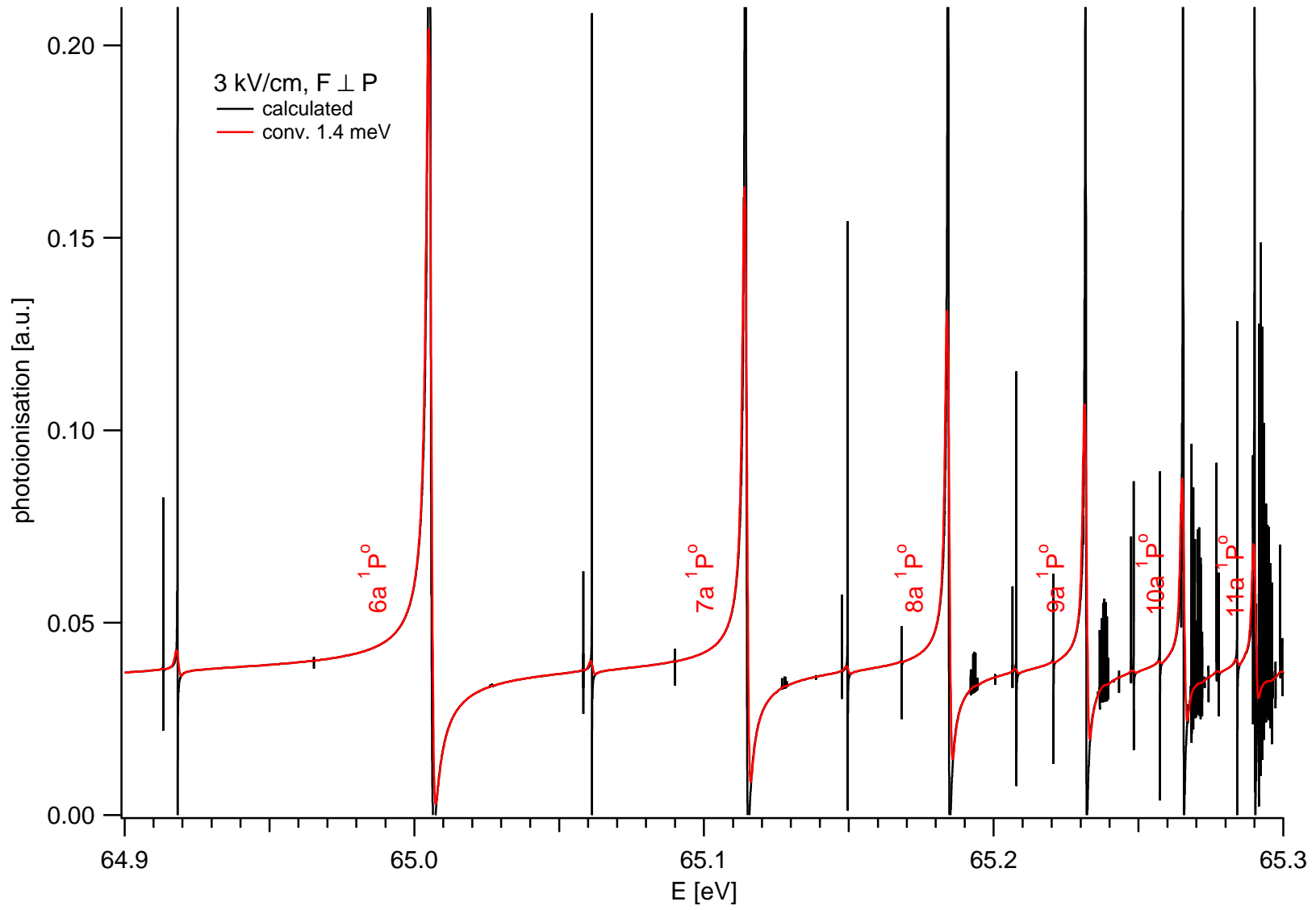
kV/cm, where the theoretical spectrum is additionally scaled by the factor of approximately 1.47 to agree with the size of the $6a$ $^1P^o$ resonance. The energy scale of the calculated spectra is used for alignment of the measured photoionisation signal. The spectra are translated vertically for clarity.

The overall agreement between the measurement and the theory is quite good. For the low field strengths, large scale oscillations are present. The noise level of the first few spectra reaches the amplitudes of the small field induced features, and the comparison with the theory is therefore rendered difficult. For the field strengths above 30 kV/cm, however, the features close to the $6a$ $^1P^o$ resonance become more pronounced and can be well discerned. The experimental data shown in Fig. 6.4 confirms the predictions of Chung et al. [42], who used the saddle point complex rotation method to calculate the order of magnitude of the effects of externally applied electric fields in photoionisation spectra for this region.

A wider energy region of $n = 6$ and $n = 7$ doubly excited states is shown in Fig. 6.5 for the case of the electric field strengths of 50.5 kV/cm and 84.4 kV/cm. The experimental data is scaled to match the amplitudes of the calculated peaks, and the spectra are again translated along the ordinate. The agreement between the theory and the experiment is rather good. It is to be noted that since the theoretical description used here is capable of completely describing the spectral features at relatively high fields, we would expect better agreement at lower electric fields. At the moment it is not clear what kind of atomic effect might be responsible for large oscillations which are recorded in the experimental spectra.

Fig. 6.5 also presents the calculated spectra for the perpendicular ($\boldsymbol{F} \perp \boldsymbol{P}$) experimental setup. Compared to the parallel geometry, the spectra for $\boldsymbol{F} \perp \boldsymbol{P}$ reveal several prominent new peaks. Identification of the features in the photoionisation cross section is the subject of the next subsection.

We conclude this subsection with Fig. 6.6. A complete series of calculated spectra for all values of the electric field strength and both polarisations is shown. For reference, the zero field photoionisation spectrum is also included.

6.2.2   Identification of states and the propensity rule

As mentioned, the peaks in the photoionisation spectra are identified by examining the field dependence of the calculated energy levels. In Figs. 6.7 and 6.8, the calculated photoionisation cross section in the $n = 6$ and $n = 7$ energy region is shown for both orientations of the polarisation vector for the field strengths selected by Harries et al. [44]. The spectra are again broadened with a Gaussian with 1.4 meV FWHM and translated vertically so that the baseline corresponds to the electric field strength (left axis). The classification scheme of Lipsky is used: the levels with the leading components belonging to the a, b, and c series are marked red, blue, and green, respectively. As can be seen from Figs. 6.7 and 6.8, the features originating from the states with parity equal to $(-1)^{L+1}$ are only present for $\boldsymbol{F} \perp \boldsymbol{P}$, as expected.

While the prominent a $^1P^o$ resonance can be clearly identified for $n = 6$, the identification of $n = 7$ resonance becomes difficult at high electric fields. The amplitudes of the a $^1P^o$ resonances are decreased: resonance strengths of the a $^1P^o$ states are redistributed among the neighbouring resonances. The latter property is described by a *sum rule* by Fang and Chung [110]: for a given set of basis functions, the total sum of all resonance strengths (i.e., the sum of all integrated resonance cross sections) is shown to be invariant under the change of the electric field strength. The reader should note, however, that the sum rule described in Ref. [110] holds exactly only if the radiative decay is neglected, as has already been explained in Chapter 4.

Due to field induced mixing, many states can be excited that have previously been unacces-
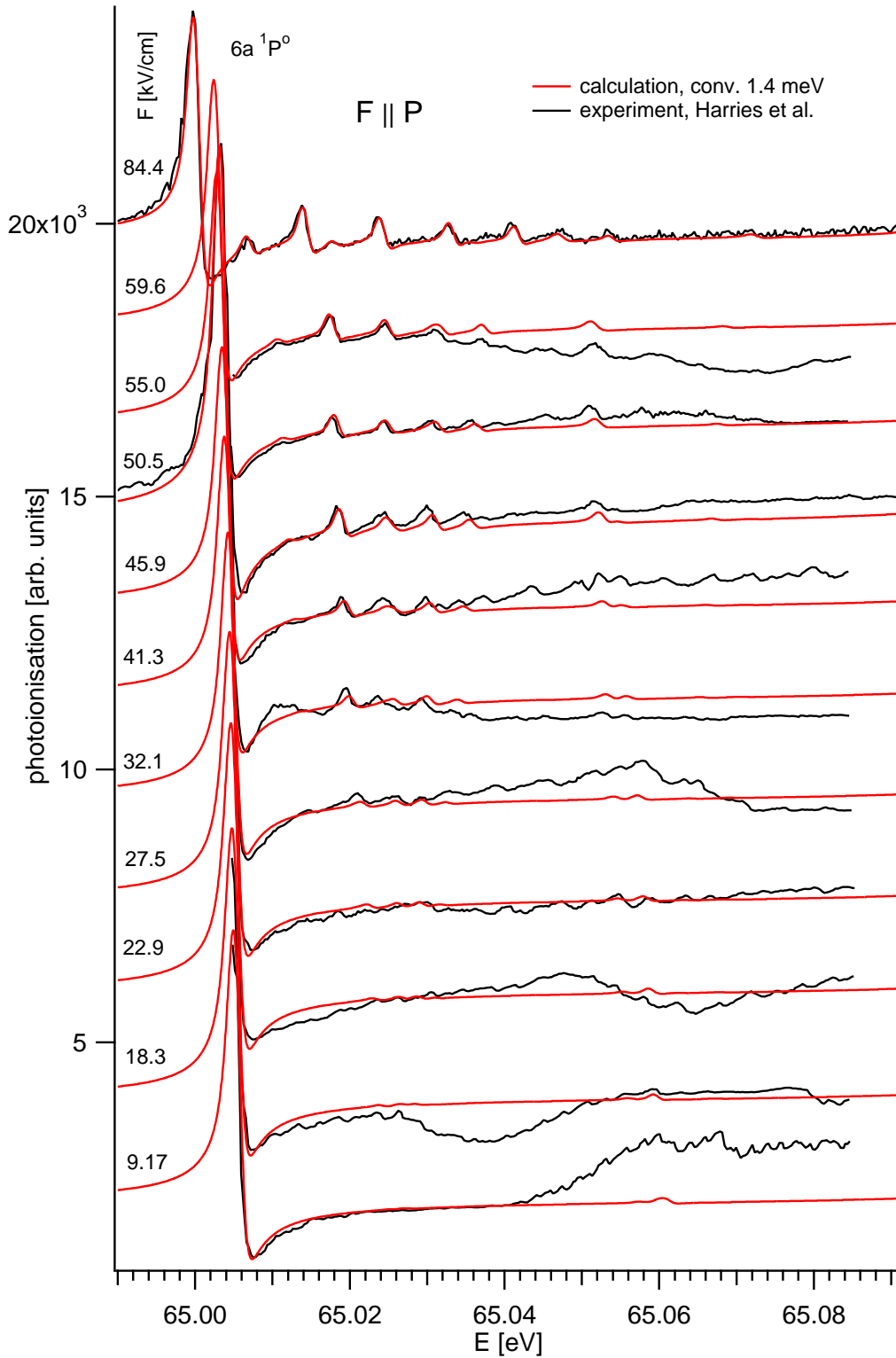
Figure 6.4: Comparison of measured and calculated photoionisation cross section for various field strengths for $\boldsymbol{F} \parallel \boldsymbol{P}$. The spectra are translated vertically for clarity. Theoretical spectra are convolved with a Gaussian with 1.4 meV FWHM and scaled to match the measurements. Where needed, the measured data is shifted in energy to agree with the theory. See text for details.
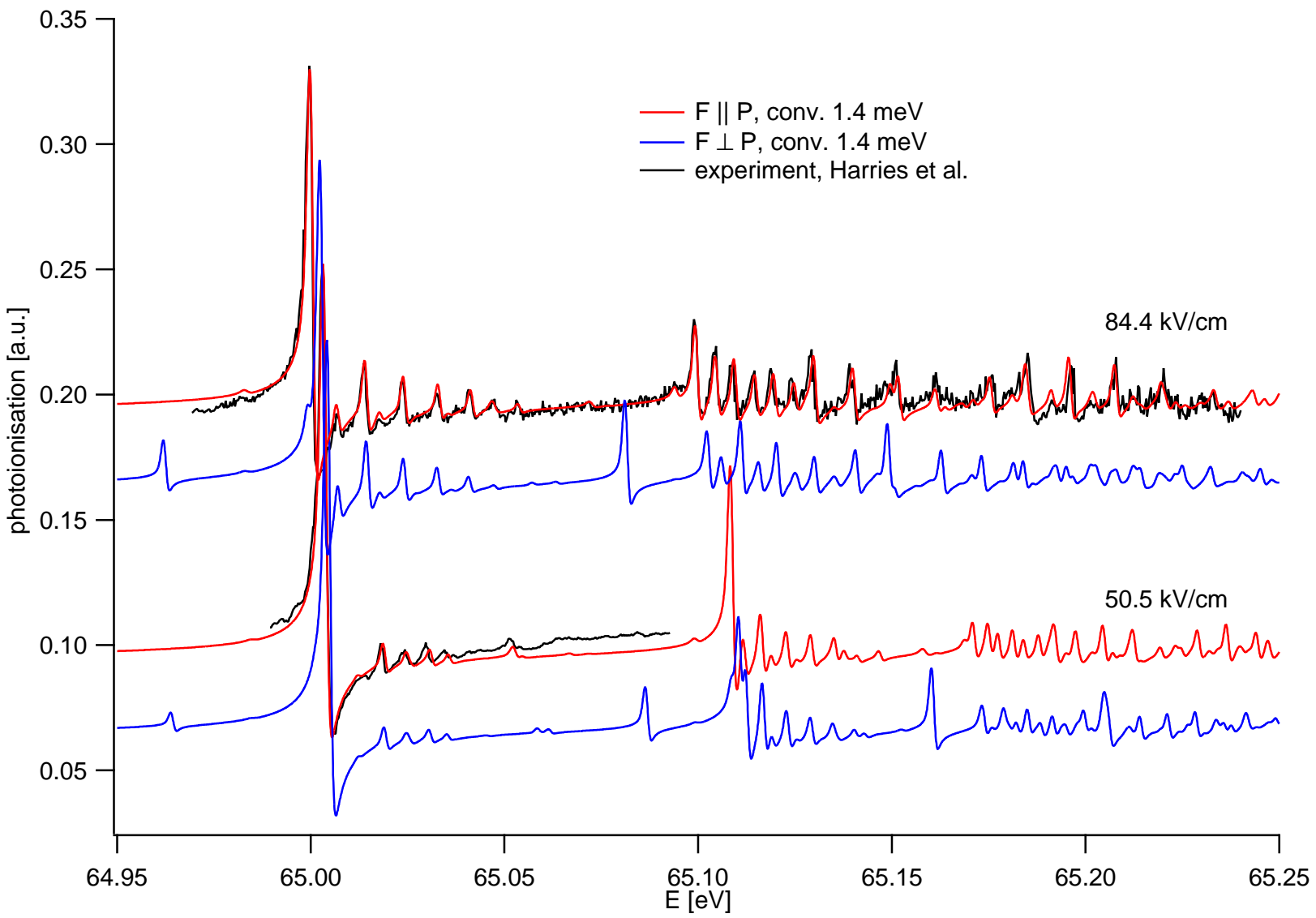
Figure 6.5: Comparison of measured (black) and calculated (red) photoionisation spectra for $F = 84.4$ kV/cm and $F = 50.5$ kV/cm ($\boldsymbol{F} \parallel \boldsymbol{P}$). The experiment is scaled to match the calculations. Predictions for $\boldsymbol{F} \perp \boldsymbol{P}$ are also shown (blue).
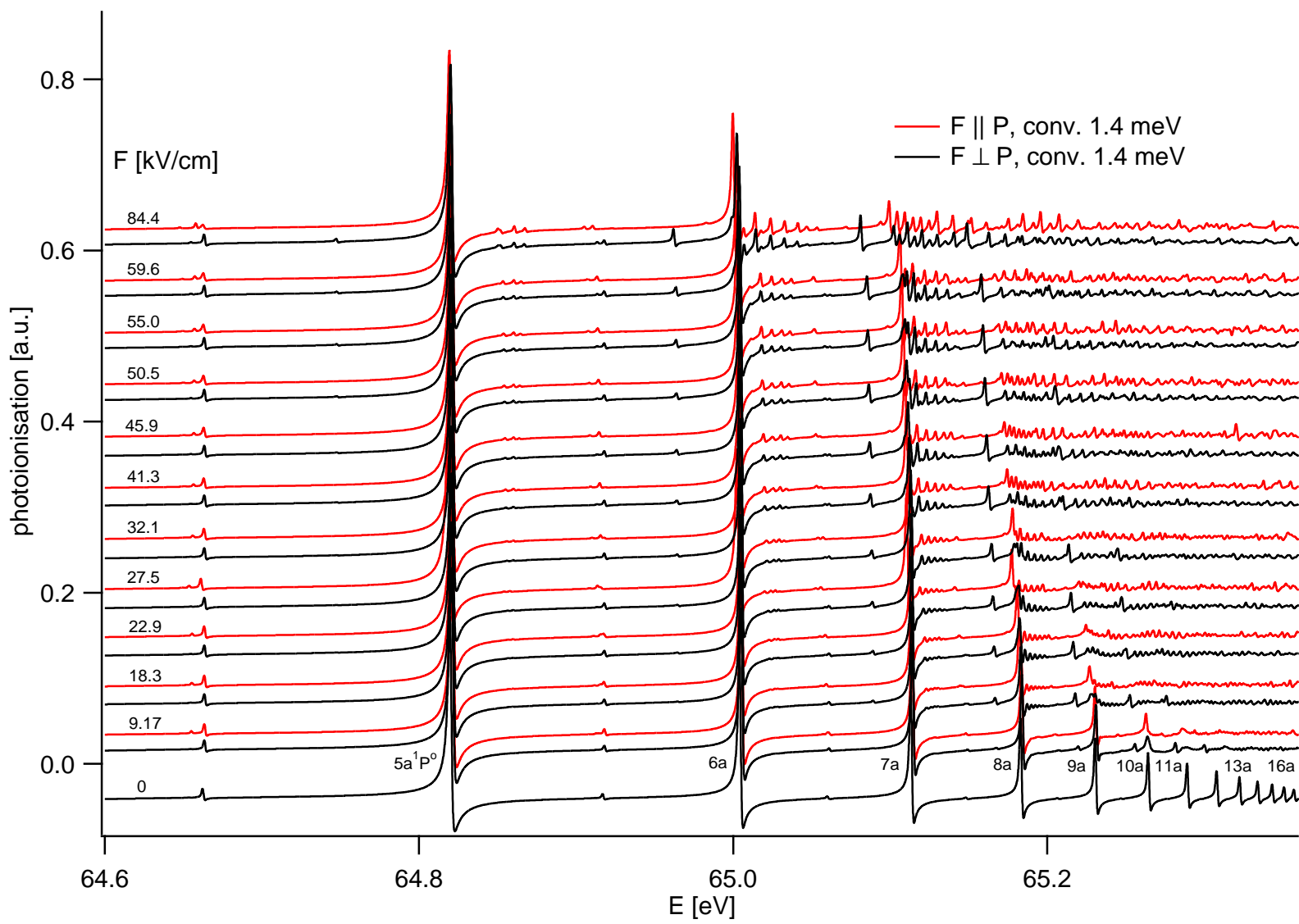
Figure 6.6: Calculated photoionisation spectra for various electric field strengths. The spectra are broadened by a Gaussian with 1.4 meV FWHM and shifted along the ordinate.

Figure 6.7: Calculated photoionisation cross section in the region of $n = 6$ and $n = 7$ resonances for $F \parallel P$. The photoionisation spectra are shifted vertically so that the elevation of the baseline indicates the field strength. The Stark diagram shows field dependence of the energy levels – red: a states, blue: b states, and green: c states. The left axis refers to the Stark map, and the right axis refers to the calculated spectra.

Figure 6.8: Same as in Fig. 6.7, but for $\boldsymbol{F} \perp \boldsymbol{P}$.

sible from the ground state. In the case of $\boldsymbol{F} \parallel \boldsymbol{P}$, the states following the $6a$ $^1P^o$ resonance are, in order of increasing energies, $6a$ $^1G^e$, $^1F^o$, $^1H^o$, and $^1I^e$. The zero field $LS\pi$ symmetries and classification labels of states are written at the bottom of the plot. The labels in square brackets follow the (zero field) energy ordering of states of individual series members. Following the four $6a$ states is a group of $6b$ states with symmetries $^1F^o$, $^1D^e$, $^1G^e$, and $^1H^e$. The region of $n = 6$ resonances ends with the $6c$ $^1G^e$, $^1F^o$, $^1D^e$, $^1P^o$ states, and the $6b$ $^1S^e$ state. Similar patterns occur in the $n = 7$ region, where additional contributions of states with higher angular momenta are present. The situation is even more complicated for the perpendicular orientation, where, as mentioned, states with parities $(-1)^{L+1}$ are also induced by the electric field.

With the underlying Stark map, the identification of the peaks in the photoionisation spectra is greatly simplified. For example, for the case $\boldsymbol{F} \parallel \boldsymbol{P}$, it is straightforward to follow the evolution of the $6a$ $^1D^e$ state with electric field. It can be seen by inspecting Fig. 6.1 that the small feature directly preceding the $6a$ $^1P^o$ resonance at 84.4 kV/cm is attributed to a state of $^1D^e$ symmetry, and not to a $^1D^o$ state, as suggested in Ref. [44]. Since the state is energetically well separated from the other states, it may be deduced that the leading component of the state is $6a$ $^1D^e$, and the calculations show that this is indeed the case.

(a)　　　　(b)
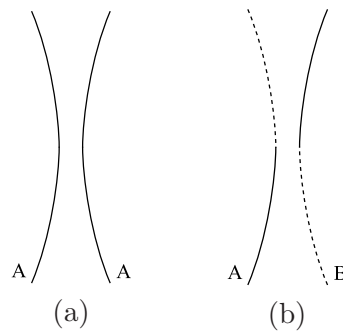
Figure 6.9: The propensity rule due to Tong and Lin [45]. Stark avoided crossings are shown. The states belonging to the same group (denoted by A) according to the a^*, b^*, and c^* classification do not cross (left). The states from different groups (denoted by A and B) are allowed to cross.

The strength of the Stark induced mixing of close lying states can be assessed by the so called *propensity rule* due to Tong and Lin [45]. In order to describe it, a short comment about the classification of doubly excited states is needed. The classification scheme used here, which follows the ideas of Lipsky, differs from the scheme used by Tong and Lin. Rather than introducing new short hand notations for the three series, the authors choose to *change the established meaning* of the a and b labels for states with angular momenta $L \leq 2$ and parity $\pi = (-1)^L$. The labelling used in Ref. [45] is *not* the one suggested by Lipsky.[1] Instead of using the labels to simply enumerate different Rydberg series according to increasing energy of the first series members, Tong and Lin use the a, b, and c labels to group the states of similar correlation character. To prevent further confusion, we use a^*, b^*, and c^* for the classification used in Ref. [45]. The transition from abc to $a^*b^*c^*$ labelling may be performed by means of Table 6.1. The Stark maps of the $n = 6$ and $n = 7$ energy region using the $a^*b^*c^*$ scheme are shown in Figs. 6.10 and 6.11.

With the new classification, the propensity rule of Tong and Lin for constructing the Stark map is: "... *Stark induced states originating from the same group do not cross, while those*

---

[1]Cf. Appendix E.
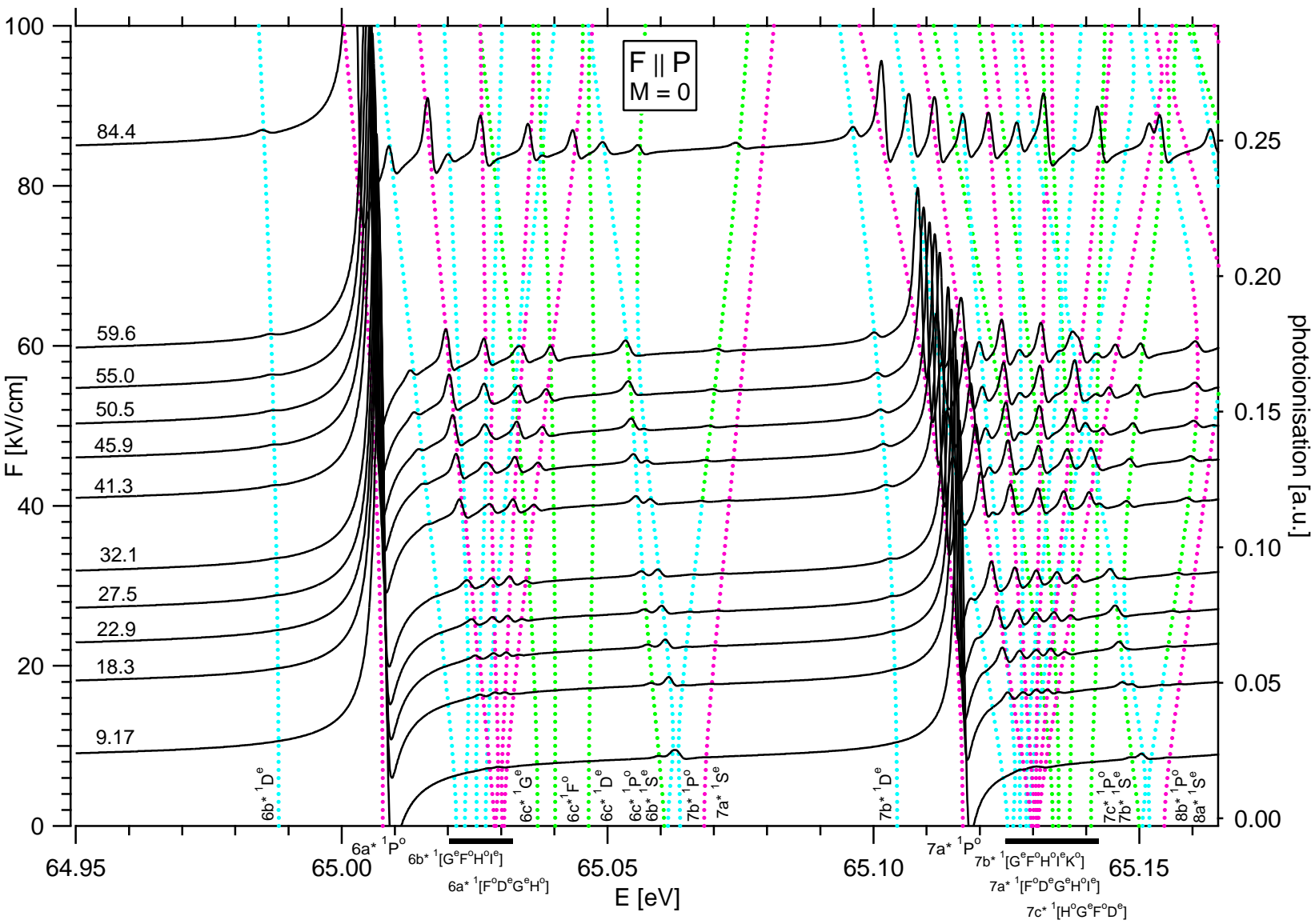
Figure 6.10: Same as in Fig. 6.7, but for the labels used in Ref. [45]. Cyan, magenta, and green are used to denote the leading components of the a^*, b^*, and c^* series, respectively.
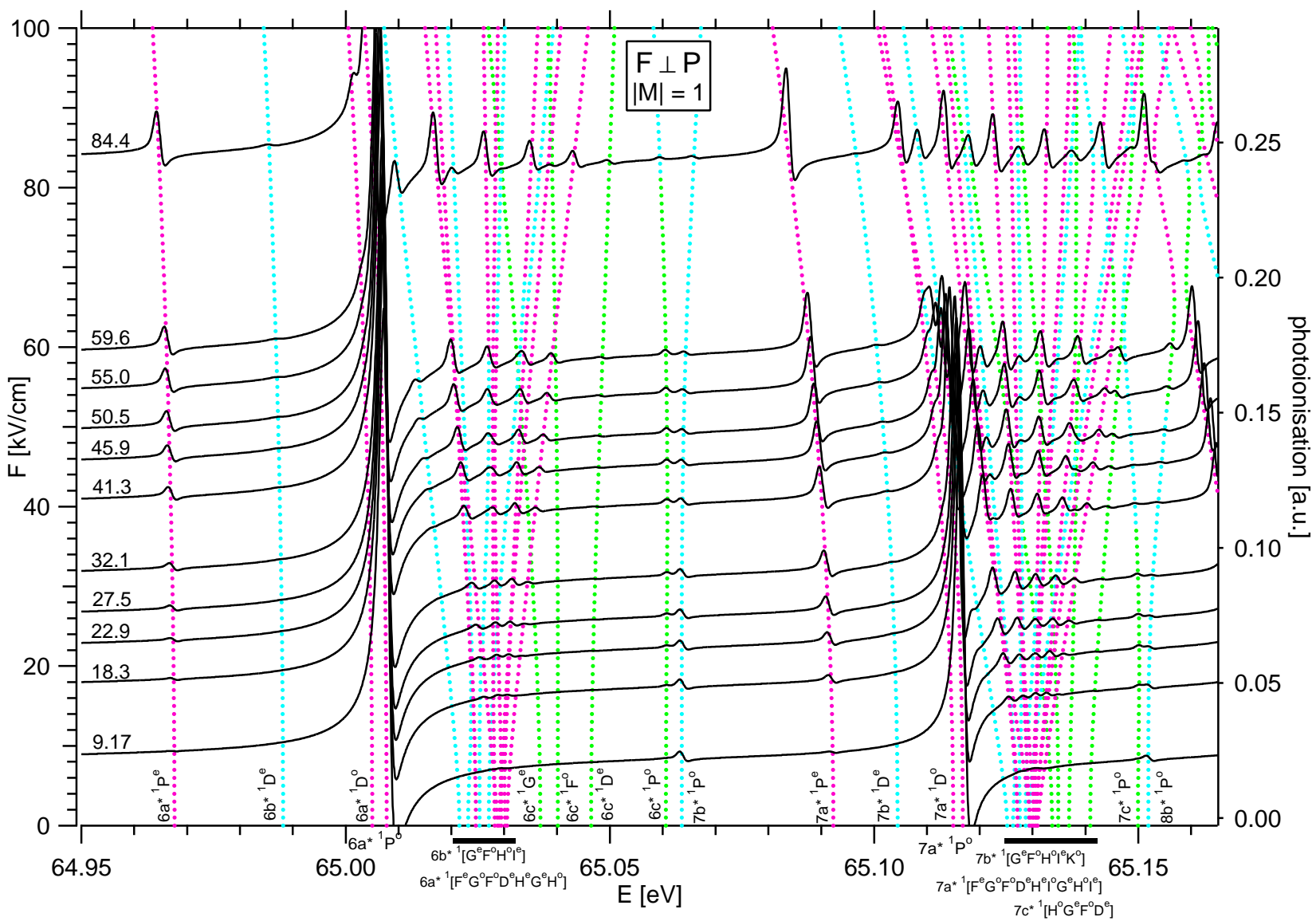
Figure 6.11: Same as in Fig. 6.10, but for $\boldsymbol{F} \perp \boldsymbol{P}$.

$F \perp P$
$|M| = 1$

F [kV/cm]

photoionisation [a.u.]

E [eV]

Lipsky	$^1S^e$	$^1P^o$	$^1D^e$	$^1F^o$	$^1G^e$	...	Tong & Lin
a	$(1,0)^+$	$(0,1)^+$	$(1,0)^+$	$(1,0)^0$	$(1,0)^0$	...	b^*
b	$(-1,0)^+$	$(1,0)^-$	$(0,1)^0$	$(0,1)^0$	$(0,1)^0$	...	a^*
c		$(-1,0)^0$	$(-1,0)^0$	$(-1,0)^0$	$(-1,0)^0$	...	c^*

Table 6.1: The classification labels used by Tong and Lin [45]. The $(K,T)^A$ correlation quantum numbers are given. The a and b states of Lipsky which are marked magenta are relabelled to a^*, whereas the states marked cyan are relabelled to b^*. All the states with $L \geq 3$ and parity $(-1)^L$ are labelled in the same manner as $^1F^o$ and $^1G^e$. The c states, which are marked green, transform to c^*. The states with parity $(-1)^{L+1}$ are labelled as a^*, and are not included in the table. The colours are chosen to match the colour coding of Figs. 6.10 and 6.11.

originating from different groups are allowed to cross." This crossing-non crossing rule of energy level Stark lines is schematically depicted in Fig. 6.9. As a consequence of the propensity rule, only the states which evolve from the a^* states at zero field will be preferentially populated. The latter is due to the fact that the field induced states derive their oscillator strength mostly from the $6a^*$ and $7a^*$ $^1P^o$ states. As described by the rule, the prominent peaks for $\boldsymbol{F} \parallel \boldsymbol{P}$ in Fig. 6.10 near the $6a$ and $7a$ $^1P^o$ resonances all have the a^* character. It seems that the rule applies even better for the $\boldsymbol{F} \perp \boldsymbol{P}$ case (Fig. 6.11): the amplitudes of the peaks evolved from the b^* and c^* states remain well bellow the half of the amplitudes of the a^* states for the $n = 7$ resonances for $\boldsymbol{F} \perp \boldsymbol{P}$. Furthermore, for $n = 6$ and $n = 7$ states the most striking example of the Stark induced mixing for the perpendicular setup is the evolution of the $6a^*$ $^1P^e$ and $7a^*$ $^1P^e$ resonances, for which the amplitudes are drastically increased in the electric field. It may also be seen that at 84.4 kV/cm the contribution originating from the $6a^*$ $^1D^o$ state becomes large enough to be resolved from the $6a^*$ $^1P^o$ peak. The cases of $^1P^e$ and $^1D^o$ states are good examples of the possibility to study properties of the LS and parity forbidden states by means of the electric field.
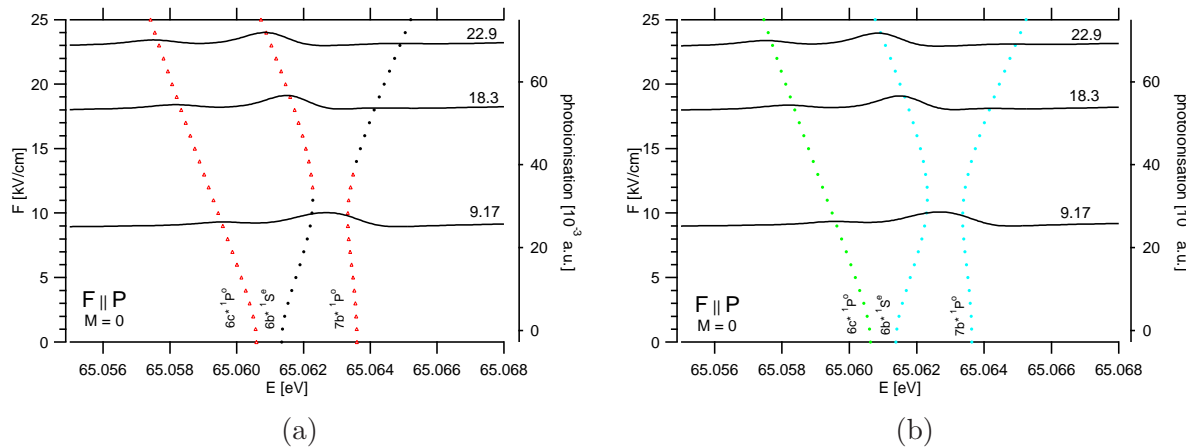
Figure 6.12: Magnified view of the $6b^*$ $^1S^e$ $7b^*$ $^1P^o$ crossing. The left graph shows the $LS\pi$ symmetry of the leading components of the states (cf. Fig. 6.1), and the right graph shows their classification according to Lin and Tong.

At the end, a short comment should be made about the diagrams in Fig. 6.9. As can be seen

by comparing the plots in Fig. 6.12, the form of a crossing of two isolated *interacting* states is the form shown in Fig. 6.9b even in the case where the states belong to the same series. Actually, the gap between the two diagram curves is a measure for the order of magnitude of the coupling matrix element. The leading components of the states *do* cross the region of intersection for the case of $6b$ $^1S^e$ and $7b$ $^1P^o$, as has been checked by examining the results at 0 kV/cm and 18 kV/cm. This somehow contradicts the propensity rule. Thus, the propensity rule is to be understood solely as a guide that helps with the interpretation of the Stark maps and with the estimation of the order of magnitude of the field coupling matrix elements.

6.3   Inelastic photon scattering cross section

6.3.1   Comparison with experiment

This subsection is dedicated to the comparison of the calculated primary fluorescence spectra (i.e., inelastic photon scattering spectra) to the VUV fluorescence data of Prince et al. [47] and the primary fluorescence yield data measured by Rubensson et al. [111].

An example of the calculated inelastic scattering cross section in $\boldsymbol{F} \perp \boldsymbol{P}$ geometry and at $F = 3$ kV/cm is presented in Fig. 6.13. The spectrum is convolved by a 3 meV broad Gaussian to account for the finite experimental resolution. As in the case of photoionisation, a wealth of new structures appears when the external field is applied. Contrary to the photoionisation spectra, the photon yield signal may be changed considerably when an external field is applied, even for moderate electric field strengths of the order of a few kV/cm.

Figs. 6.14 and 6.15 show the measured and the calculated spectra with $\boldsymbol{F}$ perpendicular and parallel to the polarisation vector of the synchrotron light, respectively. For $\boldsymbol{F} \perp \boldsymbol{P}$, the measured fluorescence yield is normalised to the integrated intensity of the $5c/6b$ $^1P^o$ doublet, since this is not expected to change strongly with electric field, as is discussed in the next subsection. On the other hand, the increase of the fluorescence signal at the $N = 2$ threshold is used for normalisation for $\boldsymbol{F} \parallel \boldsymbol{P}$. The energy scale of experimental signal is slightly changed to match the calculations, whereas the calculated spectra are scaled to one point to match the experiment.

An introductory comment is required before identifying the contributions of individual peaks in the fluorescence yield spectra. As may be seen, the intensity of the na $^1P^o$ signal is greatly enhanced when the external field is applied. Part of this intensity increase stems from fluorescence generated by collisions of charged particles [47], which originate from the autoionisation decay of doubly excited states. At high field strengths, and especially for the perpendicular experimental setup, this signal becomes predominant for the a $^1P^o$ states having the highest autoionisation rates. Therefore, as may be seen in Figs. 6.14 and 6.15, fluorescence yield seems to follow the ion yield signal: the peaks recorded at high fields start to assume Fano-like shape. A fair comparison should therefore include the subtraction of this ionic component of the signal. For the resonances other than na $^1P^o$, this effect is negligible.

For $\boldsymbol{F} \perp \boldsymbol{P}$ we note a pronounced series of peaks appearing between each $(n-1)c/nb$ $^1P^o$ pair and the na $^1P^o$ resonance. As will be shown in the next subsection, the latter peaks are attributed to na $^1P^e$ states. On the contrary, the yields of the nb and nc peaks for $\boldsymbol{F} \parallel \boldsymbol{P}$ are decreased due to Stark induced mixing. Furthermore, for high quantum numbers n, a series of broad peaks appears at the high energy shoulder of the a $^1P^o$, the intensity and the width of which seem to increase with the field.

The overall agreement between the measurements and the theory is quite good: the intensities of the peaks and their positions match the experimental data up to $n = 10$ or $n = 11$. As may be deduced from Fig. 6.13, but also by means of the knowledge obtained in the previous section, the wide peaks in the high n region are composed of a large number of contributions. These contributions originate from states containing components with higher angular momenta, and can be easily induced at sufficiently high electric fields. Since our calculations include the free states with total angular momenta $L \leq 10$, the failure of the calculation in this energy region is not unexpected.

We conclude this subsection by discussing the experimental data of Rubensson et al. [111]. These spectra are the most relevant for comparison with our theory because they contain only the signal of the primary fluorescence. Although the overall agreement seems to improve compared

to previous case, the range of validity of the calculations is still seen to remain approximately the same (Fig. 6.16).

6.3.2 Analysis of the fluorescence yield spectra

As mentioned, the contributions of individual states in the fluorescence yield spectra in the external electric field can be identified by examining their evolution from the zero field states. Plots similar to the Stark maps for photoionisation spectra are shown in Figs. 6.17 and 6.18. The cross section is calculated for the same field strengths as given by Harries et al., and again the classification of Tong and Lin is used for the underlying Stark maps. The spectra are broadened with a Gaussian of 1.4 meV FWHM.

As proposed by the propensity rule for photoionisation, the majority of intense peaks in $\boldsymbol{F} \perp \boldsymbol{P}$ geometry seems to belong to the a^* series. The most striking examples that conform to the rule are the peaks which evolve from the $6a^*$ and $7a^*$ ${}^1D^o$ states. Although the amplitudes of the peaks are expected to be small (because of the odd parity), the induced coupling is nevertheless far from negligible.

An apparent change that occurs for $\boldsymbol{F} \perp \boldsymbol{P}$ when the external field is applied is the appearance of isolated a^* ${}^1P^e$ peaks that gain intensity as the field strength is increased. This behaviour can be explained if it is remembered that the field coupling is governed by the same selection rules as the electric dipole transitions for linearly polarised light. For $M = \pm 1$ the field induced coupling to the ${}^1P^o$ states is strong and the radiative decay rate of ${}^1P^e$ states is high, resulting in an increase of the fluorescence yield. The ${}^1P^e$ peaks are absent in the $\boldsymbol{F} \parallel \boldsymbol{P}$ geometry. This is a general feature of all states for which the parity is equal to $(-1)^{L+1}$.

An interesting change also occurs in the parallel configuration ($\boldsymbol{F} \parallel \boldsymbol{P}$): the intensities of $(n-1)c/nb$ ${}^1P^o$ doublet rapidly decrease. The latter can be understood as follows. Due to the presence of strongly autoionising ${}^1S^e$ and ${}^1D^e$ states in the near vicinity, the field induced coupling of the doublet results in a substantial increase of the autoionisation decay rate. This, in turn, means that the fluorescence branching ratio is drastically reduced, and the peak intensity in the photon yield spectrum is decreased. The effect is weaker in $\boldsymbol{F} \perp \boldsymbol{P}$ geometry, since in this case due to the $M = \pm 1$ rule, the Stark induced coupling to the close lying ${}^1S^e$ states is zero. This is also the reason why for $\boldsymbol{F} \perp \boldsymbol{P}$, the integrated intensity of the doublet was used for the normalisation of spectra.
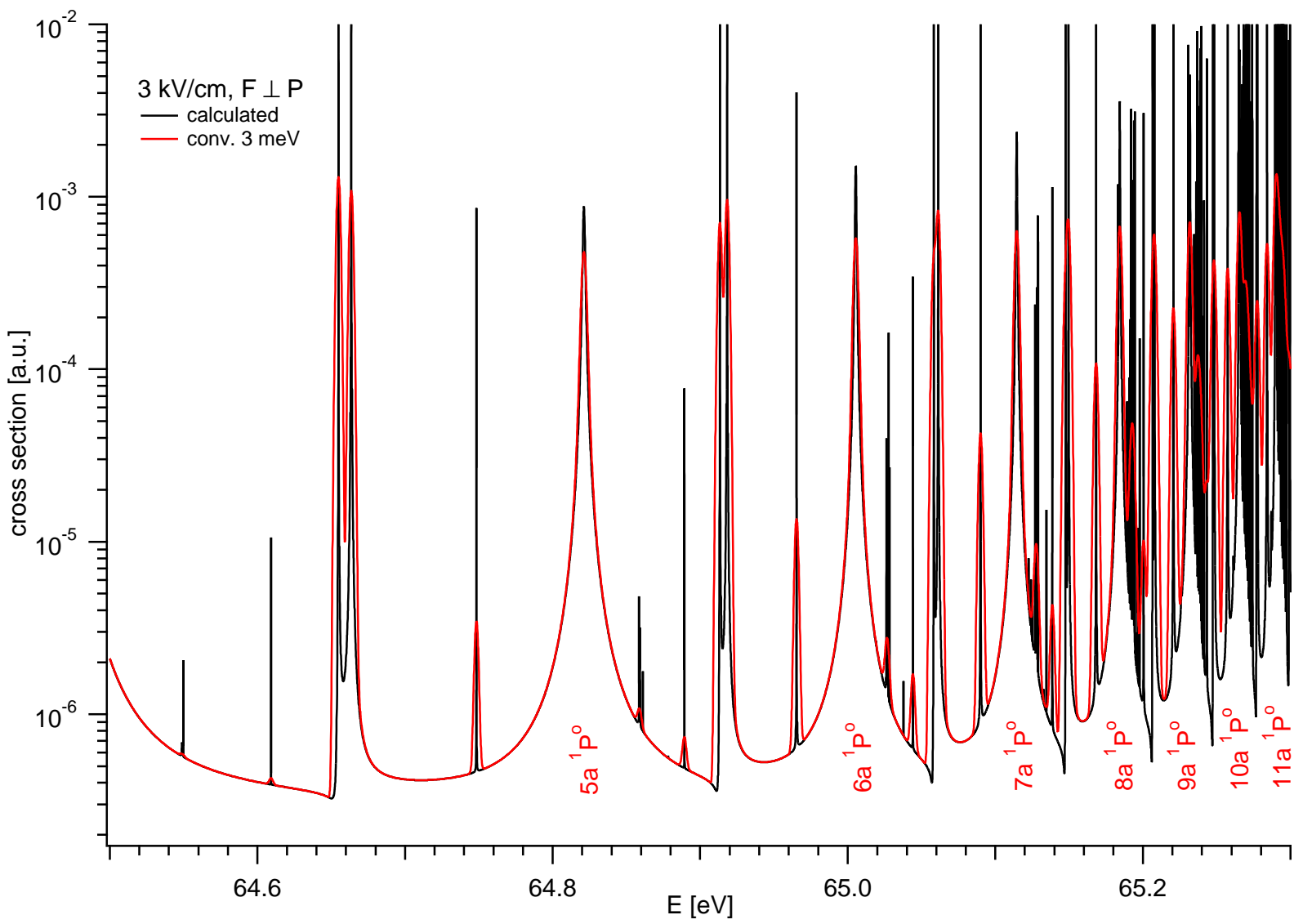
Figure 6.13: Calculated inelastic photon scattering cross section for $F = 3\,\mathrm{kV/cm}$, $\boldsymbol{F} \perp \boldsymbol{P}$. The spectrum is convolved with a Gaussian with 3 meV FWHM.
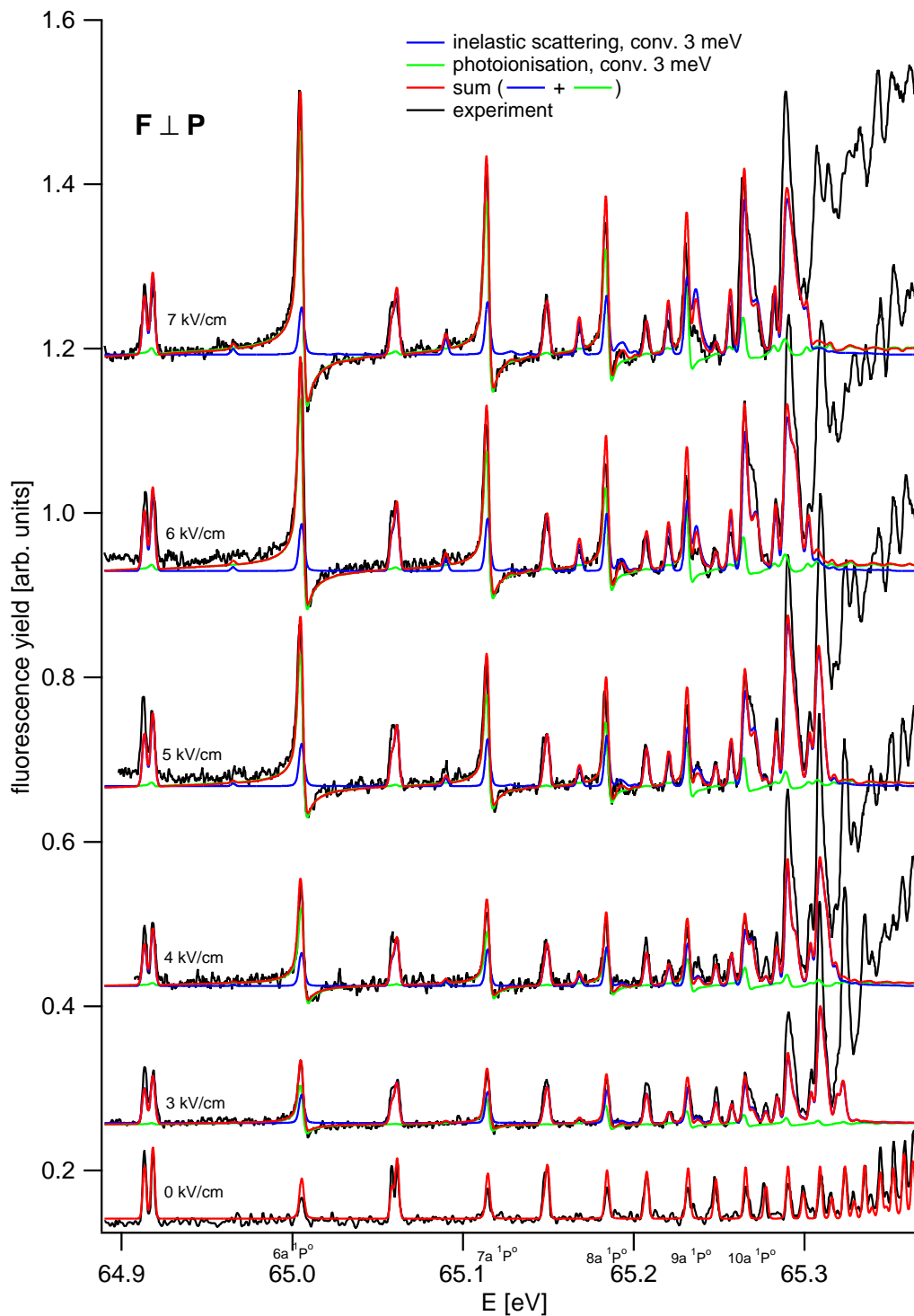
Figure 6.14: Comparison of the spectra measured by Prince et al. [47] and the calculated total fluorescence yield for $\boldsymbol{F} \perp \boldsymbol{P}$. The calculated spectra are scaled and broadened with a Gaussian with 3 meV FWHM (2.5 meV FWHM for 0 kV/cm) to match the experiment. The spectra are translated vertically for clarity. The measured yield is normalised to the integrated intensity of the $5c/6b$ $^1P^o$ doublet. The blue curve represents the photon scattering signal, the green the ion signal, and the red curve their sum. See text for a detailed explanation.

94
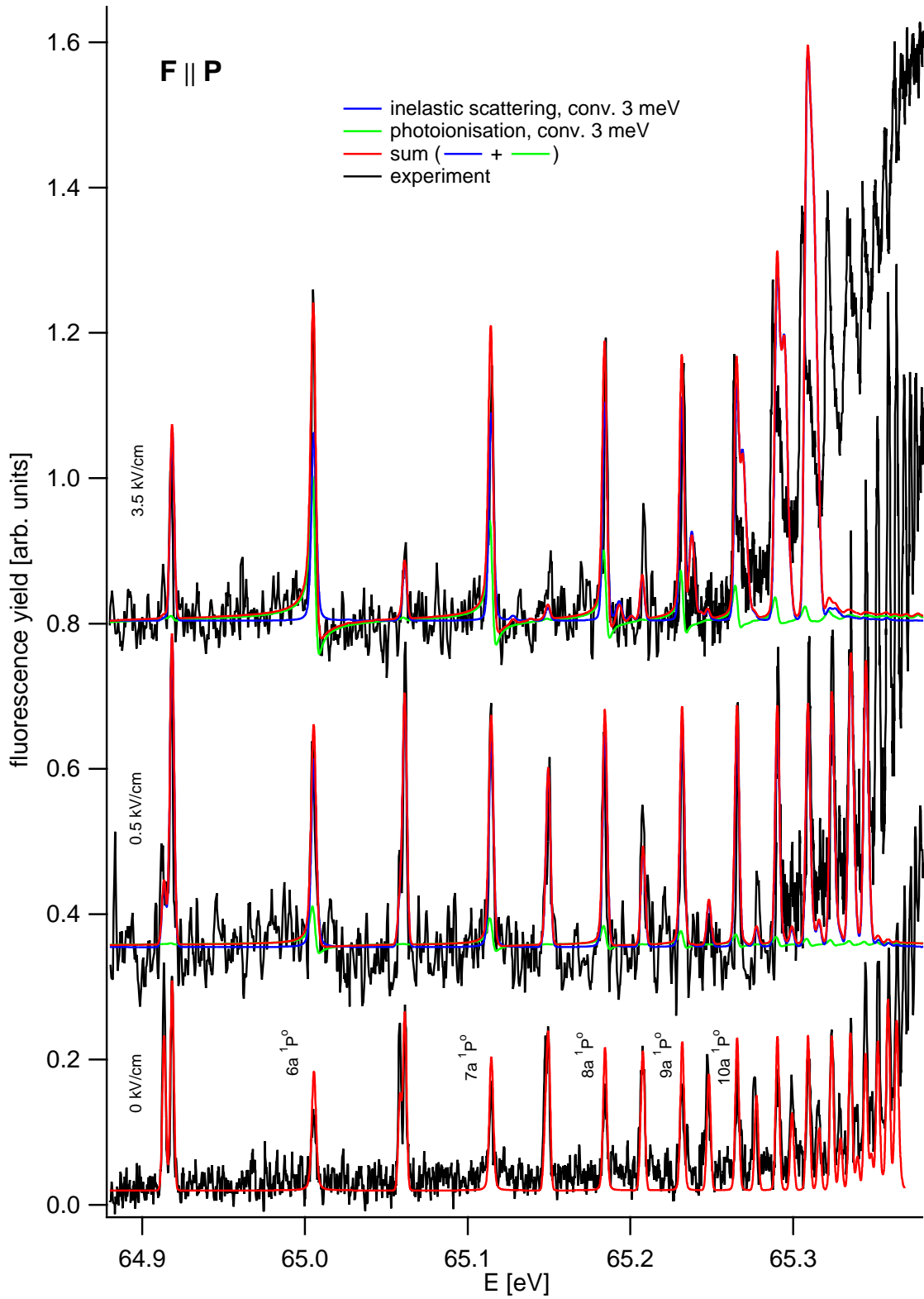
Figure 6.15: As in Fig. 6.14, but for $\boldsymbol{F} \parallel \boldsymbol{P}$. The measured signal is normalised to the increase of the fluorescence at the $N = 2$ threshold.
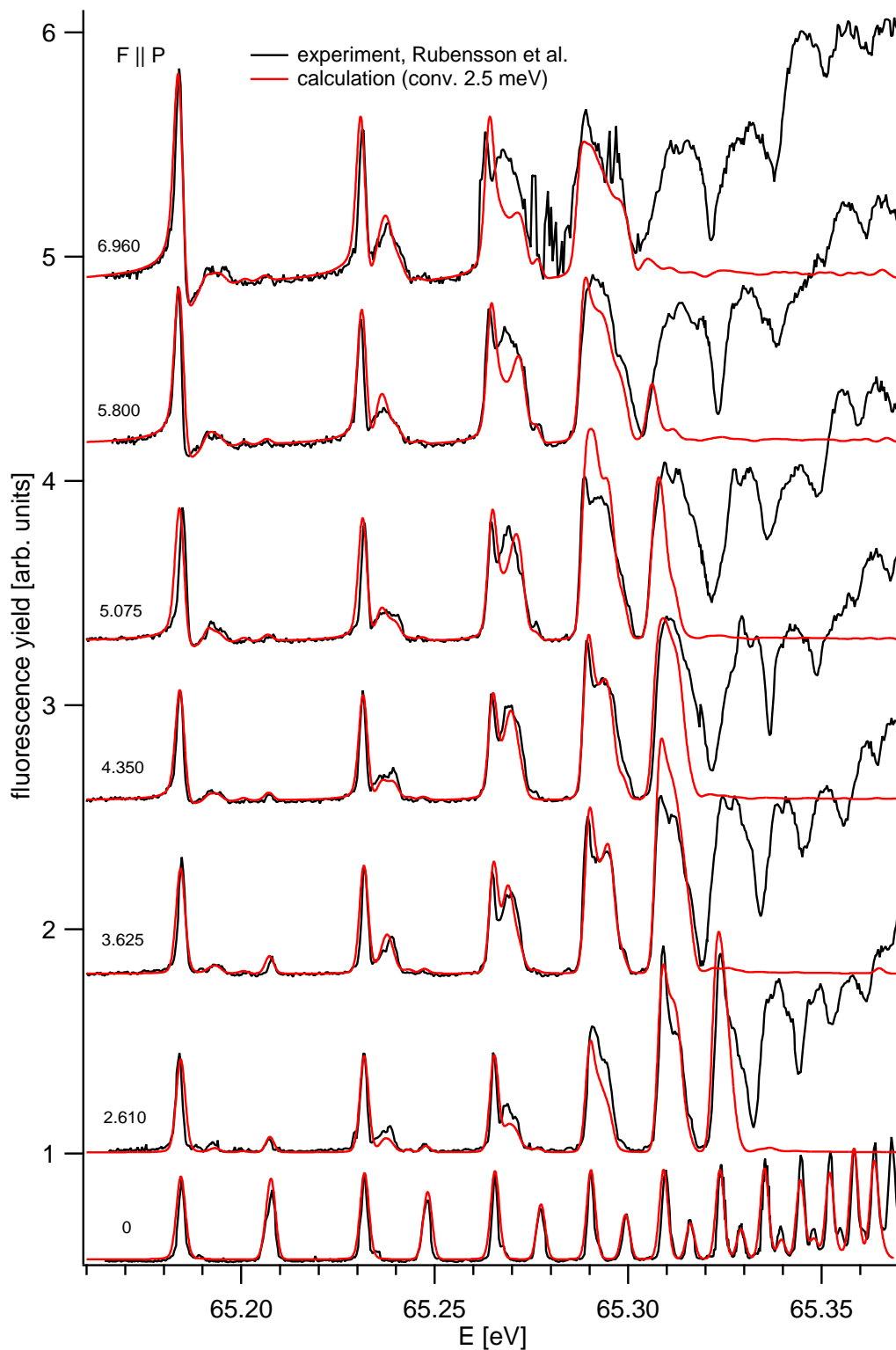
Figure 6.16: Comparison of measured and calculated primary fluorescence yield spectra. Experimental data were recorded by Rubensson et al. [111] for the parallel configuration ($\boldsymbol{F} \parallel \boldsymbol{P}$). The calculated spectra are broadened with a Gaussian (2.5 meV FWHM). Energy scale of the measurements is changed to match the theory. For each spectrum, the corresponding field strength in kV/cm is given.
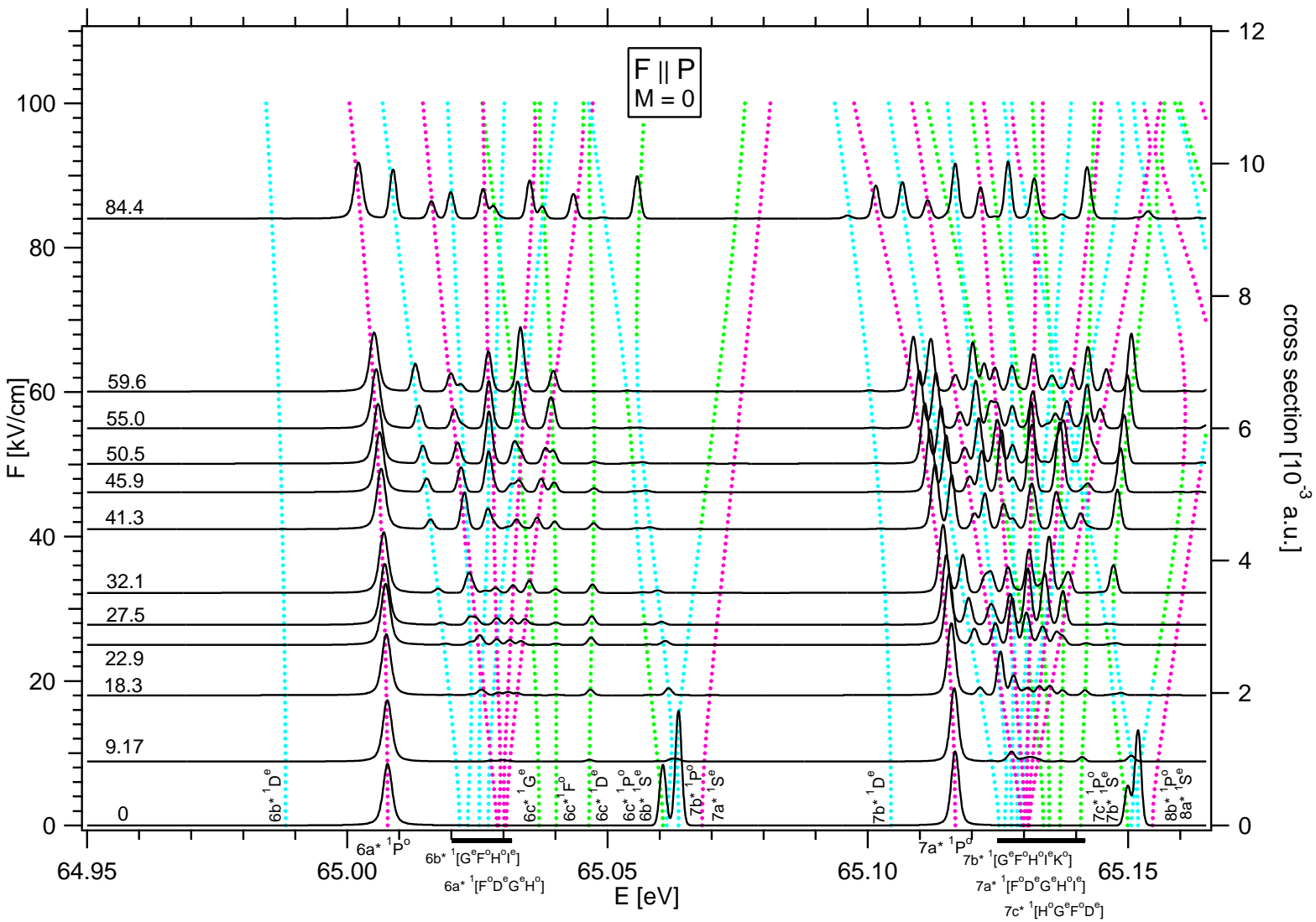
Figure 6.17: Calculated inelastic photon scattering cross section for $\boldsymbol{F} \parallel \boldsymbol{P}$ for various electric field strengths. The spectra are broadened with a Gaussian with 1.4 FWHM and shifted vertically so that the baselines approximately show the field strength. The colour coding of Tong and Lin is used. The left axis refers to the Stark map, and the right axis refers to the calculated spectra.
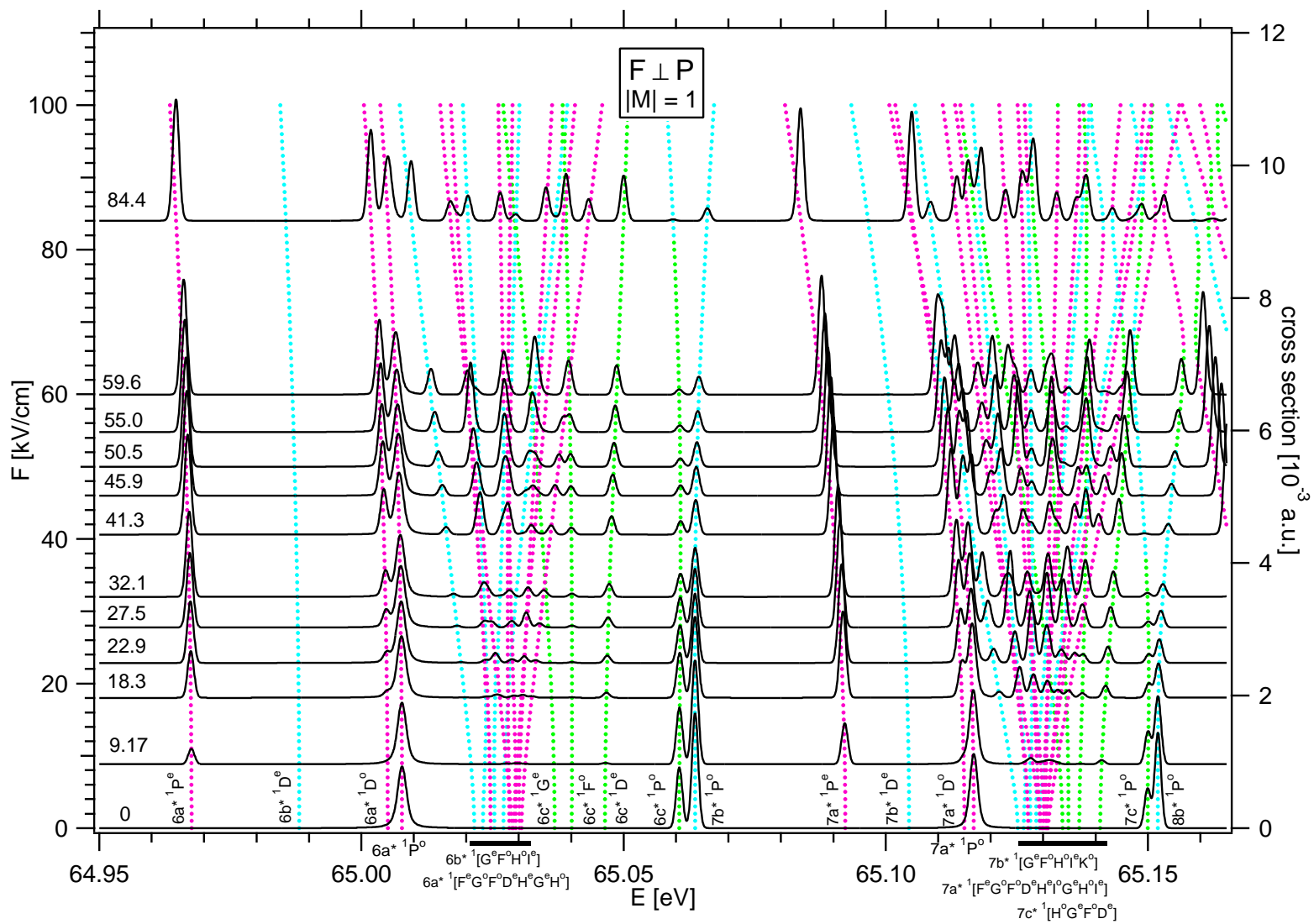
Figure 6.18: As in Fig. 6.17, but for **F ⊥ P**.

6.4 The time domain

Just recently, Žitnik et al. measured the lifetimes of several *dark* $^1P^e$ states in the weak electric fields for $\boldsymbol{F} \perp \boldsymbol{P}$. The experiment was performed at Gas Phase photoemission beamline at Elettra synchrotron in the multi bunch mode [48]. As the field was increased from 1.6 to 6.6 kV/cm, the shortening of the lifetime was observed for series members with $n = 9 - 12$. These states were chosen because the lower n states have too low oscillator strengths at weak fields, while on the high n side, the available energy resolution of the incoming photons was not enough to isolate a single state. The effect is explained by the relatively strong increase of the autoionisation decay rate for these states in the non zero field ($\propto F^2$). Because of the latter, the total decay probability is increased, since in such weak fields, the zero field fluorescence decay rate does not change substantially. We note in Fig. 6.4 that our first order perturbation
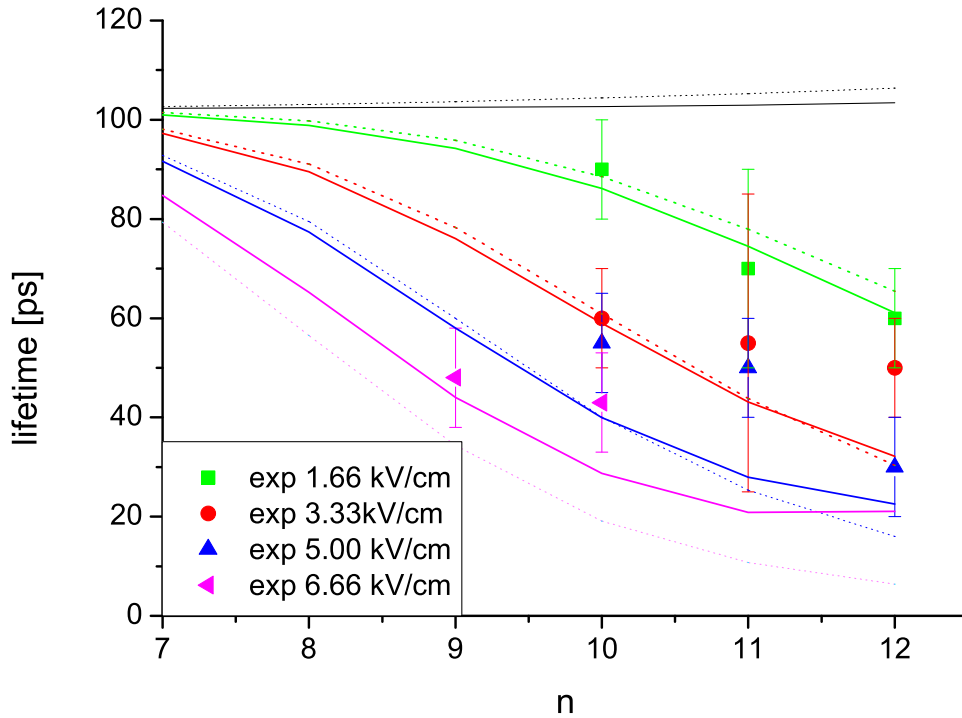
Figure 6.19: Comparison of the measured lifetimes of $^1P^e$ na states with our calculation. First order perturbation method (dotted line), complex rotation method (full line).

calculations, as well as the complex rotation method, predict the same trend but they start to depart from each other at highest fields. The effect seems to be a little overestimated by the calculations, although the recent simulations show that the actual experimental field calibration might also be wrong for approximately 10%. This would bring measured lifetimes into closer agreement with theoretical predictions.

6.5 Radiation damping of c $^1P^o$ resonances

As has been mentioned several times throughout this work, the c $^1P^o$ states are characterised by small autoionisation decay rates. Their contributions to the photoionisation spectrum are shown to be weak, but discernible. It turns out, however, that in order to describe the intensities of the c states in the measured photoionisation spectra, the inclusion of radiation corrections is essential. As can be seen from the treatment of radiation damping presented in Chapter 4, the amplitudes of the peaks which belong to the c states are a very sensitive measure of the ratio of the fluorescence and autoionisation decay rates (this is also shown in [11]).

Unfortunately, the accuracy of the present calculations does not suffice for the determination of the autoionisation widths of c $^1P^o$ states. Furthermore, to date, no reliable calculations of widths and asymmetry parameters exist to our knowledge for the higher lying states of this series. This also appears to be the case for the state of the art calculations of Rost et al. [4]. Nevertheless, for the lowest lying $3c$ $^1P^o$ state, the parameters from Ref. [4] agree well with our calculations (except for the autoionisation width, which has not been calculated correctly in our case). We therefore assume that the tabulated values are correct for the $3c$ state, and use it to assess autoionisation widths for the higher Rydberg states. This is done in the following way. The energy of a doubly excited state characterised by a set of single electron principal quantum numbers (N, n) can be written in the frame of quantum defect theory as [4]

$$E_{N,n} = -\frac{Z^2}{2N^2} - \frac{(Z-1)^2}{2\nu^2} \,. \tag{6.1}$$

We have used ν to denote the effective principal quantum number. The corresponding quantum defect is defined as

$$\delta_n = n - \nu \,. \tag{6.2}$$

Throughout a chosen series, the quantum defect δ_n, the asymmetry parameter q_n, and the reduced parameters

$$\begin{aligned} \Gamma_n^* &\equiv \Gamma_n \nu^3 \\ B_n^{*2} &\equiv B_n^2 \nu^3 \end{aligned} \tag{6.3}$$

can be shown to be approximately constant. In Eq. (6.3), B_n is the real part of the complex scaled matrix element (cf. Chapter 4). The autoionisation widths of higher lying states may therefore be extrapolated from the lower states (this is sometimes referred to as the n^3 rule). This property has already been used by Liu et al. [19], but also by several other authors. Since the calculated asymmetry parameter $q = -22.1$ for the $n = 3$ state is close to the value of Rost et al. ($q = -23.4$) and since the measured [27] and calculated [19] decay rates indicate that the order of magnitude of the half-width calculated by Rost et al. is correct, we choose their Γ^* value for extrapolation. To be more explicit, we set the values of q and Γ^* to

$$q_n(c\,{}^1P^o) \equiv \text{const.} = -22.1 \qquad \text{and} \qquad \Gamma_n^*(c\,{}^1P^o) \equiv \text{const.} = 3.4596 \times 10^{-7} \,. \tag{6.4}$$

The parameters of the $^1P^o$ resonances below the $N = 2$ threshold used in the calculation of the photoionisation and inelastic scattering cross section are tabulated in Table 6.2. To be able to compare the results to the values in Ref. [4] we have introduced

$$(\tilde{B}_n^*)^2 = 2(\text{Re}\, E_{n\Theta} - E_g)\, B_n^2 \,\nu^3 \,. \tag{6.5}$$

The results of the calculations using the above $3c$ parameters are shown on the bottom of Fig. 6.20. As can be seen from comparison with the measured photoionisation signal (Fig. 6.20,
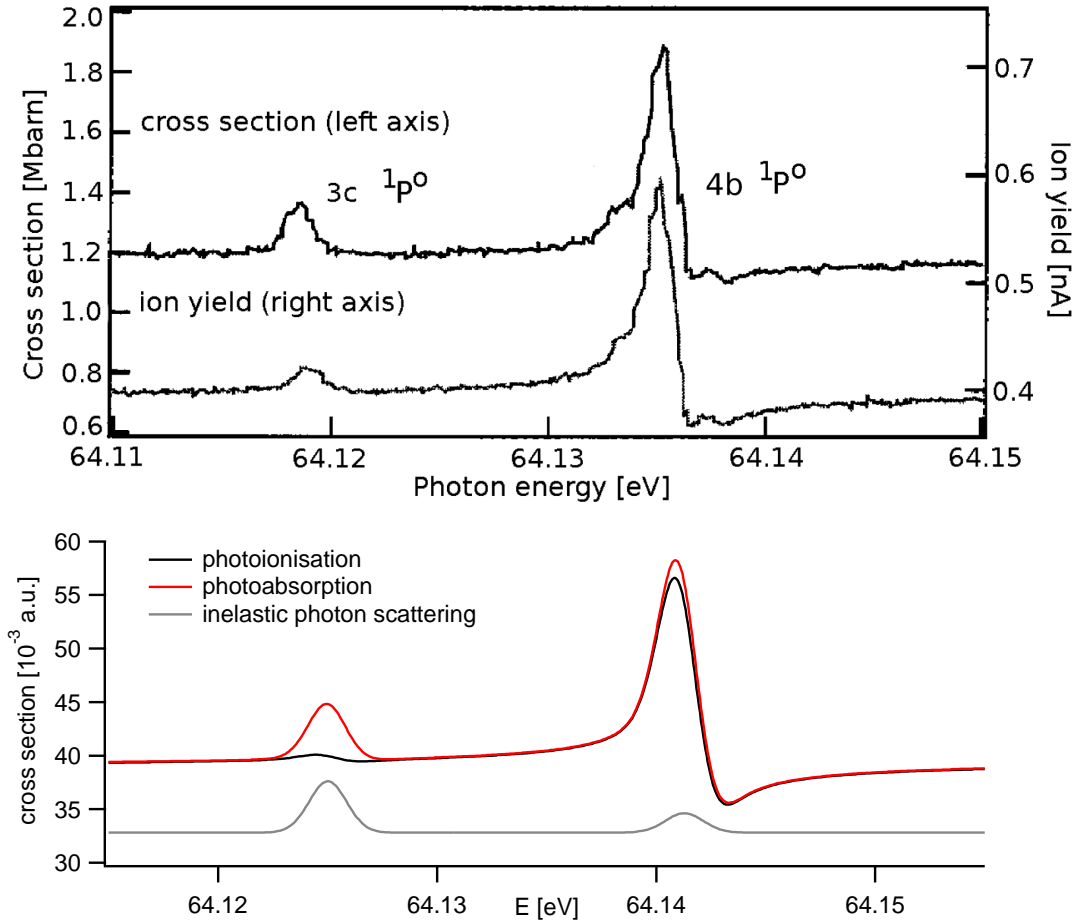
Figure 6.20: The measured (top) and calculated (bottom) photoabsorption and photoionisation cross sections. The calculated photoabsorption spectrum (red) is approximated by the sum of the photoionisation (black) and inelastic photon scattering (gray) cross sections. The calculated spectra are broadened with a Gaussian with 2 meV FWHM.

top), the amplitude of the calculated $3c$ peak is too low. This indicates that the calculated autoionisation width and/or the asymmetry parameter of the $3c$ state may be wrong. In fact, from the comparison with the experiment, it follows that the autoionisation width Γ and the q parameter are too low. Note that the effective q parameter is drastically reduced (by a factor of $\Gamma/(\gamma + \Gamma)$, cf. Chapter 4) due to radiation damping. For $\Gamma \ll \gamma$, the peaks may be almost completely smeared out.

In contrast to the photoionisation signal, the calculated *photoabsorption* cross section may be seen to agree pretty well with the measurements of Prince et al. [11]. This stems from the fact that the for the $3c$ state, the peak intensity for the case of photoabsorption comes predominantly from the inelastic photon scattering, which is largely unaffected by the autoionisation decay since the radiative widths are at least one order of magnitude larger than the autoionisation widths.

Table 6.2: Parameters of $^1P^o$ doubly excited states below the $N = 2$ threshold. The last two columns (marked by †) are from Ref. [4].

	$-E$	$\Gamma/2$	ν	Γ^*	$(B^*)^2$	q	$(\tilde{B}^*)^2$	q	$(\tilde{B}^*)^2$
2a	0.693106607	6.86350(-4)	1.61	5.7192(-3)	5.39(-3)	-2.77	2.38(-2)	-2.77†	2.38(-2)†
3a	0.564080259	1.50540(-4)	2.79	6.5622(-3)	4.47(-3)	-2.58	2.09(-2)	-2.58	2.10(-2)
4a	0.534361157	6.4152(-5)	3.81	7.1219(-3)	4.53(-3)	-2.55	2.15(-2)	-2.55	2.15(-2)
5a	0.521503669	3.2888(-5)	4.82	7.3748(-3)	4.56(-3)	-2.54	2.17(-2)	-2.54	2.17(-2)
6a	0.514733425	1.8992(-5)	5.83	7.5095(-3)	4.58(-3)	-2.53	2.19(-2)	-2.53	2.19(-2)
7a	0.510726440	1.1924(-5)	6.83	7.5895(-3)	4.59(-3)	-2.53	2.20(-2)	-2.52	2.19(-2)
8a	0.508158307	7.963(-6)	7.83	7.6410(-3)	4.59(-3)	-2.53	2.20(-2)	-2.58	2.25(-2)
9a	0.506413686	5.576(-6)	8.83	7.6761(-3)	4.60(-3)	-2.53	2.20(-2)	-2.5	2.24(-2)
10a	0.505174494	4.054(-6)	9.83	7.7010(-3)	4.60(-3)	-2.53	2.21(-2)		
11a	0.504262710	3.038(-6)	10.83	7.7194(-3)	4.60(-3)	-2.53	2.21(-2)		
12a	0.503572348	2.335(-6)	11.83	7.7333(-3)	4.60(-3)	-2.53	2.21(-2)		
13a	0.503037093	1.834(-6)	12.83	7.7490(-3)	4.61(-3)	-2.53	2.21(-2)		
14a	0.502613741	1.434(-6)	13.83	7.5863(-3)	4.60(-3)	-2.52	2.21(-2)		
15a	0.502273028	1.335(-6)	14.83	8.7093(-3)	4.62(-3)	-2.52	2.22(-2)		
3b	0.597073790	1.922(-6)	2.27	4.4946(-5)	8.67(-5)	-4.25	4.00(-4)	-4.25†	4.00(-4)†
4b	0.546491860	1.009(-6)	3.28	7.1138(-5)	7.74(-5)	-3.32	3.65(-4)	-3.32	3.67(-4)
5b	0.527297038	4.88(-7)	4.28	7.6507(-5)	8.02(-5)	-3.30	3.81(-4)	-3.31	3.83(-4)
6b	0.517936917	2.65(-7)	5.28	7.8007(-5)	8.08(-5)	-3.31	3.85(-4)	-3.31	3.88(-4)
7b	0.512679737	1.59(-7)	6.28	7.8569(-5)	8.08(-5)	-3.31	3.87(-4)	-3.32	3.89(-4)
8b	0.509435690	1.02(-7)	7.28	7.8820(-5)	8.08(-5)	-3.31	3.87(-4)	-3.3	3.94(-4)
9b	0.507294204	7.0(-8)	8.28	7.8948(-5)	8.08(-5)	-3.31	3.87(-4)		
10b	0.505806870	4.9(-8)	9.28	7.9019(-5)	8.07(-5)	-3.32	3.87(-4)		
11b	0.504732057	3.6(-8)	10.28	7.9061(-5)	8.07(-5)	-3.32	3.87(-4)		
12b	0.503930208	2.8(-8)	11.28	7.9085(-5)	8.06(-5)	-3.32	3.87(-4)		
13b	0.503316151	2.1(-8)	12.28	7.8966(-5)	8.06(-5)	-3.32	3.87(-4)		
14b	0.502835510	1.5(-8)	13.28	7.0174(-5)	8.06(-5)	-3.32	3.87(-4)		
15b	0.502452349	3.9(-8)	14.28	2.2886(-4)	8.05(-5)	-3.32	3.86(-4)		
3c	0.547089825	5(-9)	3.26	3.4596(-7)	2.01(-5)	-22.1	9.49(-5)	-23.4†	9.29(-5)†
4c	0.527614605	2(-9)	4.26	3.4596(-7)	1.89(-5)	-22.1	8.96(-5)	-133	8.75(-5)
5c	0.518117242	1(-9)	5.25	3.4596(-7)	1.86(-5)	-22.1	8.88(-5)	197	8.66(-5)
6c	0.512790392	7(-10)	6.25	3.4596(-7)	1.86(-5)	-22.1	8.87(-5)	91	8.66(-5)
7c	0.509508038	5(-10)	7.25	3.4596(-7)	1.86(-5)	-22.1	8.88(-5)	72	8.65(-5)
8c	0.507343946	3(-10)	8.25	3.4596(-7)	1.86(-5)	-22.1	8.90(-5)		
9c	0.505842475	2(-10)	9.25	3.4596(-7)	1.86(-5)	-22.1	8.91(-5)		
10c	0.504758391	2(-10)	10.25	3.4596(-7)	1.86(-5)	-22.1	8.91(-5)		
11c	0.503950219	1(-10)	11.25	3.4596(-7)	1.86(-5)	-22.1	8.92(-5)		
12c	0.503331706	9(-11)	12.25	3.4596(-7)	1.86(-5)	-22.1	8.93(-5)		
13c	0.502847834	7(-11)	13.25	3.4596(-7)	1.86(-5)	-22.1	8.92(-5)		
14c	0.502462325	6(-11)	14.25	3.4596(-7)	1.90(-5)	-22.1	9.11(-5)		
15c	0.502149666	5(-11)	15.25	3.4596(-7)	1.80(-5)	-22.1	8.65(-5)		

Chapter 7

Conclusion

In this thesis, we present the ab initio calculated photoionisation spectra of the helium atom in the region of doubly excited states below $N = 2$ in the presence of high static electric fields. The calculated photoionisation cross section is for the first time capable of reproducing the experimental data in detail. For the purpose, we have used the method of complex scaling with a large screened two electron Sturmian basis. The comparison with experimental data suggests that our results may be reliable up to the field strengths of 100 kV/cm, and may reach energies about 50 meV below the threshold. Until now, only the Stark maps have been published for high electric fields [42], together with approximately calculated oscillator strengths in the parallel ($\boldsymbol{F} \parallel \boldsymbol{P}$) geometry [45]. We have also examined the perpendicular geometry and confirmed the validity of the propensity rule for the Stark mixing, proposed by Tong and Lin [45]. The preferential mixing in the field occurs between states with similar angular correlation character, dispersing the oscillator strength of the principal a (a^*) series. Furthermore, we have predicted the shape of photoionisation spectrum for the $\boldsymbol{F} \perp \boldsymbol{P}$ geometry which remains to be measured. The most notable change should be the presence of the strong signal at the positions of a^* $^1P^e$ resonances.

The main purpose of this work was to calculate the primary fluorescence yield which is emitted from the resonant states in the electric field. We have devised the procedure to obtain the inelastic photon scattering cross sections using the eigenstates of the Stark Hamilton operator in the complex space. While the bound-continuum interaction has been treated to all orders, the photon-atom interaction has been treated as a perturbation. Several experimental spectra are available for comparison, and they were recorded only in relatively weak electric fields. In more or less all of them, the contamination with ion/electron induced fluorescence signal is present. This indicates why going to the high electric field strengths may be a challenging experimental task for the Raman spectroscopy. Nevertheless, we have calculated the total primary fluorescence yield spectra as functions of the incoming photon energy for both geometries and for the fields reaching up to 100 kV/cm. The presentation is limited to $n = 6 - 7$ manifold of states, since the comparison with the measured fluorescence yield spectra – after subtracting the ionic component – shows less satisfactory agreement than in the case of the photoionisation. The interpretation becomes questionable above $n = 11 - 12$. The main reason is probably the lack of higher angular momentum states in our zero field basis set; only the states with angular momentum $L \leq 10$ were included. There should be no higher angular momentum states than that in manifolds with $n \leq 11$. At high electric field strengths, however, the manifolds with different quantum numbers n are mixed: the higher the value of n is, the stronger mixing between the manifolds occurs. The other reason for moderate agreement is that in some cases the comparison is made with the total VUV fluorescence yield, which also includes the contribution of the secondary photon. This is emitted

at the end of the cascade reaching the ground state of the helium atom. In the absence of singlet-triplet mixing, there should be an exactly one such secondary photon emitted for each primary photon, so this should not be a problem if it is possible to neglect the effect of non isotropic photon angular distributions. It then seems that, compared to the photoionisation, the inelastic scattering spectra represent a more sensitive test for the calculations of the Stark effect. This is not surprising because the majority of the oscillator strength which is derived from the principal line is redirected into the fluorescence channel. Especially for higher angular momentum states, the autoionisation decay rate is strongly suppressed, while the fluorescence signal of all the states displays similar fluorescence decay rates. Even in high fields, the contribution of the dark states in photoionisation spectra is still relatively small when compared to the principal line intensity, while the fluorescence signals are of the same order of magnitude already in the weaker fields, as shown for the $n = 6$ manifold. Only some rare examples showing the opposite trend can be noted.

The direct observations of the total decay rate of resonances are possible in the time domain. We have reproduced the observed trend of shortening of the lifetimes of the $^1P^e$ states upon application of the electric field. Still, the error bars of the measured lifetimes will have to be reduced in the future to test more thoroughly the theoretical models.

Further extending the promising approach presented in this work, one could estimate the initial occupation of singly excited states after the primary fluorescence, i.e., decompose the fluorescence yield into contributions of different final states. It then seems straightforward to set the study of dark states by energy selective detection of the secondary fluorescence in the visible [112], similar to the zero field case [23, 24]; considering photon emission between Stark affected singly excited states should be the easier part of the problem, as mentioned before. Determination of angular distribution of the primary fluorescence in the electric field is another interesting subject which deserves our attention in the near future, especially if the experimental efforts are done to measure it.

The spin-orbit interaction should be included into the calculation scheme to gain more credibility at higher n. Finally, we do not believe that the selected methodology can ever make one reach the threshold – this would imply a very large basis set. However, we have discussed here only the doubly excited states below the $N = 2$ threshold. They represent a very small fraction of eigenstates of the complex scaled Hamilton operator: resonances converging to higher thresholds which are yet to be studied in the non zero electric field can also be – and have in fact been – calculated.

Bibliography

[1] G. Tanner, K. Richter, J.-M. Rost, Rev. Mod. Phys. **72**, 497–544 (2000)

[2] R. P. Madden, K. Codling, Phys. Rev. Lett. **10**, 516–518 (1963)

[3] J. W. Cooper, U. Fano, F. Prats, Phys. Rev. Lett. **10**, 518–521 (1963)

[4] J.-M. Rost, K. Schulz, M. Domke, G. Kaindl, J. Phys. B **30**, 4663–4694 (1997)

[5] M. Domke, G. Remmers, G. Kaindl, Phys. Rev. Lett. **69**, 1171–1174 (1992)

[6] R. Follath, Nucl. Instrum. Methods A **467-468**, 418–425 (2001)

[7] P. G. Kruger, Phys. Rev. **36**, 855–859 (1930)

[8] M. K. Odling-Smee, E. Sokell, P. Hammond, M. A. MacDonald, Phys. Rev. Lett. **84**, 2598–2601 (2000)

[9] J. G. Lambourne, F. Penent, P. Lablanquie, R. I. Hall, M. Ahmad, M. Žitnik, K. Bučar, P. Hammond, S. Stranges, R. Richter, M. Alagia, M. Coreno, J. Phys. B **36**, 4339–4350 (2003)

[10] J.-E. Rubensson, C. Såthe, S. Cramm, B. Kessler, S. Stranges, R. Richter, M. Alagia, M. Coreno, Phys. Rev. Lett. **83**, 947–950 (1999)

[11] K. C. Prince, R. Richter, M. de Simone, M. Alagia, M. Coreno, Phys. Rev. A **68**, 044701 (2003)

[12] P. Lablanquie, F. Penent, R. I. Hall, J. H. D. Eland, P. Bolognesi, D. Cooper, G. C. King, L. Avaldi, R. Camilloni, S. Stranges, M. Coreno, K. C. Prince, A. Mühleisen, M. Žitnik, Phys. Rev. Lett. **84**, 431–434 (2000)

[13] R. D. Cowan, *The theory of atomic structure and spectra* (Univ. of California, Berkeley, 1981)

[14] T. W. Gorczyca, J.-E. Rubensson, C. Såthe, M. Ström, M. Agåker, D. Ding, S. Stranges, R. Richter, M. Alagia, Phys. Rev. Lett. **85**, 1202–1205 (2000)

[15] R. P. Madden, D. L. Ederer, K. Codling, Phys. Rev. **177**, 136–151 (1969)

[16] S. E. Canton-Rogan, A. A. Wills, T. W. Gorczyca, M. Wiedenhoeft, O. Nayandin, C.-N. Liu, N. Berrah, Phys. Rev. Lett. **85**, 3113–3116 (2000)

[17] K. Codling, R. P. Madden, D. L. Ederer, Phys. Rev. **155**, 26–37 (1967)

[18] F. Penent, P. Lablanquie, R. I. Hall, M. Žitnik, K. Bučar, S. Stranges, R. Richter, M. Alagia, P. Hammond, J. G. Lambourne, Phys. Rev. Lett. **86**, 2758–2761 (2001)

[19] C.-N. Liu, M.-K. Chen, C. D. Lin, Phys. Rev. A **64**, 010501 (2001)

[20] M. Žitnik, K. Bučar, M. Štuhec, F. Penent, R. I. Hall, P. Lablanquie, Phys. Rev. A **65**, 032520 (2002)

[21] J. G. Lambourne, F. Penent, P. Lablanquie, R. I. Hall, M. Ahmad, M. Žitnik, K. Bučar, P. Hammond, S. Stranges, R. Richter, M. Alagia, M. Coreno, J. Phys. B **36**, 4351–4359 (2003)

[22] K.-H. Schartner, B. Zimmermann, S. Kammer, S. Mickat, H. Schmoranzer, A. Ehresmann, H. Liebel, R. Follath, G. Reichardt, Phys. Rev. A **64**, 040501 (2001)

[23] S. Mickat, K.-H. Schartner, S. Kammer, R. Schill, L. Werner, S. Klumpp, A. Ehresmann, H. Schmoranzer, V. L. Sukhorukov, J. Phys. B **38**, 2613–2628 (2005)

[24] M. Coreno, K. C. Prince, R. Richter, M. de Simone, K. Bučar, M. Žitnik, Phys. Rev. A **72**, 052512 (2005)

[25] G. W. F. Drake, J. Kwela, A. van Wijngaarden, Phys. Rev. A **46**, 113–124 (1992)

[26] M. Žitnik, unpublished

[27] J. G. Lambourne, F. Penent, P. Lablanquie, R. I. Hall, M. Ahmad, M. Žitnik, K. Bučar, M. K. Odling-Smee, J. R. Harries, P. Hammond, D. K. Waterhouse, S. Stranges, R. Richter, M. Alagia, M. Coreno, M. Ferianis, Phys. Rev. Lett. **90**, 153004 (2003)

[28] F. Penent, J. G. Lambourne, P. Lablanquie, R. I. Hall, S. Aloise, M. Žitnik, K. Bučar, P. Hammond, AIP Conf. Proc. **697**, 151–157 (2003)

[29] J. R. Harries, J. P. Sullivan, Y. Azuma, J. Phys. B **37**, L169–L173 (2004)

[30] H. G. Berry, J. Desesquelles, M. Dufay, Phys. Rev. A **6**, 600–606 (1972)

[31] J. W. Cooper, E. B. Saloman, Phys. Rev. A **26**, 1452–1465 (1982)

[32] E. Luc-Koenig, A. Bachelier, Phys. Rev. Lett. **43**, 921–924 (1979)

[33] D. A. Harmin, Phys. Rev. A **24**, 2491–2512 (1981)

[34] J. S. Foster, Phys. Rev. **23**, 667–684 (1924)

[35] J. S. Foster, Proc. R. Soc. London **117**, 137–163 (1927)

[36] E. Schrödinger, Ann. Phys. (Leipzig) **80**, 437–490 (1926)

[37] L. Lipsky, R. Anania, M. J. Connely, At. Data Nucl. Data Tables **20**, 127–141 (1977)

[38] M.-K. Chen, Phys. Rev. A **56**, 4537–4544 (1997)

[39] B. Krässig, E. P. Kanter, S. H. Southworth, R. Guillemin, O. Hemmers, D. W. Lindle, R. Wehlitz, N. L. S. Martin, Phys. Rev. Lett. **88**, 203002 (2002)

[40] M. J. Brunger, O. Samardzic, A. S. Kheifets, E. Weigold, J. Phys. B **30**, 3267–3285 (1997)

[41] P. J. Hicks, J. Comer, J. Phys. B **8**, 1866–1879 (1975)

[42] K. T. Chung, T. K. Fang, Y. K. Ho, J. Phys. B **34**, 165–174 (2001)

[43] P. A. M. Gram, J. C. Pratt, M. A. Yates-Williams, H. C. Bryant, J. Donahue, H. Sharifian, H. Tootoonchi, Phys. Rev. Lett. **40**, 107–111 (1978)

[44] J. R. Harries, J. P. Sullivan, J. B. Sternberg, S. Obara, T. Suzuki, P. Hammond, J. Bozek, N. Berrah, M. Halka, Y. Azuma, Phys. Rev. Lett. **90**, 133002 (2003)

[45] X. M. Tong, C. D. Lin, Phys. Rev. Lett. **92**, 223003 (2004)

[46] I. A. Ivanov, Y. K. Ho, Phys. Rev. A **68**, 033410 (2003)

[47] K. C. Prince, M. Coreno, R. Richter, M. de Simone, V. Feyer, A. Kivimäki, A. Mihelič, M. Žitnik, Phys. Rev. Lett. **96**, 093001 (2006)

[48] M. Žitnik, unpublished

[49] C. Såthe, M. Ström, M. Agåker, J. Söderström, J.-E. Rubensson, R. Richter, M. Alagia, S. Stranges, T. W. Gorczyca, F. Robicheaux, Phys. Rev. Lett. **96**, 043002 (2006)

[50] J. C. Slater, *Quantum theory of atomic structure* (McGraw-Hill, New York, 1960)

[51] M. Kregar, Phys. Scr. **29**, 438–447 (1984)

[52] C. F. Fischer, T. Brage, P. Jönsson, *Computational Atomic Structure. An MCHF Approach* (Institute of Physics, Bristol, 1997)

[53] I. Lindgren, J. Morisson, *Atomic Many-Body Theory* (Springer, Berlin, 1982)

[54] J. Kokalj, *Electron-electron correlation in He*, Seminar II, Faculty of mathematics and physics, Univ. of Ljubljana (2005)

[55] E. A. Hylleraas, Z. Phys. **65**, 209–225 (1930)

[56] M. Žitnik, K. Bučar, Few-Body Systems Suppl. **14**, 175–178 (2003)

[57] D. R. Herrick, O. Sinanoğlu, Phys. Rev. A **11**, 97–110 (1975)

[58] L. I. Schiff, *Quantum mechanics* (McGraw-Hill, New York, 1968), 3rd ed.

[59] S. I. Nikitin, V. N. Ostrovsky, J. Phys. B **11**, 1681–1693 (1978)

[60] C. D. Lin, Phys. Rev. A **29**, 1019–1033 (1984)

[61] D. A. Telnov, J. Phys. B **22**, L399–L404 (1989)

[62] G. Alvarez, R. J. Damburg, H. J. Silverstone, Phys. Rev. A **44**, 3060–3082 (1991)

[63] J. M. Feagin, J. S. Briggs, Phys. Rev. Lett. **57**, 984–987 (1986)

[64] P. R. Woodruff, J. A. R. Samson, Phys. Rev. A **25**, 848–856 (1982)

[65] H. Jäger, Phys. Scr. **T 26**, 74–83 (1989)

[66] M. L. Zimmerman, M. G. Littman, M. M. Kash, D. Kleppner, Phys. Rev. A **20**, 2251–2275 (1979)

[67] R. Schumann, M. Dammasch, U. Eichmann, Y. Kriescher, G. Ritter, G. von Oppen, J. Phys. B **30**, 2581–2590 (1997)

[68] G. D. Stevens, C.-H. Iu, T. Bergeman, H. J. Metcalf, I. Seipp, K. T. Taylor, D. Delande, Phys. Rev. A **53**, 1349–1366 (1996)

[69] H. Rottke, K. H. Welge, Phys. Rev. A **33**, 301–311 (1986)

[70] H. C. Bryant, D. A. Clark, K. B. Butterfield, C. A. Frost, H. Sharifian, H. Tootoonchi, J. B. Donahue, P. A. M. Gram, M. E. Hamm, R. W. Hamm, J. C. Pratt, M. A. Yates, W. W. Smith, Phys. Rev. A **27**, 2889–2912 (1983)

[71] J. R. Harries, Y. Azuma, Rev. Sci. Instrum **75**, 4406–4412 (2004)

[72] F. Penent, unpublished

[73] K. C. Prince, et al., unpublished

[74] M. Žitnik, A. Mihelič, J. Phys. B **39**, L167–L174 (2006)

[75] D. M. Brink, G. R. Satchler, *Angular momentum* (Clarendon, Oxford, 1975), 2nd ed.

[76] K. G. Dyall, I. P. Grant, C. T. Johnson, F. A. Parpia, E. P. Plummer, Comput. Phys. Commun. **55**, 425–456 (1989)

[77] W. F. Perger, Z. Halabuka, D. Trautmann, Comput. Phys. Commun. **76**, 250–262 (1993)

[78] M. Rotenberg, Adv. At. Mol. Phys. **6**, 233–268 (1970)

[79] C. W. Clark, K. T. Taylor, J. Phys. B **15**, 1175–1193 (1982)

[80] M. Abramowitz, I. A. Stegun (eds.), *Handbook of Mathematical Functions* (Dover, New York, 1972)

[81] A. Bürgers, D. Wintgen, J.-M. Rost, J. Phys. B **28**, 3163–3183 (1995)

[82] G. Lagmago Kamta, B. Piraux, A. Scrinzi, Phys. Rev. A **63**, 040502 (2001)

[83] Y. K. Ho, Phys. Rep. **99**, 1–68 (1983)

[84] B. R. Junker, Adv. At. Mol. Phys. **18**, 207–263 (1982)

[85] W. P. Reinhardt, Ann. Rev. Phys. Chem. **33**, 223–255 (1982)

[86] N. Moiseyev, Phys. Rep. **302**, 211–293 (1998)

[87] A. Buchleitner, B. Grémaud, D. Delande, J. Phys. B **27**, 2663–2679 (1994)

[88] A. Bürgers, J.-M. Rost, J. Phys. B **29**, 3825–3839 (1996)

[89] Z. Bai, J. Demmel, J. Dongarra, A. Ruhe, H. van der Vorst (eds.), *Templates for the solution of Algebraic Eigenvalue Problems: A Practical Guide* (SIAM, Philadelphia, 2000)

[90] J. J. Sakurai, *Advanced quantum mechanics* (Addison-Wesley, Reading, Massachusetts, 1967)

[91] C. C. Gerry, P. L. Knight, *Introductory Quantum Optics* (Cambridge Univ., New York, 2005)

[92] R. Loudon, *The quantum theory of light* (Clarendon, Oxford, 1983), 2nd ed.

[93] P. Lambropoulos, P. Zoller, Phys. Rev. A **24**, 379–397 (1981)

[94] T. N. Rescigno, V. McKoy, Phys. Rev. A **12**, 522–525 (1975)

[95] U. Fano, Phys. Rev. **124**, 1866–1878 (1961)

[96] U. Fano, J. W. Cooper, Phys. Rev. **137**, A1364–A1379 (1965)

[97] F. Robicheaux, T. W. Gorczyca, M. S. Pindzola, N. R. Badnell, Phys. Rev. A **52**, 1319–1333 (1995)

[98] W. Greiner, J. Reinhardt, *Quatum Electrodynamics* (Springer, Berlin, 1992)

[99] G. S. Agarwal, S. L. Haan, J. Cooper, Phys. Rev. A **29**, 2552–2564 (1984)

[100] G. S. Agarwal, S. L. Haan, J. Cooper, Phys. Rev. A **29**, 2565–2577 (1984)

[101] S. Kilic, J.-P. Karr, L. Hilico, Phys. Rev. A **70**, 042506 (2004)

[102] E. Lindroth, J. Wallenius, S. Jonsell, Phys. Rev. A **68**, 032502 (2003)

[103] T. Grosges, B. Piraux, R. Shakeshaft, Phys. Rev. A **59**, 3088–3091 (1999)

[104] G. H. Golub, C. F. Van Loan, *Matrix Computations* (John Hopkins Univ., Baltimore, 1996), 3rd ed.

[105] G. Lagmago Kamta, private communication

[106] A. K. Bhatia, Y. K. Ho, J. Phys. B **31**, 3307–3319 (1998)

[107] P. J. Davis, *Interpolation and Approximation* (Dover, New York, 1975)

[108] *Mathematica 5.1*, Wolfram Research Inc., Champaign, Illinois (2004)

[109] E. Anderson, Z. Bai, C. Bischof, S. Blackford, J. Demmel, J. Dongarra, J. J. Du Croz, A. Greenbaum, S. Hammarling, A. McKenney, D. Sorensen, *LAPACK Users' Guide* (SIAM, Philadelphia, 1999), 3rd ed.

[110] T. K. Fang, K. T. Chung, J. Phys. B **34**, 1245–1259 (2001)

[111] J.-E. Rubensson, private communication

[112] K. C. Prince, unpublished

[113] P. J. Mohr, B. N. Taylor, Rev. Mod. Phys. **77**, 1 (2005)

[114] A. Filipponi, J. Phys. B **33**, 2835–2846 (2000)

[115] C. E. Theodosiou, At. Data Nucl. Data Tables **36**, 97–127 (1987)

[116] G. W. F. Drake, Phys. Rev. Lett. **65**, 2769–2772 (1990)

[117] G. W. F. Drake, Z.-C. Yan, Phys. Rev. A **46**, 2378–2409 (1992)

[118] M. Žitnik, A. Stanič, K. Bučar, J. G. Lambourne, F. Penent, R. I. Hall, P. Lablanquie, J. Phys. B **36**, 4175–4189 (2003)

[119] E. Lindroth, Phys. Rev. A **49**, 4473–4480 (1994)

[120] A. Scrinzi, B. Piraux, Phys. Rev. A **56**, R13–R16 (1997)

Appendix A

Atomic units

To present the results of the calculations in a clear and compact form, the physical quantities in this work are expressed in atomic units: their values in SI units are replaced by dimensionless quantities. Hartree atomic units are used ($e, \hbar, m = 1$, $4\pi\epsilon_0 = 1$, $c = 1/\alpha$, where e is the elementary charge, m the electron mass, ϵ_0 the vacuum permittivity, c the speed of light in vacuo, and α the fine structure constant).

Most commonly used atomic units expressed in SI units are listed in Table A.1.

quantity	symbol	numerical value	unit
a.u. of charge	e	$1.60217653(14) \times 10^{-19}$	As
a.u. of mass	m	$9.1093826(16) \times 10^{-31}$	kg
a.u. of action	$\hbar$	$1.05457168(18) \times 10^{-34}$	Js
		$3.13566743(35) \times 10^{-15}$	eV s
a.u. of length	$a_0 = \hbar/(\alpha\,mc)$	$0.5291772108(18) \times 10^{-10}$	m
a.u. of energy	$E_H = e^2/(4\pi\epsilon_0 a_0)$	$4.35974417(75) \times 10^{-18}$	J
		$27.2113845(23)$	eV
a.u. of time	$\hbar/E_H$	$2.418884326505(16) \times 10^{-17}$	s
a.u. of velocity (αc)	$a_0 E_H/\hbar$	$2.1876912633(73) \times 10^6$	m/s
a.u. of electric field	$E_H/(e\,a_0)$	$5.14220642(44) \times 10^{11}$	V/m
a.u. of magnetic flux density	$\hbar/(e\,a_0^2)$	$2.35051742(20) \times 10^5$	T

Table A.1: Atomic units expressed in SI units. The uncertainty of the last digits is shown in the parenthesis. The value of the fine structure constant is $\alpha = e^2/(4\pi\epsilon_0\,\hbar c) = 7.297352568(24) \times 10^{-3}$. All the values are taken from Ref. [113].

Appendix B

Matrix elements of the Hamilton operator in Sturmian basis

In this appendix, the expressions for matrix elements of the Hamilton operator in the basis of Coulomb Sturmian functions are derived. The total Hamiltonian H describing a two-electron atom with infinitely heavy point nucleus of charge Z in the homogeneous electric field $\boldsymbol{F}$ is written as

$$H = H_0 + \Delta H = T + U + V + \Delta H \tag{B.1}$$

with

$$
\begin{aligned}
T &= \frac{\boldsymbol{p}_1^2}{2} + \frac{\boldsymbol{p}_2^2}{2} = -\frac{\nabla_1^2}{2} - \frac{\nabla_2^2}{2}\,, \\
U &= -\frac{Z}{r_1} - \frac{Z}{r_2}\,, \\
V &= -\frac{1}{|\boldsymbol{r}_1 - \boldsymbol{r}_2|}\,, \qquad \text{and} \\
\Delta H &= -\boldsymbol{F} \cdot (\boldsymbol{r}_1 + \boldsymbol{r}_2)\,.
\end{aligned}
\tag{B.2}
$$

In the following, the matrix elements of individual terms and the elements describing the electric dipole transitions are derived.

B.1 Kinetic energy

Kinetic energy matrix elements $\langle \psi_{LMSM_S}^{knl\kappa\nu\lambda} | T | \psi_{LMSM_S}^{k'n'l'\kappa'\nu'\lambda'} \rangle$ are formed from the single particle kinetic energy operators by means of

$$T = -\frac{\nabla_1^2}{2} - \frac{\nabla_2^2}{2}\,. \tag{B.3}$$

The orbital integration and summation over the spin variables can readily be performed:

$$
\begin{aligned}
&\langle \Upsilon_{LMSM_S}^{l\lambda} | \Upsilon_{L'M'S'M_{S'}}^{l'\lambda'} \rangle \\
&= \sum_{\substack{m,\mu \\ m_s,\mu_s}} \sum_{\substack{m',\mu' \\ m_{s'},\mu_s'}} (lm\lambda\mu|LM)(1/2\,m_s 1/2\,\mu_s|SM_S)\, \langle lm|l'm'\rangle\langle m_s|m_{s'}\rangle\langle\lambda\mu|\lambda'\mu'\rangle\langle\mu_s|\mu_s'\rangle \\
&= \delta_{LL'}\delta_{MM'}\delta_{SS'}\delta_{M_S M_{S'}}\delta_{ll'}\delta_{\lambda\lambda'}\,.
\end{aligned}
\tag{B.4}
$$

113

The last equality follows from the well known orthogonality relations of spherical harmonics and spin functions,

$$\int d^2\hat{r}\, Y_{lm}^*(\hat{\boldsymbol{r}}) Y_{l'm'}(\hat{\boldsymbol{r}}) = \langle lm|l'm'\rangle = \delta_{ll'}\delta_{mm'}$$

$$\sum_\sigma \chi_{m_s}(\sigma)\chi_{m_{s'}}(\sigma) = \langle m_s|m_{s'}\rangle = \delta_{m_s m_{s'}}\,, \tag{B.5}$$

together with the reality and completeness relations of the Clebsch-Gordan coefficients [13, 53]. Since the kinetic energy operator is diagonal in quantum numbers $LMSM_S$, only diagonal matrix elements will be considered:

$$\langle \psi_{LMSM_S}^{knl\kappa\nu\lambda}|T|\psi_{LMSM_S}^{k'n'l'\kappa'\nu'\lambda'}\rangle =$$
$$\langle\!\langle knl;\kappa\nu\lambda|T|k'n'l;\kappa'\nu'\lambda\rangle\!\rangle \,\delta_{ll'}\delta_{\lambda\lambda'} + (-1)^{L+S+l+\lambda}\,\langle\!\langle \kappa\nu\lambda;knl|T|k'n'\lambda;\kappa'\nu'l\rangle\!\rangle \,\delta_{l\lambda'}\delta_{\lambda l'} \tag{B.6}$$
$$+ (-1)^{L+S+l+\lambda}\,\langle\!\langle knl;\kappa\nu\lambda|T|\kappa'\nu'l;k'n'\lambda\rangle\!\rangle \,\delta_{l\lambda'}\delta_{\lambda l'} + \langle\!\langle \kappa\nu\lambda;knl|T|\kappa'\nu'\lambda;k'n'l\rangle\!\rangle \,\delta_{ll'}\delta_{\lambda\lambda'}\,.$$

In Eq. (B.6), the double bra-ket notation $\langle\!\langle\ldots\rangle\!\rangle$ denotes the radial parts of the integrals. The expression can be simplified since radial integrals are symmetric with respect to the interchange $r_1 \leftrightarrow r_2$,

$$\langle\!\langle \psi_{LMSM_S}^{knl\kappa\nu\lambda}|T|\psi_{LMSM_S}^{k'n'l'\kappa'\nu'\lambda'}\rangle\!\rangle = 2\,\big[\langle\!\langle knl;\kappa\nu\lambda|T|k'n'l;\kappa'\nu'\lambda\rangle\!\rangle \,\delta_{ll'}\delta_{\lambda\lambda'}$$
$$+ (-1)^{L+S+l+\lambda}\,\langle\!\langle \kappa\nu\lambda;knl|T|k'n'\lambda;\kappa'\nu'l\rangle\!\rangle \,\delta_{l\lambda'}\delta_{\lambda l'}\big]\,. \tag{B.7}$$

The integrals in Eq. (B.7) are ($t = -\nabla^2/2$):

$$\langle\!\langle knl;\kappa\nu\lambda|T|k'n'l;\kappa'\nu'\lambda\rangle\!\rangle = \langle\!\langle knl|t|k'n'l\rangle\!\rangle\langle\!\langle \kappa\nu\lambda|\kappa'\nu'\lambda\rangle\!\rangle + \langle\!\langle knl|k'n'l\rangle\!\rangle\,\langle\!\langle \kappa\nu\lambda|t|\kappa'\nu'\lambda\rangle\!\rangle$$
$$\langle\!\langle \kappa\nu\lambda;knl|T|k'n'\lambda;\kappa'\nu'l\rangle\!\rangle = \langle\!\langle \kappa\nu\lambda|t|k'n'\lambda\rangle\!\rangle\,\langle\!\langle knl|\kappa'\nu'l\rangle\!\rangle + \langle\!\langle \kappa\nu\lambda|k'n'\lambda\rangle\!\rangle\,\langle\!\langle knl|t|\kappa'\nu'l\rangle\!\rangle\,, \tag{B.8}$$

where

$$\langle\!\langle k_a n_a l|k_b n_b l\rangle\!\rangle = \int_0^\infty dr\, S_{n_a l}^{k_a}(r)\, S_{n_b l}^{k_b}(r) \tag{B.9}$$

and

$$\langle\!\langle k_a n_a l|t|k_b n_b l\rangle\!\rangle = \langle\!\langle k_a n_a l|\left(-\frac{1}{2}\frac{d^2}{dr^2} + \frac{1}{2}\frac{l(l+1)}{r^2}\right)|k_b n_b l\rangle\!\rangle$$
$$= \langle\!\langle k_a n_a l|\left(\frac{n_b k_b}{r} - \frac{k_b^2}{2}\right)|k_b n_b l\rangle\!\rangle \tag{B.10}$$
$$= \int_0^\infty dr\, S_{n_a l}^{k_a}(r)\left(\frac{n_b k_b}{r} - \frac{k_b^2}{2}\right) S_{n_b l}^{k_b}(r)\,.$$

The last two lines in Eq. (B.10) follow from Eq. (4.2).

B.2   Potential energy

The treatment used for kinetic energy matrix elements is applicable to the nuclear potential energy operator if we define

$$U = -\frac{Z}{r_1} - \frac{Z}{r_2} \qquad \text{and} \qquad u = -Z/r \tag{B.11}$$

and make the replacements $T \to U$ and $t \to u$ in Eqs. (B.7) and (B.8):

$$\langle \psi_{LMSM_S}^{knl\kappa\nu\lambda}|U|\psi_{LMSM_S}^{k'n'l'\kappa'\nu'\lambda'}\rangle = 2\,\big[\langle\!\langle knl;\kappa\nu\lambda|U|k'n'l;\kappa'\nu'\lambda\rangle\!\rangle \,\delta_{ll'}\delta_{\lambda\lambda'}$$
$$+ (-1)^{L+S+l+\lambda}\,\langle\!\langle \kappa\nu\lambda;knl|U|k'n'\lambda;\kappa'\nu'l\rangle\!\rangle \,\delta_{l\lambda'}\delta_{\lambda l'}\big]\,. \tag{B.12}$$

The radial integrals in Eq. (B.12) are

$$\langle\!\langle knl;\kappa\nu\lambda|U|k'n'l;\kappa'\nu'\lambda\rangle\!\rangle = \langle\!\langle knl|u|k'n'l\rangle\!\rangle \langle\!\langle \kappa\nu\lambda|\kappa'\nu'\lambda\rangle\!\rangle + \langle\!\langle knl|k'n'l\rangle\!\rangle \langle\!\langle \kappa\nu\lambda|u|\kappa'\nu'\lambda\rangle\!\rangle$$
$$\langle\!\langle \kappa\nu\lambda;knl|U|k'n'\lambda;\kappa'\nu'l\rangle\!\rangle = \langle\!\langle \kappa\nu\lambda|u|k'n'\lambda\rangle\!\rangle \langle\!\langle knl|\kappa'\nu'l\rangle\!\rangle + \langle\!\langle \kappa\nu\lambda|k'n'\lambda\rangle\!\rangle \langle\!\langle knl|u|\kappa'\nu'l\rangle\!\rangle\,, \tag{B.13}$$

where

$$\langle\!\langle k_a n_a l|u|k_b n_b l\rangle\!\rangle = -\int_0^\infty \mathrm{d}r\, S_{n_a l}^{k_a}(r)\, \frac{Z}{r}\, S_{n_b l}^{k_b}(r)\,. \tag{B.14}$$

B.3   Electron-electron interaction

The electron-electron interaction term

$$V = \frac{1}{|\boldsymbol{r}_1 - \boldsymbol{r}_2|} = \frac{1}{r_{12}} \tag{B.15}$$

represents spin independent internal forces. Matrix elements are therefore diagonal in quantum numbers $LMSM_S$ [13, 53], and only diagonal matrix elements need to be considered:

$$\langle\psi_{LMSM_S}^{knl\kappa\nu\lambda}|V|\psi_{LMSM_S}^{k'n'l'\kappa'\nu'\lambda'}\rangle =$$
$$\left[1 + (-1)^{l+\lambda+l'+\lambda'}\right] \langle knl;\kappa\nu\lambda;LMSM_S|V|k'n'l';\kappa'\nu'\lambda';LMSM_S\rangle \tag{B.16}$$
$$+ \left[(-1)^{L+S+l+\lambda} + (-1)^{L+S+l'+\lambda'}\right] \langle \kappa\nu\lambda;knl;LMSM_S|V|k'n'l';\kappa'\nu'\lambda';LMSM_S\rangle\,.$$

As before, the symmetry of the integrals with respect to the $r_1 \leftrightarrow r_2$ interchange has been used. Angular parts of the integrals in Eq. (B.16) can be calculated if $|\boldsymbol{r}_1 - \boldsymbol{r}_2|^{-1}$ is expressed as a multipole series. The following relation is obtained as a result [13, 53]:

$$\langle k_a n_a l_a; k_b n_b l_b; LMSM_S|V|k_c n_c l_c; k_d n_d l_d; LMSM_S\rangle_c =$$
$$\sum_q R_{\mathrm{int}}^q(ab;cd)\,(-1)^{l_c+l_b+L} \begin{Bmatrix} l_a & l_b & L \\ l_d & l_c & q \end{Bmatrix} \langle l_a\|C^q\|l_c\rangle\langle l_b\|C^q\|l_d\rangle\,. \tag{B.17}$$

In Eq. (B.17) $R^q(ab;cd)$ denotes the Slater integral

$$R_{\mathrm{int}}^q(ab;cd) = \langle\!\langle k_a n_a l_a; k_b n_b l_b|r_<^q/r_>^{q+1}|k_c n_c l_c; k_d n_d l_d\rangle\!\rangle$$
$$= \int_0^\infty \mathrm{d}r_1 \int_0^\infty \mathrm{d}r_2\, S_{n_a l_a}^{k_a}(r_1) S_{n_b l_b}^{k_b}(r_2)\, \frac{r_<^q}{r_>^{q+1}}\, S_{n_c l_c}^{k_c}(r_1) S_{n_d l_d}^{k_d}(r_2)\,. \tag{B.18}$$

The notation $r_> = \max\{r_1,r_2\}$ and $r_< = \min\{r_1,r_2\}$ has been introduced for brevity. For fixed l_a, l_b, l_c, and l_d, the summation over q runs over those values for which the triangle relations for (l_a,q,l_c) and (l_b,q,l_d) are satisfied [13, 53], as can be seen from

$$\langle j_1\|C^q\|j_2\rangle = (-1)^{j_1}\sqrt{(2j_1+1)(2j_2+1)} \begin{pmatrix} j_1 & q & j_2 \\ 0 & 0 & 0 \end{pmatrix}\,. \tag{B.19}$$

The summation index q is therefore limited to the interval

$$\max\{|l_a - l_c|, |l_b - l_d|\} \le q \le \min\{l_a + l_c, l_b + l_d\}\,, \tag{B.20}$$

with $l_a + q + l_c$ and $l_b + q + l_d$ even [13, 53]. This, in turn, implies that the parity should be conserved,

$$(-1)^{l_a+l_c} = (-1)^{l_b+l_d} \qquad \text{and} \qquad (-1)^{l_a+l_b} = (-1)^{l_c+l_d}\,, \tag{B.21}$$

as expected from a scalar operator. Using this latter property, Eq. (B.16) becomes

$$
\begin{aligned}
\langle\psi_{LMSM_S}^{knl\kappa\nu\lambda}|V|\psi_{LMSM_S}^{k'n'l'\kappa'\nu'\lambda'}\rangle = \\
2\big[\langle knl;\kappa\nu\lambda;LMSM_S|r_{12}^{-1}|k'n'l';\kappa'\nu'\lambda';LMSM_S\rangle \\
+ (-1)^{L+S+l+\lambda}\langle\kappa\nu\lambda;knl;LMSM_S|r_{12}^{-1}|k'n'l';\kappa'\nu'\lambda';LMSM_S\rangle\big]\,.
\end{aligned}
\tag{B.22}
$$

B.4 Overlap matrix elements

Overlap matrix elements are treated in a similar manner as the kinetic energy or the potential energy matrix elements. An expression similar to Eq. (B.7) is obtained:

$$
\begin{aligned}
\langle\psi_{LMSM_S}^{knl\kappa\nu\lambda}|\psi_{LMSM_S}^{k'n'l'\kappa'\nu'\lambda'}\rangle = 2\big[\langle\!\langle knl|k'n'l'\rangle\!\rangle\langle\!\langle\kappa\nu\lambda|\kappa'\nu'\lambda'\rangle\!\rangle\,\delta_{ll'}\delta_{\lambda\lambda'} \\
+ (-1)^{L+S+l+\lambda}\langle\!\langle\kappa\nu\lambda|k'n'l'\rangle\!\rangle\langle\!\langle knl|\kappa'\nu'\lambda'\rangle\!\rangle\,\delta_{l\lambda'}\delta_{l'\lambda}\big]\,.
\end{aligned}
\tag{B.23}
$$

B.5 Spherical dipole operator

Matrix elements describing the interaction between an atom and an externally applied homogeneous electric field or dipole transitions between atomic states in the length approximation are expressed by means of the spherical dipole operator

$$
\mathcal{D}_q = r_1 C_q^1(\hat{\boldsymbol r}_1) + r_2 C_q^1(\hat{\boldsymbol r}_2)\,.
\tag{B.24}
$$

The operator $\mathcal{D}_q$ is spin independent, therefore its matrix elements are diagonal in quantum numbers S and M_S. For $S = S'$ and $M_S = M_{S'}$, the matrix element equals to

$$
\begin{aligned}
\langle\psi_{LMSM_S}^{knl\kappa\nu\lambda}|\mathcal{D}_q|\psi_{L'M'SM_S}^{k'n'l'\kappa'\nu'\lambda'}\rangle = \langle knl;\kappa\nu\lambda;LMSM_S|\mathcal{D}_q|k'n'l';\kappa'\nu'\lambda';L'M'SM_S\rangle \\
+ (-1)^{L+S+l+\lambda}\langle\kappa\nu\lambda;knl;LMSM_S|\mathcal{D}_q|k'n'l';\kappa'\nu'\lambda';L'M'SM_S\rangle \\
+ (-1)^{L'+S+l'+\lambda'}\langle knl;\kappa\nu\lambda;LMSM_S|\mathcal{D}_q|\kappa'\nu'\lambda';k'n'l';L'M'SM_S\rangle \\
+ (-1)^{L+l+\lambda+L'+l'+\lambda'}\langle\kappa\nu\lambda;knl;LMSM_S|\mathcal{D}_q|\kappa'\nu'\lambda';k'n'l';L'M'SM_S\rangle\,.
\end{aligned}
\tag{B.25}
$$

To simplify Eq. (B.25), the integration variables $\boldsymbol r_1$ and $\boldsymbol r_2$ are interchanged. This results in additional phase factors in the angular parts due to the properties of the Clebsch-Gordan coefficients,

$$
\begin{aligned}
\langle\psi_{LMSM_S}^{knl\kappa\nu\lambda}|\mathcal{D}_q|\psi_{L'M'SM_S}^{k'n'l'\kappa'\nu'\lambda'}\rangle = \\
2\bigg[\langle\!\langle knl;\kappa\nu\lambda|r_1|k'n'l';\kappa'\nu'\lambda'\rangle\!\rangle\langle\Upsilon_{LMSM_S}^{l\lambda}|C_q^1(\hat{\boldsymbol r}_1)|\Upsilon_{L'M'SM_S}^{l'\lambda'}\rangle \\
+ (-1)^{L+L'+l+l'+\lambda+\lambda'}\langle\!\langle\kappa\nu\lambda;knl|r_1|\kappa'\nu'\lambda';k'n'l'\rangle\!\rangle\langle\Upsilon_{LMSM_S}^{\lambda l}|C_q^1(\hat{\boldsymbol r}_1)|\Upsilon_{L'M'SM_S}^{\lambda'l'}\rangle \\
+ (-1)^{l+\lambda+L+S}\langle\!\langle\kappa\nu\lambda;knl|r_1|k'n'l';\kappa'\nu'\lambda'\rangle\!\rangle\langle\Upsilon_{LMSM_S}^{\lambda l}|C_q^1(\hat{\boldsymbol r}_1)|\Upsilon_{L'M'SM_S}^{l'\lambda'}\rangle \\
+ (-1)^{l'+\lambda'+L'+S}\langle\!\langle knl;\kappa\nu\lambda|r_1|\kappa'\nu'\lambda';k'n'l'\rangle\!\rangle\langle\Upsilon_{LMSM_S}^{l\lambda}|C_q^1(\hat{\boldsymbol r}_1)|\Upsilon_{L'M'SM_S}^{\lambda'l'}\rangle\bigg]\,,
\end{aligned}
\tag{B.26}
$$

where

$$
\langle\Upsilon_{LMSM_S}^{l\lambda}|C_q^1(\hat{\boldsymbol r}_2)|\Upsilon_{L'M'SM_S}^{l'\lambda'}\rangle = (-1)^{l+\lambda+l'+\lambda'-L-L'}\langle\Upsilon_{LMSM_S}^{\lambda l}|C_q^1(\hat{\boldsymbol r}_1)|\Upsilon_{L'M'SM_S}^{\lambda'l'}\rangle
\tag{B.27}
$$

has been used. The radial integrals in Eq. (B.26) are

$$
\langle\!\langle k_a n_a l_a; k_b n_b l_b|r_1|k_c n_c l_c; k_d n_d l_d\rangle\!\rangle = \langle\!\langle k_a n_a l_a|r|k_c n_c l_c\rangle\!\rangle\langle\!\langle k_b n_b l_b|k_d n_d l_d\rangle\!\rangle
\tag{B.28}
$$

with

$$\langle\langle k_a n_a l_a | r | k_c n_c l_c \rangle\rangle = \int_0^\infty \mathrm{d}r \, S_{n_a l_a}^{k_a}(r) \, r \, S_{n_c l_c}^{k_c}(r) \,. \tag{B.29}$$

The angular integration can be performed analytically. As can be seen, the angular parts have the form

$$\langle \Upsilon_{LMSM_S}^{l\lambda} | C_q^p(\hat{\boldsymbol{r}}_1) | \Upsilon_{L'M'SM_S}^{l'\lambda'} \rangle = \delta_{\lambda\lambda'} \sum_{m,m',\mu} (lm\lambda\mu | LM)\,(l'm'\lambda\mu | L'M')\,\langle lm | C_q^p | l'm' \rangle \,. \tag{B.30}$$

With the help of the known relations between the Clebsch-Gordan coefficients and 3-j symbols [13, 53]

$$(j_1 m_1 j_2 m_2 | jm) = (-1)^{j_1 - j_2 + m} \sqrt{2j+1} \begin{pmatrix} j_1 & j_2 & j \\ m_1 & m_2 & -m \end{pmatrix} \,, \tag{B.31}$$

the Wigner-Eckart theorem

$$\langle j_1 m_1 | C_q^p | j_2 m_2 \rangle = (-1)^{j_1 - m_1} \begin{pmatrix} j_1 & p & j_2 \\ -m_1 & q & m_2 \end{pmatrix} \langle j_1 \| C^p \| j_2 \rangle \,, \tag{B.32}$$

and summation formula taken from Ref. [75]

$$\sum_{m,m',\mu} (-1)^{L'-l-q-\mu} \begin{pmatrix} p & l' & l \\ q & m' & -m \end{pmatrix} \begin{pmatrix} \lambda & L & l \\ \mu & -M & m \end{pmatrix} \begin{pmatrix} l' & \lambda & L' \\ m' & \mu & -M' \end{pmatrix} =$$

$$(-1)^{p+l'+L+\lambda} \begin{Bmatrix} p & l' & l \\ \lambda & L & L' \end{Bmatrix} \begin{pmatrix} L & p & L' \\ -M & q & M' \end{pmatrix} \,, \tag{B.33}$$

Eq. (B.30) reduces to

$$\langle \Upsilon_{LMSM_S}^{l\lambda} | C_q^p(\hat{\boldsymbol{r}}_1) | \Upsilon_{L'M'SM_S}^{l'\lambda'} \rangle = \delta_{\lambda\lambda'} (-1)^{p+l+\lambda+L+L'+M} \,.$$

$$\cdot \sqrt{(2L+1)(2L'+1)} \, \langle l \| C^p \| l' \rangle \begin{pmatrix} L & p & L' \\ -M & q & M' \end{pmatrix} \begin{Bmatrix} p & l' & l \\ \lambda & L & L' \end{Bmatrix} \,. \tag{B.34}$$

It follows from Eq. (B.34) that the total matrix element $\langle \psi_{LMSM_S}^{knl\kappa\nu\lambda} | \mathcal{D}_q | \psi_{L'M'SM_S}^{k'n'l'\kappa'\nu'\lambda'} \rangle$ is proportional to

$$(-1)^{L-M} \begin{pmatrix} L & 1 & L' \\ -M & q & M' \end{pmatrix} \,, \tag{B.35}$$

in agreement with the Wigner-Eckart theorem. The reduced matrix element

$$\langle \psi_{LS}^{knl\kappa\nu\lambda} \| \mathcal{D} \| \psi_{L'S}^{k'n'l'\kappa'\nu'\lambda'} \rangle \tag{B.36}$$

is therefore obtained from Eq. (B.26) if the angular matrix elements are replaced with the suitable reduced matrix elements,

$$\langle \Upsilon_{LMSM_S}^{l\lambda} | C_q^1(\hat{\boldsymbol{r}}_1) | \Upsilon_{L'M'SM_S}^{l'\lambda'} \rangle \quad \longrightarrow \quad \langle \Upsilon_{LS}^{l\lambda} \| C^1(\hat{\boldsymbol{r}}_1) \| \Upsilon_{L'S}^{l'\lambda'} \rangle \,, \tag{B.37}$$

where

$$\langle \Upsilon_{LS}^{l\lambda} \| C^p(\hat{\boldsymbol{r}}_1) \| \Upsilon_{L'S}^{l'\lambda'} \rangle = \delta_{\lambda\lambda'} (-1)^{p+l+\lambda+L'} \,.$$

$$\cdot \sqrt{(2L+1)(2L'+1)} \, \langle l \| C^p \| l' \rangle \begin{Bmatrix} p & l' & l \\ \lambda & L & L' \end{Bmatrix} \,. \tag{B.38}$$

The Wigner-Eckart theorem can now be used to calculate the total matrix element:

$$\langle\psi_{LMSM_S}^{knl\kappa\nu\lambda}|\mathcal{D}_q|\psi_{L'M'SM_S}^{k'n'l'\kappa'\nu'\lambda'}\rangle = (-1)^{L-M}\begin{pmatrix} L & 1 & L' \\ -M & q & M' \end{pmatrix}\langle\psi_{LS}^{knl\kappa\nu\lambda}\|\mathcal{D}\|\psi_{L'S'}^{k'n'l'\kappa'\nu'\lambda'}\rangle. \quad \text{(B.39)}$$

An important property of the reduced matrix elements follows from Eqs. (B.19), (B.38), and the properties of the 3-j and 6-j symbols:[1]

$$\langle\psi_{LS}^{knl\kappa\nu\lambda}\|\mathcal{D}\|\psi_{L'S}^{k'n'l'\kappa'\nu'\lambda'}\rangle = (-1)^{L'+L}\langle\psi_{L'S}^{k'n'l'\kappa'\nu'\lambda'}\|\mathcal{D}\|\psi_{LS}^{knl\kappa\nu\lambda}\rangle. \quad \text{(B.40)}$$

B.6 Electric field interaction

The atom-field interaction for the homogeneous electric field $\boldsymbol{F}$ is

$$\Delta H = -\boldsymbol{F}\cdot\boldsymbol{r}_1 - \boldsymbol{F}\cdot\boldsymbol{r}_2. \quad \text{(B.41)}$$

The electric field may be chosen to point along the z axis, thus the interaction term simplifies to

$$\Delta H = -F\,\mathcal{D}_0 \qquad (\text{for } \boldsymbol{F}\parallel\hat{\boldsymbol{z}}). \quad \text{(B.42)}$$

For the latter particular orientation of the electric field vector, selection rules can easily be derived from the properties of the 3-j and 6-j symbols: a non-vanishing coupling matrix element

$$\langle\psi_{LMSM_S}^{knl\kappa\nu\lambda}|\Delta H|\psi_{L'M'SM_S}^{k'n'l'\kappa'\nu'\lambda'}\rangle = -F\,(-1)^{L-M}\begin{pmatrix} L & 1 & L' \\ -M & 0 & M' \end{pmatrix}\langle\psi_{LS}^{knl\kappa\nu\lambda}\|\mathcal{D}\|\psi_{L'S'}^{k'n'l'\kappa'\nu'\lambda'}\rangle, \quad \text{(B.43)}$$

is obtained for

$$\begin{aligned} (-1)^{l+\lambda} &= (-1)^{l'+\lambda'+1}, & \text{(parity change)} \\ |L-L'| &\leq 1 \text{ and } L+L' \geq 1, & \text{(triangular relation with } 0\to 0 \text{ forbidden)} \\ M &= M'. \end{aligned} \quad \text{(B.44)}$$

B.7 Dipole transition operator

The dipole transition operator in the length form describing linearly polarised light with polarisation vector $\hat{\boldsymbol{e}}$ is proportional to

$$\begin{aligned} D(\hat{\boldsymbol{e}}) = \hat{\boldsymbol{e}}\cdot(\boldsymbol{r}_1+\boldsymbol{r}_2) &= r_1\sum_{q=-1}^{1}(-1)^q\epsilon_{-q}C_q^1(\hat{\boldsymbol{r}}_1) + r_2\sum_{q=-1}^{1}(-1)^q\epsilon_{-q}C_q^1(\hat{\boldsymbol{r}}_2) \\ &= \sum_{q=-1}^{1}(-1)^q\epsilon_{-q}\mathcal{D}_q, \end{aligned} \quad \text{(B.45)}$$

where $\hat{\boldsymbol{e}}$ has been decomposed into spherical tensor components ϵ_q as

$$\epsilon_0 = e_z \qquad \text{and} \qquad \epsilon_{\pm 1} = \mp\frac{e_x\pm ie_y}{\sqrt{2}}. \quad \text{(B.46)}$$

The result for matrix elements of $D(\hat{\boldsymbol{e}})$ then follows directly from Eq. (B.39):

$$\langle\psi_{LMSM_S}^{knl\kappa\nu\lambda}|D(\hat{\boldsymbol{e}})|\psi_{L'M'SM_S}^{k'n'l'\kappa'\nu'\lambda'}\rangle =$$

$$(-1)^{L-M}\langle\psi_{LS}^{knl\kappa\nu\lambda}\|\mathcal{D}\|\psi_{L'S'}^{k'n'l'\kappa'\nu'\lambda'}\rangle\sum_{q=-1}^{1}(-1)^q\epsilon_{-q}\begin{pmatrix} L & 1 & L' \\ -M & q & M' \end{pmatrix}. \quad \text{(B.47)}$$

---

[1] See also Brink and Satchler [75], pg. 61. Note that a different definition of reduced matrix elements is used in Ref. [75].

B.8   Reduced dipole matrix element of complex dilatated states

Reduced dipole matrix elements between the eigenstates of the complex scaled free atom Hamiltonian $H_0(\Theta)$ are obtained by means of Eq. (4.32) and from the known reduced matrix elements of the Sturmian basis states:

$$\langle \overline{\Psi_{i\Theta}} \| \mathcal{D}_\Theta \| \Psi_{n\Theta} \rangle = e^{i\Theta} \sum_{\beta,\gamma} x_{i,\beta} \langle \psi_\beta \| \mathcal{D} \| \psi_\gamma \rangle x_{n,\gamma} \,. \tag{B.48}$$

The indices β and γ are used to denote the quantum numbers of the Sturmian basis states $|\psi_\beta\rangle$ and $|\psi_\gamma\rangle$, respectively. The fact that $\mathcal{D}_q(\Theta) = e^{i\Theta}\mathcal{D}_q$ has been used. Since matrix elements of complex dilatated Hermitian operators are symmetric in the basis of real Sturmian functions, an equality similar to (B.40) also applies for complex scaled states,

$$\langle \overline{\Psi_{n\Theta}} \| \mathcal{D}_\Theta \| \Psi_{i\Theta} \rangle = (-1)^{L_n+L_i} \langle \overline{\Psi_{i\Theta}} \| \mathcal{D}_\Theta \| \Psi_{n\Theta} \rangle \,, \tag{B.49}$$

as can be shown by using Eq. (B.40) by noting that for non zero expansion coefficients $x_{i,\beta}$ and $x_{n,\gamma}$ $L_\beta = L_i$ and $L_\gamma = L_n$.

B.9   Dipole matrix elements in electric field

To calculate dipole matrix element between complex dilatated eigenstates $|\Phi_{n\Theta}\rangle$ and $|\Phi_{g\Theta}\rangle$ of the total Hamilton operator $H(\Theta)$,

$$\langle \overline{\Phi_{n\Theta}} | D_\Theta(\hat{e}) | \Phi_{g\Theta} \rangle \,, \tag{B.50}$$

the state vectors are expanded in the basis of the field free eigenstates [cf. Eq. (4.42)],

$$|\Phi_{g\Theta}\rangle = \sum_i y_{g,i} |\Psi_{i\Theta}\rangle \qquad \text{and} \qquad |\Phi_{n\Theta}\rangle = \sum_j y_{n,j} |\Psi_{j\Theta}\rangle \,. \tag{B.51}$$

From Eq. (B.51), it follows that

$$\begin{aligned}
\langle \overline{\Phi_{n\Theta}} | D_\Theta(\hat{e}) | \Phi_{g\Theta} \rangle &= \sum_{i,j} y_{n,j} y_{g,i} \langle \overline{\Psi_{j\Theta}} | D_\Theta(\hat{e}) | \Psi_{i\Theta} \rangle \\
&= \sum_q \sum_{i,j} y_{n,j} y_{g,i} (-1)^q \epsilon_{-q} \langle \overline{\Psi_{j\Theta}} | R(\Theta) \mathcal{D}_q R(-\Theta) | \Psi_{i\Theta} \rangle \\
&\equiv \sum_q (-1)^q \epsilon_{-q} \mathbf{y}_n^{\mathsf{T}} \mathbf{D}_q \, \mathbf{y}_g \\
&= \sum_q \sum_{i,j} y_{n,j} y_{g,i} (-1)^q \epsilon_{-q} (-1)^{L_j-M_j} \begin{pmatrix} L_j & 1 & L_i \\ -M_j & q & M_i \end{pmatrix} \langle \overline{\Psi_{i\Theta}} \| \mathcal{D}_\Theta \| \Psi_{j\Theta} \rangle \,,
\end{aligned} \tag{B.52}$$

where the decomposition (B.45) has been used. In Eq. (B.52), $\mathbf{D}_q$ denotes the matrix representation of $R(\Theta)\mathcal{D}_q R(-\Theta)$ in the basis of field free complex scaled eigenstates, whereas column vectors $\mathbf{y}_g$ and $\mathbf{y}_n$ are used for the expansion (B.51).

If the electric field is applied along the z axis, field induced mixing of the field free states is present only among states with equal magnetic quantum numbers. This means that $M_g = M_i$ and $M_n = M_j$ for all the terms in Eq. (B.51). Therefore, a single term with $q = M_n - M_g$ in the sum over q is nonzero in Eq. (B.52).

For the case $\boldsymbol{F} \parallel \hat{\boldsymbol{z}}$, a simple expression is obtained for the square of the complex scaled matrix element [Eq. (4.102)]. Since $\epsilon_q^* = (-1)^q \epsilon_{-q}$, it follows that

$$
\begin{aligned}
\langle \overline{\Phi_{n\Theta}} | D_\Theta(\hat{\boldsymbol{e}}) | \Phi_{g\Theta} \rangle^2 &= \langle \overline{\Phi_{g\Theta}} | D_\Theta(\hat{\boldsymbol{e}}) | \Phi_{n\Theta} \rangle \langle \overline{\Phi_{n\Theta}} | D_\Theta(\hat{\boldsymbol{e}}) | \Phi_{g\Theta} \rangle \\
&= (-1)^{M_g - M_n} \epsilon_{-M_g + M_n} (-1)^{M_n - M_g} \epsilon_{-M_n + M_g} \left(\mathbf{y}_g^\mathsf{T} \, \boldsymbol{\mathcal{D}}_{M_g - M_n} \, \mathbf{y}_n \right) \left(\mathbf{y}_n^\mathsf{T} \, \boldsymbol{\mathcal{D}}_{M_n - M_g} \, \mathbf{y}_g \right) \\
&= (-1)^{M_g - M_n} |\epsilon_{M_g - M_n}|^2 \left(\mathbf{y}_g^\mathsf{T} \, \boldsymbol{\mathcal{D}}_{M_g - M_n} \, \mathbf{y}_n \right) \left(\mathbf{y}_n^\mathsf{T} \, \boldsymbol{\mathcal{D}}_{M_n - M_g} \, \mathbf{y}_g \right) .
\end{aligned}
\tag{B.53}
$$

Appendix C

Angular integration for the field free spontaneous emission

The angular integration in the spontaneous photon emission rate equation [Eq. (4.97)],

$$\gamma_n \approx \frac{\alpha^3}{2\pi} \sum_\beta \sum_i \int \mathrm{d}^2\hat{k} \, (E_n - E_i)^3 \langle \Psi_i | D(\hat{e}_\beta) | \Psi_n \rangle^2 \,, \tag{C.1}$$

can be performed as follows. If the direction of the emitted photon is parameterised as (Fig. C.1),
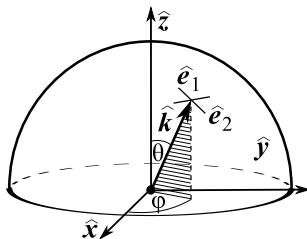
Figure C.1: Photon emission in the direction $\hat{k}$: $\hat{e}_1$ and $\hat{e}_2$ are two mutually orthogonal polarisation vectors.

$$\hat{k} \equiv \hat{e}_r = \hat{x} \sin\theta \cos\phi + \hat{y} \sin\theta \sin\phi + \hat{z} \cos\theta \,, \tag{C.2}$$

where θ and ϕ are the usual spherical polar coordinates, the polarisation vectors $\hat{e}_\beta$, $\beta = 1, 2$, may be chosen as

$$\hat{e}_1 \equiv \hat{e}_\theta = \frac{\partial \hat{e}_r}{\partial \theta}$$
$$\hat{e}_2 \equiv \hat{e}_\phi = \frac{1}{\sin\theta} \frac{\partial \hat{e}_r}{\partial \phi} \,. \tag{C.3}$$

The dipole operator $D(\hat{e}_\beta)$ can be written as [cf. Eq. (B.45)]

$$D(\hat{e}_\beta) = \sum_{q=-1}^{1} (-1)^q \epsilon_{-q}^\beta \mathcal{D}_q \,, \tag{C.4}$$

where

$$\epsilon_q^1(\theta, \phi) = \frac{\partial C_q^1(\theta, \phi)}{\partial \theta} \qquad \text{and} \qquad \epsilon_q^2(\theta, \phi) = \frac{1}{\sin\theta} \frac{\partial C_q^1(\theta, \phi)}{\partial \phi} \,. \tag{C.5}$$

Since $|\Psi_{i\Theta}\rangle$ and $|\Psi_{n\Theta}\rangle$ are characterised by the orbital quantum numbers L_i and L_n in the absence of the external field, we can apply the Wigner-Eckart theorem to obtain

$$
\begin{aligned}
&\langle\overline{\Psi_{i\Theta}}|D_\Theta(\hat{\boldsymbol{e}}_\beta)|\Psi_{n\Theta}\rangle^2 \\
&= \langle\overline{\Psi_{n\Theta}}|D_\Theta(\hat{\boldsymbol{e}}_\beta)|\Psi_{i\Theta}\rangle\langle\overline{\Psi_{i\Theta}}|D_\Theta(\hat{\boldsymbol{e}}_\beta)|\Psi_{n\Theta}\rangle \\
&= \left[\sum_q(-1)^q\epsilon^\beta_{-q}(-1)^{L_n-M_n}\begin{pmatrix} L_n & 1 & L_i \\ -M_n & q & M_i \end{pmatrix}\right]\left[\sum_{q'}(-1)^{q'}\epsilon^\beta_{-q'}(-1)^{L_i-M_i}\begin{pmatrix} L_i & 1 & L_n \\ -M_i & q' & M_n \end{pmatrix}\right] \\
&\quad\cdot \langle\overline{\Psi_{n\Theta}}\|\mathcal{D}_\Theta\|\Psi_{i\Theta}\rangle\langle\overline{\Psi_{i\Theta}}\|\mathcal{D}_\Theta\|\Psi_{n\Theta}\rangle\,.
\end{aligned}
$$
(C.6)

The 3-j symbol in the first pair of brackets can be rewritten as [75]

$$
\begin{aligned}
\begin{pmatrix} L_n & 1 & L_i \\ -M_n & q & M_i \end{pmatrix} &= (-1)^{L_n+1+L_i}\begin{pmatrix} L_n & 1 & L_i \\ M_n & -q & -M_i \end{pmatrix} \\
&= \begin{pmatrix} L_i & 1 & L_n \\ -M_i & -q & M_n \end{pmatrix}\,,
\end{aligned}
$$
(C.7)

and the summation index q replaced by $-q$. The resulting sums over q and q' both have only a single non vanishing term ($q = q' = M_i - M_n$), and can be replaced by a single sum

$$
\begin{aligned}
&\langle\overline{\Psi_{i\Theta}}|D_\Theta(\hat{\boldsymbol{e}}_\beta)|\Psi_{n\Theta}\rangle^2 \\
&= \left[\sum_q(-1)^{-q}\epsilon^\beta_q(-1)^{L_n-M_n}\begin{pmatrix} L_i & 1 & L_n \\ -M_i & q & M_n \end{pmatrix}(-1)^q\epsilon^\beta_{-q}(-1)^{L_i-M_i}\begin{pmatrix} L_i & 1 & L_n \\ -M_i & q & M_n \end{pmatrix}\right] \\
&\quad\cdot \langle\overline{\Psi_{n\Theta}}\|\mathcal{D}_\Theta\|\Psi_{i\Theta}\rangle\langle\overline{\Psi_{i\Theta}}\|\mathcal{D}_\Theta\|\Psi_{n\Theta}\rangle\,.
\end{aligned}
$$
(C.8)

Since $\epsilon^{\beta*}_q = (-1)^q\epsilon^\beta_{-q}$ and for the non zero term of the sum $q = M_i - M_n$, it follows that

$$
\begin{aligned}
&\langle\overline{\Psi_{i\Theta}}|D_\Theta(\hat{\boldsymbol{e}}_\beta)|\Psi_{n\Theta}\rangle^2 \\
&= \left[\sum_q|\epsilon^\beta_q|^2(-1)^{L_n+L_i}\begin{pmatrix} L_i & 1 & L_n \\ -M_i & q & M_n \end{pmatrix}\begin{pmatrix} L_i & 1 & L_n \\ -M_i & q & M_n \end{pmatrix}\right]\cdot \\
&\quad\cdot \langle\overline{\Psi_{n\Theta}}\|\mathcal{D}_\Theta\|\Psi_{i\Theta}\rangle\langle\overline{\Psi_{i\Theta}}\|\mathcal{D}_\Theta\|\Psi_{n\Theta}\rangle\,.
\end{aligned}
$$
(C.9)

The summation over q can now be interchanged with the integration over the possible directions of the emitted photon and the summation over β. It turns out that

$$
\sum_\beta\int\mathrm{d}^2\hat{k}\,|\epsilon^\beta_q|^2 = \frac{8\pi}{3} \qquad \text{for } q = 0, \pm 1\,.
$$
(C.10)

To further simplify the radiation width formula, the sum over the final quantum states is decomposed as

$$
\sum_i = {\sum_i}'\sum_{M_i}\,,
$$
(C.11)

where the prime denotes the summation over all quantum numbers *except* M_i. After summing over all possible magnetic quantum numbers and taking into account that the energy E_i is independent of M_i for the field free eigenvectors [13], the completeness relation for the 3-j symbols is used. One finally obtains

$$
\gamma_n = \frac{4\alpha^3}{3(2L_n+1)}\sum_{\substack{i,\pi_i\neq\pi_n \\ \Delta(L_i,1,L_n)\neq 0}}' (E_n - E_i)^3\,\mathrm{Re}\,\langle\overline{\Psi_{i\Theta}}\|\mathcal{D}_\Theta\|\Psi_{n\Theta}\rangle^2\,.
$$
(C.12)

In the derivation of Eq. (C.12), Eq. (B.49) has been used to simplify the product of reduced matrix elements. Only those final states are considered in Eq. (C.12) for which the triangular relation

$$|L_i - L_n| \leq 1 \leq L_i + L_n \tag{C.13}$$

holds and for which the parities of the initial and final states differ. This has been written symbolically as $\Delta(L_n, 1, L_i) \neq 0$ and $\pi_i \neq \pi_n$.

Appendix D

Convolution of calculated spectra

To be comparable to the measured spectra, the calculated photoionisation and inelastic scattering cross section should be broadened by the instrumental function of the experimental apparatus. Very often, the instrumental function is well described by a Gaussian,

$$g_\sigma(E) = \frac{1}{\sqrt{2\pi}\sigma} \exp\left(-\frac{E^2}{2\sigma^2}\right),$$ (D.1)

with FWHM equal to $2\sqrt{2\ln 2}\,\sigma \approx 2.35482\,\sigma$. Although only the convolution with a Gaussian distribution will be considered here, the results of this appendix are general and straightforward to implement for an arbitrary instrumental function.

To save space, the theoretical spectra are not evenly spaced in energy: the sampling step is more dense in the regions of narrow resonances. The direct convolution in this case results in spurious oscillatory behaviour near the energies where the step is changed. Furthermore, for the convolution in the conjugate space, the FFT algorithm cannot be used since it requires a constant sampling step. The trivial solution of this problem would be to interpolate the data to equidistant spacing and to convolve the spectra using FFT. This, however, results in the spectra with a large number of points, and one is left with the possibility to join several smaller regions of the spectrum that have previously been convolved separately.

Another approach was used by Filipponi [114] in a different context of deconvolution of measured absorption spectra. Similar approach is used here to simulate the experimental broadening of the theoretical spectrum. In the following, the formulae for the convolution of the calculated theoretical spectra with a Gaussian are derived.

Let $\beta(E)$ denote a real integrable function. Its Fourier transform is defined by

$$\tilde{\beta}(q) = \mathcal{F}(\beta) = \int_{-\infty}^{\infty} e^{iqE}\beta(E)\mathrm{d}E.$$ (D.2)

If $\beta(E)$ is tabulated on a finite interval represented by N points $\beta(E_j)$, $j = 0, \ldots, N-1$, the Fourier transform $\tilde{\beta}(q)$ can be approximated by

$$\tilde{\beta}(q) \approx \sum_{j=0}^{N-2} \int_{E_j}^{E_{j+1}} e^{iqE}\beta(E)\mathrm{d}E \equiv \sum_{j=0}^{N-2} I_j.$$ (D.3)

To eliminate the oscillations resulting from the use of non-equidistant energy mesh, the integrand

$\beta(E)$ is expanded to the second order,

$$
\begin{aligned}
I_j &= \int_{E_j}^{E_{j+1}} e^{iqE} \left(\beta_0^j + \beta_1^j (E - E_c^j) + \frac{\beta_2^j}{2}(E - E_c^j)^2 \right) dE \\
&= e^{iqE_c^j} \int_{-\Delta_j/2}^{\Delta_j/2} e^{iqx} \left(\beta_0^j + \beta_1^j x + \frac{\beta_2^j}{2} x^2 \right) dx \,,
\end{aligned}
\tag{D.4}
$$

where the notation

$$
\Delta_j = E_{j+1} - E_j \qquad \text{and} \qquad E_c^j = \frac{E_{j+1} + E_j}{2} \,,
\tag{D.5}
$$

and

$$
\beta_0^j = \beta(E_c^j) \,, \qquad \beta_1^j = \beta'(E_c^j) \,, \qquad \text{and} \qquad \beta_2^j = \beta''(E_c^j)
\tag{D.6}
$$

has been introduced. Evaluation of the integral I_j gives

$$
\begin{aligned}
I_j = e^{iqE_c^j} \Delta_j \Bigg\{ &\beta_0^j \frac{\sin(q\Delta_j/2)}{q\Delta_j/2} + i\frac{\beta_1^j}{q} \left(\frac{\sin(q\Delta_j/2)}{q\Delta_j/2} - \cos(q\Delta_j/2) \right) \\
&+ \beta_2^j \left[\frac{\Delta_j^2}{8} \frac{\sin(q\Delta_j/2)}{q\Delta_j/2} - \frac{1}{q^2} \left(\frac{\sin(q\Delta_j/2)}{q\Delta_j/2} - \cos(q\Delta_j/2) \right) \right] \Bigg\} \,.
\end{aligned}
\tag{D.7}
$$

The constants β_0^j, β_1^j, and β_2^j are approximated by means of the finite differences and the Taylor expansion. The parameter β_0^j is obtained from the expansion around E_{j+1} and E_j,

$$
\begin{aligned}
\beta_0^j &= \beta(E_c^j) \\
&= \frac{1}{2}\beta(E_{j+1} - \Delta_j/2) + \frac{1}{2}\beta(E_j + \Delta_j/2) \\
&= \frac{1}{2}\Bigg(\beta(E_{j+1}) - \frac{\Delta_j}{2}\beta'(E_{j+1}) + \frac{1}{2}\frac{\Delta_j^2}{4}\beta''(E_{j+1}) \\
&\qquad + \beta(E_j) + \frac{\Delta_j}{2}\beta'(E_j) + \frac{1}{2}\frac{\Delta_j^2}{4}\beta''(E_j) \Bigg) + \mathcal{O}(\Delta_j^3) \,,
\end{aligned}
\tag{D.8}
$$

and the derivatives in Eq. (D.8) are further expressed as

$$
\begin{aligned}
\beta'(E_{j+1}) &= \beta'(E_j) + \beta''(E_j)\Delta_j + \mathcal{O}(\Delta_j^2) \,, \\
\beta''(E_{j+1}) &= \beta''(E_c^j) + \mathcal{O}(\Delta_j) \,, \qquad \text{and} \\
\beta''(E_j) &= \beta''(E_c^j) + \mathcal{O}(\Delta_j) \,.
\end{aligned}
\tag{D.9}
$$

Inserting (D.9) into (D.8) gives

$$
\beta_0^j = \frac{\beta(E_{j+1}) + \beta(E_j)}{2} - \frac{\Delta_j^2}{8}\beta_2^j + \mathcal{O}(\Delta_j^3) \,.
\tag{D.10}
$$

The first derivative β_1^j is approximated by the difference

$$
\beta_1^j \approx \frac{\beta(E_{j+1}) - \beta(E_j)}{E_{j+1} - E_j} \,,
\tag{D.11}
$$

and the second derivative β_2^j by the average of the differences in the neighbouring points,

$$
\begin{aligned}
\beta_2^j &\approx \frac{1}{2}\left\{\frac{\beta'(E_c^{j+1})-\beta'(E_c^j)}{\frac{\Delta_{j+1}}{2}+\frac{\Delta_j}{2}}+\frac{\beta'(E_c^j)-\beta'(E_c^{j-1})}{\frac{\Delta_j}{2}+\frac{\Delta_{j-1}}{2}}\right\} \\
&= \frac{1}{E_{j+2}-E_j}\left\{\frac{\beta(E_{j+2})-\beta(E_{j+1})}{E_{j+2}-E_{j+1}}-\frac{\beta(E_{j+1})-\beta(E_j)}{E_{j+1}-E_j}\right\} \\
&\quad + \frac{1}{E_{j+1}-E_{j-1}}\left\{\frac{\beta(E_{j+1})-\beta(E_j)}{E_{j+1}-E_j}-\frac{\beta(E_j)-\beta(E_{j-1})}{E_j-E_{j-1}}\right\}.
\end{aligned}
\tag{D.12}
$$

The final result for the approximate Fourier transform follows from Eqs. (D.10)-(D.12), (D.3), and (D.7):

$$
\begin{aligned}
\tilde\beta(q) = \sum_{j=1}^{N-3} e^{iqE_c}&\left\{\left(\frac{\beta(E_{j+1})+\beta(E_j)}{2}\right)\frac{\sin(q\Delta_j/2)}{q\Delta_j/2}\Delta_j\right. \\
&\left. + \left(\frac{i[\beta(E_{j+1})-\beta(E_j)]}{q}-\frac{\Delta_j\beta_2^j}{q^2}\right)\left(\frac{\sin(q\Delta_j/2)}{q\Delta_j/2}-\cos(q\Delta_j/2)\right)\right\}.
\end{aligned}
\tag{D.13}
$$

To convolute the spectrum, $\tilde\beta(q)$ should be multiplied by the Fourier transform of the instrumental function and transformed back to the energy space. If a Gaussian [Eq. (D.1)] is used, the transform is equal to

$$
\exp\left(-\frac{\sigma^2 q^2}{2}\right).
\tag{D.14}
$$

Although the q-space mesh from Eq. (D.13) may be chosen arbitrarily, it will be taken equidistant,

$$
q_j = j\,\delta q\,, \qquad \delta q = \text{const.}
\tag{D.15}
$$

This, together with the assumption that $\beta(E)$ is real $[\tilde\beta(-q)=\tilde\beta(q)^*]$, gives for the inverse Fourier transform

$$
\begin{aligned}
\beta(E) &= \mathcal{F}^{-1}(\tilde\beta) \\
&= \frac{1}{2\pi}\int_{-\infty}^{\infty} e^{-iqE}\tilde\beta(q)\mathrm{d}q \\
&\approx \frac{\delta q}{2\pi}\sum_j e^{-iq_j E}\tilde\beta(q_j) \\
&= \frac{\delta q}{2\pi}\left(\tilde\beta(0)+\sum_{j>0}2\,\mathrm{Re}\left[e^{-iq_j E}\tilde\beta(q_j)\right]\right),
\end{aligned}
\tag{D.16}
$$

or, if the real and imaginary parts are written explicitly,

$$
\beta(E) = \frac{\delta q}{2\pi}\left(\tilde\beta(0)+\sum_{j>0}2\left[\cos q_j E\,\mathrm{Re}\,\tilde\beta(q_j)+\sin q_j E\,\mathrm{Im}\,\tilde\beta(q_j)\right]\right).
\tag{D.17}
$$

A comment should be made on the range of q values needed in the calculation. Since the convolved spectra are broadened, the minimum distance between two peaks that can be resolved is of the order of σ. Therefore, the maximum q may be determined by

$$
q_{\max} = \frac{2\pi}{2\epsilon\sigma}\,,
\tag{D.18}
$$

where $0 < \epsilon \leq 1$ is a free parameter (e.g. $\epsilon = 1/4$). It should be noted that the number of points in the conjugate space need not be equal to N but may be smaller. Its order of magnitude may be obtained by

$$N_q = \frac{\max_j\{E_j\} - \min_j\{E_j\}}{\epsilon\sigma} \ . \tag{D.19}$$

This in turn also means that the mesh of the inverse Fourier transform may involve fewer points than were originally used to represent the calculated spectrum.

Appendix E

Tables of singly and doubly excited states below the $N = 2$ threshold

In this appendix, the parameters of singly and doubly excited singlet states of the free helium atom used in the calculations are tabulated. For each state, its energy E, quantum defect δ, and radiative width γ are given. Furthermore, for doubly excited states, autoionisation half-widths $\Gamma/2$, and reduced widths $\Gamma^* = \Gamma (n - \delta)^3$ are included if $\Gamma \gtrsim 10^{-11}$ a.u. and the results are consistent with the $1/(n - \delta)^3$ rule. When available, comparison with the existing results from the literature is made. The errors of the tabulated energies and autoionisation widths range from 10^{-5} a.u. for lower lying states of angular momenta S, P, D, and F, and decrease to 10^{-9} a.u. and less for higher lying states and higher momenta. Where the references provide results with more than ten significant digits, the reported results are rounded to ten digit accuracy. Although only the singly excited states for $n \leq 15$ are reported, singly excited states with $n \leq 18$ are included in the calculation. Where a conversion value is not given, $t_0 = 2.418884326505 \times 10^{-17}$ s is used to convert the reference widths to atomic units (cf. Appendix A and Ref. [113] for recommended values).

E.1 Singly excited states

[a] Bürgers et al. [81] – Perimetric coordinates are used, and the wavefunctions are expanded in a Sturmian basis set. Singly excited $^1S^e$ and $^3S^e$ states with $n \leq 16$ are calculated variationally. The complex dilatation method is used to determine energies and autoionisation widths of doubly excited $^1S^e$ and $^3S^e$ states with $n \leq 10$ below $N = 2$, $N = 3$, and $N = 4$ ionisation thresholds.

[b] Theodosiou [115] – A semi empirical method is used to calculate radiative widths of singly excited states for $L \leq 4$ and $n \leq 21$: the atomic potential is taken to be the Hartree-Slater prediction, while experimental energy values are used. Energies of higher lying states (that at the time the article was written have not yet been measured) are calculated using asymptotic quantum defects derived from lower states.

[c] Drake [116], Drake et al. [117] – Singly excited states for $1 \leq L \leq 7$ are calculated variationally. A Hylleraas-like explicitly correlated basis is used.

[d] Žitnik et al. [118] – MCHF wavefunctions of singly excited $^1P^o$ states are obtained using the ATSP codes [52]. Total radiative widths are calculated for the states with $n \leq 8$.

[e] Lagmago Kamta et al. [82] – A CI method using a Sturmian basis set with several different pairs of nonlinear scaling parameters (cf. Chapter 4) is used to calculate energies of singly excited $^1K^o$, $^1N^e$, and $^1O^o$ states for $n \le 17$, $n \le 20$, and $n \le 21$, respectively. The method is combined with complex scaling to calculate energies and autoionisation widths of the a series of $^1S^e$ doubly excited states.

Table E.1: Singly excited $^1S^e$ states.

	present	refs.		present	refs.
	$-E$	$-E$	δ	γ	γ
1	2.903640620	2.903724377[a]	0.2561		
2	2.145968113	2.145974046	0.1492		
3	2.061270331	2.061271990	0.1433	4.43(-10)	4.37(-10)[b]
4	2.033586038	2.033586717	0.1416	2.75(-10)	2.72(-10)
5	2.021176510	2.021176851	0.1409	1.65(-10)	1.63(-10)
6	2.014562903	2.014563097	0.1405	1.04(-10)	1.03(-10)
7	2.010625654	2.010625775	0.1403	6.88(-11)	6.82(-11)
8	2.008093541	2.008093619	0.1401	4.76(-11)	4.71(-11)
9	2.006369497	2.006369551	0.1400	3.42(-11)	3.39(-11)
10	2.005142951	2.005142987	0.1400	2.53(-11)	2.51(-11)
11	2.004239385	2.004239408	0.1399	1.93(-11)	1.91(-11)
12	2.003554601	2.003554611	0.1399	1.50(-11)	1.49(-11)
13	2.003023271	2.003023271	0.1398	1.19(-11)	1.18(-11)
14	2.002602747	2.002602732	0.1398	9.56(-12)	9.46(-12)
15	2.002264229	2.002264191	0.1398	7.81(-12)	7.73(-12)

Table E.2: Singly excited $^1P^o$ states.

	present	refs.		present	refs.
	$-E$	$-E$	δ	γ	γ
2	2.123838800	2.123843086[c]	-0.0094	4.36(-8)	4.35(-8)[d]
3	2.055144969	2.055146362	-0.0111	1.40(-8)	1.40(-8)
4	2.031069045	2.031069650	-0.0116	6.10(-9)	6.09(-9)
5	2.019905676	2.019905990	-0.0118	3.17(-9)	3.17(-9)
6	2.013833796	2.013833980	-0.0119	1.85(-9)	1.85(-9)
7	2.010169199	2.010169315	-0.0120	1.17(-9)	1.17(-9)
8	2.007789049	2.007789127	-0.0120	7.89(-10)	7.88(-10)
9	2.006156330	2.006156385	-0.0121	5.56(-10)	5.54(-10)[b]
10	2.004987944	2.004987984	-0.0121	4.06(-10)	4.04(-10)
11	2.004123162		-0.0121	3.05(-10)	3.04(-10)
12	2.003465230		-0.0121	2.36(-10)	2.35(-10)
13	2.002953076		-0.0121	1.85(-10)	1.85(-10)
14	2.002546610		-0.0121	1.49(-10)	1.48(-10)
15	2.002218635		-0.0121	1.21(-10)	1.21(-10)

Table E.3: Singly excited $^1D^e$ states.

	present	refs.		present	refs.
	$-E$	$-E$	δ	γ	γ
3	2.055620642	2.055620733[c]	0.0018	1.54(-9)	1.54(-9)[b]
4	2.031279794	2.031279846	0.0019	6.53(-10)	6.54(-10)
5	2.020015806	2.020015836	0.0020	3.37(-10)	3.38(-10)
6	2.013898209	2.013898227	0.0020	1.96(-10)	1.97(-10)

continued on next page

Table E.3 – continued

	present	refs.		present	refs.
	$-E$	$-E$	δ	γ	γ
7	2.010210016	2.010210028	0.0020	1.25(-10)	1.25(-10)
8	2.007816504	2.007816513	0.0020	8.39(-11)	8.43(-11)
9	2.006175666	2.006175671	0.0021	5.92(-11)	5.94(-11)
10	2.005002067	2.005002072	0.0021	4.33(-11)	4.35(-11)
11	2.004133789		0.0021	3.26(-11)	3.28(-11)
12	2.003473424		0.0021	2.52(-11)	2.53(-11)
13	2.002959527		0.0021	1.99(-11)	1.99(-11)
14	2.002551780		0.0021	1.59(-11)	1.60(-11)
15	2.002222838		0.0021	1.30(-11)	1.30(-11)

Table E.4: Singly excited $^1F^o$ states.

	present	refs.		present	refs.
	$-E$	$-E$	δ	γ	γ
4	2.031255144	2.031255144[c]	0.000329	3.35(-10)	3.34(-10)[b]
5	2.020002936	2.020002937	0.000367	1.73(-10)	1.73(-10)
6	2.013890683	2.013890684	0.000388	1.01(-10)	1.01(-10)
7	2.010205248	2.010205248	0.000400	6.44(-11)	6.44(-11)
8	2.007813297	2.007813297	0.000408	4.35(-11)	4.35(-11)
9	2.006173407	2.006173407	0.000413	3.07(-11)	3.08(-11)
10	2.005000417	2.005000418	0.000417	2.25(-11)	2.25(-11)
11	2.004132544		0.000416	1.70(-11)	1.70(-11)
12	2.003472455		0.000403	1.32(-11)	1.32(-11)
13	2.002958738		0.000347	1.04(-11)	1.04(-11)
14	2.002551092		0.000195	8.32(-12)	8.34(-12)
15	2.002222212		-0.000033	6.73(-12)	6.80(-12)

Table E.5: Singly excited $^1G^e$ states.

	present	refs.		present	refs.
	$-E$	$-E$	δ	γ	γ
5	2.020000711	2.020000711[c]	0.000089	1.03(-10)	1.03(-10)[b]
6	2.013889345	2.013889345	0.000099	6.00(-11)	6.00(-11)
7	2.010204386	2.010204386	0.000104	3.81(-11)	3.80(-11)
8	2.007812711	2.007812711	0.000108	2.57(-11)	2.56(-11)
9	2.006172992	2.006172992	0.000111	1.82(-11)	1.81(-11)
10	2.005000113	2.005000113	0.000113	1.34(-11)	1.32(-11)
11	2.004132317		0.000114	1.01(-11)	9.97(-12)
12	2.003472288		0.000114	7.81(-12)	7.70(-12)
13	2.002958630		0.000111	6.17(-12)	6.07(-12)
14	2.002551059		0.000107	4.96(-12)	4.87(-12)
15	2.002222267		0.000151	4.04(-12)	3.97(-12)

Table E.6: Singly excited $^1H^o$ states.

	present	refs.		
	$-E$	$-E$	δ	γ
6	2.013889035	2.013889035[c]	0.000031	3.98(-11)
7	2.010204183	2.010204183	0.000035	2.52(-11)
8	2.007812572	2.007812572	0.000037	1.70(-11)
9	2.006172892	2.006172892	0.000038	1.20(-11)

Table E.6 – continued

	present	refs.		
	$-E$	$-E$	δ	γ
10	2.005000039	2.005000039	0.000039	8.82(-12)
11	2.004132262		0.000040	6.66(-12)
12	2.003472247		0.000042	5.16(-12)
13	2.002958601		0.000047	4.08(-12)
14	2.002551041		0.000056	3.28(-12)
15	2.002222235		0.000045	2.68(-12)

Table E.7: Singly excited $^1I^e$ states.

	present	refs.		
	$-E$	$-E$	δ	γ
7	2.010204121	2.010204121[c]	0.000013	1.79(-11)
8	2.007812529	2.007812529	0.000015	1.21(-11)
9	2.006172861	2.006172861	0.000015	8.51(-12)
10	2.005000016	2.005000016	0.000016	6.24(-12)
11	2.004132244		0.000016	4.72(-12)
12	2.003472232		0.000017	3.65(-12)
13	2.002958587		0.000016	2.89(-12)
14	2.002551027		0.000017	2.32(-12)
15	2.002222229		0.000023	1.90(-12)

Table E.8: Singly excited $^1K^o$ states.

	present	refs.		
	$-E$	$-E$	δ	γ
8	2.007812513	2.007812513[c]	0.000006	9.01(-12)
9	2.006172849	2.006172849	0.000007	6.35(-12)
10	2.005000007	2.005000007	0.000007	4.65(-12)
11	2.004132237	2.004132237[e]	0.000008	3.51(-12)
12	2.003472227	2.003472227	0.000008	2.72(-12)
13	2.002958583	2.002958584	0.000008	2.15(-12)
14	2.002551023	2.002551023	0.000007	1.73(-12)
15	2.002222224	2.002222225	0.000007	1.41(-12)

Table E.9: Singly excited $^1L^e$ states.

	$-E$	δ	γ
9	2.006172844	0.000003	4.93(-12)
10	2.005000004	0.000004	3.60(-12)
11	2.004132234	0.000004	2.72(-12)
12	2.003472225	0.000004	2.10(-12)
13	2.002958582	0.000004	1.66(-12)
14	2.002551022	0.000005	1.33(-12)
15	2.002222224	0.000007	1.09(-12)

Table E.10: Singly excited $^1M^o$ states.

	$-E$	δ	γ
10	2.005000002	0.000002	2.87(-12)
11	2.004132233	0.000002	2.16(-12)
12	2.003472223	0.000002	1.67(-12)
13	2.002958581	0.000002	1.32(-12)
14	2.002551021	0.000002	1.06(-12)
15	2.002222223	0.000002	8.66(-13)

Table E.11: Singly excited $^1N^e$ states.

	present	refs.		
	$-E$	$-E$	δ	γ
11	2.004132232	2.004132232[e]	0.000001	1.77(-12)
12	2.003472223	2.003472223	0.000001	1.36(-12)
13	2.002958580	2.002958580	0.000001	1.07(-12)
14	2.002551021	2.002551021	0.000001	8.62(-13)
15	2.002222223	2.002222222	0.000001	7.03(-13)

E.2   Doubly excited states

[a] Bürgers, et al. [81] – see pg. 129

[b] Žitnik et al. [74] – A CI approach is used to express atomic wavefunctions in a basis of hydrogen-like ($Z = 2$) two electron LS coupled functions. The ATSP codes [52] are used to calculate radiative transition matrix elements. Autoionisation rates are calculated from the zero order states by means of electron-electron repulsion matrix elements. Continuum wavefunctions of ejected electrons are obtained with the GRASP continuum module [76, 77].

[c] Lagmago Kamta et al. [82] – see pg. 129

[d] Lindroth [119] – The method of complex scaling is used with a finite basis set obtained by placing the helium atom in a spherical volume, inside of which a discrete radial grid is used. Diagonalisation of a discretised one-particle Hamiltonian gives a discrete complete basis set which is used to construct correlated wavefunctions. Low lying singlet and triplet doubly excited states below $N = 2$ and $N = 3$ thresholds with $L \leq 3$ are calculated.

[e] Rost et al. [4] – The complex dilatation method is used to obtain parameters of $^1P^o$ resonances converging to the thresholds $N = 2 - 7$.

[f] Liu et al. [19] – Radiative and autoionisation widths from doubly excited $^1P^o$ states with $n \leq 7$ below the $N = 2$ ionisation threshold are calculated. In the calculation of radiative widths, transitions to singly excited $^1S^e$ and $^1D^e$ are included, and the doubly excited states are treated as bound. Wavefunctions of the singly excited states are calculated variationally using B spline functions, whereas wavefunctions of the doubly excited states are calculated with the B spline saddle point complex dilatation method.

[g] Scrinzi et al. [120] – Energies and autoionisation widths of low lying states with $L \leq 4$ and parity $(-1)^L$ below the $N = 2$ and $N = 3$ thresholds are calculated using the complex dilatation method. Hylleraas-like explicitly correlated basis is used.

Table E.12: Doubly excited $^1S^e$ states.

	present		refs.				present	refs.
	$-E$	$\Gamma/2$	$-E$	$\Gamma/2$	δ	Γ^*	γ	γ
2a	0.777866028	2.271651(-3)	0.777867636	2.270653(-3)[a]	0.6586	1.10(-2)	6.51(-8)	1.47(-9)[b]
2b	0.621876000	1.06872(-4)	0.621927254	1.07818(-4)	-0.0255	1.78(-3)	2.01(-7)	1.99(-8)
3a	0.589893480	6.81402(-4)	0.589894682	6.81239(-4)	0.6416	1.79(-2)	7.55(-8)	8.78(-8)
3b	0.548079569	3.7344(-5)	0.548085535	3.7392(-5)	-0.2248	2.50(-3)	1.39(-7)	1.10(-7)
4a	0.544881002	2.46015(-4)	0.544881618	2.46030(-4)	0.6623	1.83(-2)	1.06(-7)	1.16(-7)
4b	0.527714192	2.3121(-5)	0.527716640	2.3101(-5)	-0.2475	3.54(-3)	1.12(-7)	9.22(-8)
5a	0.526686500	1.09289(-4)	0.526686857	1.09335(-4)	0.6715	1.77(-2)	1.28(-7)	1.39(-7)
5b	0.518102999	1.4924(-5)	0.518104252	1.4894(-5)	-0.2554	4.33(-3)	9.59(-8)	7.84(-8)
6a	0.517640889	5.6752(-5)	0.517641112	5.6795(-5)	0.6762	1.71(-2)	1.43(-7)	1.55(-7)
6b	0.512762516	9.996(-6)	0.512763242	9.970(-6)	-0.2592	4.90(-3)	8.55(-8)	6.89(-8)
7a	0.512513341	3.2959(-5)	0.512513488	3.2992(-5)	0.6788	1.66(-2)	1.53(-7)	1.65(-7)
7b	0.509483111	6.938(-6)	0.509483569	6.918(-6)	-0.2612	5.31(-3)	7.84(-8)	6.22(-8)
8a	0.509332585	2.0770(-5)	0.509332686	2.0795(-5)	0.6805	1.63(-2)	1.60(-7)	1.72(-7)
8b	0.507324033	4.975(-6)	0.507324340	4.959(-6)	-0.2625	5.61(-3)	7.34(-8)	5.73(-8)
9a	0.507225762	1.3916(-5)	0.507225835	1.3936(-5)	0.6815	1.60(-2)	1.65(-7)	1.77(-7)
9b	0.505826927	3.670(-6)	0.505827143	3.657(-6)	-0.2633	5.83(-3)	6.98(-8)	5.37(-8)
10a	0.505759052	9.777(-6)	0.505759104	9.790(-6)	0.6823	1.58(-2)	1.68(-7)	1.79(-7)
10b	0.504746230	2.776(-6)	0.504746388	2.766(-6)	-0.2639	6.00(-3)	6.71(-8)	5.66(-8)
11a	0.504697299	7.131(-6)	0.504697187	7.131(-6)[c]	0.6828	1.57(-2)	1.71(-7)	
11b	0.503940615	2.146(-6)			-0.2643	6.13(-3)	6.50(-8)	
12a	0.503904132	5.362(-6)	0.503904047	5.360(-6)	0.6832	1.55(-2)	1.73(-7)	
12b	0.503324031	1.690(-6)			-0.2646	6.24(-3)	6.34(-8)	
13a	0.503296078	4.134(-6)	0.503296011	4.131(-6)	0.6835	1.54(-2)	1.74(-7)	
13b	0.502841626	1.350(-6)			-0.2648	6.30(-3)	6.21(-8)	
14a	0.502819726	3.253(-6)	0.502819669	3.239(-6)	0.6838	1.54(-2)	1.75(-7)	
14b	0.502457222	1.136(-6)			-0.2647	6.59(-3)	6.02(-8)	
15a	0.502439676	2.617(-6)	0.502439599	2.689(-6)	0.6841	1.54(-2)	1.77(-7)	
15b	0.502145517	8.06(-7)			-0.2658	5.73(-3)	6.16(-8)	

Table E.13: Doubly excited $^1P^e$ states.

	present	refs.		present	refs.
	$-E$	$-E$	δ	γ	γ
3a	0.580246463	0.58025[d]	0.5038	2.53(-7)	2.54(-7)[b]
4a	0.540041588		0.4663	2.41(-7)	2.42(-7)
5a	0.524178980		0.4526	2.38(-7)	2.38(-7)
6a	0.516208610		0.4459	2.37(-7)	2.36(-7)
7a	0.511626536		0.4422	2.37(-7)	2.36(-7)
8a	0.508748011		0.4399	2.37(-7)	2.35(-7)
9a	0.506821044		0.4383	2.37(-7)	2.33(-7)
10a	0.505467675		0.4372	2.37(-7)	2.32(-7)
11a	0.504480744		0.4364	2.37(-7)	
12a	0.503738897		0.4359	2.36(-7)	
13a	0.503167185		0.4354	2.36(-7)	
14a	0.502717276		0.4351	2.35(-7)	
15a	0.502356913		0.4349	2.34(-7)	

Table E.14: Doubly excited $^1P^o$ states.

	present		refs.				present	refs.
	$-E$	$\Gamma/2$	$-E$	$\Gamma/2$	δ	Γ^*	γ	γ
2a	0.693106607	6.86350(-4)	0.693134920	6.86625(-4)^e	0.3909	5.72(-3)	1.76(-7)	1.68(-7)^f
3b	0.597073790	1.922(-6)	0.597073804	1.923(-6)	0.7305	4.49(-5)	1.25(-7)	1.29(-7)
3a	0.564080259	1.50540(-4)	0.564085188	1.50594(-4)	0.2067	6.56(-3)	1.78(-7)	1.75(-7)
3c	0.547089825		0.547092709	5(-9)	-0.2585		1.15(-7)	1.02(-7)
4b	0.546491860	1.009(-6)	0.546493257	1.014(-6)	0.7206	7.11(-5)	1.93(-7)	1.78(-7)
4a	0.534361157	6.4152(-5)	0.534363144	6.4173(-5)	0.1854	7.12(-3)	1.83(-7)	1.82(-7)
4c	0.527614605		0.527616338	7(-11)	-0.2552		9.87(-8)	9.12(-8)
5b	0.527297038	4.88(-7)	0.527297770	4.91(-7)	0.7202	7.65(-5)	1.99(-7)	1.91(-7)
5a	0.521503669	3.2888(-5)	0.521504666	3.2898(-5)	0.1780	7.37(-3)	1.86(-7)	1.86(-7)
5c	0.518117242		0.518118268	1.7(-11)	-0.2534		9.07(-8)	8.56(-8)
6b	0.517936917	2.65(-7)	0.517937328	2.67(-7)	0.7203	7.80(-5)	2.03(-7)	2.01(-7)
6a	0.514733425	1.8992(-5)	0.514733994	1.8998(-5)	0.1745	7.51(-3)	1.88(-7)	1.88(-7)
6c	0.512790392		0.512791034	4.7(-11)	-0.2523		8.61(-8)	7.21(-8)
7b	0.512679737	1.59(-7)	0.512679987	1.60(-7)	0.7204	7.86(-5)	2.05(-7)	2.07(-7)
7a	0.510726440	1.1924(-5)	0.510726795	1.1926(-5)	0.1726	7.59(-3)	1.89(-7)	1.89(-7)
7c	0.509508038		0.509508462	4(-11)	-0.2517		8.32(-8)	8.90(-8)^b
8b	0.509435690	1.02(-7)	0.509435853	1.03(-7)	0.7206	7.88(-5)	2.07(-7)	2.02(-7)
8a	0.508158307	7.963(-6)	0.50815854	7.96(-6)	0.1714	7.64(-3)	1.90(-7)	1.87(-7)
8c	0.507343946		0.507344240	5(-11)	-0.2513		8.12(-8)	8.66(-8)
9b	0.507294204	7.0(-8)	0.507294315	6.8(-8)	0.7207	7.89(-5)	2.08(-7)	2.03(-7)
9a	0.506413686	5.576(-6)	0.50641384	5.59(-6)	0.1706	7.68(-3)	1.90(-7)	1.88(-7)
9c	0.505842475		0.50584269		-0.2510		7.98(-8)	8.49(-8)
10b	0.505806870	4.9(-8)	0.50580696	1.0(-7)	0.7207	7.90(-5)	2.09(-7)	2.02(-7)
10a	0.505174494	4.054(-6)	0.505175	4(-6)	0.1701	7.70(-3)	1.91(-7)	1.88(-7)
10c	0.504758391		0.5047590		-0.2507		7.87(-8)	
11b	0.504732057	3.6(-8)			-0.2792	7.91(-5)	2.10(-7)	
11a	0.504262710	3.038(-6)			0.1697	7.72(-3)	1.91(-7)	
11c	0.503950219				-0.2506		7.79(-8)	
12b	0.503930208	2.8(-8)			-0.2792	7.91(-5)	2.10(-7)	
12a	0.503572348	2.335(-6)			0.1694	7.73(-3)	1.91(-7)	
12c	0.503331706				-0.2504		7.73(-8)	
13b	0.503316151	2.1(-8)			-0.2791	7.90(-5)	2.11(-7)	
13a	0.503037093	1.834(-6)			0.1691	7.75(-3)	1.91(-7)	
13c	0.502847834				-0.2504		7.67(-8)	
14b	0.502835510	1.5(-8)			-0.2791	7.02(-5)	2.10(-7)	
14a	0.502613741	1.434(-6)			0.1690	7.59(-3)	1.91(-7)	
14c	0.502462325				-0.2499		7.58(-8)	
15b	0.502452349	3.9(-8)			-0.2789	2.29(-4)	2.10(-7)	
15a	0.502273028	1.335(-6)			0.1686	8.71(-3)	1.92(-7)	
15c	0.502149666				-0.2510		7.61(-8)	

Table E.15: Doubly excited $^1D^e$ states.

	present		refs.				present	refs.
	$-E$	$\Gamma/2$	$-E$	$\Gamma/2$	δ	Γ^*	γ	γ
2a	0.701907220	1.181476(-3)	0.701946	1.181(-3)^d	0.4263	9.21(-3)	2.66(-7)	9.77(-9)^b
3a	0.569210651	2.77846(-4)	0.56922	2.78(-4)	0.3122	1.08(-2)	1.71(-7)	1.58(-7)
3b	0.556424541	9.951(-6)	0.55643	1.00(-5)	0.0232	5.25(-4)	9.60(-8)	9.29(-8)
4a	0.536722371	1.15957(-4)			0.3101	1.17(-2)	1.55(-7)	1.52(-7)
4b	0.531509853	5.546(-6)			0.0165	7.01(-4)	1.10(-7)	1.07(-7)
4c	0.529292568	5(-9)			-0.1315	6.83(-7)	2.16(-7)	2.16(-7)
5a	0.522740566	5.8144(-5)			0.3110	1.20(-2)	1.49(-7)	1.49(-7)
5b	0.520116280	3.158(-6)			0.0145	7.83(-4)	1.16(-7)	1.13(-7)

continued on next page

Table E.15 – continued

	present		refs.				present	refs.
	$-E$	$\Gamma/2$	$-E$	$\Gamma/2$	δ	Γ^*	γ	γ
5c	0.519000960	5(-9)			-0.1298	1.34(-6)	2.14(-7)	2.15(-7)
6a	0.515453312	3.3014(-5)			0.3118	1.22(-2)	1.47(-7)	1.48(-7)
6b	0.513951996	1.927(-6)			0.0136	8.27(-4)	1.20(-7)	1.16(-7)
6c	0.513311130	4(-9)			-0.1288	1.81(-6)	2.13(-7)	2.15(-7)
7a	0.511179769	2.0466(-5)			0.3124	1.22(-2)	1.46(-7)	1.47(-7)
7b	0.510242446	1.251(-6)			0.0131	8.53(-4)	1.22(-7)	1.18(-7)
7c	0.509840160	3(-9)			-0.1283	2.14(-6)	2.13(-7)	2.14(-7)
8a	0.508461372	1.3537(-5)			0.3129	1.23(-2)	1.45(-7)	1.46(-7)
8b	0.507837657	8.54(-7)			0.0128	8.70(-4)	1.23(-7)	1.19(-7)
8c	0.507568560	2(-9)			-0.1279	2.37(-6)	2.12(-7)	2.14(-7)
9a	0.506625950	9.408(-6)			0.3132	1.23(-2)	1.44(-7)	1.45(-7)
9b	0.506190263	6.08(-7)			0.0127	8.82(-4)	1.24(-7)	1.20(-7)
9c	0.506001395	2(-9)			-0.1276	2.54(-6)	2.12(-7)	2.14(-7)
10a	0.505328784	6.799(-6)			0.3134	1.24(-2)	1.44(-7)	1.44(-7)
10b	0.505012580	4.47(-7)			0.0126	8.91(-4)	1.25(-7)	1.21(-7)
10c	0.504874929	1(-9)			-0.1275	2.66(-6)	2.12(-7)	
11a	0.504378303	5.071(-6)			0.3136	1.24(-2)	1.44(-7)	
11b	0.504141617	3.38(-7)			0.0125	8.97(-4)	1.26(-7)	
11c	0.504038200	1(-9)			-0.1273	2.75(-6)	2.12(-7)	
12a	0.503661148	3.882(-6)			0.3137	1.24(-2)	1.44(-7)	
12b	0.503479414	2.62(-7)			0.0124	9.02(-4)	1.26(-7)	
12c	0.503399748	8(-10)			-0.1272	2.83(-6)	2.11(-7)	
13a	0.503106766	3.037(-6)			0.3138	1.24(-2)	1.43(-7)	
13b	0.502964214	2.07(-7)			0.0124	9.06(-4)	1.26(-7)	
13c	0.502901543	7(-10)			-0.1272	3.03(-6)	2.11(-7)	
14a	0.502669381	2.421(-6)			0.3139	1.24(-2)	1.43(-7)	
14b	0.502555511	1.62(-7)			0.0123	8.85(-4)	1.27(-7)	
14c	0.502505327				-0.1271		2.11(-7)	
15a	0.502318305	1.939(-6)			0.3141	1.23(-2)	1.42(-7)	
15b	0.502225953	1.76(-7)			0.0126	1.19(-3)	1.27(-7)	
15c	0.502185075				-0.1270		2.11(-7)	

Table E.16: Doubly excited $^1D^o$ states.

	present	refs.		
	$-E$	$-E$	δ	γ
3a	0.563800349	0.56380^d	0.2005	2.27(-7)
4a	0.534576361		0.1973	2.35(-7)
5a	0.521659004		0.1953	2.38(-7)
6a	0.514833587		0.1942	2.39(-7)
7a	0.510792615		0.1935	2.40(-7)
8a	0.508203761		0.1931	2.40(-7)
9a	0.506446070		0.1928	2.40(-7)
10a	0.505198308		0.1926	2.40(-7)
11a	0.504280701		0.1924	2.40(-7)
12a	0.503586255		0.1923	2.40(-7)
13a	0.503048058		0.1922	2.40(-7)
14a	0.502622519		0.1922	2.40(-7)
15a	0.502280251		0.1921	2.40(-7)

Table E.17: Doubly excited $^1F^e$ states.

	$-E$	δ	γ
4a	0.531995404	0.0469	2.42(-7)
5a	0.520385649	0.0475	2.42(-7)
6a	0.514113204	0.0479	2.42(-7)
7a	0.510345728	0.0481	2.42(-7)
8a	0.507907542	0.0482	2.42(-7)
9a	0.506239653	0.0483	2.42(-7)
10a	0.505048736	0.0484	2.42(-7)
11a	0.504168860	0.0484	2.42(-7)
12a	0.503500442	0.0485	2.42(-7)
13a	0.502980779	0.0485	2.42(-7)
14a	0.502568795	0.0485	2.42(-7)
15a	0.502236674	0.0485	2.42(-7)

Table E.18: Doubly excited $^1F^o$ states.

	present		refs.		δ	Γ^*	γ
	$-E$	$\Gamma/2$	$-E$	$\Gamma/2$			
3a	0.558277197	6.357(-6)	0.55828	6.4(-6)[d]	0.0709	3.19(-4)	2.20(-7)
4a	0.532254529	3.552(-6)			0.0628	4.34(-4)	2.15(-7)
4b	0.531481304	7(-9)			0.0147	9.03(-7)	4.12(-8)
5a	0.520490708	2.030(-6)			0.0602	4.89(-4)	2.15(-7)
5b	0.520124213	3(-9)			0.0155	8.53(-7)	4.24(-8)
5c	0.519401678				-0.0765		2.26(-7)
6a	0.514166715	1.241(-6)			0.0591	5.20(-4)	2.14(-7)
6b	0.513962516	2(-9)			0.0158	7.05(-7)	4.31(-8)
6c	0.513543372				-0.0761		2.26(-7)
7a	0.510376934	8.06(-7)			0.0585	5.39(-4)	2.14(-7)
7b	0.510251092	9(-10)			0.0161	5.83(-7)	4.35(-8)
7c	0.509986699				-0.0758		2.25(-7)
8a	0.507927432	5.51(-7)			0.0582	5.52(-4)	2.15(-7)
8b	0.507844268	5(-10)			0.0162	4.91(-7)	4.38(-8)
8c	0.507666923				-0.0756		2.25(-7)
9a	0.506253155	3.92(-7)			0.0580	5.60(-4)	2.15(-7)
9b	0.506195282	3(-10)			0.0163	4.25(-7)	4.41(-8)
9c	0.506070605				-0.0755		2.25(-7)
10a	0.505058342	2.88(-7)			0.0578	5.66(-4)	2.15(-7)
10b	0.505016428	2(-10)			0.0164	3.76(-7)	4.42(-8)
10c	0.504925466				-0.0754		2.25(-7)
11a	0.504175949	2.18(-7)			0.0577	5.71(-4)	2.15(-7)
11b	0.504144611	1(-10)			0.0164	3.44(-7)	4.44(-8)
11c	0.504076225				-0.0753		2.25(-7)
12a	0.503505827	1.69(-7)			0.0577	5.74(-4)	2.15(-7)
12b	0.503481779	1(-10)			0.0165	3.53(-7)	4.45(-8)
12c	0.503429075				-0.0753		2.25(-7)
13a	0.502984969	1.33(-7)			0.0576	5.77(-4)	2.15(-7)
13b	0.502966109	8(-11)			0.0165	3.43(-7)	4.46(-8)
13c	0.502924637				-0.0752		2.25(-7)
14a	0.502572121	1.07(-7)			0.0575	5.78(-4)	2.15(-7)
14b	0.502557054				0.0165		4.47(-8)
14c	0.502523838	6(-11)			-0.0752	3.19(-7)	2.25(-7)
15a	0.502239372	7.5(-8)			0.0575	4.99(-4)	2.14(-7)
15b	0.502227191				0.0167		4.49(-8)
15c	0.502200122				-0.0751		2.25(-7)

Table E.19: Doubly excited $^1G^e$ states.

	present		refs.		δ	Γ^*	γ
	$-E$	$\Gamma/2$	$-E$	$\Gamma/2$			
4a	0.532356912	5.9(-8)	0.53236	4.82(-6)^g	0.0690	7.16(-6)	2.28(-7)
5a	0.520577986	4.8(-8)			0.0707	1.15(-5)	2.25(-7)
5b	0.520033572	6(-11)			0.0042	1.44(-8)	2.74(-8)
6a	0.514226769	3.4(-8)			0.0717	1.42(-5)	2.23(-7)
6b	0.513909579	7(-11)			0.0045	2.81(-8)	2.88(-8)
6c	0.513664386				-0.0491		2.32(-7)
7a	0.510418077	2.4(-8)			0.0723	1.59(-5)	2.22(-7)
7b	0.510217589	6(-11)			0.0046	3.91(-8)	2.98(-8)
7c	0.510062829				-0.0490		2.32(-7)
8a	0.507956356	1.7(-8)			0.0727	1.70(-5)	2.21(-7)
8b	0.507821756	5(-11)			0.0047	4.61(-8)	3.06(-8)
8c	0.507717911				-0.0489		2.32(-7)
9a	0.506274095	1.2(-8)			0.0729	1.78(-5)	2.21(-7)
9b	0.506179440	4(-11)			0.0048	5.24(-8)	3.12(-8)
9c	0.506106418				-0.0488		2.32(-7)
10a	0.505073921	9(-9)			0.0731	1.83(-5)	2.20(-7)
10b	0.505004864	3(-11)			0.0049	5.87(-8)	3.16(-8)
10c	0.504951581				-0.0488		2.32(-7)
11a	0.504187823	7(-9)			0.0733	1.87(-5)	2.20(-7)
11b	0.504135915	2(-11)			0.0049	5.33(-8)	3.19(-8)
11c	0.504095852				-0.0487		2.32(-7)
12a	0.503515070	6(-9)			0.0734	1.91(-5)	2.20(-7)
12b	0.503475076	2(-11)			0.0049	6.33(-8)	3.22(-8)
12c	0.503444199				-0.0487		2.32(-7)
13a	0.502992296	4(-9)			0.0734	1.93(-5)	2.20(-7)
13b	0.502960835	1(-11)			0.0050	4.48(-8)	3.24(-8)
13c	0.502936537				-0.0487		2.32(-7)
14a	0.502578024	4(-9)			0.0735	2.08(-5)	2.19(-7)
14b	0.502552832				0.0050		3.26(-8)
14c	0.502533370				-0.0487		2.32(-7)
15a	0.502244181				0.0736		2.19(-7)
15b	0.502223695				0.0050		3.27(-8)
15c	0.502207870				-0.0487		2.32(-7)

Table E.20: Doubly excited $^1G^o$ states.

	$-E$	δ	γ
5a	0.520159326	0.0198	2.42(-7)
6a	0.513982234	0.0201	2.42(-7)
7a	0.510263288	0.0202	2.43(-7)
8a	0.507852344	0.0203	2.43(-7)
9a	0.506200908	0.0204	2.43(-7)
10a	0.505020505	0.0204	2.43(-7)
11a	0.504147661	0.0205	2.43(-7)
12a	0.503484120	0.0205	2.43(-7)
13a	0.502967946	0.0205	2.43(-7)
14a	0.502558525	0.0205	2.43(-7)
15a	0.502228326	0.0206	2.43(-7)

Table E.21: Doubly excited $^1H^e$ states.

	$-E$	δ	γ
6a	0.513936261	0.0102	2.43(-7)
7a	0.510234193	0.0103	2.43(-7)
8a	0.507832792	0.0104	2.43(-7)
9a	0.506187149	0.0104	2.43(-7)
10a	0.505010461	0.0104	2.43(-7)
11a	0.504140107	0.0105	2.43(-7)
12a	0.503478298	0.0105	2.43(-7)
13a	0.502963364	0.0105	2.43(-7)
14a	0.502554855	0.0105	2.43(-7)
15a	0.502225342	0.0105	2.43(-7)

Table E.22: Doubly excited $^1H^o$ states.

	$-E$	$\Gamma/2$	δ	Γ^*	γ
5a	0.520337950	3(-10)	0.0417	6.95(-8)	2.33(-7)
6a	0.514086145	3(-10)	0.0422	1.32(-7)	2.32(-7)
6b	0.513895815		0.0015		1.79(-8)
7a	0.510328910	3(-10)	0.0424	1.78(-7)	2.31(-7)
7b	0.510208703		0.0016		1.83(-8)
7c	0.510104597		-0.0344		2.35(-7)
8a	0.507896377	2(-10)	0.0426	2.12(-7)	2.31(-7)
8b	0.507815708		0.0016		1.85(-8)
8c	0.507745803		-0.0344		2.35(-7)
9a	0.506231864	2(-10)	0.0427	2.38(-7)	2.30(-7)
9b	0.506175147		0.0017		1.88(-8)
9c	0.506125968		-0.0344		2.35(-7)
10a	0.505043085	1(-10)	0.0428	2.56(-7)	2.30(-7)
10b	0.505001710		0.0017		1.89(-8)
10c	0.504965814		-0.0344		2.35(-7)
11a	0.504164631	1(-10)	0.0429	2.71(-7)	2.30(-7)
11b	0.504133532		0.0017		1.91(-8)
11c	0.504106537		-0.0344		2.35(-7)
12a	0.503497195	8(-11)	0.0429	2.82(-7)	2.30(-7)
12b	0.503473233		0.0017		1.92(-8)
12c	0.503452424		-0.0344		2.35(-7)
13a	0.502978231	7(-11)	0.0430	2.87(-7)	2.30(-7)
13b	0.502959381		0.0018		1.93(-8)
13c	0.502943004		-0.0344		2.35(-7)
14a	0.502566759	6(-11)	0.0430	3.14(-7)	2.30(-7)
14b	0.502551665		0.0018		1.94(-8)
14c	0.502538546		-0.0344		2.35(-7)
15a	0.502235020		0.0430		2.29(-7)
15b	0.502222740		0.0017		1.94(-8)
15c	0.502212077		-0.0344		2.35(-7)

Table E.23: Doubly excited $^1I^e$ states.

	$-E$	δ	γ
6a	0.514022568	0.0287	2.36(-7)
7a	0.510288600	0.0288	2.35(-7)
7b	0.510205948	0.0006	1.28(-8)
8a	0.507869260	0.0289	2.35(-7)
continued on next page			

Table E.23 – continued

	$-E$	δ	γ
8b	0.507813817	0.0007	1.29(-8)
8c	0.507763957	-0.0250	2.37(-7)
9a	0.506212768	0.0290	2.35(-7)
9b	0.506173797	0.0007	1.29(-8)
9c	0.506138731	-0.0250	2.37(-7)
10a	0.505029140	0.0290	2.35(-7)
10b	0.505000715	0.0007	1.30(-8)
10c	0.504975126	-0.0250	2.37(-7)
11a	0.504154142	0.0290	2.34(-7)
11b	0.504132778	0.0007	1.30(-8)
11c	0.504113538	-0.0250	2.37(-7)
12a	0.503489108	0.0291	2.34(-7)
12b	0.503472648	0.0007	1.30(-8)
12c	0.503457820	-0.0250	2.37(-7)
13a	0.502971867	0.0291	2.34(-7)
13b	0.502958918	0.0007	1.30(-8)
13c	0.502947249	-0.0250	2.37(-7)
14a	0.502561662	0.0291	2.34(-7)
14b	0.502551294	0.0007	1.31(-8)
14c	0.502541947	-0.0250	2.37(-7)
15a	0.502230876	0.0291	2.34(-7)
15b	0.502222443	0.0007	1.31(-8)
15c	0.502214844	-0.0250	2.37(-7)

Table E.24: Doubly excited $^1I^o$ states.

	$-E$	δ	γ
7a	0.510221502	0.0060	2.43(-7)
8a	0.507824249	0.0060	2.43(-7)
9a	0.506181129	0.0060	2.43(-7)
10a	0.505006063	0.0061	2.43(-7)
11a	0.504136797	0.0061	2.43(-7)
12a	0.503475745	0.0061	2.43(-7)
13a	0.502961355	0.0061	2.43(-7)
14a	0.502553244	0.0061	2.43(-7)
15a	0.502224032	0.0061	2.43(-7)

Table E.25: Doubly excited $^1K^e$ states.

	$-E$	δ	γ
8a	0.507819925	0.0038	2.43(-7)
9a	0.506178079	0.0038	2.43(-7)
10a	0.505003833	0.0038	2.43(-7)
11a	0.504135118	0.0038	2.43(-7)
12a	0.503474450	0.0038	2.43(-7)
13a	0.502960335	0.0039	2.43(-7)
14a	0.502552427	0.0039	2.43(-7)
15a	0.502223367	0.0039	2.43(-7)

Table E.26: Doubly excited $^1K^o$ states.

	$-E$	δ	γ
7a	0.510265932	0.0211	2.38(-7)
8a	0.507854020	0.0212	2.37(-7)
8b	0.507813106	0.0003	9.60(-9)
9a	0.506202040	0.0212	2.37(-7)
9b	0.506173286	0.0003	9.61(-9)
9c	0.506146935	-0.0189	2.38(-7)
10a	0.505021307	0.0212	2.37(-7)
10b	0.505000336	0.0003	9.60(-9)
10c	0.504981110	-0.0189	2.38(-7)
11a	0.504148250	0.0213	2.37(-7)
11b	0.504132490	0.0003	9.58(-9)
11c	0.504118036	-0.0189	2.38(-7)
12a	0.503484567	0.0213	2.37(-7)
12b	0.503472425	0.0004	9.56(-9)
12c	0.503461286	-0.0189	2.39(-7)
13a	0.502968293	0.0213	2.37(-7)
13b	0.502958741	0.0004	9.54(-9)
13c	0.502949977	-0.0189	2.39(-7)
14a	0.502558799	0.0213	2.37(-7)
14b	0.502551151	0.0004	9.52(-9)
14c	0.502544131	-0.0189	2.39(-7)
15a	0.502228548	0.0213	2.37(-7)
15b	0.502222329	0.0004	9.49(-9)
15c	0.502216621	-0.0189	2.39(-7)

Table E.27: Doubly excited $^1L^e$ states.

	$-E$	δ	γ
8a	0.507844363	0.0163	2.39(-7)
9a	0.506195244	0.0163	2.39(-7)
9b	0.506173066	0.0002	7.48(-9)
10a	0.505016346	0.0163	2.38(-7)
10b	0.505000172	0.0002	7.48(-9)
10c	0.504985175	-0.0149	2.39(-7)
11a	0.504144520	0.0163	2.38(-7)
11b	0.504132365	0.0002	7.45(-9)
11c	0.504121092	-0.0149	2.39(-7)
12a	0.503481691	0.0163	2.38(-7)
12b	0.503472328	0.0002	7.41(-9)
12c	0.503463640	-0.0149	2.39(-7)
13a	0.502966030	0.0163	2.38(-7)
13b	0.502958664	0.0002	7.36(-9)
13c	0.502951829	-0.0149	2.39(-7)
14a	0.502556987	0.0163	2.38(-7)
14b	0.502551089	0.0002	7.31(-9)
14c	0.502545615	-0.0149	2.39(-7)
15a	0.502227074	0.0163	2.38(-7)
15b	0.502222279	0.0002	7.26(-9)
15c	0.502217827	-0.0149	2.39(-7)

Table E.28: Doubly excited $^1L^o$ states.

	$-E$	δ	γ
9a	0.506176367	0.0026	2.43(-7)
10a	0.505002581	0.0026	2.43(-7)
11a	0.504134176	0.0026	2.43(-7)
12a	0.503473723	0.0026	2.43(-7)
13a	0.502959762	0.0026	2.43(-7)
14a	0.502551968	0.0026	2.43(-7)
15a	0.502222993	0.0026	2.43(-7)

Table E.29: Doubly excited $^1M^e$ states.

	$-E$	δ	γ
10a	0.505001823	0.0018	2.43(-7)
11a	0.504133605	0.0018	2.43(-7)
12a	0.503473282	0.0018	2.43(-7)
13a	0.502959415	0.0018	2.43(-7)
14a	0.502551690	0.0018	2.43(-7)
15a	0.502222767	0.0018	2.43(-7)

Table E.30: Doubly excited $^1M^o$ states.

	$-E$	δ	γ
9a	0.506190617	0.0129	2.39(-7)
10a	0.505012969	0.0129	2.39(-7)
10b	0.505000094	0.0001	6.00(-9)
11a	0.504141980	0.0130	2.39(-7)
11b	0.504132305	0.0001	5.98(-9)
11c	0.504123259	-0.0120	2.40(-7)
12a	0.503479734	0.0130	2.39(-7)
12b	0.503472281	0.0001	5.95(-9)
12c	0.503465311	-0.0120	2.40(-7)
13a	0.502964490	0.0130	2.39(-7)
13b	0.502958627	0.0001	5.90(-9)
13c	0.502953143	-0.0120	2.40(-7)
14a	0.502555753	0.0130	2.39(-7)
14b	0.502551059	0.0001	5.84(-9)
14c	0.502546667	-0.0120	2.40(-7)
15a	0.502226071	0.0130	2.39(-7)
15b	0.502222254	0.0001	5.76(-9)
15c	0.502218683	-0.0120	2.40(-7)

Table E.31: Doubly excited $^1N^e$ states.

	$-E$	δ	γ
10a	0.505010553	0.0105	2.40(-7)
11a	0.504140163	0.0105	2.40(-7)
11b	0.504132274	0.0001	2.62(-9)
12a	0.503478334	0.0105	2.40(-7)
12b	0.503472256	0.0001	2.67(-9)
12c	0.503466538	-0.0098	7.09(-12)
13a	0.502963388	0.0106	2.40(-7)
13b	0.502958608	0.0001	2.71(-9)
continued on next page			

Table E.31 – continued

	$-E$	δ	γ
13c	0.502954109	-0.0098	6.57(-12)
14a	0.502554871	0.0106	2.40(-7)
14b	0.502551043	0.0001	2.74(-9)
14c	0.502547440	-0.0098	6.16(-12)
15a	0.502225353	0.0106	2.40(-7)
15b	0.502222241	0.0001	2.77(-9)
15c	0.502219311	-0.0098	5.83(-12)

Table E.32: Doubly excited $^1N^o$ states.

|	$-E$	δ	γ
11a	0.504133238	0.0013	2.43(-7)
12a	0.503472999	0.0013	2.43(-7)
13a	0.502959192	0.0013	2.43(-7)
14a	0.502551511	0.0013	2.43(-7)
15a	0.502222622	0.0013	2.43(-7)

Appendix F

Razširjeni povzetek v slovenščini

F.1 Uvod

Atom helija je najenostavnejši tridelčni sistem v atomski fiziki, ki je eksperimentalno in računsko obvladljiv, obenem pa dovolj zapleten, da omogoča študij pojavov, katerih opis presega standardne približke s povprečnim poljem [1]. Odstopanje od tovrstnega opisa je najizrazitejše v primeru dvojno vzbujenih stanj. Že prve meritve fotoabsorpcije (sl. F.1) pri vzbujanju s sinhrotronsko svetlobo [2] so jasno pokazale, da je potrebno pri modeliranju spektrov že v najnižjem približku uporabiti korelirana dvoelektronska stanja [3].
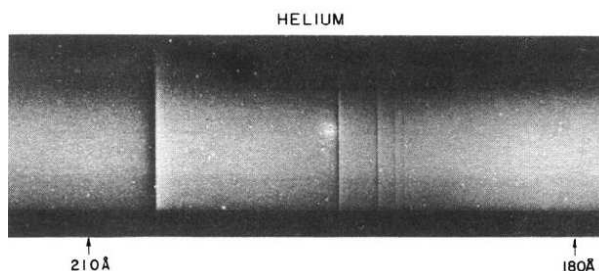
Slika F.1: Absorpcijski spekter na območju dvojno vzbujenih stanj helijevega atoma, ki sta ga posnela Madden in Codling na fotografsko ploščo leta 1963 [2].

Dvojno vzbujena stanja helijevega atoma ležijo nad prvim pragom za ionizacijo ($N = 1$) pri 24.587 eV in pod pragom za dvojno ionizacijo ($N \to \infty$), ki je 79.003 eV nad osnovnim stanjem atoma (sl. 1.1). V nadaljevanju nas bodo zanimala dvojno vzbujena stanja, ki ležijo pod drugim pragom za ionizacijo ($N = 2$). Tista s parnostjo $(-1)^L$, kjer je L skupna tirna vrtilna količina, lahko razpadejo z emisijo elektrona. Takšna stanja imenujemo resonance, razpadni proces pa avtoionizacijo. Valovno funkcijo resonančnega stanja opišemo s superpozicijo lokaliziranih (vezanih) in kontinuumskih komponent (gl. npr. [95, 96]).

Od resonanc s simetrijo $^1P^o$ - takšna atomska stanja so namreč dosegljiva iz osnovnega stanja atoma pri vzbujanju s fotoni - razpadajo z avtoionizacijo razmeroma hitro stanja, ki pripadajo Rydbergovi seriji z oznako a, stanja t.i. serij b in c pa razpadajo z manjšo verjetnostjo [4, 37]. Črte v absorpcijskih in fotoionizacijskih spektrih, ki pripadajo stanjem c, so zato ostre. Ker je tudi njihova oscilatorska moč iz osnovnega stanja majhna, ni prav nič presenetljivo, da so obstoj serije c v fotoionizacijskih spektrih eksperimentalno potrdili šele leta 1992 [5].

Praktično do konca devetdesetih let je avtoionizacija veljala za dominantni razpadni kanal dvojno vzbujenih stanj z vrtilno količino $L = 1$. Leta 1999 pa so pri razpadu zaznali tudi UV svetlobo in atome helija v metastabilnem stanju [8, 10]. Pokazali so, da je za nekatere vrste resonanc najverjetnejši fluorescenčni razpad. Povsem razumljivo je, da fluorescenčni razpad prevladuje za visoko vzbujena Rydbergova stanja, pri katerih se elektrona v povprečju gibljeta daleč narazen in je zato verjetnost za avtoionizacijo majhna. V primeru omenjene serije c pa je fluorescenčni razpad dominanten že za najnižje stanje z $n = 3$.

Pod pragom $N = 2$ lahko v fluorescenčnih spektrih dosežemo boljšo ločljivost kot v fotoionizacijskih spektrih, kjer imajo spektralne črte značilno široko asimetrično obliko zaradi interakcije s kontinuumskim kanalom. Identifikacija vrhov, katerih energije se le malo razlikujejo, je zato v fluorescenčnih spektrih lažja. Pod drugim pragom za ionizacijo je bilo tako mogoče opaziti več novih podrobnosti, recimo signal tripletnih serij dvojno vzbujenih stanj, v katera se preseli oscilatorska moč singletnih stanj zaradi sklopitve spin-tir [18].

Poleg stanj s simetrijo $^1P^o$ so za preučevanje koreliranega gibanja v atomu pomembna tudi druga, t.i. *temna stanja*, ki niso neposredno dostopna z vzbuditvijo atoma v osnovnem stanju. Stroga izbirna pravila, ki veljajo za dipolno vzbuditev s fotoni, je mogoče zaobiti, če izpostavimo atom zunanjemu električnemu polju (Starkov efekt). To med seboj sklaplja stanja z različnimi vrtilnimi količinami obeh parnosti; temna stanja tako postanejo dostopna zaradi sklopitve z optično dovoljenimi stanji $^1P^o$.

Kvantnomehanska stanja prostega atoma so lahko vezana ali kontinuumska. Ob vklopu električnega polja se atomski potencial spremeni (sl. 2.1): ionizacijski prag se pomakne k nižjim energijam, debelina potencialne bariere pa postane končna (za $z > 0$ v primeru $\boldsymbol{F} \parallel \hat{\boldsymbol{z}}$). Stanja pod premaknjenim ionizacijskim pragom, ki so bila prej vezana, se zato spremenijo v resonance. Predstavljamo si lahko, da elektron tunelira skozi nastalo bariero. Verjetnost za ta proces je majhna, če je stanje močno vezano in energijsko ločeno od ostalih stanj, kot velja npr. za osnovno stanje helijevega atoma. Osnovno stanje zato upravičeno obravnavamo kot vezano tudi v prisotnosti električnega polja.

Študij Starkovega efekta dvojno vzbujenih stanj helijevega atoma se šele pričenja. Vpliv močnega homogenega statičnega električnega polja jakosti do 84.4 kV/cm v fotoionizacijskih spektrih so do zdaj izmerili Harries in sodelavci [44]. Potrdili so teoretične napovedi Chunga in Fanga [42], da so pod pragom $N = 2$ za merljive učinke električnega polja za resonance z $n = 6 - 7$ potrebne poljske jakosti velikosti 50 kV/cm.

Vpliv električnega polja na fluorescenčni pridelek in pridelek metastabilnih atomov pa je nedavno preučevalo več eksperimentalnih skupin (Penent, Rubensson, Prince in Harries, vsi s sodelavci). Opazovali so učinke zunanjega polja na primarno in sekundarno fluorescenco dvojno vzbujenih stanj pod drugim ionizacijskim pragom v časovni in energijski domeni. Meritve so pokazale, da lahko že električne poljske jakosti velikosti nekaj kV/cm močno spremenijo obliko fluorescenčnih spektrov in zaznavno vplivajo na življenjske čase resonanc.

Vseh teh rezultatov ni mogoče razumeti brez podrobnega modeliranja prehodov med enojno in dvojno vzbujenimi stanji helija v električnem polju. Za analizo izmerjenih fotoionizacijskih in fluorescenčnih spektrov je *nujna* podrobnejša teoretična obravnava Starkovega efekta, kar je cilj pričujoče disertacije. V nadaljevanju opisujemo metodo in računske rezultate, s katerimi je mogoča resna analiza omenjenih eksperimentov. Predstavljamo torej prve celovite izračune ionskega pridelka na območju dvojno vzbujenih stanj helija v močnem električnemu polju. Napovedi smo izdelali za dve vrsti geometrije: vpadna svetloba je lahko polarizirana pravokotno ali vzporedno glede na vektor zunanjega električnega polja. Izračunali smo tudi totalni sipalni presek za neelastično sipanje fotonov na atomu helija v električnem polju za obe orientaciji vpadne svetlobe.

F.2 Formulacija problema

Helijev atom v homogenem statičnem električnem polju opišemo s Hamiltonovim operatorjem

$$H = H_0 + \Delta H \,, \tag{F.1}$$

kjer smo s H_0 označili operator prostega atoma

$$H_0 = \frac{\boldsymbol{p}_1^2}{2} + \frac{\boldsymbol{p}_2^2}{2} - \frac{Z}{r_1} - \frac{Z}{r_2} + \frac{1}{|\boldsymbol{r}_1 - \boldsymbol{r}_2|} \,, \tag{F.2}$$

z ΔH pa sklopitev z zunanjim električnim poljem:

$$\Delta H = -\boldsymbol{F} \cdot (\boldsymbol{r}_1 + \boldsymbol{r}_2) \,. \tag{F.3}$$

Uporabili smo atomske enote (gl. Dodatek A). V zgornjih enačbah sta $\boldsymbol{p}_1$ in $\boldsymbol{p}_2$ operatorja gibalnih količin obeh elektronov, z operatorjema $\boldsymbol{r}_1$ in $\boldsymbol{r}_2$ opišemo vektorja koordinat, $\boldsymbol{F}$ pa je vektor električnega polja. Naboj točkastega jedra, ki smo mu pripisali neskončno maso, smo označili z Z. Smer osi z si izberemo vzdolž električnega polja ($\boldsymbol{F} \parallel \hat{\boldsymbol{z}}$). Izbira koordinatnega sistema seveda ne vpliva na rezultate izračunov.

Izračunati želimo fotoionizacijski presek helijevega atoma v osnovnem stanju in presek za neelastično sipanje fotonov na atomu helija za vpadno svetlobo z energijo na področju dvojno vzbujenih stanj pod pragom $N = 2$ (približno 65.40 eV).

Problem helijevega atoma v električnem polju obravnavamo na dva načina: perturbativno, v prvem redu časovno neodvisne teorije motenj, in eksaktno, z metodo kompleksne rotacije. V obeh primerih izrazimo rešitve problema lastnih vrednosti v električnem polju z rešitvami prostega atoma. Pri tem obravnavamo sklopitev s fotonskim poljem v najnižjem (t.j. prvem oz. drugem) redu. V nadaljevanju se bomo na kratko posvetili neperturbativni obravnavi. Za opis atoma v električnem polju uporabimo pristop mešanja konfiguracij (configuration interaction). Stanja v električnem polju pri tem predstavimo v bazi realnih senčenih Sturm-Coulombovih funkcij [78, 82] (gl. Dodatek B).

F.3 Obravnava problema

Metoda kompleksne rotacije je že dodobra uveljavljena na področju atomske, molekularne in jedrske fizike. Z njeno pomočjo lahko predstavimo valovne funkcije kontinuumskih in nevezanih stanj v bazi kvadratno integrabilnih funkcij $\mathcal{L}^2$ [83–87]. To pomeni, da lahko s takšno bazo v celoti opišemo interakcije tipa vezano stanje-kontinuum in kontinuum-kontinuum, kljub temu, da stanja obravnavamo na enak način, kot navadno obravnavamo vezana stanja. Kompleksno rotirani Hamiltonov operator $H(\Theta)$ dobimo, če nadomestimo koordinate in momente v operatorju H po predpisu

$$\boldsymbol{r}_k \to \boldsymbol{r}_k \, e^{i\Theta} \qquad \text{in} \qquad \boldsymbol{p}_k \to \boldsymbol{p}_k \, e^{-i\Theta} \,, \qquad k = 1, 2 \,. \tag{F.4}$$

Pri tem je Θ realen parameter, ki mu pravimo rotacijski kot. V praksi je prehod v kompleksni prostor enostaven: kinetični (T), potencialni (V) in interakcijski (ΔH) del celotnega Hamiltonovega operatorja se pomnožijo s faznimi faktorji: $T \to T \, e^{-2i\Theta}$, $V \to V \, e^{-i\Theta}$, $\Delta H \to \Delta H \, e^{i\Theta}$.

Metoda kompleksne rotacije temelji na analitičnem nadaljevanju Greenovega operatorja $G(E) = (E - H)^{-1}$ v kompleksni ravnini. Vsakemu vezanemu stanju operatorja H pripada pol Greenovega operatorja, kontinuumskemu stanju pa poltrak (z začetkom pri enem od ionizacijskih pragov), kjer Greenov operator ni definiran. Resonancam, ki zadoščajo robnim pogojem

izhajajočih valov, pripadajo poli v spodnji polovici kompleksne ravnine. Pokazati se da, da je mogoče Greenov operator izraziti z operatorjema $H(\Theta)$ in $H(-\Theta)$ in se na ta način izogniti singularnostim na realni osi [87].

Operator $H(\Theta)$ ni več hermitski, njegov spekter je kompleksen. Zanj veljajo naslednje lastnosti (gl. sl. 4.1 in 4.2).

1. Kontinuumski poltraki se zavrtijo za kot -2Θ okrog ionizacijskih pragov. V primeru, ko je nabor baznih funkcij iz prostora $\mathcal{L}^2$, je kontinuum predstavljen z izoliranimi točkami, ki ležijo približno na premici.

2. Spekter vezanih stanj ostane nespremenjen (realen), valovne funkcije pa kvadratno integrabilne.

3. Če je parameter Θ dovolj velik, da zasuk kontinuumov odkrije resonance, so njihove lastne vrednosti neodvisne od Θ. Lastne vrednosti E_Θ imajo obliko $E - i\Gamma/2$, kjer je E resonančna energija, Γ pa energijska širina za avtoionizacijo.

Z Greenovim operatorjem in lastnimi stanji Hamiltonovega operatorja $H(\Theta)$ lahko enostavno izrazimo fotoionizacijski presek, če obravnavamo osnovno stanje kot vezano (gl. npr. [87, 110]):

$$\sigma(\omega_0) = 4\pi\alpha\omega_0 \operatorname{Im} \sum_n \frac{\langle\overline{\Phi_{n\Theta}}|D(\hat{\boldsymbol{e}}_0)\,e^{i\Theta}|\Phi_{g\Theta}\rangle^2}{\mathcal{E}_{n\Theta} - \mathcal{E}_g - \omega_0}\,. \tag{F.5}$$

V enačbi (F.5) je ω_0 energija linearno polariziranih vpadnih fotonov s polarizacijo $\hat{\boldsymbol{e}}_0$, α je konstanta fine strukture, $|\Phi_{g\Theta}\rangle$ in $|\Phi_{n\Theta}\rangle$ sta lastni stanji operatorja $H(\Theta)$, ki opisujeta osnovno stanje atoma v zunanjem električnem polju oz. končna stanja, ki so dosegljiva z absorpcijo fotona. Z $\mathcal{E}_{n\Theta}$ smo označili lastno vrednost, ki pripada $|\Phi_{n\Theta}\rangle$, $\mathcal{E}_g$ pa predstavlja realni del lastne vrednosti $\mathcal{E}_{g\Theta}$. Z $D(\hat{\boldsymbol{e}}_0)$ smo označili dipolni operator,

$$D(\hat{\boldsymbol{e}}_0) = \hat{\boldsymbol{e}}_0 \cdot (\boldsymbol{r}_1 + \boldsymbol{r}_2)\,. \tag{F.6}$$

Matrični element iz enačbe (F.5) izračunamo tako, da pod integralom po elektronskih koordinatah dekonjugiramo radialni del valovne funkcije $\langle\boldsymbol{r}_1, \boldsymbol{r}_2|\Phi_{n\Theta}\rangle$, medtem ko ostane kotni del nespremenjen [83, 86–88]. Ta nenavadni predpis je posledica dejstva, da operator $H(\Theta)$ ni hermitski: v bazi realnih funkcij zapišemo $H(\Theta)$ s kompleksno simetrično matriko.

V izrazu za fotoionizacijski presek (F.5) nismo upoštevali, da lahko končno stanje razpade radiativno, zaradi česar ne pride nujno do emisije elektrona. Tovrstni razpadi lahko zaznavno spremenijo obliko fotoionizacijskih spektrov, zlasti pri stanjih z majhno avtoionizacijsko širino: prispevek resonančnega stanja k celotnemu preseku za fotoionizacijo se zmanjša zaradi fluorescenčnega razpada. Razpad resonančnega stanja lahko upoštevamo z optičnim potencialom, s katerim vpeljemo v gibalne enačbe dušenje zaradi radiativnega razpada [97]. Če označimo verjetnost za fluorescenčni razpad resonance $|\Phi_{n\Theta}\rangle$ z γ_n, se njen popravljeni prispevek k fotoionizacijskemu preseku glasi

$$\sigma_n(\omega_0) \equiv 4\pi\alpha\omega_0 \operatorname{Im} \frac{\langle\overline{\Phi_{n\Theta}}|D(\hat{\boldsymbol{e}}_0)\,e^{i\Theta}|\Phi_{g\Theta}\rangle^2 + \mathcal{R}_n}{\mathcal{E}_n - i(\gamma_n + \Gamma_n)/2 - \mathcal{E}_g - \omega_0}\,,$$
$$\mathcal{R}_n = -\frac{\gamma_n}{\gamma_n + \Gamma_n}\left|\langle\overline{\Phi_{n\Theta}}|D(\hat{\boldsymbol{e}}_0)\,e^{i\Theta}|\Phi_{g\Theta}\rangle\right|^2\,. \tag{F.7}$$

Pri tem smo z Γ_n označili avtoionizacijsko širino stanja. Za izračun γ_n uporabimo izraz

$$\gamma_n \approx \frac{\alpha^3}{2\pi} \sum_\beta \sum_i (\mathcal{E}_n - \mathcal{E}_i)^3 \int \mathrm{d}^2\hat{k} \operatorname{Re} \langle\overline{\Phi_{i\Theta}}|D(\hat{\boldsymbol{e}}_\beta)\,e^{i\Theta}|\Phi_{n\Theta}\rangle^2\,. \tag{F.8}$$

V enačbi (F.8) smo upoštevali le prehode v končna enojno vzbujena stanja $|\Phi_{i\Theta}\rangle$, ki jih obravnavamo kot vezana tudi v prisotnosti polja. Uporabili smo realni del kvardata sicer kompleksnega matričnega elementa, s čimer zanemarimo sklopitev s kontinuumom pri začetnem stanju $|\Phi_{n\Theta}\rangle$ [4, 88, 95]. Energiji $\mathcal{E}_n$ in $\mathcal{E}_i$ sta realna dela lastnih vrednosti $\mathcal{E}_{n\Theta}$ in $\mathcal{E}_{i\Theta}$. Integracija v enačbi (F.8) poteka po smereh valovnega vektorja izsevane svetlobe $\boldsymbol{k}$, z $\hat{\boldsymbol{e}}_\beta$, $\beta = 1, 2$, pa smo označili linearno neodvisni polarizaciji izsevanih fotonov. Integral v (F.8) zlahka izvrednotimo z izbrano parametrizacijo za vektorje $\hat{\boldsymbol{k}}$ in $\hat{\boldsymbol{e}}_\beta$ (gl. npr. Dodatek C).

Podobno lahko zapišemo presek za neelastično sipanje fotonov na atomu helija v osnovnem stanju s pomočjo Kramers-Heisenbergove formule [90–92]. Rezultat je

$$\sigma(\omega_0) = \alpha^4 \omega_0 \sum_\beta \sum_m (\mathcal{E}_g + \omega_0 - \mathcal{E}_m)^3 \int \mathrm{d}^2 \hat{k} \, |\mathcal{M}_{mg}|^2 \,, \tag{F.9}$$

kjer je matrični element enak

$$\mathcal{M}_{mg} = \sum_n \frac{\langle \overline{\Phi_{m\Theta}} | D(\hat{\boldsymbol{e}}_\beta) e^{i\Theta} | \Phi_{n\Theta} \rangle \langle \overline{\Phi_{n\Theta}} | D(\hat{\boldsymbol{e}}_0) e^{i\Theta} | \Phi_{g\Theta} \rangle}{\mathcal{E}_g + \omega_0 - \mathcal{E}_{n\Theta}} \,. \tag{F.10}$$

Privzeli smo, da je osnovno stanje vezano, poleg tega pa kot vezana obravnavamo tudi končna stanja $|\Phi_{m\Theta}\rangle$, zato postavimo $\mathcal{E}_m = \mathrm{Re} \, \mathcal{E}_{m\Theta}$. Vsota po m zajema le enojno vzbujena stanja v električnem polju, vsota po n pa vsa stanja, ki so dostopna z absorpcijo fotona iz osnovnega stanja. V enačbi (F.10) smo zanemarili prispevke elastičnega sipanja fotonov (gl. sl. 4.3c), ker je njihov prispevek na energijskem območju dvojno vzbujenih stanj pod drugim ionizacijskim pragom relativno majhen (gl. npr. [90]). Učinke fluorescenčnega razpada resonančnih stanj $|\Phi_{n\Theta}\rangle$ tokrat upoštevamo tako, da v enačbi (F.10) nadomestimo $\mathcal{E}_{n\Theta} = \mathcal{E}_n - i\Gamma_n/2$ z izrazom $\mathcal{E}_n - i(\gamma_n + \Gamma_n)/2$.

F.4 Rezultati

F.4.1 Starkovi diagrami

Omenili smo že, da izrazimo rešitve helijevega atoma v električnem polju z rešitvami prostega atoma. V račune, ki ji predstavljamo v tem razdelku, smo vključili stanja z vrtilnimi količinami $L \leq 10$ sode in lihe parnosti. Koordinatni sistem smo zavrteli tako, da kaže zunanje električno polje v smeri osi z.

Vpliv električnega polja na energijske nivoje nazorno prikažemo s Starkovimi diagrami. Celotna tirna vrtilna količina L in parnost π v električnem polju nista več dobri kvantni števili, za $\boldsymbol{F} \parallel \hat{\boldsymbol{z}}$ pa se ohranja projekcija M celotne vrtilne količine na os z. V Starkovih diagramih zato prikažemo simetrijo $^1 L^\pi$ vodilne komponente v razvoju po stanjih prostega atoma za različne vrednosti M. Na slikah 6.1 in 6.2 sta prikazana Starkova diagrama za vzporedno ($\boldsymbol{F} \parallel \boldsymbol{P}$) in pravokotno ($\boldsymbol{F} \perp \boldsymbol{P}$) polarizacijo vpadne svetlobe glede na vektor električnega polja za energijsko območje resonanc s kvantnimi števili $n = 7 - 9$. Energijska skala je premaknjena za 2.29715 meV, za kolikor je napačno izračunana energija osnovnega stanja (gl. Dodatek E). Ta premik bomo odslej upoštevali povsod, kjer je prikazana Starkova shema energijskih nivojev. Diagram za $\boldsymbol{F} \parallel \boldsymbol{P}$ prikazuje samo stanja s parnostjo $(-1)^L$: pri izbrani smeri električnega polja in $M = 0$ je sklopitev zaradi električnega polja med stanji s parnostjo $(-1)^L$ in stanji s parnostjo $(-1)^{L'+1}$ enaka nič za poljubni vrednosti L in L'. V nadaljevanju bomo pokazali, da se optično dovoljena stanja a, b in c $^1 P^o$ zaznavno mešajo le z nekaterimi stanji iz množice stanj z različnimi simetrijami $^1 L^\pi$, ki so jim energijsko blizu.

F.4.2 Fotoionizacija

Na sliki 6.4 je prikazana primerjava med spektri, ki so jih izmerili Harries in sodelavci [44], in izračunanimi fotoionizacijskimi spektri za električne poljske jakosti med 9.17 kV/cm in 84.4 kV/cm, pri vzporedni polarizaciji vpadne svetlobe glede na smer električnega polja. Vsi izračunani spektri so raztegnjeni v navpični smeri z istim konstantnim faktorjem, tako da se cela skupina najbolje ujema z meritvami. Spektri so dodatno razmaknjeni vzdolž ordinate zaradi preglednosti. Zaradi primerjave je izračunani fotoionizacijski presek razmazan z Gaussovo funkcijo širine 1.4 meV FWHM, ki opisuje eksperimentalno prenosno funkcijo.

Izmerjeni in izračunani preseki se ujemajo razmeroma dobro. Pri nizkih električnih poljih so prisotna večja nihanja izmerjenega signala. Iz izračunani spektrov bi pričakovali, da tam šum meritev preglasi učinek zunanjega polja. Za poljske jakosti nad 30 kV/cm pa so vrhovi blizu resonance $6a$ $^1P^o$ že jasno vidni. To potrjuje teoretične napovedi Chunga in Fanga [42], ki jih je dala metoda SP-CR (Saddle Point Complex Rotation).

Širše območje ($n = 6, 7$) prikazuje slika 6.5 za električni poljski jakosti 50.5 kV/cm in 84.4 kV/cm. Teorija in eksperiment se v obeh primerih zelo dobro ujemata: račun lahko pojasni vse prikazane podrobnosti pri višji jakosti polja. Zato bi pri nižji jakosti pričakovali kvečjemu boljše ujemanje, vendar se to ne zgodi. Trenutno še ni jasno, kateri atomski efekti bi lahko pojasnili oscilacije, ki se kažejo pri nižjih poljih.

Na slikah 6.5 in 6.6 so prikazani tudi spektri za pravokotno polarizacijo ($\boldsymbol{F} \perp \boldsymbol{P}$), ki pa še niso bili izmerjeni. Poleg modulacije amplitud posameznih vrhov zaradi spremembe jakosti električnega polja, opazimo v teh spektrih tudi vrhove, ki jih pri vzporedni geometriji ($\boldsymbol{F} \parallel \boldsymbol{P}$) ni. Sklepamo, da gre za prispevke stanj s parnostjo $(-1)^{L+1}$.

Natančnejšo obravnavo fotoionizacijskih spektrov omogoča analiza Starkovih diagramov. Na slikah 6.10 in 6.11 so prikazani izračunani spektri za vzporedno in pravokotno polarizacijo glede na smer električnega polja. Vsak izmed spektrov je navpično premaknjen tako, da njegov premik ustreza električni poljski jakosti, pri kateri je bil izračunan. Barve, s katerimi so predstavljeni nivoji Starkovega diagrama ustrezajo klasifikaciji stanj, ki sta jo uporabila Tong in Lin pri opisu *prednostnega pravila* (propensity rule) [45]. Pri tem je treba opozoriti, da oznake stanj a, b in c, ki sta jih uporabila avtorja, niso enake oznakam, ki jih je uvedel Lipsky za stanja pod pragom $N = 2$ [37]. Tong in Lin sta v isto skupino uvrstila stanja, ki imajo podoben korelacijski vzorec. Zaradi preglednosti smo njune oznake preimenovali v a^*, b^* in c^*. Povezavo med obema vrstama oznak podaja tabela 6.1. Na slikah 6.10 in 6.11 smo uporabili vijolično v primeru, ko pripada vodilna komponenta stanja seriji a^*, svetlo modro v primeru, ko pripada seriji b^*, in zeleno, ko pripada seriji c^*.

Medtem ko prispevek resonance $6a^*$ $^1P^o$ ostane izrazit tudi pri višjih poljih, je identifikacija vrha, ki pripada stanju $7a^*$ $^1P^o$ pri večjih poljskih jakostih težja. Oscilatorska moč se porazdeli med bližnja stanja, s katerimi je stanje $7a^*$ $^1P^o$ močno skopljeno zaradi polja. Takšno prerazporeditev moči opisuje t.i. *sumacijsko pravilo* (sum rule), ki sta ga za fotoionizacijo v električnem polju zapisala Fang in Chung [110]. Omeniti velja, da drži pravilo samo v primeru, ko ne upoštevamo radiativnega razpada na način, ki je bil opisan v prejšnjem razdelku. Kot je razvidno s slik 6.10 in 6.11, se lahko v električnem polju stanja s simetrijo $^1P^o$ mešajo s stanji prostega atoma, ki prej niso bila dostopna z absorpcijo. Vrhove v spektru $\boldsymbol{F} \parallel \boldsymbol{P}$, ki sledijo $6a^*$ $^1P^o$, pripišemo po naraščajočih energijah največji primesi stanja prostega atoma $6b^*$ $^1G^e$, $^1F^o$, $^1H^o$ in $^1I^e$. Sledijo jim vrhovi $6a^*$ $^1F^o$, $^1D^e$, $^1G^e$ in $^1H^e$, $6c^*$ $^1G^e$, $^1F^o$ in $^1D^e$, $^1P^o$ ter $6b^*$ $^1S^e$. Podobno mešanje je prisotno v primeru $n = 7$ in tudi za pravokotno polarizacijo ($\boldsymbol{F} \perp \boldsymbol{P}$), kjer pa so prisotne še primesi stanj s parnostjo $(-1)^{L+1}$.

Sliki 6.10 in 6.11 govorita v prid že omenjenemu prednostnemu pravilu, ki v grobem pravi,

da polje močneje sklaplja stanja z istim tipom korelacij. Ker so v odsotnosti električnega polja iz osnovnega stanja z daleč največjo verjetnostjo dostopna stanja a^* $^1P^o$, v skladu s pravilom pričakujemo, da bodo izraziti vrhovi izhajali iz stanj a^*. Kot je razvidno s slik, potrdi račun veljavnost pravila tudi za pravokotno eksperimentalno postavitev ($\boldsymbol{F} \perp \boldsymbol{P}$), kjer ostajajo amplitude vrhov z vodilnimi komponentami tipa b^* in c^* razmeroma majhne tudi za stanja z $n = 7$.

F.4.3 Neelastično sipanje fotonov

Sliki 6.14 in 6.15 prikazujeta primerjavo med izračunanimi in eksperimentalnimi fluorescenčnimi pridelki, ki so jih izmerili Prince in sodelavci [47]. Za $\boldsymbol{F} \perp \boldsymbol{P}$ so izmerjeni spektri normirani na ploščino dubleta $5c/6b$ $^1P^o$, medtem ko so spektri za $\boldsymbol{F} \parallel \boldsymbol{P}$ normirani na velikost skoka v fluorescenčnem signalu na pragu $N = 2$. Izračunani spektri so razmazani z Gaussovo funkcijo širine 3 meV (FWHM) in pomnoženi s skupnim konstantnim faktorjem, tako da se ujemajo z eksperimentom. Spektri so zaradi jasnosti razmaknjeni v vzdolžni smeri.

Amplitude vrhov, ki pripadajo seriji a $^1P^o$, se močno povečajo, ko vklopimo električno polje. Ta sprememba intenzitete je v glavnem posledica fluorescence, ki izhaja iz trkov nabitih delcev [47] z deli eksperimentalne opreme; ioni in elektroni se najbolj sproščajo iz dvojno vzbujenih stanj, ki rada razpadejo z avtoionizacijo. Emisijske črte v fluorescenčnih pridelkih imajo v tem primeru asimetrično (Fanovo) obliko. Pri primerjavi izračunov z meritvami je zato potrebno upoštevati tudi omenjeno ionsko komponento. Omeniti pa velja, da je ta efekt zanemarljiv pri stanjih drugih simetrij. Na slikah 6.14 in 6.15 je celotni fluorescenčni pridelek (rdeča) razklopljen na vsoto fotonskega (modra) in ionskega (zelena) signala.

V splošnem izračunani spektri dobro opišejo izmerjeni signal. Lege in intenzitete vrhov izračunanih spektrov se ujemajo z eksperimentalnimi podatki do približno $n = 10$ ali $n = 11$. Široki vrhovi, ki se pojavijo v spektrih nad stanji na $^1P^o$ v bližini praga $N = 2$, vsebujejo prispevke stanj, ki so sklopljena z optično dovoljenimi stanji simetrije $^1P^o$. Pri visokih kvantnih številih n prispevajo tudi stanja z višjimi vrtilnimi količinami, ki pa jih nismo vključili v račun. Model zato odpove pri stanjih z $n \gtrsim 10$. Računi se nekoliko bolje ujemajo z meritvami Rubenssona in sodelavcev [111], ki vsebujejo le primarni fluorescenčni signal (slika 6.16), vendar je njihov doseg približno enak.

Posamezne vrhove v izmerjenih spektrih prepoznamo s pomočjo Starkovih diagramov (sliki 6.17 in 6.18). Za obe orientaciji polarizacije vpadne svetlobe pripada večji del najmočnejših vrhov stanjem z vodilnimi komponentami iz (super)serije a^*, kar potrjuje veljavnost prednostnega pravila tudi pri fluorescenci. Pri pravokotni polarizaciji vpadne svetlobe tako opazimo serijo močnih vrhov, ki so na spodnji strani omejeni z dubletom $(n-1)c^*/nb^*$ $^1P^o$, na drugi pa z vrhom na^* $^1P^o$; večina jih izvira iz stanj a^* $^1P^e$. Prednostnemu pravilu v prid govorijo tudi močni vrhovi, ki se razvijejo iz stanj $6a^*$ in $7a^*$ $^1D^o$ (sl. 6.18). Pričakovali bi namreč, da je zaradi lihe parnosti sklopitev, ki jo inducira zunanje polje, šibka.

Pri vzporedni polarizaciji vpadne svetlobe opazimo, da se velikost dubleta $(n-1)c^*/nb^*$ $^1P^o$ močno zmanjša, ko vklopimo električno polje. To razložimo z mešanjem bližnjih stanj $^1S^e$ in $^1D^e$, za katera je značilen zelo verjeten razpad z avtoionizacijo, ki zmanjša fluorescenčni pridelek. Vpliv primesi avtoionizirajočih stanj je manj izrazit v primeru $\boldsymbol{F} \perp \boldsymbol{P}$, saj je sklopitev s stanji s simetrijo $^1S^e$ enaka nič.

Izjava

Disertacija predstavlja rezultate mojega samostojnega znanstvenoraziskovalnega dela.

Ljubljana, 5. 9. 2006   Andrej Mihelič